Materials Science & Engineering R 139 (2020) 100518

Contents lists available at ScienceDirect

Materials Science & Engineering R

journal homepage: www.elsevier.com/locate/mser

Materials development and potential applications of transparent ceramics: A review

Zhuohao Xiao[a], Shijin Yu[b], Yueming Li[a], Shuangchen Ruan[c], Ling Bing Kong[c,*], Qing Huang[d], Zhengren Huang[d], Kun Zhou[e], Haibin Su[f], Zhengjun Yao[g], Wenxiu Que[h], Yin Liu[i], Tianshu Zhang[i], Jun Wang[j], Peng Liu[j], Deyuan Shen[j], Mathieu Allix[k], Jian Zhang[l], Dingyuan Tang[m]

[a] School of Materials Science and Engineering
[b] School of Mechanical and Electronic Engineering, Jingdezhen Ceramic Institute, Jingdezhen, 333001, Jiangxi, China
[c] College of New Materials and New Energies, Shenzhen Technology University, Shenzhen, 518118, Guangdong, China
[d] Ningbo Institute of Materials Engineering and Technology, Chinese Academy of Science, Ningbo 315201, Zhejiang, China
[e] School of Mechanical & Aerospace Engineering, Nanyang Technological University, 50 Nanyang Avenue, Singapore 639798, Singapore
[f] Department of Chemistry, The Hong Kong University of Science and Technology, Clear Water Bay, Hong Kong, China
[g] College of Materials and Technology, Nanjing University of Aeronautics and Astronautics, Nanjing 211100, Jiangsu, China
[h] Electronic Materials Research Laboratory, School of Electronic and Information Engineering, Xi'an Jiaotong University, Xi'an 710049, Shaanxi, China
[i] School of Materials Science and Engineering, Anhui University of Science and Technology, Huainan 232001, Anhui, China
[j] Jiangsu Key Laboratory of Advanced Laser Materials and Devices, School of Physics and Electronic Engineering, Jiangsu Normal University, Xuzhou, 221116, Jiangsu, China
[k] Laboratoire CEMHTI, UPR 3079-CNRS, Orléans, France
[l] Shanghai Institute of Ceramics, Chinese Academy of Sciences, Shanghai, 201800, P. R. China
[m] School of Electric and Electronic Engineering, Nanyang Technological University, 50 Nanyang Avenue, Singapore 639798, Singapore

ARTICLE INFO

Keywords:
Transparent ceramics
Hot pressing (HP)
Hot isostatic pressing (HIP)
Spark plasma sintering (SPS)
Vacuum sintering
Densification
Microstructure
Optical transmittance
IR transmittance
Mechanical strength
Thermal stability
Solid-state lasers
Composite armor
IR window/dome
White lighting
Nanocomposite ceramics

ABSTRACT

Transparent ceramics have various potential applications such as infrared (IR) windows/domes, lamp envelopes, opto-electric components/devices, composite armors, and screens for smartphones and they can be used as host materials for solid-state lasers. Transparent ceramics were initially developed to replace single crystals because of their simple processing route, variability in composition, high yield productivity, and shape control, among other factors. Optical transparency is one of the most important properties of transparent ceramics. In order to achieve transparency, ceramics must have highly symmetric crystal structures; therefore, the majority of the transparent ceramics have cubic structures, while tetragonal and hexagonal structures have also been reported in the open literature. Moreover, the optical transparency of ceramics is determined by their purity and density; the production of high-purity ceramics requires high-purity starting materials, and the production of high-density ceramics requires sophisticated sintering techniques and optimized sintering aids. Furthermore, specific mechanical properties are required for some applications, such as window materials and composite armor. This review aims to summarize recent progress in the fabrication and application of various transparent ceramics.

1. Introduction

Conventional transparent materials include glasses, polymers, and alkali hydrides, all of which are mechanically weak and chemically unstable [1]. Single crystals of some inorganic materials are also optically transparent, and these are much stronger and more stable than their conventional counterparts. However, the fabrication of single crystals is usually called "growth" as it is mainly controlled by thermodynamic processes that are relatively slow. Furthermore, growing large single crystals is often challenging, especially for oxide materials with extremely high melting points, and the as-grown single crystals cannot be directly used because their shapes are determined by the

* Corresponding author.
E-mail addresses: lbkongntunus@126.com, konglingbing@sztu.edu.cn (L.B. Kong).

https://doi.org/10.1016/j.mser.2019.100518
Received 28 May 2019; Accepted 19 August 2019
Available online 01 October 2019
0927-796X/ © 2019 The Authors. Published by Elsevier B.V. This is an open access article under the CC BY-NC-ND license (http://creativecommons.org/licenses/BY-NC-ND/4.0/).

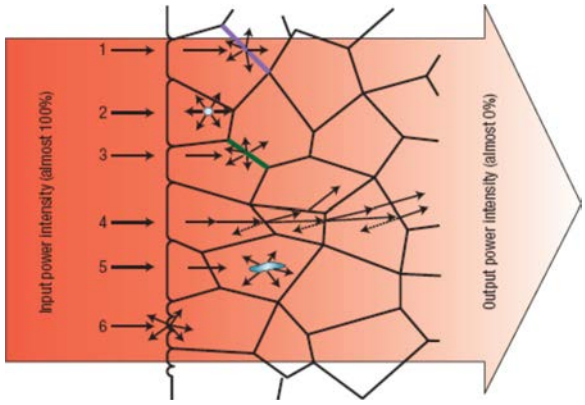

Fig. 1. Possible sources of light scattering in ceramics: (1) grain boundaries, (2) pores, (3) impurities, (4) double refraction, (5) secondary phase, and (6) surface roughness. Reused from [2], Copyright © 2008, Nature Publishing Group.

growth process. Consequently, transparent ceramics have emerged as promising candidates to replace their single-crystal counterparts because of their outstanding advantages, which include low cost, large-scale production, malleability, and high mechanical strength. Moreover, ceramic microstructures have more sources of light scattering than single crystals, such as pores, grain boundaries, impurities, and birefringence effects, which are schematically illustrated in Fig. 1 [2].

Of the factors that contribute to light scattering, scattering by pores is the main contributor to light attenuation in transparent ceramics. Near the surface of pores light is reflected and refracted by both trapped air and the ceramic material, which has different optical properties. Therefore, porous ceramics are not transparent, regardless of whether the pores are intergrained or intragrained. Of the two pore types, intragrained pores are more difficult to remove and their formation is closely related to the quality of the precursor powders, especially when using hard agglomerates.

Grains and grain boundaries in ceramics are likely to have different properties; thus, interfaces act as scattering sources. Because grains are the main phase of ceramics, the properties of grain boundaries play a significant role in determining the transparency of ceramics and thus controlling the quality of grain boundaries is an important strategy for achieving high optical transparency. Moreover, impurities are often located at grain boundaries, which increases the difference between the grains and boundaries and causes further light scattering. Therefore, precursor materials should have sufficiently high purities. However, when using sintering aids, there is a competitive effect between densification and the impurity concentration that should be optimized. Generally, the amount of sintering aids added to transparent ceramics is much lower than that added to ceramics for other applications with requisite mechanical and electrical properties.

Not all materials can be used to make transparent ceramics as the grains in ceramics with low symmetric structures are optically anisotropic, which causes light to scatter when it travels across the grain boundaries. Therefore, transparent ceramic materials must have highly symmetric crystal structures; the majority of transparent ceramics have a cubic structure [3–5], and some materials with tetragonal and hexagonal structures can also be made into transparent ceramics, although these are more difficult to process. Consequently, the development of transparent ceramics is an important and interesting research topic [6].

Ceramic processing involves three main steps: (i) powder preparation, (ii) green body formation, and (iii) sintering [7]. These steps are critical to transparent ceramics with high optical properties. If the ceramics are directly prepared from precursor powders – such as oxides, hydroxides, carbonates, or other salts – the process is considered to be a solid-state reaction method, which is the most popular method for industrial production [8–13]. Alternatively, powders can be prepared by various chemical routes, including chemical precipitation (for single oxides) or coprecipitation (for complex oxides) [14–22], sol-gel processes [23,24], gel combustion [25–28], and hydrothermal reactions [29–32].

The solid-state reaction method is simple and scalable, which make it more cost-effective than other methods. However, sample homogeneity can be a serious issue for solid-state reactions because they use solid precursors. Conversely, while wet-chemical routes ensure high homogeneity and good sintering behavior, they are only suitable for laboratory studies because they are complicated, require expensive chemicals, and have low productivity. In solid-state laser applications, homogeneous distribution of active materials is critical to laser performance; therefore, hybrid processes are used to ensure homogeneous distribution of the dopants. For example, a combined solid-state and wet-chemical synthesis has been developed, wherein the main materials are solids and the dopants are incorporated through a wet-chemical process [33].

In most studies, cold isostatic pressing (CIP) is crucial in order to achieve high densification during the final sintering process as CIP can increase the densities of the green bodies by 5–10% [34,35]. While pressure-less sintering, such as vacuum sintering and microwave sintering, usually results in ceramics with large grain sizes (up to hundreds of micrometers), pressure sintering, including hot-pressing (HP), hot isostatic pressing (HIP), and spark plasma sintering (SPS), has been used to suppress the grain growth of transparent ceramics as fine-grained ceramics have relatively high mechanical properties [36–42].

Initially, transparent ceramics were mainly used in solid-state lasers, but a recent survey has indicated that potential applications of transparent ceramics include solid-state lighting, scintillating applications, composite armors, optical components, electro-optical devices, and even biomedical materials. Although the development of transparent ceramics has progressed significantly and specific reviews have been published, a comprehensive and critical review of transparent ceramics is still lacking. For example, Johnson et al. published a condensed, 13-page review of transparent ceramics in 2012 [43], Goldstein summarized the relationship between processing and the performance of transparent $MgAl_2O_4$ ceramics in the same year [44], and du Merac et al. followed with a relatively detailed review of $MgAl_2O_4$ in 2013 [45]. More recently, Goldstein and Krell provided a comprehensive review of various transparent ceramics developed in the last 50 years, but they did not include many of the new potential applications, such as scintillation, lighting, opto-electric devices, and non-oxide materials [46]. The authors of this review published a review of transparent ceramics nearly six years ago; however, the earlier review did not cover non-oxide transparent ceramics or discuss the applications of transparent ceramics in sufficient detail [1]. More importantly, significant advances in transparent ceramics have been made in the last five years. Therefore, this review aims to provide a comprehensive summary of recent progress in the development, characterization, and applications of transparent ceramics, with a focus on materials that have been reported in the open literature over the last decade.

2. Transparent ceramic materials

2.1. Metal oxides

Oxides form the largest group of transparent ceramics. The majority of studies have focused on oxide-based transparent ceramics because they are mechanically stronger than fluorides, more chemically stable than non-oxides, and easier to synthesize than non-oxides such as ALON and Si_3N_4. Representative oxides that have been used to develop transparent ceramics are listed in Table 1, which includes basic crystal lattice parameters and physical properties.

2.1.1. Alumina (Al_2O_3)

Alumina (Al_2O_3), also known as corundum, has potential applications as high-pressure metal halide lamp envelopes, electromagnetic

SDC EX. 1018 - 2/66

Table 1
Representative transparent oxide ceramics and some of their basic physical properties.

Chemical formula	Crystal structure	Lattice constant	W_m	Density (g/cm^3)	T_m (°C)	T_b (°C)	Ref.
Al_2O_3	Hexagonal	a = 4.754 Å c = 12.99 Å	101.69	3.60	2054	2980	[844,845]
MgO	Cubic	a = 4.217 Å	40.30	3.59	2852	3600	[846]
ZrO_2	Monoclinic (RT) Tetragonal (> 1100 °C) Cubic (> 1900 °C)	a = 5.143 Å b = 5.194 Å c = 5.298 Å β = 99.218° a = 5.094 Å b = 5.174 Å a = 5.105 Å	123.22	5.85	2680	4300	[847,848]
Y_2O_3	Cubic	a = 10.6 Å	225.81	5.01	2430	4300	[849]
Sc_2O_3	Cubic	a = 9.84 Å	138.20	3.86	2403	/	[850]
Lu_2O_3	Cubic	a = 10.393 Å	397.93	9.42	2510	/	[851]
$Y_3Al_5O_{12}$	Cubic	a = 12.02 Å	593.70	4.55	1950	/	[852]
$MgAl_2O_4$	Cubic	a = 8.08 Å	142.26	3.60	2250	/	[853]
$3A1_2O_3{\cdot}2SiO_2$	Orthorhombic	a = 7.540 Å b = 7.680 Å c = 2.885 Å	432.10	3.16	1840	/	[854]

domes, and transparent armors, and transparent Al_2O_3 ceramics can be used to replace sapphires [47,48]. Some applications require specific mechanical properties (e.g. transparent armors), and the mechanical properties of Al_2O_3 ceramics can be optimized by controlling grain size [49–53]. Transparent Al_2O_3 ceramics can be fabricated by different methods, which have different effects on grain size. During the early stage of development, only translucent Al_2O_3 ceramics could be fabricated, and these were used as lamp envelopes. Because the early methods required very high sintering temperatures (≥ 1900 °C), the grain sizes of the ceramics were on the scale of tens of micrometers and the in-line transmittance was only approximately 10% [54]. In order to increase the transmittance of these ceramics to 15–20%, the sintering temperature would need to be increased, which would consequently form grains as large as 200 μm. Moreover, mechanical strength was tremendously weakened by increasing the sintering temperature. In order to reduce the sintering temperature, ceramic synthesis must use more advanced sintering techniques, optimize the concentration of sintering aids, and adopt new processing strategies as these promote densification and prohibit grain growth.

Representative examples of the fabrication of transparent Al_2O_3 ceramics are listed in Table 2. Hot isostatic pressing (HIP) has been widely acknowledged as an effective technique; for example, Mizuta et al. developed fine-grained translucent Al_2O_3 ceramics with in-line transmittance up to 46% and mechanical strength of 600–800 MPa using HIP combined with a vacuum-pressure slip-casting process [54]. The green bodies were presintered in air at 1240 °C for 2 h, with heating and cooling rates of 40 °C/min and 5 °C/min, respectively. The sintered samples were further treated with HIP: 1050–1400 °C for 1 h at 150 MPa. During HIP, the heating rates were 30 °C/min to 500 °C, 20 °C/min to 1050 °C, and 10 °C/min to the final sintering temperature, and the pressure was increased at a rate of 3.4 MPa/min above 500 °C. Samples typically demonstrated maximum transparency after sintering at 1350 °C, reaching 46%.

Experimental results have shown that high sintering temperatures form transparent Al_2O_3 ceramics with very large grains, which impair mechanical strength. Moreover, large grains cause birefringence and thus reduce the optical transparency of the ceramics [55]. Therefore, if both high transmittance and high mechanical strength are required, the grain growth of ceramics must be controlled during the sintering process [49,50,54–58].

Petit et al. reported a strategy for fabricating Al_2O_3 ceramics using HIP combined with a colloidal dispersion casting step and pre-sintering process [59]. The optical transmittance of these Al_2O_3 ceramics reached 60% for 1-mm thick samples, while the average grain size was only approximately 600 nm. The precursor used by Petit et al. was a commercial Al_2O_3 suspension, in which the Al_2O_3 particles were high purity α-alumina and ranged from 100 to 150 nm. The green bodies were prepared by vacuum filtration through nylon filters with 0.2 μm diameter pores. After vacuum drying at 65 °C for 15 h and subsequent calcination at 600 °C for 0.5 h, the green bodies were sintered at 1200 °C for 2–17 h under 10^{-6} mbar. The presintered samples had relative densities greater than 90% and finally underwent HIP in Ar at 1200 °C and 170 MPa for 3–5 h. This is a promising strategy for developing Al_2O_3 ceramics with fine grains in order to achieve high mechanical strength.

Trunec et al. developed a process for fabricating transparent Al_2O_3 ceramics by combining HIP with a gel-casting process and pressure-less calcination [60]. This process yielded highly transparent Al_2O_3 ceramics when zirconia and spinel nanoparticles were used as the sintering aids; the optimal doping concentrations were 0.3 wt% zirconia and 0.175 wt% spinel. The grain size of the transparent Al_2O_3 ceramics was effectively controlled by the dual-dopant and the increased densification of the powder improved the in-line transmittance. Under the optimal processing conditions, the resultant Al_2O_3 ceramics possessed a maximum in-line transmittance of 70.4% at 632.8 nm for samples that were 0.8-mm thick, and the IR transmittance between 2000 and 4000 nm reached theoretical levels. Moreover, this process was comparable to near-net shape and thus has potential for large-scale production and industrial applications.

Drdlíková et al. prepared transparent Al_2O_3 ceramics for visible light photoluminescence applications by doping the ceramics with 0.1–0.17 at% Er^{3+} and using HIP combined with a wet shaping method [61]. These samples demonstrated real in-line transmittance ranging from 28 to 56%. The starting material was high-purity commercial Al_2O_3 powder with 150 nm particles and a specific surface area of 13.7 m^2/g, and aqueous suspensions with 45 vol% Al_2O_3 were prepared using high purity deionized (DI) water and a commercial dispersant. Two Er_2O_3 nanopowders were used as the dopant; one was derived from a commercially available large-grained Er_2O_3 powder by dissolving in HNO_3 and precipitating with citric acid, and the other was a commercially available high purity Er_2O_3 nanopowder with 20–30 nm particles. The Er_2O_3 powders were added to the Al_2O_3 suspensions before drying under ambient conditions and subsequent drying at 80 °C for 5 h. All green bodies were presintered by one of two processes – single-step presintering (SSP) or two-step presintering (TSP) – to obtain 95–96% relative density with only closed pores [61]. The SSP process consisted of heating the samples to 1480 °C at 20 °C/min without dwelling, and then cooling at the same rate. For TSP, the samples were first heated to 1430–1440 °C (T1) without dwelling in order to reach 88–90% relative density, and were then cooled to 1280 °C (T2) at 20 °C/min; the T2 sintering step was 10 h, followed by HIP in Ar at 1280 °C and 200 MPa for 3 h. The TSP process was determined to yield high transparency Al_2O_3 ceramics more effectively than the SSP process. Representative scanning electron microscopy (SEM) and transmission electron microscopy (TEM) results of the transparent Al_2O_3 ceramics are shown in Figs. 2 and 3, and their high quality optical performance is depicted in the Fig. 4.

Transparent Al_2O_3 ceramics have also been developed using spark plasma sintering (SPS) [62–66]; for example, Suarez et al. attempted to manipulate the grain size of transparent Al_2O_3 ceramics using SPS and a self-doping method [62]. Moreover, Schehl et al. doped high-purity commercial Al_2O_3 nanopowder with aluminum ethoxide through a

SDC EX. 1018 - 3/66

Table 2
Processing parameters and optical transmittance of transparent Al_2O_3 ceramics.

No.	Powder processing	Sintering parameters	Transmittance	Ref.
1	Slip casting 77 wt% Al_2O_3	Presintering: 1240 °C/2 h Heating rate: 40 °C/min Cooling rate: 5 °C/min HIP: 1050–1400 °C/1 h, 150 MPa	46% at 600 nm	[54]
2	Gel casting, 76–78 wt% Al_2O_3, pH = 4 (acidic) or 8–9 (basic); 0.03 wt% MgO	Pre-sintering: 1240–1250 °C/2 h HIP: 1150–1400 °C, 200 MPa	55–65% at 650 nm	[49]
3	Colloidal casting Particle size: 100–150 nm	Presintering: 1200 °C/2–17 h Vacuum: 10^{-6} mbar HIP: 1200 °C/3–5h, 170 MPa	60% at 600 nm	[59]
4	Gel casting 0.3 wt% ZrO_2, 0.175 wt% spinel	Presintering: 1210–1340 °C/2 h Heating rate: 5 °C/min HIP: 1190–1295 °C/3 h, 198 MPa	70.4% 632.8 nm	[60]
5	Solution casting 0.10–0.17 at% Er^{3+}	One step presintering: 1480 °C/0 h Two step pre-sintering: T1 = 1430–1440 °C/0 h; T2 = 1280 °C/10 h HIP: 1280 °C/10 h, 200 MPa	28–56% at 300–700 nm	[61]
6	Commercial powder with self-doping of nanoparticles	SPS: 1100–1400 °C/0–30 min Heating rate: 100 °C/min Pressure: 80 MPa Vacuum: 0.1 mbar	50% at 700 nm	[62]
7	Commercial powder doped with 0.5 wt% CeO_2	SPS: 1430 °C/2 min Pressure: 80 MPa	55% at 1000 nm	[63]
8	Commercial powder doped with La_2O_3, MgO, Y_2O_3 (450 ppm)	SPS: 1350–1400 °C Pressure: 50 MPa, 100 MPa	55% at 640 nm	[64]
9	Commercial slurry doped with La_2O_3, MgO, ZrO_2 (100–500 ppm)	SPS: 800 °C; 1100 °C at 1 °C/min; 1180–1280 °C at 1 °C/min Pressure: 80 MPa	45% at 750 nm	[65]
10	Commercial powder	SPS: 1150 °C/1 h Heating rate: 100 °C/min Pressure: 80 MPa	20% at 645 nm	[66]
11	Commercial powder with no dopant	SPS: 950–1000 °C/20 min Heating rate: ~10 °C/min Pressure: 200, 400, and 500 MPa	65% at 645 nm	[70]
12	Commercial powder (~100 nm)	SPS: 800 °C Pressure: 7.7 GPa	71% at 640 nm	[71]
13	Freeze drying with slip casting	SPS: 900–1100 °C Heating rate: 100 °C/min Pressure: 70 MPa; 30 min; 500 MPa/20 min; 1000 GPa/20 min	70% at 600 nm	[72]
14	Tape casting with copolymers, isobutylene and maleic anhydride	Sintering: 1750–1850 °C/5 h Heating rate: 10 °C/min Vacuum: 10^{-5}–10^{-6} Pa	28% at 600 nm	[77]
15	Tape casting with PVA (8–10 vol%)	CIP: 200 MPa/2 min Sintering: 1810 °C/5 h Vacuum: 10^{-3} Pa	35% at 600 nm	[78]
16	Tape casting with PVB (6 wt%)	CIP: 200 MPa/10 min Warm pressing: 30 MPa, 100 °C/10 min Sintering: 1200 °C/0 h (5 °C/min); 1500 °C/5 h (2 °C/min); 1700 °C/10 h (1 °C/min)	35% at 600 nm	[79]

Fig. 2. Representative SEM image of Er^{3+}-doped Al_2O_3 ceramics after HIP. Reused from [61]. Copyright © 2017, Elsevier.

colloidal process [67]. In this process, a precursor solution of aluminum ethoxide dissolved in anhydrous ethanol under Ar was added to a suspension of Al_2O_3 in ethanol to form slurries, which were predried at 60–70 °C with magnetic stirring and dried at 120 °C in air to completely remove the ethanol. The dried samples were calcined at 800 °C for 2 h and pellet samples were made from the powders at a uniaxial pressure of 30 MPa. The pellet samples were sintered at 1100–1400 °C for 0–0.5 h; the heating rate, pressure, and vacuum were 100 °C/min, 80 MPa, and 0.1 mbar, respectively. Schehl et al. demonstrated that doping altered the mechanism of atomic diffusion during the SPS process as a transition from volume diffusion to grain boundary diffusion occurred; therefore, the microstructure and grain size of the resultant Al_2O_3 ceramics could be controlled. Furthermore, the activation energy of SPS Al_2O_3 was approximately 50% less than that of conventional sintering.

The doped powders synthesized by Schehl et al. began to shrink at lower temperatures than their pure counterparts because the applied pressure induced rearrangement of the Al_2O_3 grains without sintering. Without dwelling during sintering, the pure and doped samples possessed similar microstructures; however, after sintering at 1100 °C for 30 min, significant differences were observed as the pure samples were highly densified with visible grain growth whereas almost no grain growth was visible in the self-doped samples. In the doped samples, the Al_2O_3 nanoparticles were attached to the surface of the large particles and consequently separated, which modified the sintering behavior. The densification of the doped powders did not approach completion until the temperature reached 1340 °C, which was approximately 50 °C higher than that of the pure samples because self-doping increased the energy barrier for atomic diffusion. Grain reorientation during the initial stage of sintering was hindered by the nucleated particles present in the doped samples before ions began diffusing through the grain boundaries. The doped samples sintered at 1300 °C possessed larger grains than the undoped samples; this suggests that the dopant hindered the grain growth of Al_2O_3, which may be explained in terms of the stages of sintering as sintering is governed by grain rearrangement during the initial stage [68,69]. Therefore, dopants are very useful for controlling the grain growth of transparent ceramics.

Grasso et al. used high-pressure (> 400 MPa) SPS to fabricate highly transparent alumina ceramics with 65.4% optical transmittance and an average grain size of 200 nm [70]. One of the important conclusions of this study was that low-cost carbon fiber composite (CFC)

SDC EX. 1018 - 4/66

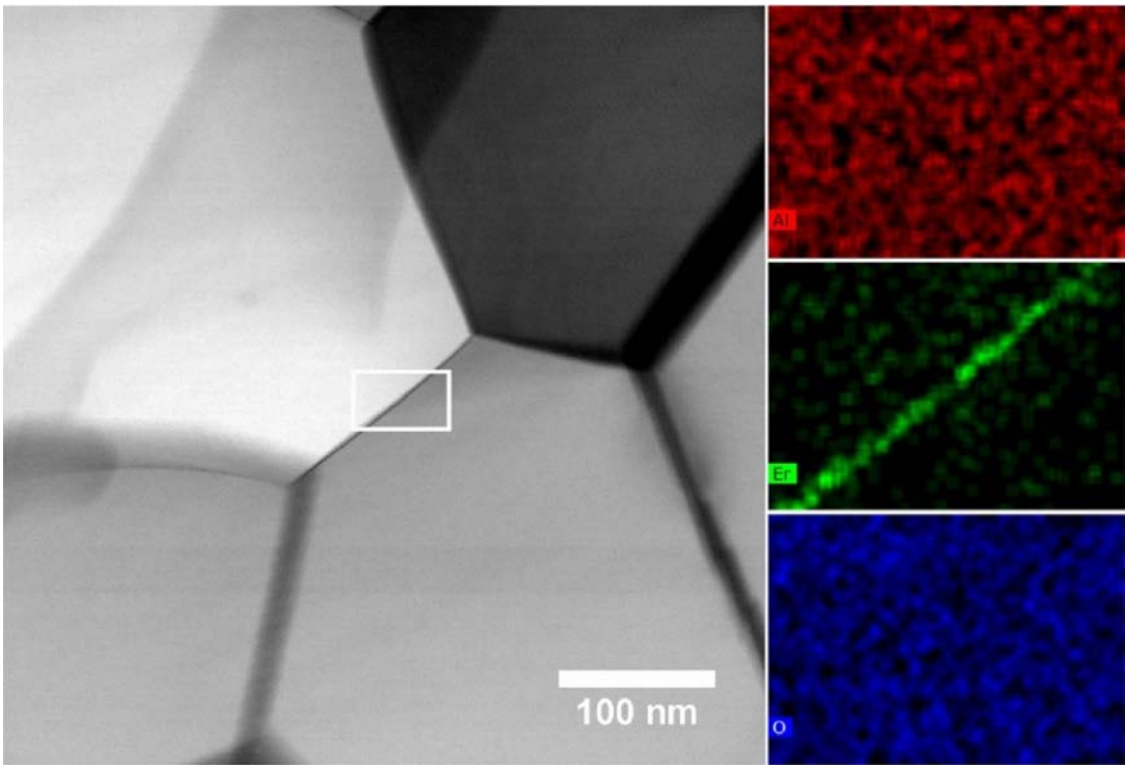

Fig. 3. TEM image and EDS profiles (Al, Er, O) of the 0.1 at% Er^{3+}-doped Al_2O_3 grain boundary. Reused from [61]. Copyright © 2017, Elsevier.

can be used for the pressing punches. In this study, 0.6 g of high-purity commercial Al_2O_3 powder was heated to 1000 °C at 10 °C/min and the pressure was gradually raised when the temperature was 800–1000 °C at 10 °C/min. After reaching 1000 °C, the displacements of the samples with CFC and tungsten carbide (WC) punches were 5.7 mm and 2.7 mm, respectively; the sample with CFC punches shrank much more than the sample with WC punches because the pressure-induced strain on the CFC punches was greater than that on the WC punches. As the pressure was removed, the strain on the CFC configurations recovered slightly. The optical transmittances of 0.8-mm thick samples sintered at 400 MPa (CFC) and 500 MPa (WC) were comparable: 61.3% and 63.0% at 645 nm, respectively.

Nishiyama et al. reported an extremely high pressure (7.7 GPa) and low temperature (800 °C) SPS process to develop transparent Al_2O_3 ceramics with nanocrystalline grains [71]. The average grain size of the final samples was 0.15 μm while the maximum in-line transmission was 71% at 640 nm for 0.8-mm thick samples. More importantly, the transparent Al_2O_3 ceramics demonstrated strong mechanical characteristics, with microhardness and fracture toughness of 25.5 ± 0.3 GPa and 2.9 ± 0.3 MPa·$m^{1/2}$, respectively. After sintering at 400 °C, the sample sintered was already opaque; however, it was fragile after thermal annealing. After sintering at 600, 700, and 800 °C, all samples were highly transparent and the sample sintered at 800 °C for 30 min exhibited the highest in-line transmittance. When the sintering temperature exceeded 1000 °C, the samples became translucent and the grain size increased significantly. Cross-sectional surface SEM images revealed that the sample sintered at 800 °C had prominent intergranular fractures and grains on the scale of nanometers with random orientation.

Recently, Ghanizadeh et al. used nanocrystalline Al_2O_3 powder with ≤ 50 nm grains to prepare transparent Al_2O_3 ceramics using both SPS and HP for comparison [72]. The authors reported that both the SPS and hot pressed samples derived from the as-synthesized powder had large grain sizes as the result of excessive grain growth, which could not be prevented by granulation using spray freeze drying. However, excessive grain growth was able to be prevented using slip casting with a relative green body density of 53%. When SPS was conducted at 1200 °C and 500 MPa for 20 min, the average grain size of the resultant Al_2O_3 ceramics was 0.32 μm, the in-line transmittance was as high as 80%, and the microhardness was 22 GPa.

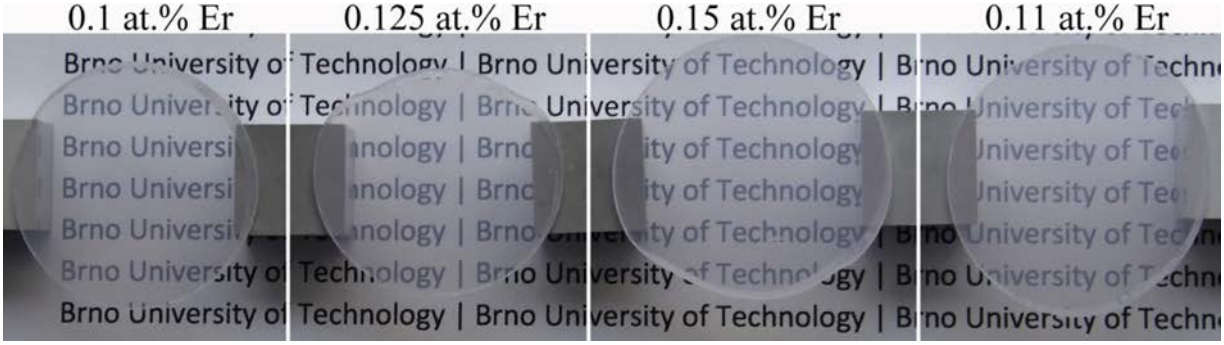

Fig. 4. Photographs of transparent Er^{3+}-doped Al_2O_3 ceramics with an approximate diameter of 3 cm, positioned 1 cm above the text. Reused from [61]. Copyright © 2017, Elsevier.

SDC EX. 1018 - 5/66

For the SPS process used by Ghanizadeh et al., Al_2O_3 ceramics were prepared by dispersing Al_2O_3 powder in DI water at a loading level of 60 wt% with an anionic polyelectrolyte as the dispersant. After slip casting, the green bodies were dried first at room temperature and 50% relative humidity for 72 h and then at 60 °C in an oven. Granulated powders were also prepared from the slurry by spraying and freeze drying. The binders were completely removed before sample density was measured. For the hot pressed samples, the Al_2O_3 powder was directly heated to 900 °C at 10 °C/min, first under vacuum and then in Ar, and sintering was conducted at 1400–1700 °C for 5 h. During the sintering process, 40 MPa of pressure was applied to both ends of the die with graphite plungers.

For the SPS experiment, two sample sizes were studied; 20 mm diameter samples were sintered at 70 MPa and 5 mm diameter samples were densified at either 500 or 1000 MPa. In both cases, the temperature was increased at 100 °C/min to an intermediate temperature (700 °C), at which point pressure was applied; the samples were sintered for 30 min and 20 min at 70 MPa and 500/1000 MPa, respectively. The SPS samples reached 70% in-line transmittance at 645 nm. Photographs and SEM images of representative HP and SPS samples are shown in Figs. 5 and 6, respectively.

Crystallographic orientation is an effective way to improve the transparency of birefringent ceramics such as Al_2O_3 because birefringence at grain boundaries can be suppressed when the optical axes are aligned [73]. Ashikaga et al. fabricated high-transparency Al_2O_3 with an oriented c-axis and fine microstructure using slip casting under a strong magnetic field, followed by SPS at 1150 °C for 20 min. The real in-line transmittance of the textured Al_2O_3 was 70% at 640 nm for 0.80-mm thick samples, which was higher than that of randomly-oriented alumina because the c-axis orientation reduced the actual difference of the refractive index and remarkably suppressed the birefringence.

Ashikaga et al. used commercial Al_2O_3 powder with an average grain size of 0.39 μm and a Brunauer-Emmett-Teller (BET) specific surface area of 4.5 m^2/g as the precursor. The Al_2O_3 powder was suspended in distilled water with a dispersant to promote dispersion by mutual electrosteric repulsion, and suspensions with 30 vol% solid loading were used for slip casting. During the consolidation process, a 12 T strong magnetic field parallel to the orientation and pressing directions was applied at room temperature to align the green bodies. The aligned green bodies were further compacted by CIP at 392 MPa for 10 min without changing the particle orientation. After CIP, the samples were thermally treated at 500 °C for 60 min in air to remove organic compounds, followed by SPS at 1150 °C and 100 MPa. During SPS, the temperature was rapidly increased to 600 °C, and then increased to 1150 °C at either 5 °C/min or 2 °C/min; the samples were sintered for 10 min and 20 min after heating at 5 °C/min and 2 °C/min, respectively. All the as-sintered samples were annealed at 1000 °C for 10 min.

Fig. 7 shows the X-ray diffraction (XRD) spectra of the planes perpendicular and parallel to the magnetic field in samples sintered at 1150 °C for 20 min after heating at 2 °C/min. On the surface that was perpendicular to the magnetic field, i.e. the T plane, both the (006) peak and (1010) peak, which belongs to the (00 l) plane, were present and the (1010) peak was stronger. For comparison, the XRD spectrum of the surfaces parallel to the magnetic field, i.e. the S planes, exhibited stronger (hk0) peak intensities than the T plane. These results suggest that the Al_2O_3 ceramics had a crystalline structure wherein the c-axis was parallel to the applied magnetic field, which confirms that alignment was retained during the sintering process. Similar results have been reported by other studies [74,75].

Powder processing is also an important strategy for developing

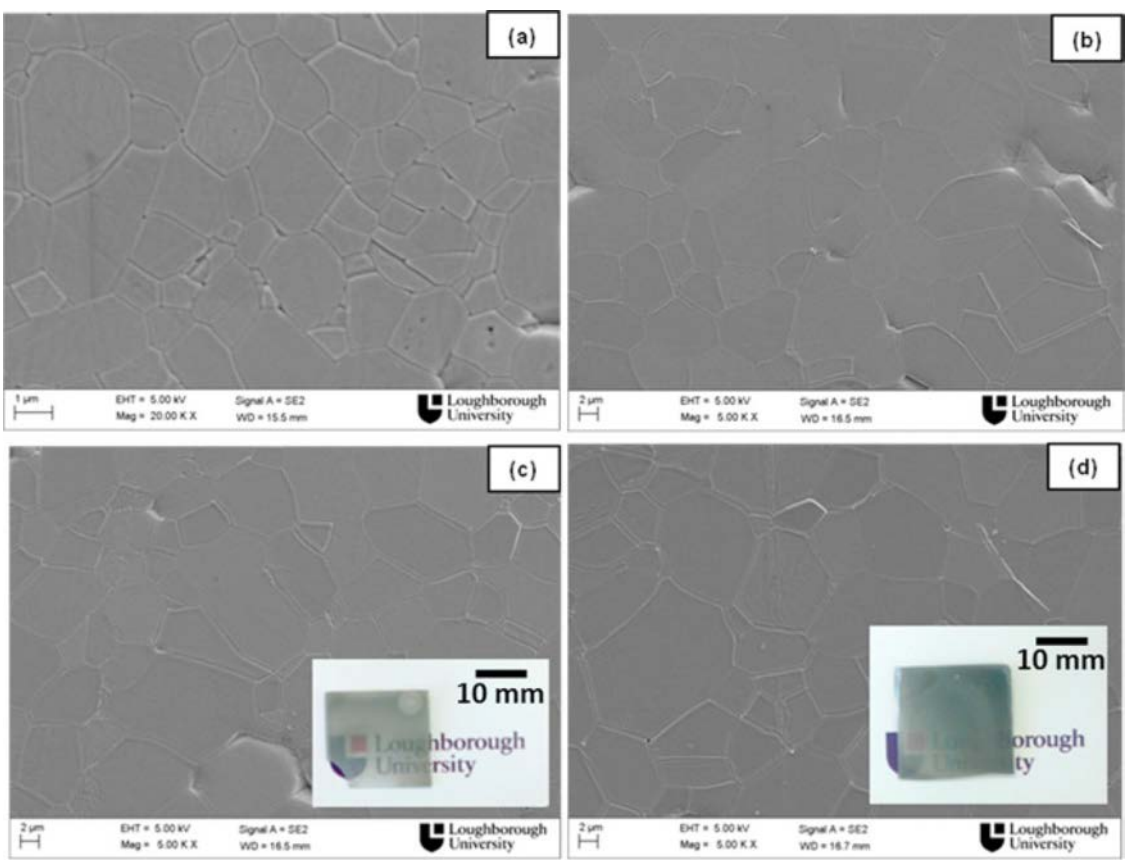

Fig. 5. SEM images of Al_2O_3 samples that were hot pressed for 5 h: (a) 1400 °C, (b) 1500 °C, (c) 1600 °C, and (d) 1700 °C. Insets show the respective photographs. Reused from [72]. Copyright © 2017, Elsevier.

SDC EX. 1018 - 6/66

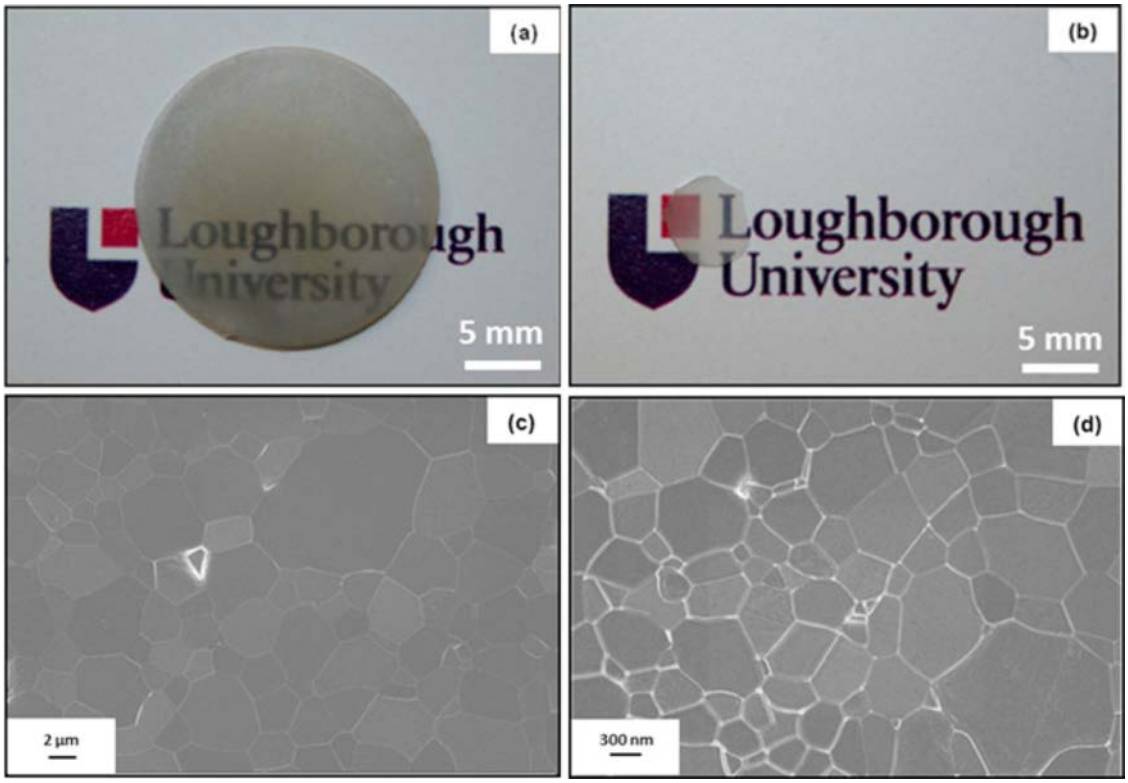

Fig. 6. Photographs and SEM images of transparent Al_2O_3 ceramics prepared under different SPS conditions: (a, c) SPS70-14, (b, d) SPS-500-12. Reused from [72]. Copyright © 2017, Elsevier.

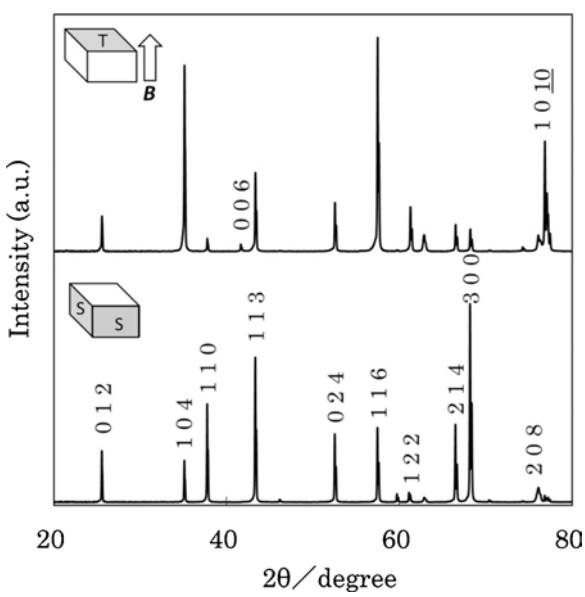

Fig. 7. XRD spectra of the planes perpendicular and parallel to the magnetic field; the Al_2O_3 samples were sintered at 1150 °C for 20 min after heating at 2 °C/min. Reused from [73]. Copyright © 2018, Elsevier.

transparent Al_2O_3 ceramics. As an example, Godinski reported a float packing process that increases the packing density of the precursor powder in order to obtain transparent Al_2O_3 ceramics with submicron grains [76]. In this study, Al_2O_3 powder was dispersed in water to form aqueous suspensions, which were de-aired and subsequently transferred to a specially designed mold wherein the particles precipitated under well-controlled conditions. Because of the electrostatic and electrosteric repulsion forces, large particles precipitated at the bottom of the mold and a stable floating suspension of small particles with uniform size was formed. The large and agglomerate particles were removed from the fine ones, and the suspension was concentrated and dried by controlling the temperature and humidity in the chamber. The resultant green bodies were uniform, homogenous, and free of defects because the large particles had been removed and the fine particles were in a quasi-equilibrium state as the consolidation process was sufficiently slow. As a result of the fine grains, the transparent ceramics had a uniform microstructure and high optical properties comparable to those of sapphire and some commercial products (RB92), which have relative large grains size (e.g. 15 μm). Therefore, transparent Al_2O_3 ceramics synthesized using this method are expected to have greater mechanical strength than the commercial products.

Tape-casting has been widely used to fabricate transparent Al_2O_3 ceramics that are both large and thin [77–79]. Yang and Wu used an aqueous tape-casting slurry composed of environmentally friendly copolymers, isobutylene, and maleic anhydride to prepare transparent alumina ceramic wafers [77]. By optimizing the plasticizer content, the mechanical properties of the dried tapes (240–740 μm thick) could be controlled. For debinding and presintering, the green sheets were calcined at 1000 °C for 3–5 h after heating at 3–5 °C/min. The sheets were then sintered at 1750–1850 °C under 10^{-5}–10^{-6} Pa for 5 h, after heating at 10 °C/min. After sintering, the Al_2O_3 ceramic sheets were 150–660 μm thick. Unpolished, 660 μm thick transparent wafers exhibited 26% in-line transmittance at 600 nm; thus there is still room to improve the optical transparency of these ceramics.

Translucent Al_2O_3 ceramics have also produced by aqueous tape-casting and vacuum sintering [78]. In this study, Zhou et al. studied the influence of the binder content on the rheological behavior of the slurries, the microstructures of the green tapes, and the microstructures and optical performance of the Al_2O_3 ceramics. The rheological characterization indicated that the slurries used in the study had promising shear-thinning behavior. After a series of processing steps, the laminated Al_2O_3 green bodies were treated with CIP at 200 MPa for 2 min and then sintered at 1810 °C under 10^{-3} Pa for 5 h. The samples

SDC EX. 1018 - 7/66

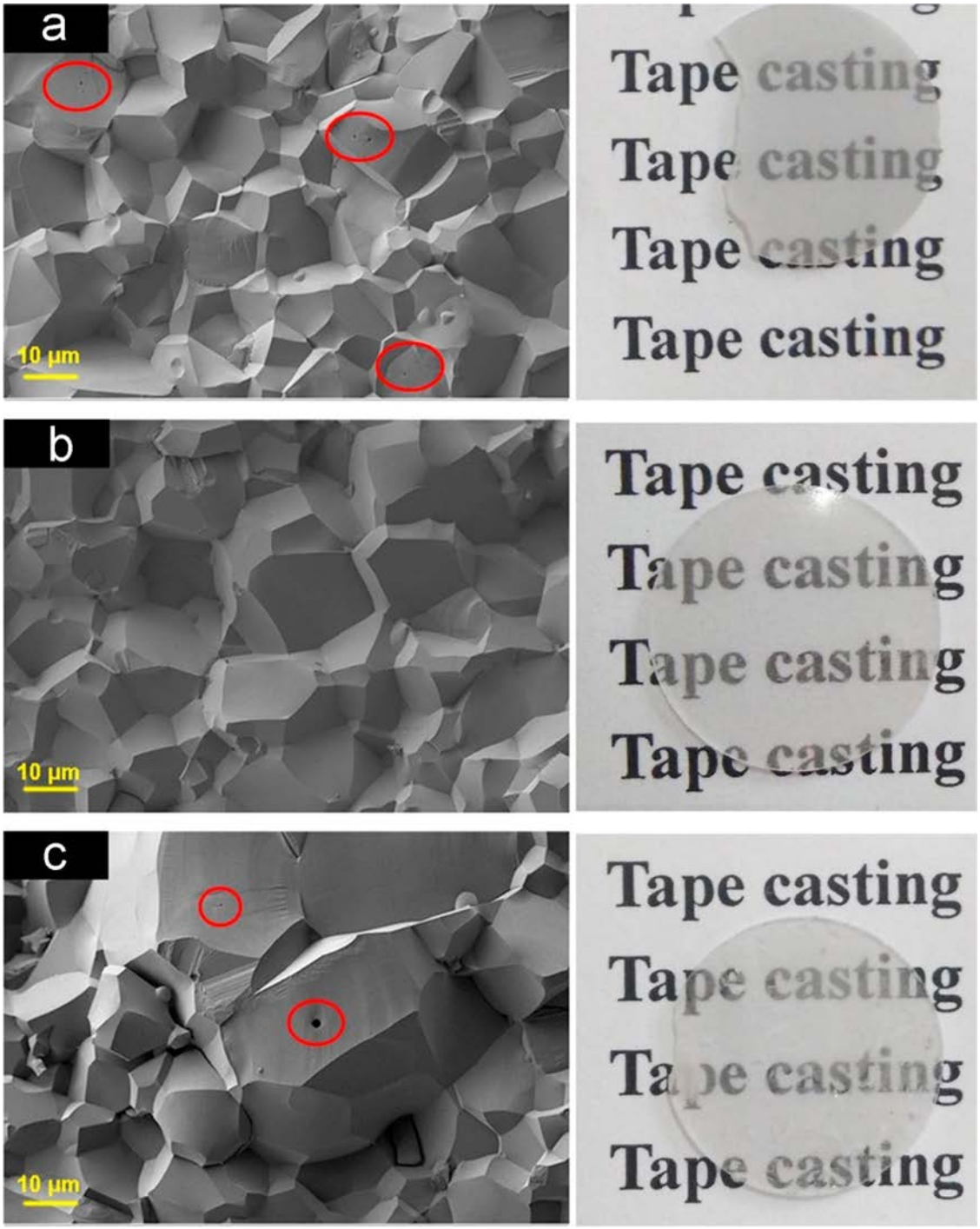

Fig. 8. Cross-sectional SEM images (left) and photographs (right) of the Al_2O_3 ceramics derived from slurries with different PVA contents after sintering at 1810 °C for 5 h: (a) 8 vol%, (b) 10 vol%, and (c) 12 vol%. Reused from [78]. Copyright © 2016, Elsevier.

derived from the slurries with 10 vol% polyvinyl alcohol (PVA) displayed the highest transparency as they had perfect microstructures and high-quality grain boundaries with typical triple junctions and without pores or secondary phases, as shown in Fig. 8b. Conversely, the cross-sectional SEM image of the Al_2O_3 ceramics obtained from the slurries containing 8 vol% PVA, which had a mean grain size of 20 μm, shows pores in the grains and at the grain boundaries (Fig. 8a). When the PVA content was increased to 12 vol%, the number and size of pores increased and abnormal grain growth occurred, as shown in Fig. 8c. Therefore, the PVA content must be optimized in order to obtain Al_2O_3 ceramics with high optical transparency.

More recently, Feng et al. reported a method that uses nonaqueous tape casting and vacuum sintering to prepare transparent Al_2O_3 ceramic sheets without deformation and cracking [79]. This study employed several laminating methods to obtain green bodies, including cold pressing, CIP, warm pressing, and combined warm pressing and CIP. Of these methods, the warm pressing pretreatment demonstrated a positive effect on microstructure and hence densification of the green tapes; the resultant transparent Al_2O_3 ceramic wafers were 500 μm thick. This study used menhaden fish oil as the dispersing agent, a mixture of absolute ethyl alcohol and xylenes as the solvent, 2.5 wt% butyl benzyl phthalate and 3.5 wt% polyethylene glycol (PEG) as plasticizers to

SDC EX. 1018 - 8/66

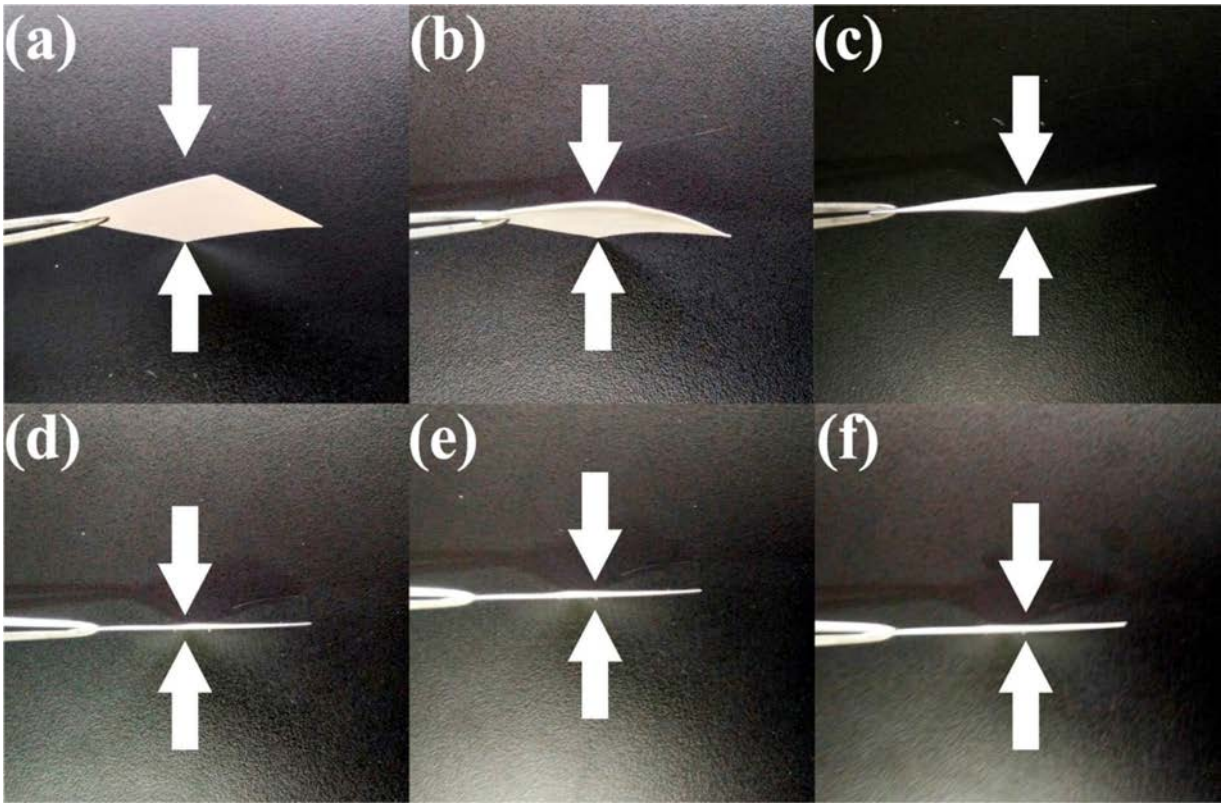

Fig. 9. Side-view photographs of the sintered Al_2O_3 tapes pretreated with different methods and debinded at different heating rates: (a) cold pressing at 30 MPa and heating at 1 °C/min; (b) CIP at 200 MPa and heating at 1 °C/min; (c) warm pressing at 30 MPa and heating at 1 °C/min; (d) warm pressing at 30 MPa, CIP at 200 MPa, and heating at 1 °C/min; (e) warm pressing at 30 MPa, CIP at 200 MPa, and heating at 5 °C/min; (f) warm pressing at 30 MPa, CIP at 200 MPa, and heating at 10 °C/min. Reused from [79]. Copyright © 2018, Elsevier.

prevent adsorption, and 6 wt% polyvinyl butyral (PVB) as the binder. The Al_2O_3 powder and 0.05 wt% MgO sintering aid were thoroughly mixed with the solvent by ball milling. The green bodies were sintered under vacuum according to the following temperature program: heat to 1200 °C at 5 °C/min, heat to 1500 °C at 2 °C/min, hold at 1500 °C for 5 h, heat to 1700 °C at 1 °C/min, and hold for 10 h.

Photographs of the samples treated with different pressing techniques and presintered with different heating rates are illustrated in Fig. 9 to demonstrate the relationship between processing and physical properties. In Fig. 10a, a representative SEM image of the transparent Al_2O_3 ceramic sheets shows the dense microstructure of the fracture surface without lamination; the main fracture profile was intergranular with minor intragranular ruptures. Based on the SEM image of the polished sample shown in Fig. 10b, grains were in the range of 10–25 μm with very thin grain boundaries. The in-line transmittance curve of the transparent Al_2O_3 ceramic wafer is shown in Fig. 11. Similarly, the optical performances need to be further

Slip-casting is also a popular method for fabricating transparent

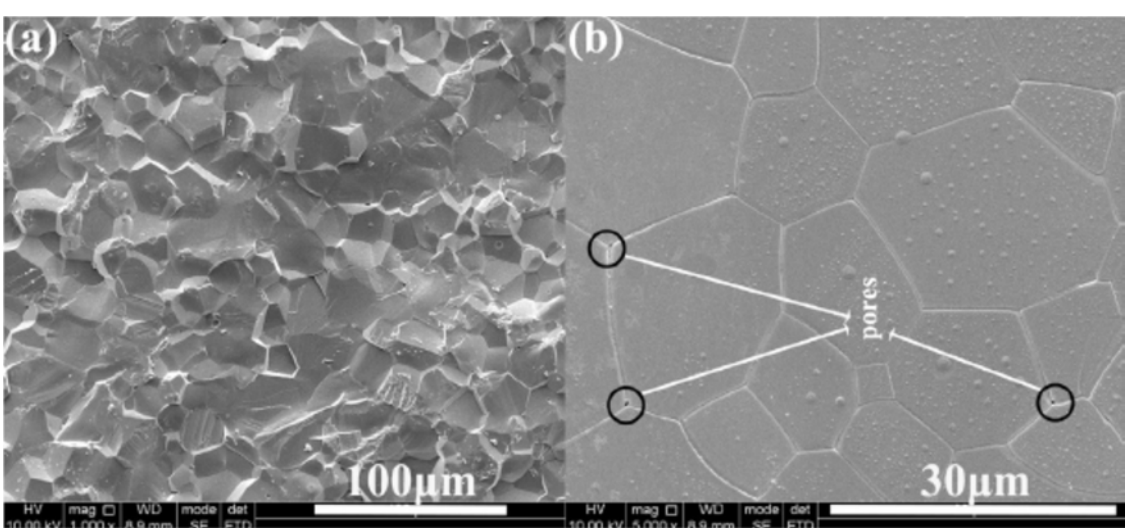

Fig. 10. Representative SEM images of the transparent Al_2O_3 ceramic wafers: (a) fracture surface and (b) thermally etched polished surface. Reused from [79], Copyright © 2018, Elsevier.

SDC EX. 1018 - 9/66

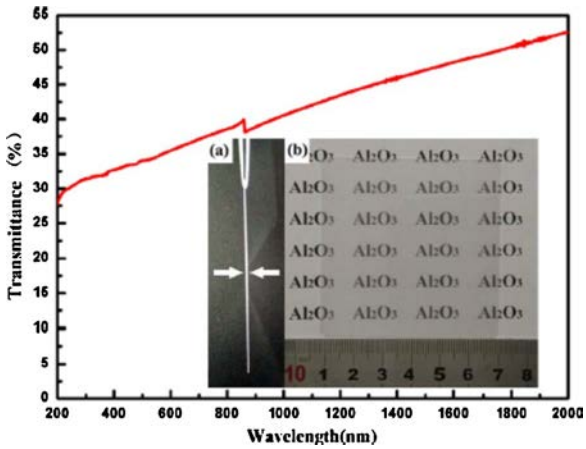

Fig. 11. Transmittance curve of the transparent Al_2O_3 ceramic wafers with a (a) side view photograph and (b) planetary view photograph. Reused from [79], Copyright © 2018, Elsevier.

ceramics. Drdlik et al. reported a slip casting technique that can produce transparent Al_2O_3 ceramics doped with different concentrations of Er^{3+} (0–0.15 at%), which can be used to optimize photoluminescence properties [80]. Commercial Al_2O_3 powder with an average size of 150 nm and Er_2O_3 powder with 20–30 nm particles were used to prepare homogeneous suspensions with 45 vol% Al_2O_3 in DI water, which were poured into PVC dishes. After drying in air at room temperature for three days, the samples were dried at 80 °C for 5 h and a two-step method was used to presinter the pellets to discs with 95–96% relative density. The first step of presintering was to heat to 1440 °C without dwelling, and the second step was to heat to and hold at 1280 °C for 10 h, which was followed by cooling at 20 °C/min. After the two-step presintering, all samples were subjected to HIP in Ar at 1280 °C and 200 MPa in order to eliminate the closed pores. The resultant Al_2O_3 ceramics were fully densified with submicron grain size and up to 60% transparency, and the optimized Vickers hardness was as high as 27 GPa for a load of 10 N.

Liu et al. found that transparent Al_2O_3 ceramics could be derived from coarse spherical particles cemented with Al_2O_3 nanopowder at high pressures and modest temperatures [81]. The coarse spherical powder was 99.8% Al_2O_3 – 90% α-Al_2O_3 and 10% δ-Al_2O_3 – with 1–38 μm particles, and the nanopowder was 99.99% – 90% α-Al_2O_3 and 10% θ-Al_2O_3 – with an average particle size of 80 nm. The micro- and nanopowders were combined at a 17:3 weight ratio; the sintering mixtures were ultrasonicated to disperse the nanoparticles, and subsequently mixed mechanically with a tumbling mixer. The mixtures were dried under vacuum at $\sim 1.5 \times 10^{-3}$ Pa and 800 °C to remove gas molecules before they were pressed into pellets at 300 MPa to obtain 80% relative density. High-pressure (5.0 GPa) and high-temperature (500–1200 °C) sintering treatments were performed using a cubic presser. The application of high pressure triggered plastic deformation of the spherical particles, during which the Al_2O_3 nanoparticles filled the cracks, acting as a binder and promoting densification. The nanoparticles also served to strengthen the grain boundaries of the Al_2O_3 ceramics, which increased microhardness without compromising optical performance.

Photographs and SEM images of the samples with and without nanopowder are shown in Fig. 12. After the high-pressure treatment, the samples without nanoparticles exhibited Y-shaped grain boundaries (Fig. 12a), which were caused by the plastic deformation of the spherical particles. Although many of the pores were removed after sintering at a modest temperature (Fig. 12b), the pores could not be completely eliminated and non-uniform crystallites formed at the grain boundaries of samples sintered at high temperatures (Fig. 12c). Therefore, in terms of optical transmittance, the optimal sintering temperature was 900 °C when the sintering mixture did not contain Al_2O_3 nanopowder.

The addition of Al_2O_3 nanopowder modified the microstructure of the ceramic, as illustrated in Fig. 12d–f. After sintering at 700 °C, continuous grain boundaries were formed in the samples with nanopowder (Fig. 12d) whereas particle interfaces were clearly visible in the sample without the nanopowder (Fig. 12a); this suggests that the large spherical particles were bound together by the small nanoparticles. By forming continuous grain boundaries, the light scattering and absorption at grain boundaries were reduced and thus optical transparency improved. Moreover, increasing the sintering temperature to 900 and 1100 °C did not significantly affect the optical performance of the ceramics with nanopowder.

In summary, although transparent Al_2O_3 ceramics have been extensively studied, it is challenging to develop high quality products using simple and cost-effective methods because Al_2O_3 has a non-cubic crystal structure. For example, the sizes and shapes of ceramic samples processed with HP, HIP, and SPS are restricted by the crystal facets, and those that use sintering aids could have poor optical and mechanical properties. While magnetic alignment is an interesting strategy for enhancing the transparency of Al_2O_3 ceramics, the required magnetic field is too high for practical applications. Therefore, future studies should focus on developing high quality precursors in order to reduce sintering temperatures and thus increase sinterability.

2.1.2. Magnesia (MgO)

Magnesia (MgO) has also been extensively studied for transparent ceramics, and nearly all of the techniques discussed for Al_2O_3 can be used to fabricate transparent MgO ceramics. Promoting densification of MgO-based ceramics to achieve near theoretical density has long been attempted [82,83]; for example, in 1974, Ikegami et al. reported a multiple-step process to obtain transparent MgO ceramics by vacuum sintering, with high purity MgO or $Mg(OH)_2$ powder as the precursor and LiF as the sintering aid [83]. The halide employed as sintering aids were introduced via two methods: (i) wet-mixing with MgF and/or MgCl in an organic solvent (e.g., benzene or ethyl alcohol), and (ii) adding small amounts of HF and/or HCl solution to the organic solvent used to suspend the MgO powder. The suspensions were dried at 70 °C, calcined in N_2 at 600–1200 °C for 3 h, and sintered at 1600 °C for 1 h. The transparency of the final MgO ceramics was influenced by several factors, including the F^- ion concentration, the calcination parameters, and the particle size of the precursor powders. A low concentration of F^-, 0.02 wt%, was sufficient to ensure the densification of MgO; however, sinterability gradually increased with increasing F^- content, which was accompanied by increased weight loss during the sintering process. While Cl^- ions were unable to significantly enhance densification, co-doping with Cl^- and F^- ions worked very well. Furthermore, the calcination temperature was carefully optimized to ensure a high sinterability and small precursor particles were shown to promote densification; when the particles were larger than 0.15 μm, F^- ions were unable to enhance the densification of MgO.

Chen et al. developed a simple pressure-less sintering process for fabricating transparent MgO ceramics [84]. The authors synthesized the $Mg(NO_3)_2{\cdot}6H_2O$ precursor powder by chemical precipitation with a mixture of NH_4HCO_3 and NH_4OH (28.0%) as the precipitation agent. After drying, the precipitate was thermally treated for 2 h at different temperatures; the optimal calcination temperature was determined to be 700 °C, but samples had the highest relative density, 98.1%, after sintering at 1400 °C for 2 h. The average grain size was 6 μm and the average hardness was 6.8 GPa, but the optical transparency required further improvement.

Fang et al. obtained translucent MgO ceramics by hot pressing with LiF as the sintering aid and high-purity commercial MgO nanopowder with large surface area, small grain size, and a low degree of agglomeration as the starting material [85]. The LiF sintering aid was first dispersed in 2-propanol and then added to the MgO powder to reach 2–4 wt%. The hot-pressing experiments were conducted with a graphite

SDC EX. 1018 - 10/66

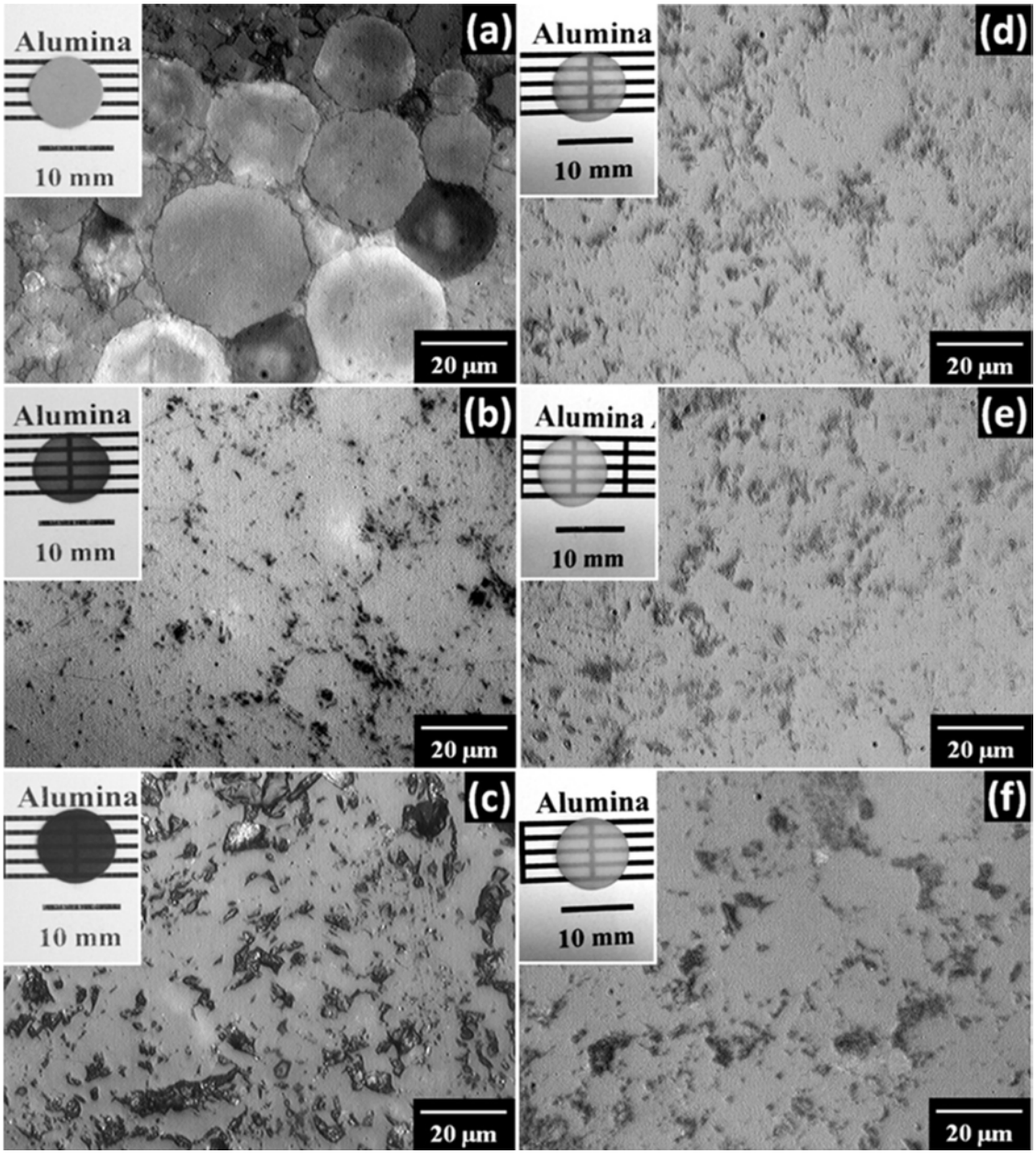

Fig. 12. SEM images and photographs of the Al_2O_3 samples sintered at 5.0 GPa and high temperature: (a–c) coarse powder, (d–f) mixture of coarse powder and nanopowder, (a, d) 5.0 GPa and 700 °C, (b, e) 5.0 GPa and 900 °C, and (c, f) 5.0 GPa and 1100 °C. Reused from [81], Copyright © 2016, Elsevier.

die at 45 MPa in Ar and heating rates of either 3 °C/min or 10 °C/min. While optical transmittance was not reported, the sintered samples were said to be transparent. Similar results have been reported by other studies [86–88]. The presence of LiF is believed to cause the formation of a liquid phase that lubricates the MgO particles during the initial sintering stage and thus enhances the densification process.

Studies have shown that when advanced sintering technologies are used, sintering aids can be avoided. For instance, transparent MgO ceramics have been fabricated without sintering aids by using the HIP technique [89]. Itatani et al. synthesized transparent MgO ceramics using > 99.98% commercial MgO powder with a specific surface area of 34.3 m^2/g and an average particle size of 57 nm as the starting material. The green bodies were formed under 36 MPa of uniaxial pressure, followed by CIP at 50 MPa and pressure-less presintering in air for 5 h at 1600 °C after heating at 10 °C/min. Subsequent HIP was conducted in Ar at 195 MPa by heating at 10 °C/min to 1500–1600 °C for 0.5 h. After presintering, the sample had a relative density of 96.7% and an average grain size of 10.7 μm, which increased to 99.9% and 132–199 μm, respectively, after HIP between 1500 and 1600 °C. The in-line transmission of the MgO ceramic after HIP at 1600 °C for 0.5 h was 55% at 500–900 nm, which is approximately 65% of that of MgO single crystals.

Spark plasma sintering is another technique for fabricating transparent MgO ceramics without the use of a sintering aid [90,91]. In one study, a graphite die with an inner diameter of 12 mm was filled with commercial MgO, pre-pressed under 150 MPa, and heated under 10 MPa until the desired sintering temperature was approached, at which point the pressure was rapidly increased to 100 MPa in as little as 20 s [90]. If a high pressure of 150 MPa was used, the sintering temperature and sintering time could both be reduced. The optical transmittance of the fully densified MgO ceramics was approximately 60% of that of their single crystal counterpart.

Jiang et al. employed SPS to prepare transparent MgO ceramics from commercial MgO powder and LiF, which was added to promote

SDC EX. 1018 - 11/66

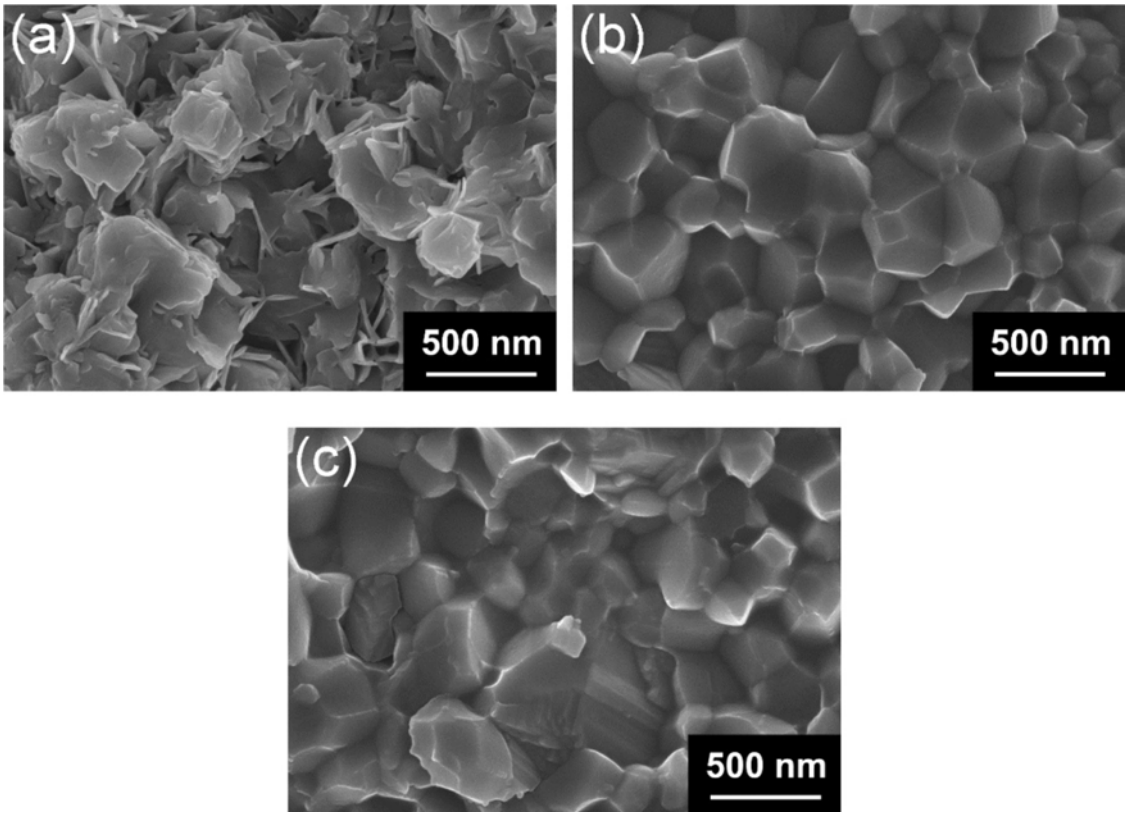

Fig. 13. Fractured surface SEM images of the sintered MgO ceramics with different LiF contents: (a) 0 wt%, (b) 1 wt%, and (c) 2 wt%. Reproduced from [91]. Copyright © 2017, Elsevier.

densification [91]. In this study, 0.3 μm LiF powder was added to high-purity commercial MgO powder with an average particle size of 100 nm; the powders were mixed by ball milling with acetone, followed by drying and granulation. The SPS experiments were conducted at 800–1100 °C for 5 min after heating at 10–300 °C/min, and the pressure was maintained at 30 MPa throughout the sintering process. The authors found that LiF promoted grain growth and densification of MgO such that densification could be readily achieved at moderate temperature and relatively low pressure. Furthermore, the microstructure and thus transparency of the MgO ceramics exhibited a strong dependence on the heating rate and sintering temperature; when MgO powder with 1 wt% LiF was heated at 100 °C/min and sintered at 900 °C for 5 min, the average in-line transmittance of the resultant ceramic was 85% at wavelengths between 3 and 5 μm.

Fig. 13 shows fractured surface SEM images of the MgO ceramics with different concentrations of LiF, which demonstrate the significant impact of the LiF content on the microstructure and optical performance of the MgO ceramics. While the pure MgO sample had a whisker-like morphology with open pores (Fig. 13a), the grains were clearly connected in the samples with LiF. The sample with 1 wt% LiF had a homogeneous microstructure and the sample with 2 wt% LiF exhibited transgranular fractures (Fig. 13c), which were closely related to the presence of the large grains caused by excessive LiF. Therefore, 1 wt% LiF was the optimal content of sintering aid in order to achieve high optical transparency.

Fig. 14 shows cross-sectional SEM images of MgO ceramics with 1 wt% LiF sintered at different temperatures. Residual pores were present in the sample after sintering at 800 °C (Fig. 14a), and the number of pores decreased when the sintering temperature was increased to 850 °C (Fig. 14b). Once the sintering temperature was ≥ 900 °C, all samples exhibited a nearly pore-free microstructure, as demonstrated in Fig. 14(c–e). The average grain sizes of the samples were 0.41, 0.59, 0.70, 0.84, and 1.44 μm, after sintering at 800, 850, 900, 950, and 1000 °C, respectively. Moreover, the relative density increased from 93.5% to 99.3% when the sintering temperature increased from 800 to 900 °C, and decreased slightly when the temperature reached 1000 °C; therefore, 900 °C yielded the highest optical transmittance. While these results demonstrate the relationships between sintering temperature, grain size, relative density, and ultimately optical transmittance, the optical performance of these MgO ceramics can still be improved.

Although MgO has a cubic crystal structure, fully transparent MgO ceramics are difficult to fabricate because MgO has a high vapor pressure at elevated temperatures. Currently, the optical properties of MgO ceramics reported in the open literature are still considerably lower than those of their single-crystal counterparts. Future work should focus on systematic studies of MgO ceramics in order to establish the interrelationships among the precursor properties, processing parameters, sintering technique, sintering aids, microstructure, and optical performance, and identify the key factors that determine the optical qualities of the resultant ceramics.

2.1.3. Zirconia (ZrO_2)

Zirconia (ZrO_2) ceramics have excellent mechanical and functional properties, including high toughness, low thermal conductivity, and high oxygen conductivity; therefore, transparent ZrO_2 ceramics are of great interest to the research community. Yttria (Y_2O_3) is often used to stabilize the cubic and tetragonal crystal structures of ZrO_2, which generates oxygen vacancies, and transparent ZrO_2 ceramics with a Y_2O_3-stabilized cubic crystalline structure (8 mol% Y_2O_3:ZrO_2, abbreviated as c-YSZ) have both high mechanical strength and good optical performance [92–102]. Cubic ZrO_2 has a refractive index of 2.2 and has consequently attracted more interest than optical glasses and other oxides. Therefore, transparent YSZ ceramics with high optical transparency, a high refractive index, and a high dielectric constant have potential applications as optical components [98,103,104].

Translucent cubic ZrO_2 ceramics have been obtained using a high-

SDC EX. 1018 - 12/66

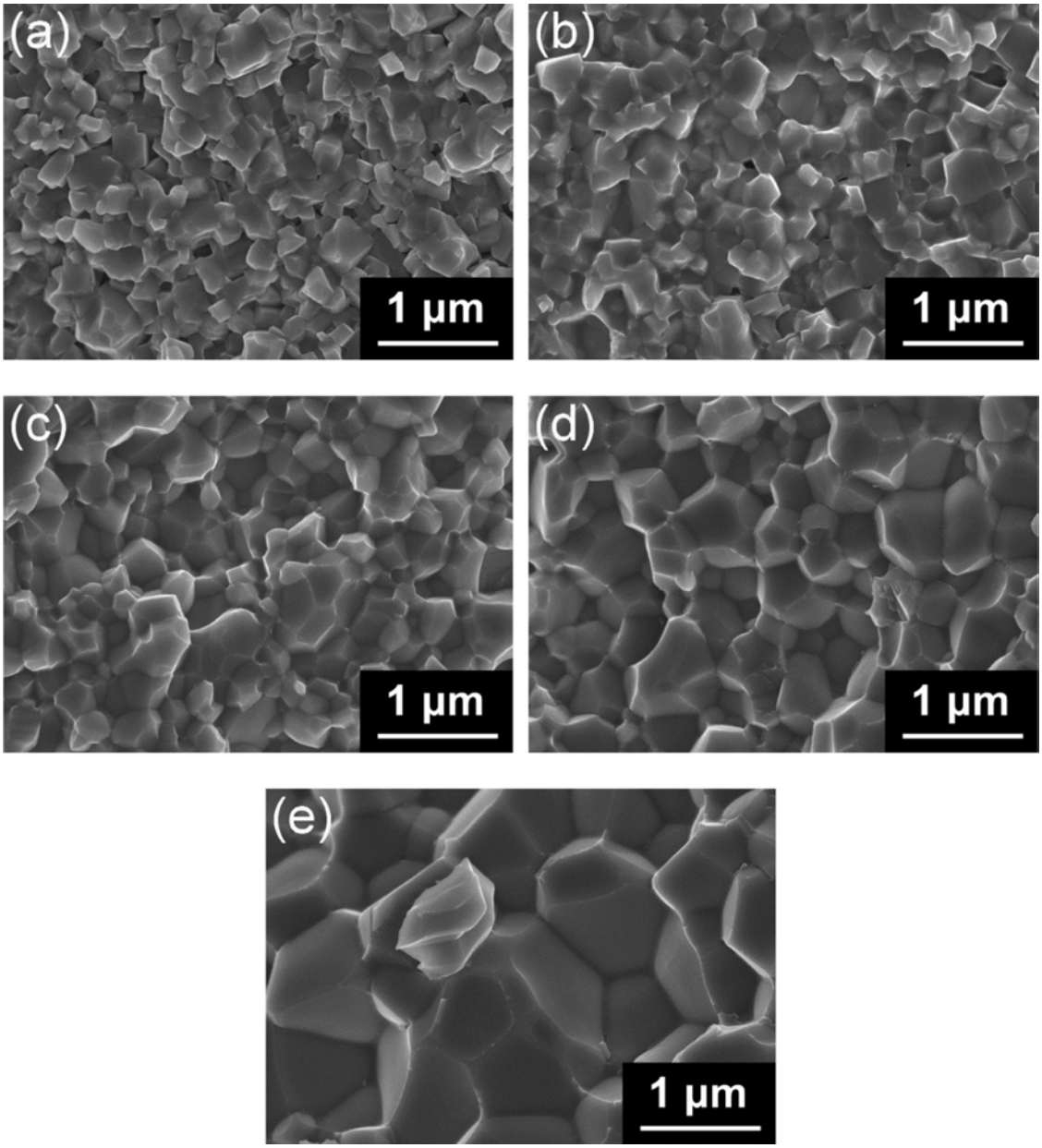

Fig. 14. Cross-sectional SEM images of the MgO ceramics doped with 1 wt% LiF and prepared by SPS at different temperatures: (a) 800 °C, (b) 850 °C, (c) 900 °C, (d) 950 °C, and (e) 1000 °C. Reproduced from [91]. Copyright © 2017, Elsevier.

pressure HP technique developed 50 years ago [92], whereby commercial powders are compacted and sintered at 0.5–30 kbar and 1300–1750 °C, heating and cooling at 1000 °C/h and 500 °C/h, respectively. This technique can stabilize monoclinic ZrO_2 by mixing a stabilizing oxide, either CaO or Y_2O_3, with the commercial ZrO_2 powder prior to sintering. While the stabilized ZrO_2 ceramics have either a monoclinic or cubic crystal structure, they are translucent with a maximum in-line light transmittance of 12%.

In another study, translucent cubic ZrO_2 ceramics with 6 mol% Y_2O_3 were prepared using the conventional sintering technique [93]. The mixed oxide precursor powder was obtained from the decomposition of yttrium and zirconium alkoxides, and had high surface reactivity and submicron particle sizes. The mixed oxide powder was compacted and calcined at 1000 °C for 0.5 h and the 6 mol% Y_2O_3:ZrO_2 ceramics prepared by sintering at 1450 °C exhibited full densification and stabilization.

Similarly, translucent 3 mol% Er_2O_3:ZrO_2 with a tetragonal crystal structure was prepared by the conventional sintering of powders synthesized by the hydrolysis of alkoxides [95]. The powders were sintered in air at 800–1500 °C for 1 min to 20 h, and the heating and cooling rates were both 5 °C/min. Both the properties of the precursor powders and the sintering conditions were found to have a strong impact on the microstructural properties and optical performance of the final ZrO_2 ceramics. Fully dense, translucent samples were obtained after sintering below 1400 °C.

Tsukuma et al. adapted an HIP process to prepare highly transparent 8 mol% Y_2O_3:ZrO_2 (8YSZ) ceramics with an in-line transmittance close to that of single crystals [103]. The green bodies were made from commercial 8YSZ powder by dry pressing at 50 MPa and CIP at 200 MPa, and were presintered in air for 2 h at 1300 °C, 1500 °C, and 1650 °C after heating at 100 °C/h. The HIP process was performed in Ar at 1350–1750 °C and 150 MPa for 1 h after heating at 500 °C/h. The grain sizes of the samples presintered at 1350 °C were 3 μm, 6 μm, and 20 μm after HIP at 1300 °C, 1500 °C, and 1650 °C, respectively. Optical performance was very sensitive to the microstructure of the presintered samples as the microstructural characteristics of the fine grains and

SDC EX. 1018 - 13/66

Table 3
Processing parameters and optical transmittance of representative transparent sesquioxide ceramics.

No.	Powder processing	Sintering parameters	Transmittance	Ref.
1	Y_2O_3 from precipitation	Calcination: 1100 °C/4 h CIP: 200 MPa Vacuum sintering: 1700 °C/1 h	/	[21]
2	Y_2O_3 from precipitation	Calcination: 1050 °C/4 h Pre-sintering: 1700 °C, 10 °C/min HIP: 1300 °C/3 h, 206 MPa	70% at 600 nm	[41]
3	Er:Y_2O_3 from co-precipitation and combustion	Calcination: 900–1100 °C/4 h CIP: 200 MPa Vacuum sintering: 1700 °C/4 h Vacuum: 10^{-5} Pa	/	[39]
4	Y_2O_3 from precipitation of carbonate	Calcination: 1100 °C/4 h Heating rate: 200 °C/h Vacuum sintering: 1700 °C/4 h Vacuum: 10^{-3} Pa	79% at 600 nm	[115]
5	10 at% La_2O_3-doped Y_2O_3 from coprecipitation	Calcination: 900 °C/4 h CIP: 200 MPa Three-step sintering: T1 = 1450 °C/0 h; T2 = 900 °C/20 h; T3 = 1700 °C Vacuum: 5×10^{-3} Pa	77% at 580 nm	[117]
6	5.0 mol% ZrO2–Y2O3 slip casting	Calcination: 900 °C/2 h Vacuum sintering: 1860 °C/8 h Vacuum: 2×10^{-3} Pa	80% at 600 nm	[118]
7	Yb^{3+}:Y_2O_3 (0–40 at%) from coprecipitation	Calcination: 1100 °C/2 h Vacuum sintering: 1850 °C Atmosphere: H_2	80% at 600 nm	[119]
8	Nd^{3+}:Y2O3 (1–7 at%) solid-state reaction	CIP: 200 MPa Vacuum sintering: 1800 °C/20 h Vacuum: 1×10^{-3} Pa	65% at 500 nm	[121]
9	Eu^{3+}:Y_2O_3 (0–5 at%) solid-state reaction	HP: 1580 °C/8 h Pressure: 40 MPa	70% at 600 nm	[122]
10	5.0 mol% ZrO_2–Y_2O_3 solid-state reaction	Calcination: 800 °C/8 h HP: 1600–1700 °C/3 h Pressure: 20–40 MPa Vacuum: 9×10^{-3} Pa Post-annealing: 1200 °C/2 h	76% at 600 nm	[123]
11	La^{3+}/Nd^{3+}:Y_2O_3 modified citrate method	CIP: 250 MPa HP: 1450 °C/2 h; 40 MPa	50% at 450–1100 nm	[128]
12	Y_2O_3 commercial nanopowder	HIP: 1650 °C/6 h, 203 MPa	40% at 600 nm	[124]
13	Y_2O_3 commercial powder	CIP: 200 MPa Presintering: 1650 °C/3 h; 800 °C/h HIP: 1625 °C/3 h, 200 MPa	80% at 600 nm	[125]
14	5.0 mol% ZrO_2–Y_2O_3 commercial powder	Calcination: 800 °C/4 h CIP: 200 MPa Vacuum sintering: 1650–1800 °C/3 h Vacuum: 9×10^{-3} Pa HIP: 1450 °C/5 h, 180 MPa	60% at 700 nm	[126]
15	Y_2O_3 from precipitation	Calcination: 1300 °C/3 h CIP: 200 MPa/5 min Pre-sintering: 1500–1400 °C/4 h HIP: 1600 °C/3 h, 200 MPa	73% at 600 nm	[127]
16	5 at% Yb:Y_2O_3 doped with 1 at% ZrO_2 from coprecipitation	CIP: 200 MPa Vacuum sintering: 1700 °C/2 h Vacuum: 1×10^{-3} Pa HIP: 1775 °C/4 h, 198 MPa Annealing: 1400 °C/10 h	78.9% at 600 nm	[129]
17	(0–10 at%) ZrO_2–Y_2O_3 commercial powder	CIP: 200 MPa Vacuum sintering: 1600–1800 °C/5 h Vacuum: 1×10^{-3} Pa HIP: 1600 °C/3 h, 200 MPa	75% at 700 nm	[131]
18	Y_2O_3 commercial powder	SPS: 950–1050 °C/0–8 h Heating rate: 2 °C/min	55% at 1000 nm	[855]
19	Yb^{3+}:Y_2O_3 (0–50 at%) commercial powder	SPS: 1250 °C/1 h Pressure: 82.7 MPa	70% at 1000 nm	[134]
20	Sc_2O_3 from coprecipitation	Vacuum sintering: 1700 °C/4 h Vacuum: 1×10^{-3} Pa	60% at 600 nm	[22]
21	5 at% Yb:Sc_2O_3 coprecipitation	Calcination: 1100 °C/5 h Vacuum sintering: 1850 °C/10 h Vacuum: 5×10^{-3} Pa Annealing: 1450 °C/10 h	69% at 600 nm	[156]
22	Eu:Lu_2O_3 from coprecipitation	Calcination: 1000 °C/2 h CIP: 200 MPa Sintering: 1850 °C/6 h Atmosphere: H_2	80% at 600 nm	[174]
23	Nd:Lu_2O_3 commercial powder	SPS: 1400 °C/15 min Heating rate: 100 °C/h Pressure: 130 MPa	75% at 650 nm	[183]
24	Er^{3+}:Lu_2O_3 (4 at%) commercial powder doped with TEOS	Calcination: 1100 °C/2 h CIP: 200 MPa Vacuum sintering: 1850 °C/10–12 h	67% at 700 nm	[173]

small intergranular pores were found to be crucial to optical transparency. For example, after HIP at 1300 °C and 1500 °C, submicron pores in the samples caused the optical transmittance to be relatively low. Moreover, optical transparency decreased as the presintering temperature increased, which may be qualitatively attributed to decreased sinterability.

Peuchert et al. developed transparent c-YSZ ceramics for optical lenses by HIP with TiO_2 as a sintering aid [100]. The transparent ceramics were made by sintering c-ZrO_2 powder at 1650 °C and 1×10^{-3} Pa for 3 h, followed by HIP in Ar at 1750 °C and 196 MPa for 1 h and thermal annealing at 1000 °C for decolorization. The incorporation of TiO_2 boosted grain growth and eliminated pores; thus, the optical transmittance of the c-YSZ ceramics was similar to that of single crystals with the same composition. Moreover, the optical properties of the c-YSZ ceramics were also highly dependent on the microstructural profiles of the presintered samples.

Transparent ZrO_2 ceramics can also be developed using SPS; for example, Zhang et al. employed high-pressure SPS to prepare cubic ZrO_2 ceramics at 1000–1200 °C using commercial 8 mol% Y_2O_3:ZrO_2 powder as the precursor [104]. They performed SPS at 400 MPa with a 10^{-3} Torr vacuum and 10 °C/min heating rate, and the as-sintered samples were annealed at 900 °C in air for 4 h in order to compare the optical properties before and after thermal annealing. The sample sintered at 1000 °C was opaque because of insufficient densification while the samples sintered at 1075 °C were somewhat transparent, although they had a yellowish-brown color, and the sample sintered at 1100 °C exhibited the highest transparency. As the sintering temperature was increased beyond 1100 °C, the samples gradually became darker. The yellowish-brown color was attributed to oxygen vacancies with trapped electrons, which were due to the Y_2O_3 dopant. These color centers were formed by the thermal reduction environment created by graphite dies under vacuum, and could be eliminated by thermal annealing.

Lei et al. have also used SPS to fabricate transparent ZrO_2 ceramics [105]. They prepared 8YSZ nanopowder with a cubic crystal structure using a glycine-nitrate wet-chemical approach followed by high-energy ball milling. After calcination at 900 °C, which was determined to be the optimal temperature, the 8YSZ nanopowder had spherical particles with an average size of 50 nm. The powder was densified by SPS at 1200–1350 °C for 5 min and exhibited promising densification behavior. After sintering at 1300 °C, pores had been removed from grain boundaries and transferred to intragranular ones; thus, transparent 8YSZ ceramics were obtained at this temperature.

A similar SPS approach has also been reported by Casolco et al. whereby partially stabilized (3 mol% Y_2O_3:ZrO_2) and fully stabilized (8 mol% Y_2O_3:ZrO_2) nanopowders were processed to obtain transparent ZrO_2 ceramics [99]. The final products had an average grain size of 55 nm, and while the partially stabilized 3YSZ ceramics were translucent, the fully stabilized 8YSZ ceramics were optically transparent. Moreover, the color of the transparent 8YSZ ceramics could be changed from ruby to amber by simply varying the sintering time.

Because the dopant concentration and thus composition of YSZ can be varied, the interrelationship between composition and optical properties must be understood. Although other dopants, such as CaO and MgO, could be used to stabilize ZrO_2, there are very few reports of other dopants in the open literature; therefore, transparent ZrO_2 ceramics with dopants other than Y_2O_3 should be studied.

2.1.4. Sesquioxides

2.1.4.1. Yttria (Y_2O_3). Yttria (Y_2O_3) ceramics have outstanding physical and chemical properties, such as high thermal conductivity (13.6 W/m·K at 300 K) and strong corrosion resistance, and transparent Y_2O_3 ceramics have unique optical properties, which include a wide range of transparent wavelengths (0.2–8 μm) and a refractive index of approximately 1.935 [106]. Compared to yttrium aluminum garnet

SDC EX. 1018 - 14/66

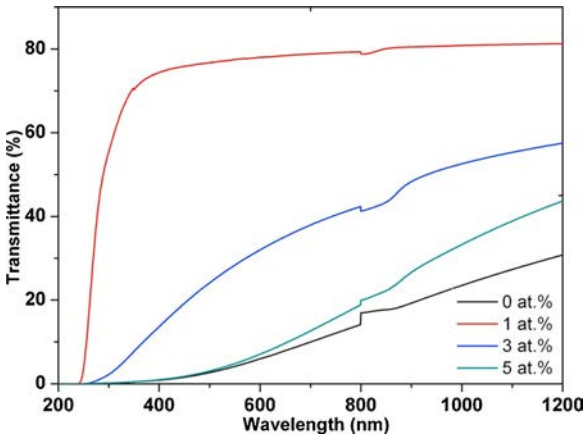

Fig. 15. In-line transmittance curves of ZrO_2-doped Y_2O_3 ceramics after hot-pressing at 1600 °C and 20 MPa for 3 h. Reproduced from [123]. Copyright © 2017, Elsevier.

(YAG), Y_2O_3 is more promising as a scintillator because of its high effective atomic number and high density [107]. Furthermore, Y_2O_3 is more suitable for high-power solid-state laser applications than YAG because it has higher thermal conductivity and a lower thermal expansion coefficient [108]. Potential applications of transparent Y_2O_3 ceramics also include IR domes, gas nozzles, refractory materials, semiconductor components, and NIR-visible upconverters [109–111]. Representative transparent Y_2O_3 ceramics are listed in Table 3.

Transparent Y_2O_3 ceramics were first reported 50 years ago [112]. These initial samples were obtained by hot-pressing under vacuum at 950 °C and 10,000–12,000 psi for 2 days. Lithium fluoride was used as the sintering aid to ensure full densification of the ceramics, and was eliminated during the sintering process. The optical transmittance of the HP-derived transparent Y_2O_3 ceramics was very close to that of single crystals.

More recently, transparent Y_2O_3 ceramics have been fabricated by pressure-less sintering in a vacuum or H_2 atmosphere [21,41,113–120]. For example, Saito et al. developed a simple method to synthesize Y_2O_3 powder with high sinterability, from which transparent ceramics could be obtained without the use of sintering aids [115]. This highly reactive Y_2O_3 powder was derived from fine, needle-shaped yttrium carbonate, which had been synthesized by the precipitation of yttrium nitrate. After yttrium carbonate was calcined at 1100 °C, the resultant Y_2O_3 powder had an average particle size of 0.1 μm and a small agglomeration size of 0.3 μm. Transparent samples were obtained by sintering at ≥ 1600 °C and while abnormal grain growth was not present, the optical transparency was still much lower than that of single crystals.

Ikegami et al. prepared thin, flake-shaped yttrium hydroxide that yielded fine Y_2O_3 powder after calcination at > 800 °C, and this powder was used to fabricate transparent Y_2O_3 ceramics [21]. As expected, the particle size of the calcined powder gradually increased with increasing calcination temperature; skeleton Y_2O_3 particles with poor sinterability were formed by calcination at temperatures < 1000 °C whereas monodispersed particles were obtained by calcination at > 1000 °C. The undoped and sulfate-doped Y_2O_3 powders possessed similar densification behaviors for similar particle sizes; however, the sulfate-doped Y_2O_3 particles had round edges, independent of calcination temperature, while the undoped Y_2O_3 particles had sharp edges. Sulfate-doping and calcining at 1100 °C were determined to be the optimal conditions for obtaining transparent ceramics.

Jin et al. prepared transparent ZrO_2-doped Y_2O_3 ceramics from commercial powder by combining vacuum sintering with an aqueous slip-casting technique [118]. After ball milling the commercial powder in alcohol for 12 h, the average particle size was reduced from 2 μm to 0.34 μm, which promoted densification of the powder. Transparent Y_2O_3 ceramics doped with ZrO_2 at > 2 mol% could be fabricated by sintering at 1860 °C for 8 h, and based on optical transmittance, the optimal concentration of ZrO_2 was 5 mol%.

Hou et al. reported the fabrication and characterization of transparent Y_2O_3 ceramics by vacuum sintering [121]. High purity Y_2O_3 and Nd_2O_3 powders were used as the precursors, and 1.0 mol% ZrO_2 was added as the sintering aid. The three powders were thoroughly mixed such that the composition was $(Nd_xY_{0.99-x}Zr_{0.01})_2O_3$ (x = 0.001–0.07). After drying, pellets were made for CIP at 200 MPa. The Nd:Y_2O_3 samples were highly transparent after sintering at 1800 °C for 20 h under a vacuum of approximately 1.0×10^{-3} Pa.

Transparent Y_2O_3 ceramics have also been fabricated using advanced sintering technologies, such as HP [122,123], HIP [124–131], and SPS [132–142]. For example, transparent Eu^{3+}-doped Y_2O_3 ceramics were developed without the use of sintering aids by HP at 40 MPa and 1580 °C, which was determined to be the optimal sintering temperature [122]. While no sintering aid was added, the Eu dopant served as a sintering aid by controlling the ionic diffusivity and thus promoting the densification of Y_2O_3. As the concentration of Eu was increased from 0 to 5 at%, the optical attenuation and optical transmittance gradually decreased and increased, respectively.

Recently, Gan et al. conducted a systematic study of the effects of temperature and pressure on the microstructure and optical properties of ZrO_2-doped Y_2O_3 ceramics fabricated using a HP method [123]. Commercial Y_2O_3 and $ZrO(CH_2COO)_2$ were used as the starting materials and mixed by ball milling in alcohol. The mixtures were dried and then calcined at 800 °C for 4 h to burn off the organic substances. After calcination, the powders were compacted into square disks at 5 MPa, followed by CIP at 20 MPa. Hot pressing was performed at 1600–1700 °C and 20–40 MPa for 3 h under a vacuum of approximately 9×10^{-3} Pa. The hot-pressed samples were annealed in air at 1200 °C for 2 h. The XRD spectra did not show ZrO_2 as there was only a small quantity in the samples.

Fig. 15 shows in-line transmittance curves of 2-mm thick samples of ZrO_2-doped Y_2O_3 ceramics. While the undoped sample had a relatively low transmittance (< 15%) between 400 and 800 nm, the in-line transmittance of the sample doped with 1 at% ZrO_2 was 74.4% at 400 nm and 81.1% at 1100 nm, the latter of which nearly reached the theoretical transmittance of Y_2O_3: 81.93% at 1100 nm [118]. Increasing the ZrO_2 content above 1 at% corresponded to reduced optical transmittance; therefore, the optimal ZrO_2 content was 1 at%. If the ZrO_2 content was to be increased to 3 at%, both the sintering temperature and pressure would need to be increased to maintain the desired optical performance; however, Y^{3+} would be reduced if the pressure was too high, which would decrease the optical transmittance of the ceramics.

Changes in the optical properties of the ZrO_2-doped Y_2O_3 ceramics were closely associated with the ZrO_2 content and resultant ceramic microstructures. Fig. 16 shows SEM images of Y_2O_3 ceramics doped with different amounts of ZrO_2, which exhibited apparent grain growth with respect to the starting powder. Without the addition of ZrO_2, both intergranular pores and a small number of intragranular pores were present in the ceramic (Fig. 16a); therefore, this sample had the lowest transmittance. While the sample doped with 1 at% ZrO_2 had very few pores and a relatively homogeneous microstructure compared to that of the undoped sample, the samples with 3 and 5 at% ZrO_2 had more intergranular pores and less homogeneous microstructures. Moreover, average grain size and size distribution analysis of the samples demonstrated that the average grain size decreased continuously from 1.22 to 0.44 μm as the ZrO_2 concentration increased from 0 to 5 at% and the full width at half maximum (FWHM) of the grain size distribution curves narrowed as the ZrO_2 content increased.

The low transmittance of the samples with 0, 3, and 5 at% ZrO_2 were ascribed to the presence of residual pores while 1 at% ZrO_2 promoted the densification of Y_2O_3 and thus enhanced the optical transmittance of Y_2O_3. The addition of ZrO_2 also reduced the grain boundary mobility of Y_2O_3, which restricted grain growth and prevented the

SDC EX. 1018 - 15/66

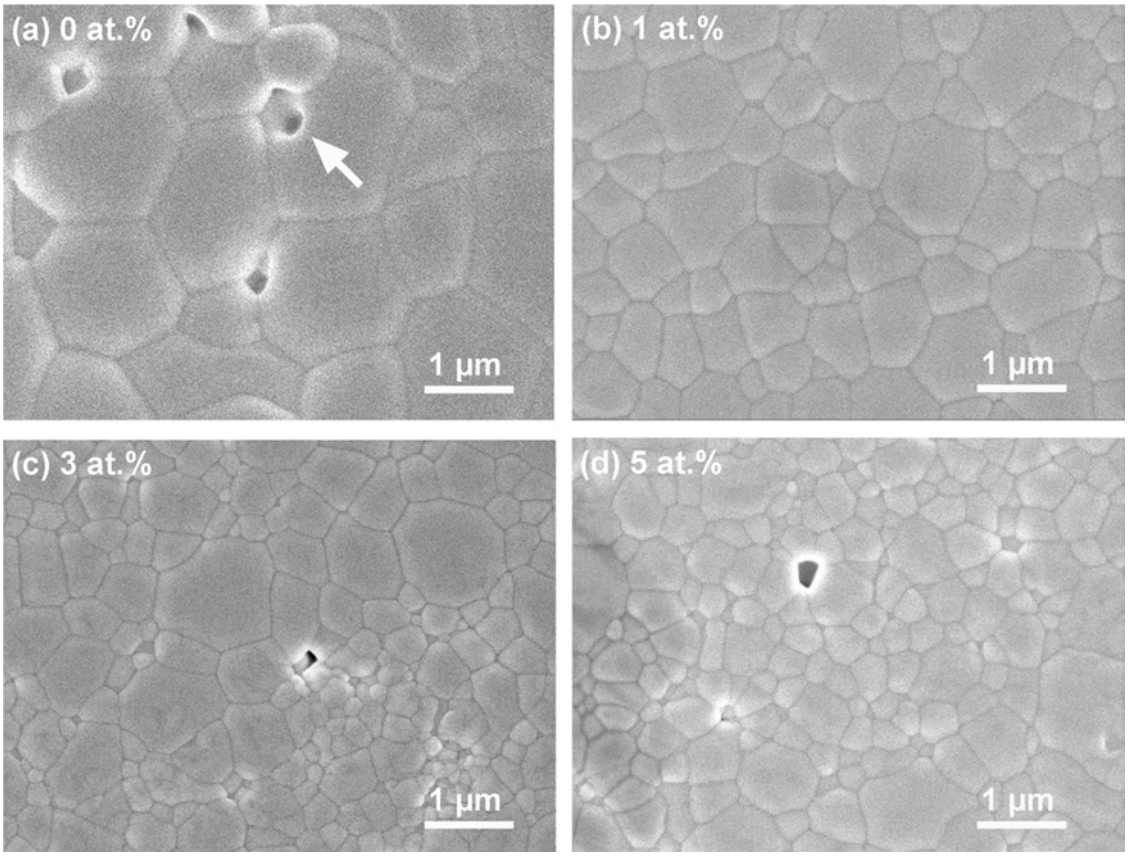

Fig. 16. SEM images of the ZrO_2-doped Y_2O_3 ceramics after hot-pressing at 1600 °C and 20 MPa for 3 h: (a) 0 at% ZrO_2, (b) 1 at% ZrO_2, (c) 3 at% ZrO_2, and (d) 5 at% ZrO_2. Reproduced from [123]. Copyright © 2017, Elsevier.

formation of intragranular pores. Compared with vacuum sintering, which requires very high sintering temperatures (> 1800 °C), HP can promote densification at relatively low temperatures by applying mechanical pressures. While the high grain boundary mobility of pure Y_2O_3 at elevated temperatures resulted in large grain sizes and numerous pores, the presence of 1 at% ZrO_2 significantly reduced the grain boundary mobility of Y_2O_3 and increased densification; thus, 1 at % ZrO_2:Y_2O_3 had a homogeneous and dense microstructure with excellent optical transparency. However, when the ZrO_2 content was too high, grain boundary mobility was suppressed and grain growth was prohibited such that the densification of Y_2O_3 was impaired, especially as the sintering temperature was not sufficiently high, and intergranular pores were formed. Therefore, a suitable grain growth rate must be maintained and the formation of both the intergranular and intragranular pores should be prevented.

Gan et al. also demonstrated that when the HP temperature was increased from 1600 °C to 1700 °C, the size of the large grains was almost unchanged whereas the size of small grains increased substantially; hence, the average grain size increased. Moreover, the homogeneity of the ceramic microstructure improved as a result of the synergistic effect of accelerated mass transport and diffusion, which enhanced the uniform distribution of Zr and effectively prevented abnormal grain growth of Y_2O_3. The optical transparency of the ZrO_2:Y_2O_3 ceramics was able to be increased further by increasing the mechanical pressure from 20 to 30 MPa. While increasing the applied pressure beyond 30 MPa caused the in-line transmittance to decrease because dark color centers were formed by the reduction of Y_2O_3, this issue could be easily addressed by thermal annealing after sintering, which would allow higher pressures to be used.

Mouzon et al. combined vacuum sintering with HIP to obtain transparent Y_2O_3 ceramics from a commercial powder with a high degree of agglomeration [125]. The HIP process was intended to eliminate the pores formed by vacuum sintering; therefore, the presintering process was designed to restrict pores to the intergranular sites so that they could be easily removed by HIP. Thus, an agglomerated powder with closely packed particles was used as the precursor in order to trap the majority of pores in the intergranular areas. The optimal processing temperatures for presintering and HIP were 1600 °C and 1500 °C, respectively. If the HIP temperature was too high temperatures, e.g., 1625 °C, the samples were opaque because Ar molecules had diffused into the capsule.

More recently, Zhu et al. reported that highly transparent Y_2O_3 ceramics with a mean grain size of 0.6 μm can be fabricated using a combination of HP and HIP with a commercial Y_2O_3 powder and ZrO_2 as the sintering aid [143]. The HP conditions were 1300–1550 °C at 20 MPa for 3 h, and the HIP conditions were 1450 °C at 180 MPa of Ar for 5 h. The optimal HP parameters were 1400 °C for 3 h, which yielded ceramics with 83.4% and 78.3% in-line transmittance at 1100 nm and 400 nm, respectively. Fig. 17 shows photographs of Y_2O_3 ceramic samples that were hot-pressed at different temperatures.

Fig. 18 shows fractured surface SEM images of hot-pressed Y_2O_3 samples doped with 1 at% ZrO_2. After hot pressing at 1300 °C, numerous interconnected intergranular pores were present. These pores had a pinning effect on the mobility of the grain boundaries and thus prevented grain growth. There were also isolated pores along the grain edges, which suggests that sintering was inconsistent during the intermediate stage and final stage at 1300 °C. When the hot-pressing temperature was increased to 1350 °C, the number of intergranular pores reduced tremendously and the residual pores became isolated, which indicates that sintering reached completion at 1350 °C. When the hot-pressing temperature was increased beyond 1350 °C, both porosity and pore size were reduced, as indicated in Fig. 18(d–f); for example,

SDC EX. 1018 - 16/66

Fig. 17. Photographs of 2-mm thick Y_2O_3 ceramic samples after HIP and HP at different temperatures (from left to right): 1300 °C, 1350 °C, 1400 °C, 1450 °C, 1500 °C, and 1550 °C. Reused from [143]. Copyright © 2018, Elsevier.

nanopores outnumbered micropores after hot-pressing at 1450 °C (Fig. 18d).

Li et al. used HIP to obtain highly transparent Y_2O_3 ceramics doped with ZrO_2 and the effects of the ZrO_2 concentration on the sintering characteristics, optical properties, grain size, size distribution, and Vickers hardness of the final Y_2O_3 ceramics were systematically studied [131]. The optimal ZrO_2 content in terms of the optical transmittance, red-shifted IR cutoff wavelength, thermal conductivity, and Vickers hardness was determined to be 0.50 at%. For this ZrO_2 content, the presintering temperature ranged from 1650 to 1750 °C, and the average grain size was 3.35 μm after sintering at 1750 °C. The maximum in-line transmittance achieved by these Y_2O_3 ceramics was approximately 75% at 500 nm; however, the optical performance was much better at IR wavelengths.

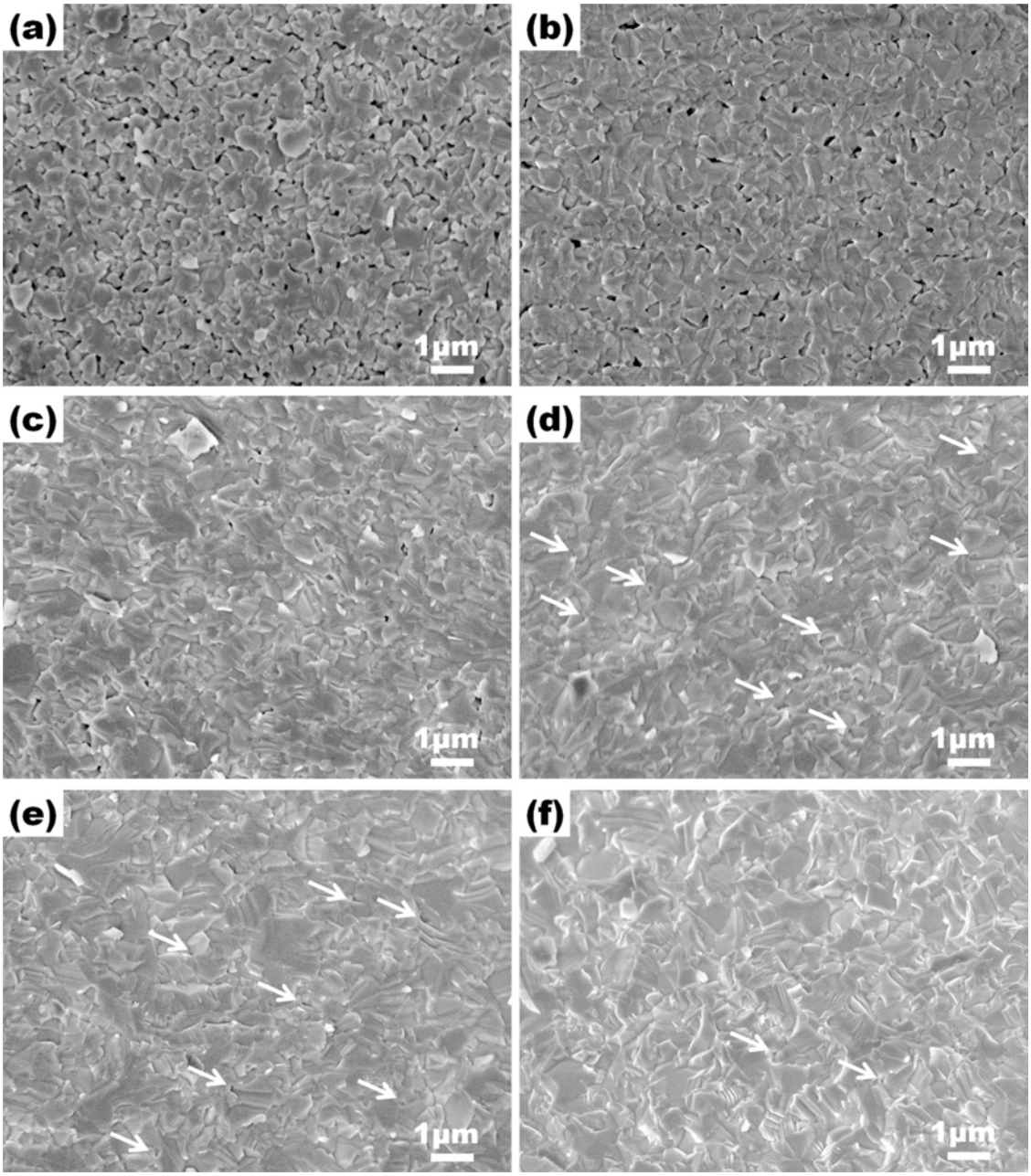

Fig. 18. Cross-sectional SEM images of the Y_2O_3 samples hot-pressed at different temperatures before HIP: (a) 1300 °C, (b) 1350 °C, (c) 1400 °C, (d) 1450 °C, (e) 1500 °C, and (f) 1550 °C. Reused from [143]. Copyright © 2018, Elsevier.

SDC EX. 1018 - 17/66

Yoshida et al. prepared nanocrystalline Y_2O_3 ceramics without sintering aids using SPS with relatively low sintering temperatures (850–1050 °C) and low heating rates (2–50 °C/min) [132]. After heating at 2 °C/min and sintering at 950 °C, the resultant Y_2O_3 sample had 99% relative density with an average grain size of 190 nm. The ceramics heated at 2 °C/min and sintered at either 950 or 1050 °C for 1 h demonstrated promising optical properties – their in-line transmittance ranged from 6% to 46% between 400 and 800 nm – as a result of the absence of an amorphous grain boundary layer and impurity contamination. Densification of the Y_2O_3 nanopowder was promoted by SPS because grain-boundary mobility and diffusion-induced defect reactions were enhanced.

The transparent Y_2O_3 ceramics fabricated by An et al. were used to study the effects of SPS temperature on densification, microstructure development, optical performance, and mechanical strength [133]. Full densification was achieved by sintering at 1200–1600 °C. The grain size was 0.24–0.32 μm after sintering at 1200–1300 °C, and 1.97 μm after sintering at 1600 °C. The Y_2O_3 ceramics sintered at 1300 °C and annealed at 1050 °C had the highest optical properties; their in-line transmittance was 81.7% at 2000 nm, which was 99% of the theoretical value.

Zhang et al. used high-pressure SPS (HP-SPS) to further decrease the sintering temperature required to process transparent Y_2O_3 ceramics [144]. They demonstrated that the sintering temperature could be as low as 1050 °C when the sample was under high pressure (300 MPa). Although oxygen vacancies were formed in the as-sintered samples, they could be eliminated by annealing at 900 °C for 3 h. The in-line transmittance of 1-mm thick samples was 68% at 700 nm, and the optical performance was close to that of single crystals in the near-IR (NIR). More importantly, these transparent Y_2O_3 ceramics had nanograins with an average value of 400 nm, which is an advantageous for the development of transparent ceramics with high mechanical strength.

Several other attempts have been made to develop Y_2O_3 ceramics with small grain sizes without compromising optical transparency. These strategies have included the use of highly sinterable starting powders, adoption of appropriate sintering aids, and manipulation of sintering processes. For example, wet chemical routes such as chemical coprecipitation, sol-gel processes, and thermal combustion have been widely employed to prepare highly sinterable Y_2O_3 nanopowders with or without dopants [145,146].

Wen et al. synthesized ultrafine Y_2O_3 powder with an average grain size of 60 nm using the chemical precipitation method with $Y_2(OH)_5NO_3{\cdot}H_2O$ as the precursor and an aqueous solution of ammonia as the precipitant [145]. High-purity commercial Y_2O_3 powder was dissolved in concentrated nitric acid to form the precursor solution of $Y_2(OH)_5NO_3{\cdot}H_2O$, which was diluted to 0.26 M with DI water, and ammonia sulfate was added to some samples. Precipitation was conducted by two methods: (i) normal striking (precipitant added to precursor solution), and (ii) reverse striking (precursor solution added to precipitant solution). According to striking method and synthetic parameters, $Y(OH)_3$ had either a card-house or spherical morphology and the powders obtained by normal striking were more reactive than those obtained by reverse striking. Furthermore, the agglomeration and particle size of the precipitated Y_2O_3 powders could be reduced by adding a small quantity of $(NH_4)_2SO_4$ to the precursor solution. For these ultrafine powders, calcination at 1100 °C for 4 h was determined to be optimal, and the in-line transmittance of the resultant transparent Y_2O_3 ceramics was 52% at 1000 nm after vacuum sintering at 1700 °C for 4 h.

A Pechini sol-gel process was used to synthesize high-purity Y_2O_3 nanopowder with citric acid and ethylene glycol as the chelating agent and Y^{3+} complexant, respectively [136]. The nanopowder was densified by SPS at 1100 °C for 5 min under 100 MPa of uniaxial pressure. The final Y_2O_3 ceramics had an average grain size of 40 μm and an in-line transmittance of 60% at 700 nm.

Compounds such as ThO_2 [113], La_2O_3 [114,147], HfO_2 [34], LiF [148], and ZrO_2 [147,149] have been employed as dopants or sintering aids to develop transparent Y_2O_3 ceramics. Furthermore, combinations of these dopants have been shown to be more effective than individual dopants [150–152]. One advantage of sintering aids is that they allow the sintering temperature to be reduced, which results in Y_2O_3 ceramics with smaller grain sizes. Moreover, the effect sintering aids can be maximized when sintering aids are combined with other process technologies, such as slip casting, vacuum sintering [118], and sintering in an O_2 atmosphere [153].

Zhu et al. prepared highly transparent Er:Y_2O_3 ceramics by vacuum sintering with two sintering aids: ZrO_2 and La_2O_3 [147]. Commercial oxide powders, Y_2O_3 (99.99%) and Er_2O_3 (99.99%), were used as the precursors, while La_2O_3 (99.99%) and $ZrO(CH_3COO)_2$ (98%) were added as sintering aids; the ceramic compositions were $(Y_{0.87-x}Er_xLa_{0.1}Zr_{0.03})_2O_3$ with x = 0, 0.01, 0.03, 0.05, and 0.1. The powders were thoroughly mixed, calcined at 1200 °C for 4 h, and uniaxially pressed into pellets at 5 MPa before CIP at 200 MPa. Vacuum sintering was conducted at 1800 °C for 16 h under 1.0×10^{-3} Pa, and the sintered samples were annealed in air at 1400 °C for 4 h. The in-line transmittance of the resultant ceramics was 83% at 1100 nm and 81% at 600 nm. When the Er concentration was increased, the thermal conductivity decreased gradually from 5.55 to 4.89 W/m·K while the average grain size, microhardness, and fractural toughness did not change.

By combining two-step presintering and vacuum sintering, Huang et al. successfully obtained transparent La-doped Y_2O_3 ceramics [117]. The first presintering step was performed at an intermediate temperature (T_1 = 1450 °C) in air, after which the temperature was rapidly decreased (T_2 = 900–1100 °C) and held for 20 h to ensure that the desired densification was obtained while grain growth was effectively controlled. The samples had a high relative density and nanometer-sized grains after the first presintering step, and after the second step, the relative density exceeded 90% and the grain size had only increased slightly. The samples were vacuum-sintered at a higher temperature (T_3 = 1700 °C), and the average grain size and optical transmittance of the resultant transparent Y_2O_3 ceramics were 25 μm and 77% at 580 nm, respectively.

Yoshida et al. doped Y_2O_3 powder with 1 mol% Zn^{2+} by SPS and systematically studied the influence of experimental parameters such as the heating rate, sintering temperature, holding time, and loading stress [142]. The optimal conditions for obtaining transparent Zn^{2+}-doped Y_2O_3 ceramics were heating at 2 °C/min, sintering at 890 °C, holding for 0.5 h, and applying 150–170 MPa of pressure. The transmittance of these Zn^{2+}:Y_2O_3 ceramics reached 65% at 600 nm, as shown in Fig. 19.

When using a solid-state reaction method to develop transparent Ho:Y_2O_3 ceramics from commercial oxide powders, Wang et al. found that one of the ball milling parameters, slurry concentration (C_S), was a critical factor influencing densification, microstructure evolution, and thus transmittance of the final products [154]. In this study, Ho:Y_2O_3 powders were ball milled with slurry concentrations ranging from 33.2 to 17.4 vol% and the processed powders were compacted and vacuum-sintered at 1400–1850 °C. As the C_S decreased from 33.2 to 18.4 vol%, the densification, grain growth, and optical transparency of the Ho:Y_2O_3 ceramics gradually increased. At 18.4 vol%, the Ho:Y_2O_3 powder exhibited optimal densification behavior as there was minimal agglomeration and the ceramics fabricated from this powder had the highest optical transmittance, as shown in Fig. 20. This observation implies that optical transmittance is as sensitive to processing as other ceramic properties (e.g., electrical, dielectric, and mechanical properties).

Although transparent Y_2O_3 ceramics have various advantages in terms of thermal and optical properties, the cost of the materials is a potential issue if large-scale applications are to be considered. Furthermore, the effects of sintering aids have not been well-studied. Therefore, future work should focus on the sintering mechanisms of

SDC EX. 1018 - 18/66

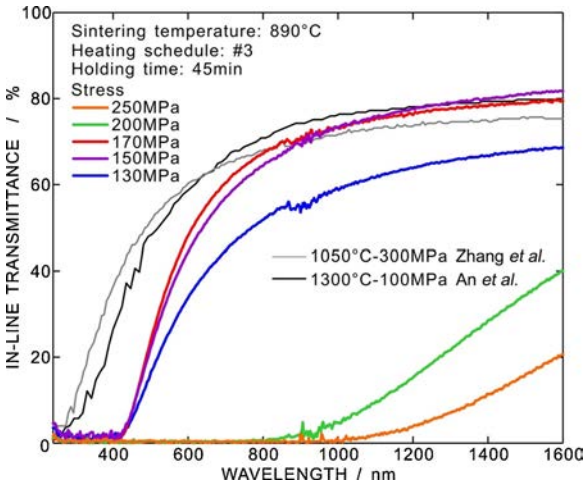

Fig. 19. In-line transmittance curves of the Y_2O_3 ceramics sintered at 890 °C for 0.5 h under different loading stresses: (a) 130 MPa, (b) 170 MPa, (c) 200 MPa, and (d) 250 MPa. Literature transmittance data for undoped transparent Y_2O_3 ceramics prepared by SPS at 1050 °C and 300 MPa [144] and 1300 °C and 100 MPa [843] are included for comparison. Reproduced from [142]. Copyright © 2018, Elsevier.

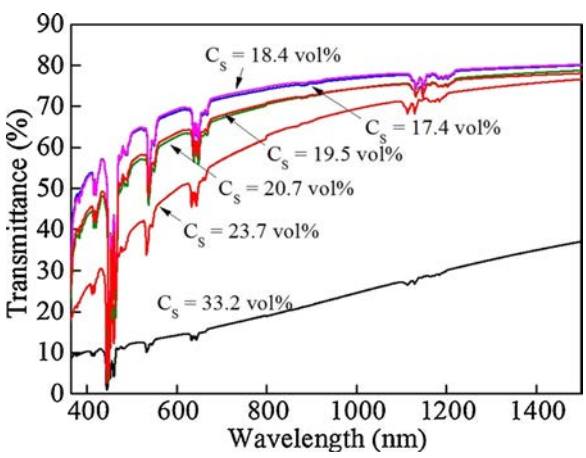

Fig. 20. In-line transmittance curves of 2.14-mm thick samples of the ZrO_2-doped Ho:Y_2O_3 ceramics derived from slurries with different concentrations. Reused from [154]. Copyright © 2015, Elsevier.

transparent Y_2O_3 ceramics when different sintering aids are used.

2.1.4.2. Scandia (Sc_2O_3). Scandia (Sc_2O_3) has outstanding optical performance and thermal properties for applications such as damage-resistant, highly reflective materials in light emitting diodes (LEDs) and high-power pulsed ultraviolet (UV) lasers [155–157]. Other applications of Sc_2O_3 include IR transmitting devices, high-power solid-state lasers with ultra-short pulses, and optical windows with heat-resistant capability [22,158–163]. Vacuum sintering is the most popular method for fabricating transparent Sc_2O_3 ceramics [22,158,159,162–165], and the synthesis of Sc_2O_3 nanopowders is of great interest as nanopowders are highly sinterable and yield high quality final products. Two examples of Sc_2O_3 ceramics are included in Table 3.

Wang et al. reported a homogeneous precipitation method for synthesizing nanocrystalline Sc_2O_3 powder, which they used to fabricate transparent ceramics [165]. High-purity commercial Sc_2O_3 powder was dissolved in an excess of nitric acid at 95–110 °C to form a scandium nitrate solution, to which an aqueous ammonia solution was added in order to trigger the precipitation of scandium hydroxide. After thorough washing and drying, the precipitate was dissolved in sulfuric acid to form a scandium sulfate solution, which was mixed with a urea solution and heated to 95 °C. The pH of the mixed solution was adjusted by adding ammonia solution. After aging for 24 h under constant stirring, the precipitate was washed and dried, followed by calcination at different temperatures to obtain Sc_2O_3 nanopowders, which were compacted and preheated in air at 1100 °C for 2 h to remove organic components. The nanopowder samples were vacuum-sintered (10^{-3} Pa) at 1700 °C for 5 h after heating at 200 °C/h. Between 190–1100 nm, the in-line transmittance of the resultant ceramics was approximately 60%, which was ~80% of that of single crystals.

Li et al. synthesized Sc_2O_3 nanopowder by pyrolysis of a basic sulfate precursor, $Sc(OH)_{2.6}(SO_4)_{0.2}{\cdot}H_2O$, which was precipitated from a scandium sulfate solution using hexamethylenetetramine [158]. The optimal calcination temperature was 1100 °C, which yielded Sc_2O_3 powder with an average particle size of 85 nm and a narrow size distribution. After vacuum sintering this powder at 1700 °C for 4 h, the resultant transparent Sc_2O_3 ceramics had an average grain size of 9 μm and an in-line transmittance of 60–62%.

More recently, a modified coprecipitation method was developed to synthesize Yb:Sc_2O_3 nanopowders that can be used to fabricate transparent ceramics for laser applications [156,157,166]. The Yb:Sc_2O_3 nanopowders were synthesized by separately dissolving commercial powders – Sc_2O_3 (99.99%) and Yb_2O_3 (99.99%) – in nitric acid at 80 °C and mixing the solutions to obtain a solution of 5 at% Yb:Sc_2O_3. Ammonium sulfate, $(NH_4)_2SO_4$, was added to the 5 at% solution as a dispersing agent to reach a 1:1 M ratio of M^{3+} (Sc^{3+} + Yb^{3+}) to $(NH_4)_2SO_4$, and NH_4HCO_3 was then added as the precipitation agent. The suspension was thoroughly washed with distilled water and absolute alcohol, and the precipitate was collected by centrifugation. The precipitate was dried at 70 °C for two days, and then calcined at 600–1200 °C for 5 h. After calcination, the Yb:Sc_2O_3 powders were dry-pressed into pellets with a diameter of 20 mm and treated with CIP at 250 MPa. The samples were then vacuum-sintered at 1600–1850 °C for 10 h under a 5×10^{-4} Pa vacuum – the heating and cooling rates were 2 °C/min and 10 °C/min, respectively – and the vacuum-sintered samples were annealed in air at 1450 °C for 10 h.

Calcination at 1100 °C for 5 h formed ultrafine, low-agglomerated 5 at% Yb:Sc_2O_3 powders with an average particle size of 65 nm, and vacuum sintering these powders at 1825 °C for 10 h yielded transparent 5 at%Yb:Sc_2O_3 ceramics with 71.1% in-line transmittance at 1100 nm. Because high sintering temperatures were used, the average grain size of the 5 at% Yb-Sc_2O_3 ceramics was relatively large: 145 μm. Quasi-CW laser oscillation was obtained by the Yb:Sc_2O_3 ceramics at 1040.6 nm, and the maximum output power (2.44 W) corresponded to a 35% slope.

The in-line transmittance of the Yb:Sc_2O_3 ceramics increased monotonically as the calcination temperature was increased from 600 °C to 1100 °C because the residual content of carbonate and sulfate decreased. However, as the calcination temperature increased to 1200 °C, the optical performance dropped abruptly as agglomerated particles were formed and the powder became less sinterable; for example, the Yb-:Sc_2O_3 sample sintered from the 1200 °C-calcined powder had the smallest grain size, 27 μm. Sintering temperature was also a critical factor influencing the optical performance of the transparent ceramics, and the sample sintered at 1850 °C exhibited the highest transmittance.

Fig. 21 shows SEM images of thermally etched and freshly fractured surfaces of the transparent 5 at% Yb:Sc_2O_3 ceramics sintered at 1650 °C and 1850 °C. These images illustrate that grain size was closely related to the sintering temperature. The sample sintered at 1650 °C had an average grain size of 34 μm and a large number of pores were present at the grain boundaries, which resulted in relatively low optical transmittance. Conversely, the sample sintered at 1850 °C exhibited a dense microstructure with an average grain size of 183 μm and very few pores. Moreover, the fracture mode was transgranular. Increasing the sintering temperature beyond 1850 °C is a challenge; therefore, optimization of other processing parameters should be a focus of future

SDC EX. 1018 - 19/66

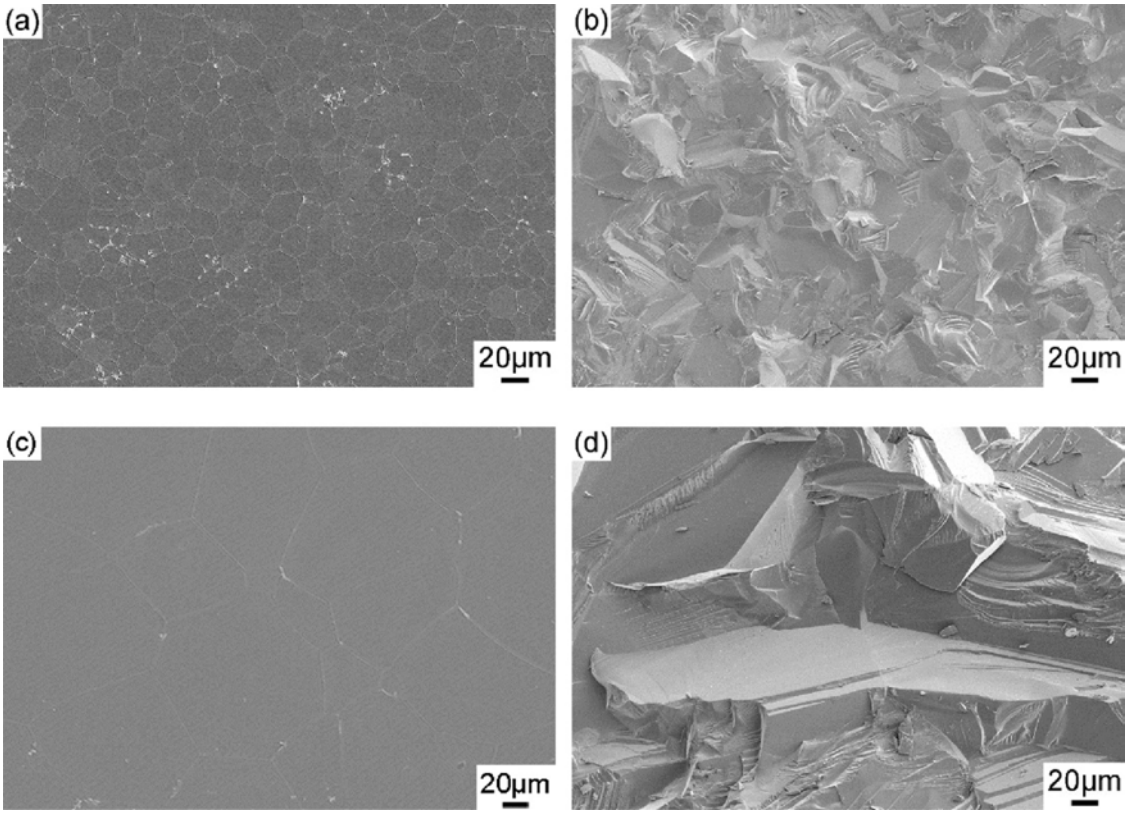

Fig. 21. SEM images of the (a, c) thermally etched and (b, d) freshly fractured surfaces of 5 at%Yb:Sc_2O_3 ceramics sintered for 10 h at either (a, b) 1650 °C or (c, d) 1850 °C. Reused from [166]. Copyright © 2017, Elsevier.

development.

Sintering technologies that apply pressure are effective strategies for developing transparent Sc_2O_3 ceramics with relatively small grains. For example, transparent Er-doped Sc_2O_3 ceramics fabricated by HIP have been reported to have an average grain size as small as 0.3 μm when solution-derived nanopowders were presintered by a two-step sintering (TSS) process [40]. The presintering was conducted at 1300–1600 °C under a vacuum < 10^{-3} Pa, and the heating rate was 10 °C/min. For TSS, the samples were heated to T_1 at 10 °C/min and then the temperature was decreased to T_2 ($T_2 < T_1$) at 50 °C/min. The samples were held at T_2 for 20 h. The transparent Sc_2O_3 ceramics obtained from the TSS presintered samples had > 98% relative density after HIP in Ar at 1300 °C and 206 MPa for 3 h (HIP-TSS).

The relatively low transmittance of HIP–TSS3, as shown in the figure, can be explained by considering the effect of T_1. For TSS3, T_1 = 1550 °C and at this temperature, rapid grain growth eliminated pores at the grain boundaries, which caused intragranular pores to form. Such pores were difficult to remove during the TSS and HIP processes; thus, they remained and acted as scattering centers, which reduced the transparency of the TSS3 samples. For comparison, the TSS6 and TSS9 samples had T_1 = 1500 and 1450 °C, respectively, and the grain growth rates at these temperatures were sufficiently low to allow pores to remain at the grain boundaries and triple grain junctions. These intergranular pores could easily escape during TSS and HIP; thus, the resultant ceramics were more transparent. Based on these results, T_1 was a critical parameter for achieving ceramics with high transparency.

2.1.4.3. Lutetia (Lu_2O_3). Lutetia (Lu_2O_3) is a potential host material for various activators because of its wide bandgap and unique chemical and physical properties, which include high phase stability, low thermal expansion, and high chemical inertness. Moreover, Lu_2O_3 can be doped with high concentrations of Yb^{3+} without compromising its thermal conductivity because Lu^{3+} and Yb^{3+} have similar atomic masses and ionic radii [167]. As compared with Y_2O_3, Lu_2O_3 is much denser (9.42 g·cm^{-3}) and has a much higher stopping power for ionizing radiation as Lu has a high *Z* number, 71. Either Nd- or Yb-doped Lu_2O_3 ceramics are promising candidates for high-power solid-state lasers, and Er^{3+}-doped Lu_2O_3 scintillators could be useful for digital X-ray imaging because of their high stopping powers, their very high efficiency for converting X-rays to visible light, and their ability to couple visible emissions with silicon-based CCD spectral responses [168,169]. Representative transparent Lu_2O_3 ceramics are also included in Table 3.

Vacuum sintering has been widely used to develop Lu_2O_3-based transparent ceramics [170–172]. For example, Ma et al. prepared mono-dispersed, spherical 5 mol% Eu:Lu_2O_3 powders using a urea-based, homogeneous precipitation process and used these powders to fabricate transparent ceramics [171]. The Eu^{3+} dopant decreased the particle size of the precipitate, and the sequential precipitation of Lu^{3+} and Eu^{3+} created a compositional gradient in the individual spheres. Fig. 22 shows representative SEM images of the spherical particles, and the spherical morphology was retained during calcination at 600–1000 °C for 4 h. The optimal calcination temperature was determined to be 600 °C, and vacuum sintering at 1700 °C for 5 h formed transparent ceramics with ~55% in-line transmittance at 600 nm.

Wang et al. combined a solid-state reaction with vacuum sintering to prepare transparent Er^{3+}:Lu_2O_3 ceramics using commercial Lu_2O_3 and Er_2O_3 powders as the precursors and tetraethyl orthosilicate (TEOS) as a sintering aid [173]. The Lu_2O_3 and Er_2O_3 powders were mixed to obtain $Lu_{1.96}Er_{0.04}O_3$, and TEOS was added to 0.5 wt%; the samples were mixed by ball-milling in alcohol with zirconia balls for 24 h. The mixed powder was calcined at 1100 °C for 2 h and compacted at 30 MPa, followed by CIP at 200 MPa. The samples were then vacuum-sintered at 1850 °C for 10–12 h. The typical transmittance of the resultant ceramics was 67% in the visible to NIR range. Under excitation at 980 nm by a laser diode (LD), the ceramics demonstrated a

SDC EX. 1018 - 20/66

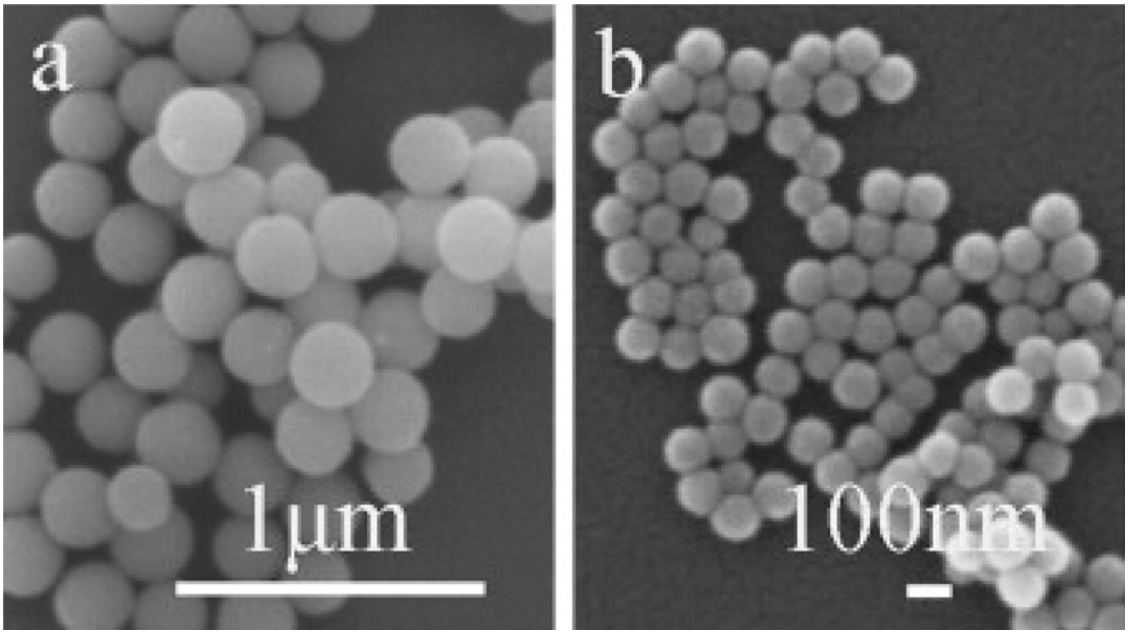

Fig. 22. SEM images of (a) $Lu(OH)CO_3$ and (b) $(Lu_{0.95}Eu_{0.05})OHCO_3$ precursor powders. Reused from [171]. Copyright © 2015, Elsevier.

broad bandwidth emission at 1.5 μm, which suggests they could be a potential tunable laser material, and a strong up-conversion luminescence centered at 565 nm and 660 nm.

Chen et al. used a coprecipitation method to prepare Lu_2O_3 nanopowder, and subsequently fabricated transparent Eu-doped Lu_2O_3 ceramics [174]. The Eu-doped Lu_2O_3 powder was synthesized using a mixture of $NH_3{\cdot}H_2O$ and NH_4HCO_3, obtained from nitrate salt solutions, as the precipitant. Highly dispersed, ultrafine powder with a high densification rate was obtained after calcining at 1000 °C for 2 h, and highly transparent Eu:Lu_2O_3 ceramics with 50–60 μm grain sizes were obtained by vacuum sintering in H_2 at 1850 °C for 6 h. The optical transmittance of the final ceramics was 80.3% between 600 to 700 nm.

Hot isostatic pressing is also an effective technique for developing transparent Lu_2O_3 ceramics [175–178], and Seeley et al. coupled HIP with vacuum sintering to develop transparent ceramics with high optical properties [179]. These authors used a commercial Eu:Lu_2O_3 nanopowder that had been synthesized by flame spray pyrolysis. The nanopowder was dispersed in an aqueous solution of polyethylene glycol (PEG) and ammonium polymethacrylate using strong ultrasonication, and was spray dried at 210 °C in flowing N_2. The dried powder was sieved (< 50 μm) to obtain uniform agglomerates and dry-compacted at 50 MPa to obtain green bodies with 35% relative density, which were calcined at 900 °C to eliminate organic substances. Vacuum sintering was conducted under a high vacuum, $< 2 \times 10^{-6}$ Torr, at 1575–1850 °C and 200 MPa in Ar to reach 94–99% relative density. The vacuum-sintered samples were treated with HIP, which formed highly transparent ceramics without post-annealing.

Transparent Yb:Lu_2O_3 ceramics have been prepared from nanopowders synthesized by laser ablation [177]. These ceramics were presintered under a vacuum and treated with HIP. The Yb:Lu_2O_3 nanopowders were uniaxially pressed and presintered at 1550 °C with a conventional temperature program: slow heating at 3 °C/min followed by subsequent holding (CRH) and rate-controlled sintering (RCS) regime, which reduced the rate of densification. While the relative density was similar for all presintered samples, approximately 97%, the RCS regime yielded samples with an average grain size that had been reduced by > 30%. After HIP processing, transparent Yb:Lu_2O_3 ceramics with high optical properties were readily obtained.

Transparent Yb:Lu_2O_3 ceramics have also been prepared from powders synthesized by coprecipitation by combining vacuum sintering and HIP [180]. Calcination temperature was found to have a significant influence on the composition and morphology of the powders; the optimal calcination conditions, 1100 °C for 4 h, yielded Yb:Lu_2O_3 nanopowders with an average particle size of 67 nm. The 5 at% Yb:Lu_2O_3 ceramics presintered at 1500 °C for 2 h and HIP-treated at 1700 °C for 8 h had an average grain size of 2.6 μm and exhibited 78.2% in-line transmittance, which is promising.

The same group reported Eu:Lu_2O_3 nanopowders synthesized by coprecipitation from europium and lutetium nitrates, with ammonium hydrogen carbonate (AHC) as the precipitation agent [181]. Again, the optimal calcination conditions were 1100 °C for 4 h, and these conditions yielded powders with fine particles, 68 nm, and a low degree of agglomeration. Transparent Eu:Lu_2O_3 ceramics with an average grain size of 46 μm were obtained by vacuum sintering at 1650 °C for 30 h, and the maximum in-line transmittance of these ceramics was 66.3% at 611 nm.

There have been several reports of Lu_2O_3-based transparent ceramics fabricated by SPS with and without sintering aids [171,182–188]. An et al. used SPS to prepare transparent Lu_2O_3 ceramics from commercial powders, and conducted a systematic study of the effects of sintering parameters – i.e., sintering temperature, sintering time, and applied pressure – on the densification, microstructure, and optical performance of the final ceramics [167,189]. Moreover, they increased the transparency of the Lu_2O_3 ceramics by using a two-step pressure strategy and slow heating process [167]. The processing conditions were optimized over the range of pre-load pressures and heating rates: 10–100 MPa and 0.03–1.67 K/s, respectively. The optical performance of the ceramics processed at 30 MPa and heated at 0.17 K/s was optimal, with 60% and 79% in-line transmittance at 550 nm and 2000 nm, respectively.

Prakasam et al. employed SPS to produce 10% Yb-doped Lu_2O_3 transparent ceramics [190]. Commercial oxides were used to prepare nanopowder by chemical coprecipitation from nitric acid solutions. Fully-compacted samples were obtained by SPS at 1250 °C, and the average grain size increased from several nanometers to 5 μm after sintering at 1700 °C; however, excessively high sintering temperatures triggered abnormal grain growth. The optical transparency of the as-sintered samples was improved by thermal annealing at 1200 °C. The ceramics sintered at 1700 °C for 5 min, after heating at 50 °C/min, exhibited the maximum transmittance: 55% at 2 μm for 2-mm thick

SDC EX. 1018 - 21/66

samples.

Xu et al. used SPS to fabricate Nd:Lu_2O_3 ceramics for efficient laser operation [188]. The transparent Nd:Lu_2O_3 ceramics were doped with 0.2 at% LiF as the sintering aid. Based on the $^4F_{3/2}$ to $^4I_{11/2}$ transition, the maximum output of the ceramic laser at 4.15 W absorbed pump power was 1.25 W, with 38% slope efficiency and simultaneous oscillation of two spectral lines, 1076.7 nm and 1080.8 nm. At this transition, the laser could be operated at 1359.7 nm with a maximum output of 200 mW at 2.7 W absorbed pump power.

As with Y_2O_3, the cost of sesquioxide-based transparent ceramics will restrict their industrial applications unless their properties are superior to those of cheaper materials.

2.1.5. Complex oxides

2.1.5.1. Garnet. Yttrium aluminate ($Y_3Al_5O_{12}$), also known as yttrium aluminum garnet (YAG), is one of the most important materials in the garnet family as YAG has a centrosymmetric cubic structure and thus is isotropic [191]. The main applications of YAG are in solid-state lasers, but transparent YAG ceramics also have potential applications in high-temperature structural materials and fluorescent host materials because YAG has high thermal stability, high chemical stability, and homogenous optical properties [35,192]. Transparent Nd:YAG ceramics were first reported as media for solid-state lasers in the mid-1990s, after which they were extensively studied in the open literature [193]. This solid-state application also triggered interest in other transparent ceramics, as evidenced by this review. Representative YAG-based transparent ceramics are listed in Table 4.

Solid-state reaction methods are the most widely adopted process for fabricating transparent YAG ceramics from commercial or synthesized precursors of oxides or other compounds [11,194–204]. In 1995, Ikesue et al. used the solid-state reaction method to fabricate YAG and Nd:YAG transparent ceramics from Al_2O_3, Y_2O_3, and Nd_2O_3 synthesized by alkoxide hydrolysis, thermal pyrolysis, and oxalate precipitation, respectively [192]. The mixed powders were compacted and sintered at 1600–1850 °C for 5 h under a 1.3×10^{-3} Pa vacuum. The optical properties and laser performance of these transparent ceramics were comparable to those of single crystals.

Li et al. have systemically studied the synthesis, densification, microstructure, and optical properties of YAG powders prepared by chemical coprecipitation from mixed solutions of aluminum and yttrium nitrates, using ammonia or ammonium hydrogen carbonate as the precipitant [205–207]. Wen et al. synthesized Y_2O_3 nanopowder by chemical precipitation from a solution of $Y(NO_3)_3$ ammonia, and combined this powder with commercial Al_2O_3 powder to prepare YAG ceramics [208]. Tachiwaki et al. reported a sol-gel method for synthesizing YAG nanopowder that can be used to fabricate transparent YAG ceramics [209]. Liu et al. used a solid-state reaction method to fabricate transparent YAG ceramics from a mixture of commercial α-Al_2O_3 and Y_2O_3 powders, using TEOS and MgO as sintering aids; the average grain size and in-line transmittance of these ceramics were 22 μm and 82.8%, respectively [210].

More recently, Liu et al. studied the effects of stoichiometry on the microstructure and optical properties of transparent YAG ceramics synthesized from commercial powders with 0.08 wt% MgO and 0.8 wt% TEOS added as sintering aids [211]. The conventional solid-state reaction method was used to prepare samples of $Y_{3(1+x)}Al_5O_{12}$, wherein the value of x varied from −4.3 mol% to 4.7 mol%. After combining the precursors and sintering aids, the powder mixtures were calcined at 600 °C for 4 h, followed by uniaxial pressing into pellets and CIP at 250 MPa. The green bodies were sintered at 1500–1750 °C under 10^{-3} Pa for 50 h, and the heating and cooling rates were 5 °C/min and 10 °C/min, respectively. After sintering, all samples were annealed in air at 1450 °C for 10 h in order to eliminate oxygen vacancies.

Both the transmittance and average grain size decreased when the samples had excessive Al_2O_3 because Al_2O_3 was present as a secondary phase. When the samples had excessive Y_2O_3 and $x \leq 0.7$ mol%, the

Table 4
Processing parameters and optical transmittance of representative transparent YAG ceramics.

No.	Powder processing	Sintering parameters	Transmittance	Ref.	Year
1	YAG, solid-state reaction	CIP: 140 MPa Vacuum sintering: 1500–1850 °C/5 h Vacuum: 1.3×10^{-3} Pa	82% at 600 nm	[192]	1995
2	Nd:YAG (0–5 at%), 0.5 wt% TEOS, solid-state reaction	Vacuum sintering: 1700–1850 °C/16 h Vacuum: 6×10^{-6} Torr	> 80% at 350–900 nm	[215]	2006
3	γ-Al_2O_3 + Y_2O_3, 1.5 at% Nd, 0.5 wt% TEOS	Calcination: 1300 °C/4 h Vacuum sintering: 1700 °C/5 h Vacuum: 1×10^{-3} Pa	81% at 700 nm	[195]	2009
4	1 at% Ho:YAG, 0.6 wt% TEOS, solid-state reaction	CIP: 250 MPa Vacuum sintering: 1760 °C/20 h Annealing: 1400 °C/1 h	82% at 700 nm	[196]	2010
5	$Y_{3-x}Tm_xAl_5O_{12}$ (x = 0, 0.18, 0.9, 1.5, 3.0), 0.5–1.0 wt% TEOS, solid-state reaction	CIP: 250 MPa Vacuum sintering: 1780 °C/20 h Vacuum: 10^{-3} Pa Annealing: 1450 °C/20 h	/	[197]	2011
6	Nd:YAG, CaF_2, solid-state reaction	Vacuum sintering: 1750 °C/5 h	44% at 600 nm	[199]	2013
7	YAG, MgO, TEOS, solid-state reaction	CIP: 250 MPa Vacuum sintering: 1500–1750 °C/50 h Vacuum: 10^{-3} Pa Annealing: 1450 °C/20 h	80% at 600 nm	[210]	2014
8	YAG, MgO + CaO (0.2 mol%), solid-state reaction	CIP: 210 MPa Vacuum sintering: 1820–1840 °C/8 h Vacuum: 10^{-6} Torr	80% at 600 nm	[202]	2017
9	YAG, CaO (0.045–0.27 wt%), solid-state reaction	CIP: 200 MPa/5 min Vacuum sintering: 1820 °C/8 h	84.4% at 1064 nm	[203]	2018
10	Nd:YAG, solid-state reaction	Vacuum sintering: 1500 °C/3 h HIP: 1500–1700 °C/3 h, 9.8–196 MPa Vacuum sintering: 1750 °C/20 h	57% at 1000 nm	[856]	1996
11	Nd:YAG, 0.02–0.14 wt% TEOS, solid-state reaction, tape casting	CIP: 200 MPa Vacuum sintering: 1600–1700 °C/2 h Vacuum: 5×10^{-3} Torr HIP: 1750 °C/2 h, 200 MPa	85% at 400 nm	[216]	2009
12	Nd:YAG (0.2 at%), 0.5 wt% TEOS, coprecipitation	Calcination: 1100 °C/24 h CIP: 200 MPa Vacuum sintering: 1450 °C/20 h Annealing: 1450 °C/20 h HIP: 1700 °C/2 h, 200 MPa Annealing: 1250–1450 °C/10 h	77.2% at 400 nm	[857]	2013
13	Nd:YAG (1 at%), 0.07 wt% SiO_2, solid-state reaction	CIP: 200 MPa Presintering: 1650 °C/0–6 h HIP: 1650 °C/1–6 h, 150 MPa	75% at 600 nm	[217]	2016
14	Nd:YAG, 0.5 wt% TEOS, coprecipitation	Calcination: 1100 °C/4 h CIP: 250 MPa Vacuum sintering: 1500–1800 °C/10 h HIP: 1600 °C/3 h, 200 MPa	79% at 600 nm	[218]	2017
15	YAG, coprecipitation	Vacuum sintering: 1700 °C/1 h Vacuum: 10^{-3} Pa	/	[205]	2000
16	YAG, coprecipitation	CIP: 392 MPa Vacuum sintering: 1600 °C/2 h Vacuum: 10^{-3} Pa	/	[209]	2001
17	YAG, coprecipitation, 0.5 wt% TEOS	Calcination: 1100 °C CIP: 200 MPa/13 min Vacuum sintering: 1700 °C/5 h Vacuum: 1.3×10^{-3} Pa	65% at 600 nm	[208]	2004
18	YAG nanopowder	SPS: 1200–1500 °C/3–9 min Pressure: 50–100 MPa	20% at 600 nm	[220]	2007
19	Nd:YAG (2 at%), co-precipitation, 0.25 wt% LiF	SPS: 1100 °C/3 min (100 °C/min); 1250–1390 °C/20 min (10 °C/min) Pressure: 28 MPa	75% at 700 nm	[223]	2016
20	YAG commercial powder, 5 wt% LiF	SPS: 800–1450 °C/20 min Heating rate: 50 °C/min Pressure: 50 MPa	/	[224]	2017
21	Er:YAG (0.5 at%) commercial powder	SPS: 1600 °C Heating rate: 50 °C/min Pressure: 30–70 MPa	/	[858]	2017

SDC EX. 1018 - 22/66

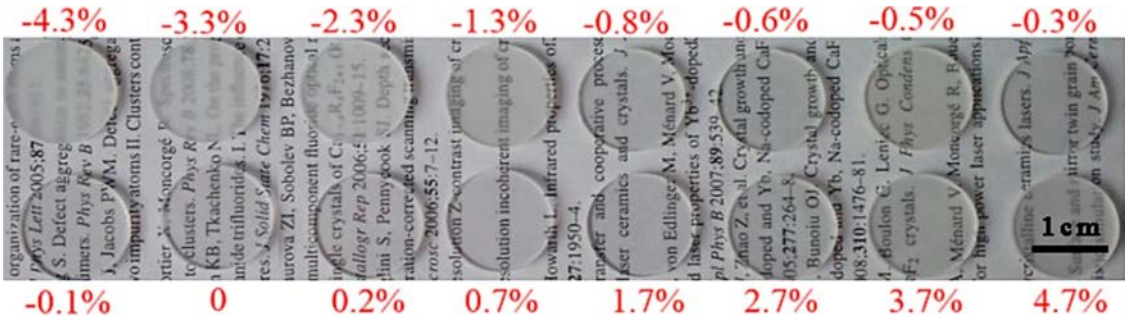

Fig. 23. Photographs of Φ16 mm × 1.5 mm samples of $Y_{3(1+x)}Al_5O_{12}$ ceramics with different values of x after sintering at 1760 °C for 10 h. Reused from [211]. Copyright © 2015, Elsevier.

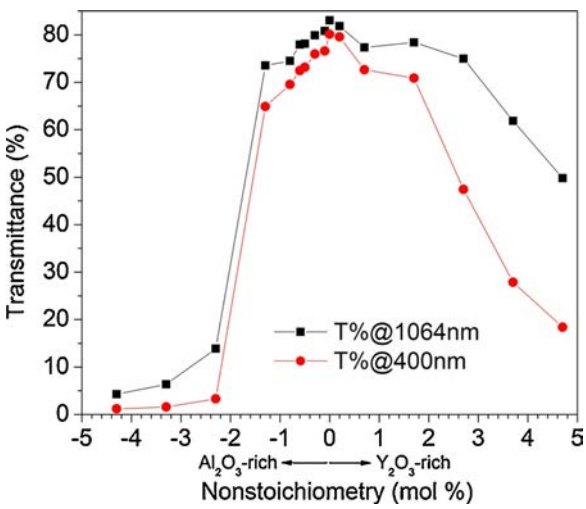

Fig. 24. In-line transmission curves of Φ16 mm × 1.5 mm samples of non-stoichiometric $Y_{3(1+x)}Al_5O_{12}$ ceramics after sintering at 1760 °C for 10 h. Reused from [211]. Copyright © 2015, Elsevier.

transmittance only slightly decreased while the average grain size increased, and when the non-stoichiometry was $x > 0.7$ mol%, the optical properties and average grain size were similar to those of the samples with excessive Al_2O_3 because of the secondary phase effect. After sintering at the optimal conditions, the maximum transmittance of the samples with stoichiometric composition was 83.1% at 1064 nm and 80.2% at 400 nm. Photographs and transmittance curves of non-stoichiometric $Y_{3(1+x)}Al_5O_{12}$ ceramics sintered at 1760 °C for 10 h are shown in Figs. 23 and 24, respectively.

Zych and Brecher used commercial Y_2O_3 and Al_2O_3 powders to fabricate transparent YAG ceramics using HP [212]. Stoichiometric mixtures of the two oxides were milled in methanol for 20 h. After milling, the slurry was dried and pressed into pellets. Hot pressing was conducted at 1750 °C and 300 MPa for 4 h using graphite punches and dies. The as-sintered samples had a dark color because of the highly reducing atmosphere of the HP process; however, transparency could be readily recovered by thermal annealing in air at 1400 °C for 4 h.

Wang et al. recently attempted to elucidate the sintering mechanism of YAG nanoceramics at high pressures [213]. They reported that high-pressure sintering of YAG nanoceramics involved three stages:(i) plastic densification caused by the applied pressure; (ii) viscous sliding of grain boundaries; and (iii) viscous sliding of grain boundaries transitioned to grain boundary diffusion. This sintering mechanism is a useful reference when developing transparent YAG ceramics with high mechanical properties.

Studies have also reported fabricating YAG or YAG-based transparent ceramics using HIP as a post-treatment process in order to further improve optical transparency [214–218]. For example, Li et al. reported a process for developing transparent Nd:YAG ceramics from Nd:YAG nanopowders, prepared by reverse precipitation, using vacuum sintering and HIP [218]. The Nd:YAG precursor was mixed with 0.5 wt % TEOS as a sintering aid and heated at 1100 °C for 4 h. The Nd:YAG nanopowders were compacted and vacuum-sintered at 1500–1800 °C for 10 h, followed by HIP in Ar at 1600 °C and 200 MPa for 3 h. After HIP, the samples that had been vacuum-sintered at 1800 °C exhibited 81.2% in-line transmittance at 1064 nm. Fig. 25 shows the in-line transmittance curves of the Nd:YAG ceramics produced by different conditions.

Transparent YAG-based ceramics have also been produced using SPS, although SPS is not as popular for YAG ceramics as it is for other transparent ceramics [219–224]. Wang et al. used SPS to transform the metastable hexagonal $YAlO_3$ (YAH) phase of YAG to a transparent ceramic [222]. The transformation of the YAH phase YAG at approximately 920 °C was accompanied by particle rearrangement, which provided an additional densification mechanism. Furthermore, the applied pressure also played an important role in promoting the phase transformation. At 920 °C and 80 MPa, the in-line transmittance was 44% and 66% at 680 nm and 1000 nm, respectively. More importantly, the average grain size was as small as 380 nm. Generally, the transparent YAG ceramics that have been fabricated using SPS have had relatively low optical transparency because of the contamination introduced by the direct contact between the samples and the dies; this contamination must be prevented in order to further utilize the SPS technique. Various multiple-step sintering processes have been found to be effective for boosting the optical performance of transparent ceramics for different sintering techniques [11,225–227].

When transparent ceramics are used for solid-state lasers, active

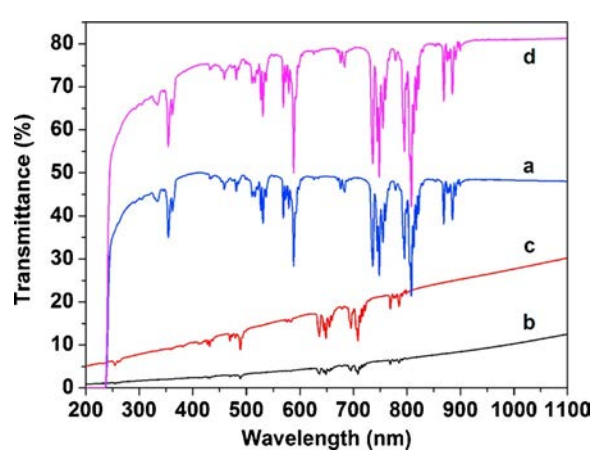

Fig. 25. In-line transmittance curves of the Nd-YAG ceramics: (a) vacuum-sintered at 1800 °C without HIP, (b) vacuum-sintered at 1600 °C followed by HIP at 1600 °C for 3 h, (c) vacuum-sintered at 1700 °C followed by HIP at 1600 °C for 3 h, and (d) vacuum-sintered at 1800 °C followed by HIP at 1600 °C for 3 h. Reused from [218]. Copyright © 2017, Elsevier.

SDC EX. 1018 - 23/66

components – most often rare earth elements – are added to the ceramic in order to achieve the desired wavelength. As mentioned earlier, the concentration of dopants in transparent ceramics is not limited by solubility. For example, transparent Er:YAG ceramics with 1–90% Er^{3+} have been readily obtained using the solid-state reaction method and vacuum-sintering technique [228]. The in-line transmittance of these Er:YAG ceramics was as high as 84% at 1100 nm, which is comparable to that of single crystals.

Various sintering aids have been employed to promote densification and achieve high optical transparency in YAG ceramics [199,203,204,229–235]. Silica has been the most frequently used sintering aid for transparent YAG ceramics and Boulesteix et al. recently conducted a systematic study of SiO_2 behavior during sintering using microstructural, chemical, dilatometric, and thermogravimetric analyses [234]. The authors found that, if the SiO_2 content exceeded the solubility limit in YAG, an intergranular transient liquid phase of mixed Y-Al-Si-O was formed, and that this liquid phase vaporized very quickly when the temperature was higher than 1350 °C. Therefore, the SiO_2 content of the final products was always less than the solubility limit, i.e., < 900 ppm.

Boulesteix et al. mixed commercial α-Al_2O_3 (> 99.99%), Y_2O_3 (> 99.99%), and Nd_2O_3 (> 99.99%) powders to obtain $Y_{2.94}Nd_{0.06}Al_5O_{12}$, 2 at% Nd:YAG, using a normal ball milling process. Fumed SiO_2 (> 98%) that contained up to 0.3 wt% Si, i.e., 1400 ppm, was used as the sintering aid. The samples were sintered under vacuum, $\leq 10^{-2}$ Pa, at 1000–1800 °C for different durations, and the heating and cooling rates were 5 °C/min and 15 °C/min, respectively. A high cooling rate was used to prevent the exsolution of silica at the grain boundaries during cooling.

Fig. 26 shows SEM images of the samples sintered at 1700 °C with different amounts of SiO_2. Intergranular pores were present in the sample without any sintering aid(Fig. 26A) while the sample with 0.05 wt% SiO_2 had a homogeneous microstructure with uniform grain size and was free of pores (Fig. 26B). However, as the SiO_2 content was increased to 0.3 wt%, the Nd:YAG sample displayed residual inter- and intra-granular pores as well as small grains of secondary phases, which had a dark anisotropic morphology because of Al_2O_3 precipitation (Fig. 26C). The average grain size was 2.15, 4.62, and 5.20 µm for samples with 0, 0.05, and 0.3 wt% SiO_2, respectively. Fig. 26D shows a SEM image of the undoped sample that was positioned near doped samples during the sintering process; compared to Fig. 26A, the microstructure of this sample was highly dense and homogeneous, and the grains were much larger, which suggests that the vaporization of SiO_2 or its derivatives affected this sample.

Magnesia is the second most effective sintering aid for transparent Nd:YAG ceramics [236]. Zhou et al. conducted a systematic study to examine the effect of MgO on the densification and optical properties of YAG ceramics and found that by adding 0.03 wt% MgO to powders sintered at 1820 °C for 8 h, transparent YAG ceramics could achieve 84.5% in-line transmittance at 1064 nm [204]. The addition of MgO largely enhanced the grain growth of the YAG ceramics sintered at 1540–1660 °C; however, excessive MgO resulted in the formation of a Mg-rich secondary phase and intragranular pores, which impaired the optical transparency of the YAG ceramics.

Small quantities of CaO have also been used to increase the density and control the microstructure of YAG ceramics [203]. As expected, high-quality transparent YAG ceramics were obtained using the reactive vacuum sintering process, and after the YAG sample was annealed at 1820 °C for 8 h, its in-line transmittance was 84.4% at 1064 nm. For 0.045 wt% CaO, the average grain size was 2.7 µm. Zhang et al. concluded that the addition of CaO enhanced both the densification and grain growth of YAG ceramics when the temperature was below 1660 °C, but significantly suppressed grain growth at higher temperatures.

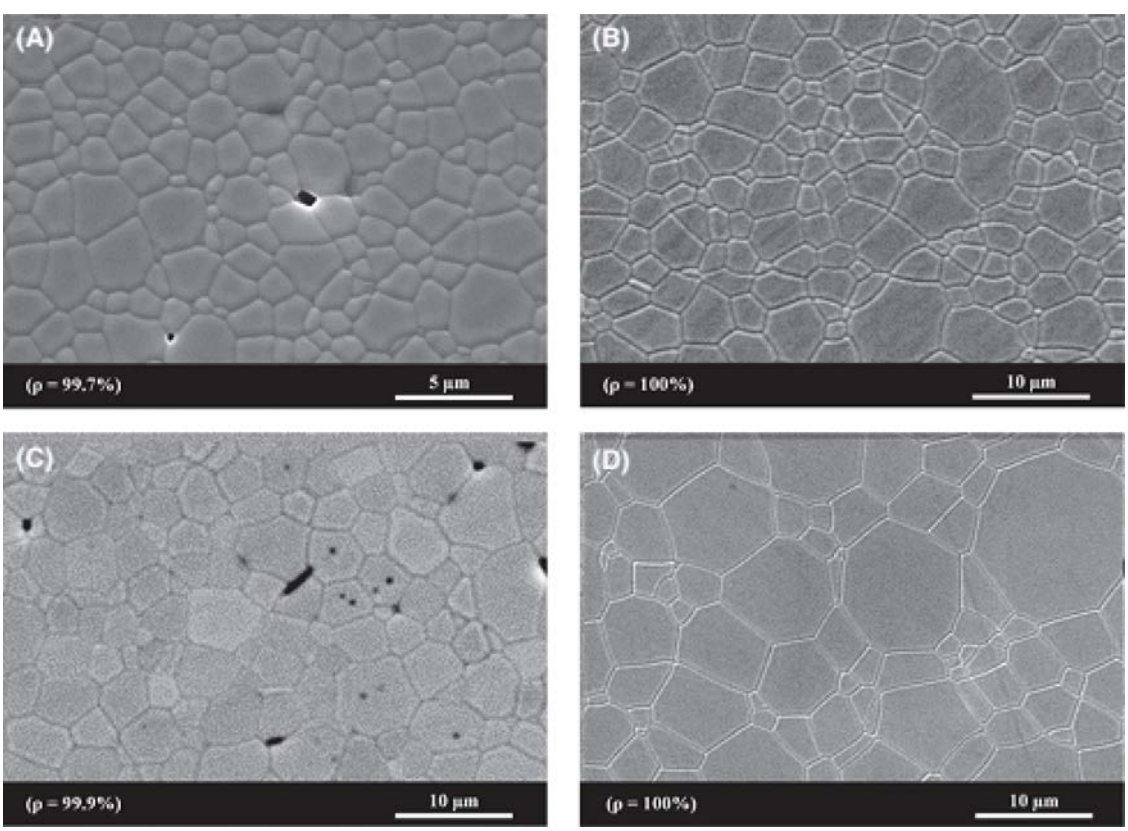

Fig. 26. SEM images of the Nd:YAG ceramics with different concentrations of silica after reactive vacuum sintering for 5 h at 1700 °C: (A) 0 wt%, (B) 0.05 wt%, and (C) 0.3 wt%. (D) SEM image of the undoped Nd:YAG sample that was close to the SiO_2-doped Nd:YAG samples during sintering. Reproduced from [234]. Copyright © 2017, John Wiley & Sons.

SDC EX. 1018 - 24/66

Co-doping is considered to be more effective than single-doping; for example, Li et al. have reported that the combination of SiO_2 and MgO improves the densification and optical transparency of YAG ceramics [237]. Another study by Yang et al. went on to use SEM to demonstrate that SiO_2 removed pores and secondary phases whereas MgO promoted the formation of a homogeneous microstructure [231]. They found that the Nd:YAG ceramics demonstrated maximum transparency and homogeneity with 0.145 wt% SiO_2 and 0.1 wt% MgO; after sintering at 1780 °C, the average grain size and in-line transmittance of this sample were 10 μm and 82% at 400 nm, respectively. Moreover, the densification and optical performance of the final ceramics were strongly associated with the properties of the starting powders, such as particle size, size distribution, morphology, and degree of agglomeration [238–240].

The effects of ball-milling parameters on the densification of Yb:YAG powder and optical properties of the resultant transparent ceramics have been studied by Chen et al. [241]. These authors synthesized Yb:YAG powder using chemical coprecipitation and ball milled the powder in ethanol with TEOS, added as a sintering aid, for 0–20 h to obtain 7.8–38.5 wt% slurries. The compacted samples were sintered at 1350–1800 °C. The effects of ball-milling time and slurry concentration on the densification, microstructure, and optical transmittance of the Yb:YAG ceramics were ultimately controlled by the quality of the powders. Ball milling for 12 h was determined to be optimal for achieving high optical transparency as the resultant ceramics achieved 81% in-line transmittance at 1100 nm, which was attributed to the absence of a sintering neck in the milled powder. Furthermore, the densification behavior of the powders and the optical transmittance of the final Yb:YAG ceramics gradually improved as the slurry concentration decreased from 38.5% to 20.3%. The Yb:YAG powders that were ball-milled for 12 h to 20.3 wt% slurry had the most homogeneous particle size distribution and highest densification rate; thus, the ceramics obtained by vacuum sintering this powder at 1750 °C for 15 h had the highest optical transmittance: 82% in the visible range and 83.5% at 1100 nm,.

Various technologies have been used to further improve the sintering of the powders to form transparent YAG ceramics, such as spray drying [242–249] and freeze-drying [250–252]; for example, Jing et al. developed a spray method to treat Nd:YAG nanopowders synthesized by chemical coprecipitation [249]. By controlling the spray speed (10–40 mL/min) and optimizing the solution concentration (0.1–0.4 M), single-phase YAG powder was readily obtained after calcination at 850 °C. High-quality transparent Nd:YAG ceramics with 80.2% and 83.1% in-line transmittance at 400 nm and 1064 nm, respectively, were obtained from gel-cast green bodies after HIP; the transmittance curve as well as surface and cross-sectional SEM images of the Nd:YAG ceramic sample sintered at 1700 °C are shown in Fig. 27. This highly transparent Nd:YAG ceramic had clean grain boundaries, no pores were observed, and no secondary phases were present at either the grain boundaries or inside the grains. When tested for solid-state laser applications, these transparent Nd:YAG ceramics exhibited a maximum laser output of 7.015 W with an oscillation threshold of 0.235 W and 59.4% slope efficiency.

Besides YAG, various other garnets such as $Lu_3Al_5O_{12}$ (LuAG), $Dy_3Al_5O_{12}$ (DyAG), $Tb_3Al_5O_{12}$ (TbAG), and $Tm_3Al_5O_{12}$ (TmAG) have been reported in the open literature [9,10,253–271]. Chen et al. used a solid-state reaction process to prepare (Ce, Mg):LuAG scintillation ceramics with 0.025–0.3 at% Ce and 0.2 at% Mg and systematically studied the effects of the Ce concentration and annealing conditions on the microstructure, optical properties, and scintillation performance of the final ceramics [272]. The powders were thoroughly mixed and compacted, followed by CIP at 250 MPa and vacuum sintering at 1800 °C for 10 h. Selected samples were post-annealed in air at 1450 °C for 10 h; Fig. 28 shows photographs of the transparent (Ce, Mg):LuAG ceramics with and without thermal annealing. Both the as-sintered and annealed samples demonstrated high optical transparency; however, the color of the annealed samples was lighter than that of the as-sintered ceramics.

Hu et al. fabricated transparent DyAG ceramics using a solid-state reaction method to combine commercial Dy_2O_3 and Al_2O_3 powders [261]. The starting powders were mixed with sintering aids, 0.5 wt% TEOS and 0.05 wt% MgO, and dried prior to compaction and CIP at approximately 200 MPa. The pellet samples were vacuum-sintered at 1760–1830 °C for 6 h under approximately 10^{-3} Pa, and then annealed in air at 1400 °C for 5 h to eliminate the oxygen vacancies produced during vacuum sintering. The optimal sintering temperature for producing high-quality transparent DyAG ceramics was determined to be 1820 °C; the samples sintered at this temperature had an average grain size < 10 μm and 80% in-line transmittance in the visible light region. Fig. 29 shows photographs of representative transparent DyAG ceramics sintered at different temperatures.

2.1.5.2. Spinel ($MgAl_2O_4$). Magnesium aluminate ($MgAl_2O_4$) has a spinel crystal structure and is transparent to electromagnetic radiation between 0.2 (UV) to 5.5 (mid-IR) μm [44,273,274]. Spinel has outstanding optical properties and high mechanical strength; thus, $MgAl_2O_4$ is one of the most important transparent ceramics. Because of their hardness, high chemical resistance, and high transparency across the UV–vis and mid-IR ranges, transparent $MgAl_2O_4$ ceramics are promising candidates for optical components and defense applications, such as optical lenses, windows for aircraft/vehicles, submarine IR sensors, and missile domes [275].

In 1974, Bratton used vacuum sintering to obtain translucent $MgAl_2O_4$ ceramics from ultrafine, coprecipitated spinel powder doped with 0.25 wt% CaO as sintering aid [276]. The fabrication of transparent $MgAl_2O_4$ ceramics using conventional pressure-less sintering technologies is challenging [276–279]; therefore, sophisticated sintering strategies such as HP, HIP, and SPS are generally employed to develop these ceramics [280–288]. Moreover, high-quality precursor powders and optimized concentrations of sintering aids, such as CaO [276], B_2O_3 [289] and LiF [290], are required to achieve $MgAl_2O_4$ ceramics with high optical transparency.

Esposito et al. used HP to produce transparent $MgAl_2O_4$ ceramics from commercial oxides, with the goal of large-scale production [291,292]; for example, they produced highly transparent, low-cost $MgAl_2O_4$ ceramics directly from a stoichiometric mixture of Al_2O_3–MgO with ultra-pure LiF added as the sintering aid [292]. The resultant ceramics reached 78% transmittance in the visible range and the authors identified a thermodynamic mechanism for the formation of the spinel phase that directly influenced the optical transparency of the final ceramics. Balabanov et al. also employed HP to fabricate transparent $MgAl_2O_4$ ceramics [293]. These ceramics were prepared using $MgAl_2O_4$ nanopowders derived from the hydrolysis of magnesium aluminum double isopropoxide, $MgAl_2(OPr^i)_8$, at 900–1200 °C. After hot pressing at 1600 °C and 50 MPa, the $MgAl_2O_4$ ceramics doped with 3 wt% LiF exhibited 83.7% in-line transmittance at 1100 nm, which is approximately 96% of that of $MgAl_2O_4$ single crystal (87% at 1100 nm), as shown in Fig. 30.

Hot isostatic pressing has been used as an effective post-treatment strategy for the fabrication of transparent $MgAl_2O_4$ ceramics [289,294–300]. For example, Luo et al. used HIP to develop transparent Co:$MgAl_2O_4$ ceramics to be used for passive Q-switching of solid-state lasers operating at an eye-safe wavelength, 1.5 μm [299]. The Co:$MgAl_2O_4$ ceramics obtained after vacuum sintering at 1500 °C for 5 h and HIP post-treatment at 1650 °C for 3 h exhibited > 80% in-line transmittance at 2500 nm. The 0.02 at% Co:$MgAl_2O_4$ sample had a ground state absorption cross section of 3.35×10^{-19} cm^2 at 1540 nm; thus, it was suitable for NIR solid-state lasers with passive Q-switching.

Gojdowski et al. fabricated transparent $MgAl_2O_4$ ceramics from commercial submicron powder using a combination of vacuum sintering and HIP [298]. Commercial $MgAl_2O_4$ powder with an average grain size of 0.43 μm and a low impurity content was compacted under

SDC EX. 1018 - 25/66

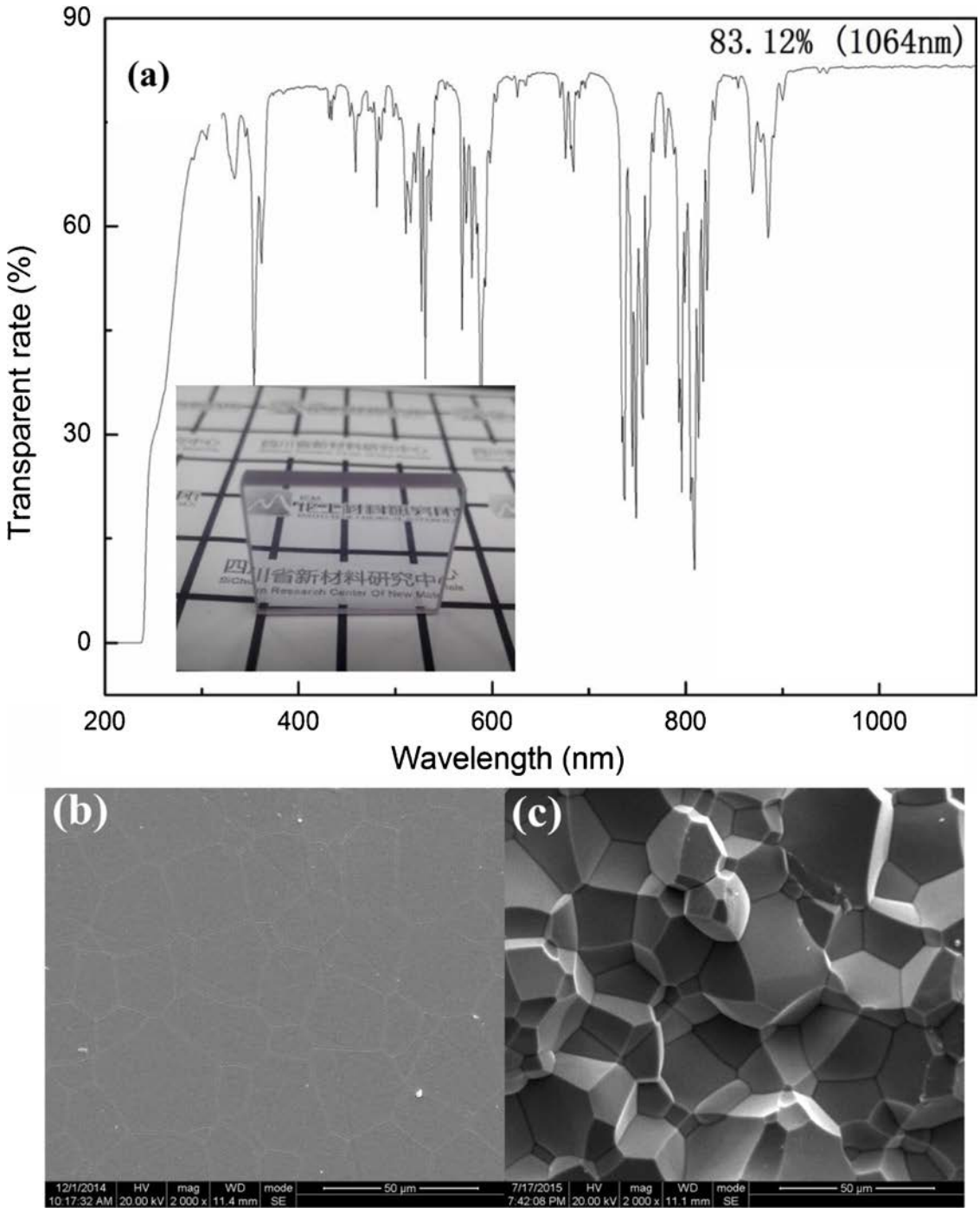

Fig. 27. (a) In-line transmittance curve and both (b) surface and (c) cross-sectional SEM images of a representative Nd:YAG ceramics sintered at 1700 °C. Reproduced from [249]. Copyright © 2018, Elsevier.

uniaxial pressure, followed by CIP at 300 MPa. The samples were vacuum-sintered at 1500 °C for 2 h and then post-treated with HIP in Ar at 190 MPa; the HIP temperatures were 1500 °C and 1800 °C, and were held for 1 h and 10 h. The samples were opaque after vacuum sintering, which indicated the presence of pores. Highly transparent $MgAl_2O_4$ ceramics were obtained after post-HIP treatment at 1800 °C for 10 h. The in-line transmittance of 2-mm thick samples was 81% at 400 nm and 86% between 950 and 3000 nm, which corresponds to 98.8% of the theoretical transmittance.

Han et al. combined reactive sintering and HIP to fabricate transparent Al-rich spinel ceramics: $MgO{\cdot}nAl_2O_3$ with n = 1.05–2.5 [300]. Commercial MgO and γ-Al_2O_3 powders were used as the starting materials. The addition of moderate Al_2O_3 ($n \geq 1.1$) was found to remove residual pores and suppress abnormal grain growth, and secondary phase could be effectively avoided by optimizing the HIP temperature. After HIP at 1550 °C, the final ceramics with n = 1.1–1.3 exhibited high optical transparency, with 84% in-line transmittance at 400 nm and fine grains < 5 μm. When the Al_2O_3 content was too high (e.g., n = 1.5), needle-like spinel grains were formed, which deteriorated the microstructure and thus optical transparency of the ceramics.

Dericioglu et al. developed a two-step process combining HP and HIP to fabricate transparent $MgAl_2O_4$ ceramics using high-purity commercial powders of MgO and Al_2O_3 [278,280]. The powders were thoroughly mixed and compacted before the green bodies were hot-

SDC EX. 1018 - 26/66

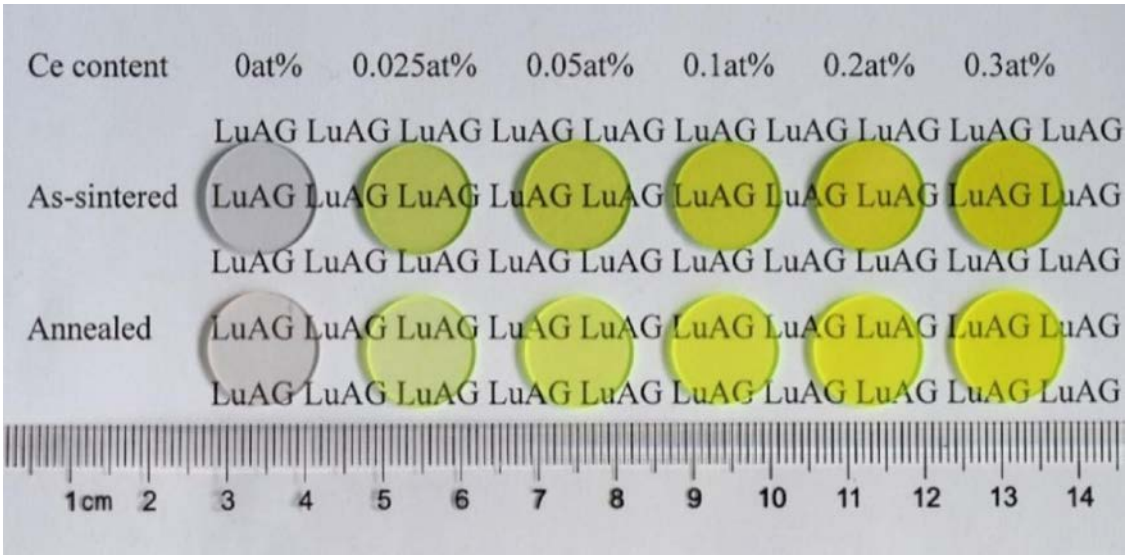

Fig. 28. Photographs of 1-mm thick samples of the as-sintered and air-annealed (Ce, Mg):LuAG ceramics. Reused from [272]. Copyright © 2018, Elsevier.

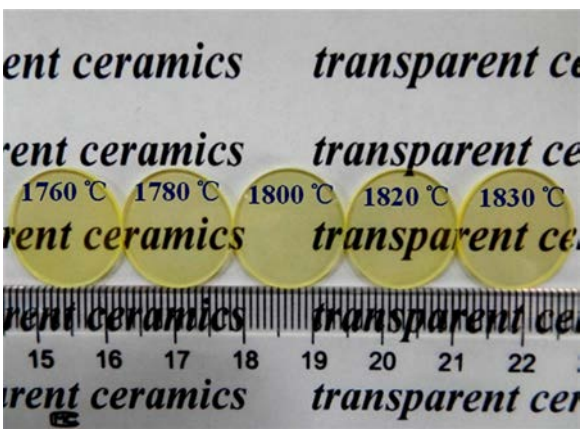

Fig. 29. Photographs of polished DyAG ceramics, Φ16 mm × 1 mm, sintered at different temperatures. Reused from [261], Copyright © 2015, John Wiley & Sons.

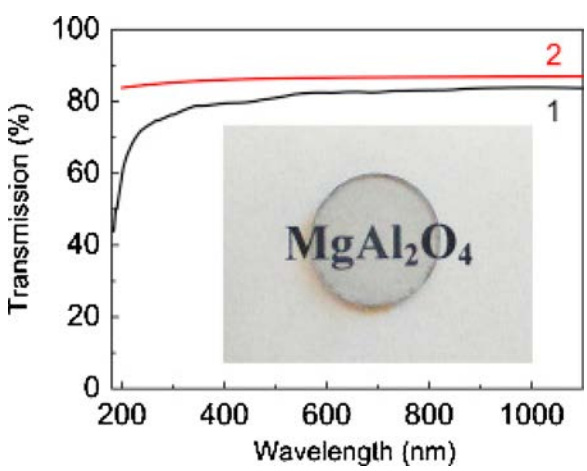

Fig. 30. Experimental (1) and calculated (2) transmission spectra of 1-mm thick transparent $MgAl_2O_4$ ceramics doped with 3 wt% LiF. Inset shows a photograph of the experimental sample. Reused from [293], Copyright © 2015, Elsevier.

pressed under a 10^{-2} Pa vacuum at 1400–1500 °C and 50 MPa for 1 h. The hot-pressed samples were then subject to HIP at 1900 °C and 189 MPa for 1 h. The maximum in-line transmittance was achieved by the samples hot-pressed at 1400 °C: 60% in the UV–vis range and 70% in the NIR range. The optical transparency of these transparent $MgAl_2O_4$ ceramic samples was found to depend on the boundary interface area per unit volume that had microcracks.

Alternatively, SPS has been used to develop transparent $MgAl_2O_4$ ceramics with relatively small grain sizes [301–305]. For example, Fu et al. used SPS (1325 °C for 10 min) to prepare transparent $(Mg_{1-x}Zn_x)Al_2O_4$ ceramics, where x was as high as 0.03 [303]. Nanopowders of $(Mg_{1-x}Zn_x)Al_2O_4$ were obtained by high temperature calcination of high-purity $MgSO_4{\cdot}7H_2O$, $ZnSO_4{\cdot}7H_2O$, and $NH_4Al(SO_4)_2{\cdot}12H_2O$ powders. During the SPS experiment, the uniaxial pressure of 80 MPa, the pulse sequences of the applied voltage were 12 on/2 off, and the vacuum level was 10 Pa, and the samples were heated in three steps: 600 °C in 2 min, 1100 °C in 5 min, and finally 1325 °C in 22.5 min. After sintering at 1325 °C for 10 min, the temperature was reduced to 1150 °C and held for 10 min to release the residual stress. The in-line transmittance of the $(Mg_{1-x}Zn_x)Al_2O_4$ sample with $x = 0.02$ was 70% and 86.5% at 550 nm and 2000 nm, respectively. Such transparent $(Mg_{1-x}Zn_x)Al_2O_4$ ceramics exhibited promising microwave dielectric properties.

Boulesteix et al. reported a two-step SPS process to obtain transparent Nd^{3+}:$MgAl_2O_4$ ceramics with up to 0.2 at% Nd [304]. Commercial $MgAl_2O_4$ nanopowder was used as the precursor, Nd-doped samples were prepared by soaking the powders in aqueous solutions of $Nd(NO_3)_3{\cdot}6H_2O$, and the mixtures were compacted into pellets with CIP at 200 MPa. The two-step SPS process consisted of (i) heating to 1100 °C at 100 °C/min and holding for 3 min without pressure, and (ii) slowly heating to 1300 °C at 20 °C/min and holding for 15 min under 130 MPa uniaxial pressure. The in-line transmittance of the undoped samples was 70% while that of the Nd-doped samples was 50%. Moreover, the cut-off wavelength of the Nd-doped ceramics was shifted to a higher UV wavelength than the undoped ceramics. However, the Nd^{3+} content of the transparent $MgAl_2O_4$ ceramics was much higher than that of single crystals, which illustrates that SPS is advantageous for developing transparent ceramics with non-equilibrium compositions.

Shahbazi et al. have produced transparent $MgAl_2O_4$ ceramics by combing colloidal gel casting with SPS [305]. The starting powder had an average particle size of 90 nm and was combined with an additive, isobutylene-maleic anhydride (ISOBAM), which acted as both the dispersant and gelation agent. The rheological behavior of the suspension

SDC EX. 1018 - 27/66

could be optimized and the optimal conditions were determined to be 85 wt% solid loading, 0.7 wt% additive content, and approximately 6 min of gelation time. The resultant green bodies had a relative density of 65% and a mechanical strength of 14.48 MPa. After SPS, these samples exhibited 86.7% in-line transmittance at 1100 nm.

Contamination is an important issue for pressure sintering and SPS techniques because the samples are in direct contact with the sintering molds. For example, graphite contamination inevitably accompanies the fabrication of transparent $MgAl_2O_4$ ceramics by SPS [306]. The densification, microstructure, and performance of ceramics are well-known to be highly dependent on the properties of their precursor powders, and this is also true for transparent ceramics. Moreover, optical properties are much more sensitive than other properties, such as mechanical strength and even electrical conductivity; therefore, the synthesis of high-quality starting powders is critical to the production of highly transparent $MgAl_2O_4$ ceramics and is an important research topic [307–310].

The addition of sintering aids is another effective strategy for promoting densification of the precursor and enhancing the optical properties of transparent $MgAl_2O_4$ ceramics. Lithium fluoride is currently the most popular sintering aid [311–316], and Goldstein et al. recently revisited the host-additive interaction mechanism of transparent $MgAl_2O_4$ ceramics doped with LiF and prepared using a HP technique [316]. This study drew several important conclusions. Firstly, when the $MgAl_2O_4$ ceramics were hot-pressed at pressures $\leq$ 50 MPa, LiF was necessary in order to achieve high transparency and the sintering temperature had to be sufficiently high, i.e., $\geq$ 1600 °C. Without LiF, the pressure had to be as high as 400 MPa Secondly, when the concentration of LiF was < 5%, LiF did not react with $MgAl_2O_4$ during HP. Because the addition of excessive LiF could cause evaporation, and consequently porosity and cracking, the LiF concentration should be optimized. At temperatures below 1350 °C, LiF would fill open pores in the samples, which prevented carbon contamination. The conclusions from this study are applicable to other sintering aids.

Although $MgAl_2O_4$ is the only compound in the MgO–Al_2O_3 binary phase diagram, the spinel phase can exist for non-stoichiometric compositions. In other words, solid solutions can be formed and the Al_2O_3 composition can be increase with increasing temperature. If $MgO{\cdot}nAl_2O_3$ is used to represent the spinel phase, $n = 1.0$ is stoichiometric $MgAl_2O_4$, $0.8 \leq n < 1$ corresponds to MgO-rich spinel composition, and $1 < n \leq 3.5$ corresponds to Al_2O_3-rich spinel compositions. Since Al-rich $MgO{\cdot}nAl_2O_3$ ceramics could have variable light transmission characteristics for IR wavelengths, they have attracted substantial interest in the research community [278,280,296,300,317–320].

Dericioglu et al. have conducted a systematic study of the optical and mechanical properties of $MgO{\cdot}nAl_2O_3$ ceramics with $n = 1.0$, 1.5, and 2.0 [280]. The samples in this study were made from commercial powders of MgO and Al_2O_3 using a combination of HP and HIP. The authors found that the stoichiometric ceramics ($n = 1.0$) exhibited relatively low transparency, 20–40% in-line transmittance in the visible range, which was attributed to the presence of microcracked grain boundaries that scattered light travelling through the samples. The Al_2O_3-rich samples exhibited 40–60% in-line transmittance. More importantly, the mechanical properties of the final ceramics were also dependent on the composition; for example, the ceramics with $n = 2.0$ demonstrated the highest mechanical strength, with a fracture toughness of 2.02 $MPa{\cdot}m^{1/2}$. Therefore, non-stoichiometric $MgAl_2O_4$ is more suitable than stoichiometric $MgAl_2O_4$ for applications that require high mechanical strength.

Sutorik et al. reported the fabrication of transparent $MgO{\cdot}1.2Al_2O_3$ ceramics using a similar HP + HIP process [318]. The optimal processing parameters included HP at 1600 °C and 20 MPa for 5 h, and HIP in Ar at 1850 °C and 200 MPa for 5 h. These samples had outstanding optical transparency, with 84.8% in-line transmittance at 550 nm and an average transmittance > 82% across the entire visible spectrum. The final ceramics had 300–1000 μm grains and exhibited promising mechanical properties, including flexural strengths of 176.8 ± 46.2 MPa, hardness of 12.3 ± 0.2 GPa, and elastic modulus of 292.9 ± 7.5 GPa. This study further confirmed that non-stoichiometric spinel (especially Al-rich) ceramics with high optical transparency could be readily obtained by optimizing the processing parameters.

Waetzig and Krell studied the transmittance and hardness of Al-rich spinel ceramics($1 < n \leq 2.5$) [296]. The samples were prepared from commercial Al_2O_3 and MgO powders with different grain sizes using a solid-state reaction and HIP. Different compositions required different presintering temperatures. For the samples with $n = 1$–1.5, a single-phase spinel was formed and the extra Al_2O_3 dissolved to form solid solutions. The as-calcined samples with $n > 1.5$ were biphasic, consisting of stoichiometric $MgAl_2O_4$ and Al_2O_3; however, after HIP at 1750 °C, the extra Al_2O_3 also dissolved into the spinel matrix to form solid solutions. The samples produced using the optimized conditions exhibited promising optical transparency, with 85% in-line transmittance in the visible range and 63% at 200 nm; therefore, this study successfully fabricated single-phase, highly transparent, non-stoichiometric spinel ceramics with $1 < n \leq 2.5$.

The hardness (HV1) of the transparent $MgO{\cdot}nAl_2O_3$ ceramics fabricated by Waetzig and Krell decreased slightly as n increased above 1. Furthermore, the samples derived from fine-grained powders exhibited higher hardness than the samples derived from coarse powders; the fine-grained powders formed a bimodal microstructure with fine grains ($\leq$ 2 μm) homogeneously distributed throughout the matrix of coarse grains ($\leq$ 156 μm) whereas the samples derived from coarse powders formed a monomodal microstructure with extremely large grains ($\leq$ 622 μm) because high sintering temperatures were required for full densification. Fig. 31 shows photographs of representative transparent $MgO{\cdot}nAl_2O_3$ ceramics with different non-stoichiometric compositions.

Transparent $MgAl_2O_4$ ceramics have similar issues as MgO ceramics, because MgO is volatile. Therefore, the densification, microstructure, and optical properties of $MgAl_2O_4$ and MgO should be compared in order to clarify the key factors controlling the development of Mg-containing transparent ceramics.

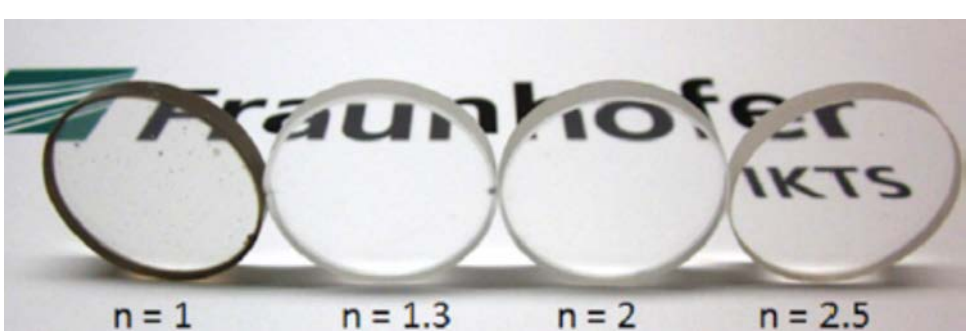

Fig. 31. Photographs of representative transparent $MgO{\cdot}nAl_2O_3$ ceramics with different values of n. Reused from [296], Copyright © 2016, John Wiley & Sons.

SDC EX. 1018 - 28/66

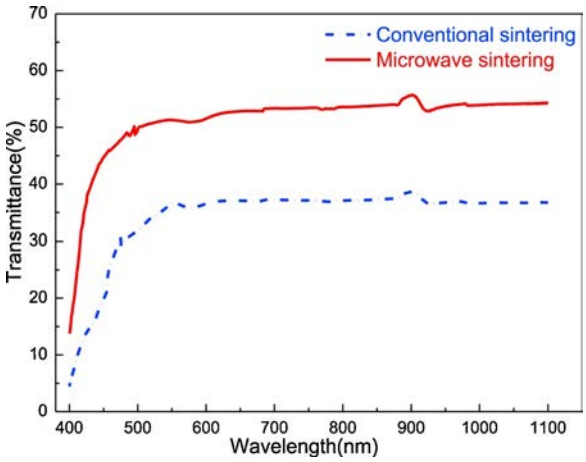

Fig. 32. In-line transmittance curves of PLZT ceramics (0.3-mm thick samples) fabricated by conventional sintering at 1200 °C for 3 h and microwave sintering at 1000 °C for 20 min. Reused from [335], Copyright © 2017, Elsevier.

2.1.6. Transparent ferroelectric ceramics

Transparent ferroelectric ceramics are perovskite-type materials with ABO_3 structures. Lanthanum-doped lead zirconate titanate ceramics, $Pb_{1-x}La_x(Zr_yTi_{1-y})_{1-x/4}O_3$ (PLZT), are typical transparent ferroelectric ceramics that have superior electro-optical properties, with electro-optic coefficients higher than that of $LiNbO_3$ single crystals, and are more transparent than other ferroelectric materials. Therefore, PLZT ceramics are potential candidates for applications as digital light modulators and large-aperture light shutters [321–324].

The optical performance of transparent PLZT ceramics is highly dependent on the quality of the starting powder [325]. Hence, various wet chemistry-based methods, including chemical coprecipitation, sol-gel synthesis, and hydrothermal treatment, have been used to synthesize high-quality PLZT powders that are ultrafine and free of agglomeration. High-energy mechanical activation is a dry method that has been demonstrated to effectively produce PLZT powders and could be used in the preparation of transparent PLZT ceramics. Furthermore, controlling the atmosphere of advanced sintering techniques, such as HP, HIP, and SPS, could allow transparent PLZT ceramics to be fabricated at relatively low temperatures with shorter sintering times than those typically used.

Because of the relatively high volatility of lead oxide (PbO), controlling the sintering atmosphere is critical when fabricating PLZT ceramics. Sun et al. reported a strategy for fabricating high-quality PLZT (7/60/40) ceramics, in which x = 0.07 and y = 0.60, by controlling the oxygen partial pressure during sintering [326]. Kong et al. developed a simple method for obtaining transparent PLZT ceramics from nanopowders that were directly synthesized from oxide precursors using high-energy mechanical milling without the calcination step [327,328]. For example, PLZT (9/65/35) nanopowder was first synthesized from commercial oxide powders by using high-energy ball milling at room temperature [328]. Oxide mixtures have also been dry-milled in WC containers with WC balls to produce phase-pure PLZT nanopowders [329–332]. Transparent PLZT ceramics were then fabricated from these nanopowders by annealing samples that were pre-sintered at 1125 °C for 6 h; annealing under ambient conditions at 1200 °C for 4 h was repeated four times.

Nie et al. used HP to prepare PLZT (x/70/30) ceramics with x = 7.45, 7.51, 7.57, and 7.63 in order to study the effect of anisotropy on their ferroelectric, optical, and electro-optical properties [333]. The ceramics were prepared by the conventional ceramic process; cylindrical samples were sintered in O_2 under ~160 kg/cm^2 of axial pressure at 1240 °C for 16 h ~160 kg/cm^2. All samples exhibited approximately 70% in-line transmittance between 500 nm to the NIR region. Furthermore, the authors found that both the transparency and light scattering contrast ratio were higher in the normal direction than in the parallel direction. The PLZT (7.63/70/30) ceramics were determined to be optimal as they exhibited the most stable electrical behavior in the parallel direction and had a high contrast ratio, 1.37, in the normal direction.

Wu et al. employed SPS to prepare transparent PLZT (8/65/35) ceramics [334]. The PLZT powder was derived from a wet-dry combination process whereby $ZrOCl_2{\cdot}8H_2O$ and $TiCl_4$ were dissolved in water and mixed to obtain the desired ratio of Zr^{4+} and Ti^{4+}, which were then coprecipitated using aqueous ammonia. The precipitate was thermally treated at 800 °C for 1 h to form $ZrTiO_4$ and ZrO_2, and PbO and La_2O_2 were added to the oxide mixture before calcination at 600–1000 °C for 2 h. The calcined powders were sintered at 700–950 °C and 29 MPa for 10 min under a 6 Pa vacuum; samples were first heated to the temperature 100 °C below the final sintering temperature at 100 °C/min, then heated to the final sintering temperature at 33 °C/min. After sintering, the samples were annealed at 700–1000 °C for 1 h. The in-line transmittance of 0.5-mm thick samples of the ceramic sintered at 900 °C and annealed at 800 °C was 31% at 700 nm.

Microwave sintering has also been demonstrated to be an effective technique for developing transparent PLZT ceramics [335]. Huang et al. synthesized PLZT 9/65/35 powder using the conventional solid-state reaction, a hydrothermal process, or a partial coprecipitation process. For the hydrothermal process, $Zr(NO_3)_4$, $La_2(NO_3)_3$, $Pb(NO_3)_2$, $C_{16}H_{36}O_4Ti$, and KOH (4 M) were mixed to form a precursor solution that was hydrothermally treated at 200 °C for 2 h. For the partial co-precipitation process, $Zr(NO_3)_4{\cdot}5H_2O$ and $TiCl_4$ were dissolved in water and coprecipitated using aqueous ammonia (pH 10) to obtain white $Zr_{0.65}Ti_{0.35}(OH)_4$. The precipitate was calcined at 1200 °C for 3 h and then mixed with PbO and La_2O_3 according to the desired compositions; a 10% excess of PbO was added to compensate for the loss of Pb at high temperatures. The sintering temperatures of the conventional and microwave methods were 1200 °C to 1000 °C, respectively, while the sintering times were 180 min to 20 min, respectively. These PLZT ceramics achieved a maximum in-line transmittance of 53.8% at 850 nm. Fig. 32 shows the in-line transmittance curves of the PLZT ceramics prepared by conventional sintering and microwave sintering.

A simple method for preparing transparent PLZT (9/65/35) fibers using an extrusion process was reported by Chen et al. [336]. Commercial powders of PbO, La_2O_3, ZrO_2, and TiO_2 were mixed according to the composition of PLZT 9/65/35, and the mixture was calcined at 900 °C for 1 h. Following calcination, the powder was ball milled in alcohol for one day, mixed with 2.0 wt% stearic acid, and then blended with low density polyethylene (LDPE) at 150 °C to obtain a paste with 60 vol% solid content. The paste was used to fabricate fibers that were approximately 500 μm in diameter by extrusion at 120 °C. The as-extruded PLZT fibers were sintered in O_2 at 1250 °C for 24 h to obtain highly transparent fibers, as illustrated in Fig. 33.

Perovskite-structured $Pb(Mg_{1/3}Nb_{2/3})O_3$ (PMN) is a typical relaxor ferroelectric material with promising dielectric properties [337]. The Curie temperature (T_C) of PMN is below room temperature and thus it is difficult to directly synthesize PMN using the solid-state reaction process. Ferroelectric $PbTiO_3$ (PT), which has a T_C of 490 °C, has previously been used to produce solid solutions with PMN (PMN-PT) so that ferroelectric behavior can be obtained above room temperature [338–343]. The electro-optic coefficient of PMN-PT is higher than that of PLZT by a factor of ~20 and PMN-PT has a strong photorefractive effect [344]; therefore, transparent PMN-PT ceramics have applications across the entire visible and mid-IR region.

Fujii et al. fabricated transparent PMN-0.10 P T ceramics using the conventional solid-state reaction method [345]. Commercial powders of MgO and Nb_2O_5 were mixed and calcined at 1150 °C for 4 h to form $MgNb_2O_6$, and the $MgNb_2O_6$ powder was mixed with La_2O_3, TiO_2, and PbO (2 wt% excess). The mixtures were calcined at 880 °C for 4 h after heating at 200 °C/h. A planetary ball mill was used to mill the calcined powders at 500 rpm for 20 min in distilled water. Stabilized zirconia

SDC EX. 1018 - 29/66

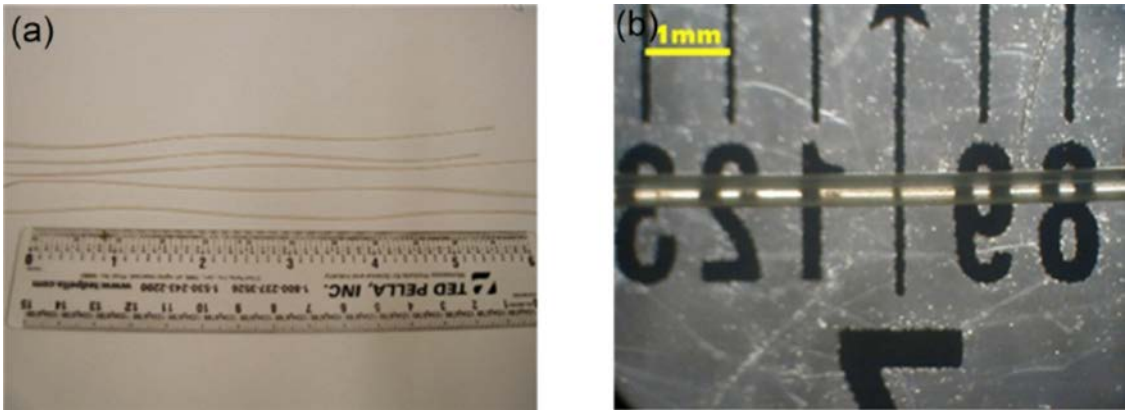

Fig. 33. Photographs of (a) the as-extruded PLZT green fibers and (b) a sintered transparent PLZT ceramic fiber. Reused from [336], ©Copyright 2016, Elsevier.

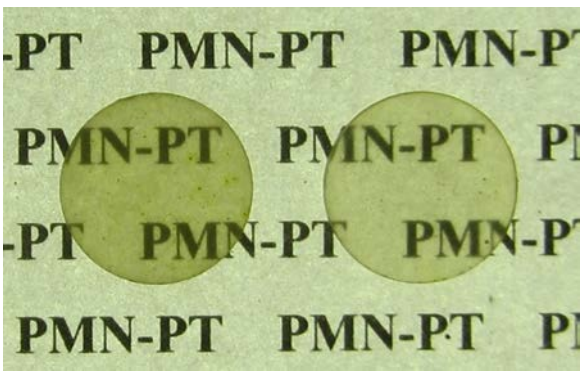

Fig. 34. Photographs of representative undoped (left) and 3 mol% La-doped (right) 0.9PMN-0.1 P T ceramics (1-mm thick). Reused from [345], ©Copyright 2013, John Wiley & Sons.

balls with diameters of 3, 1, 0.5, 0.3, 0.1, and 0.05 mm were used for the milling experiments; when zirconia balls with diameters < 0.3 mm were used, there was 10 wt% 3-mm diameter zirconia balls. Green bodies were prepared from the milled powders under 70 MPa of uniaxial pressure, followed by CIP at 200 MPa. The samples were finally sintered at 1280 °C for 4 h and 15 h; the sintering atmosphere was either N_2/O_2 (80/20 by volume) or O_2 introduced at 80 mL/min. The optical transparency of the PMN-PT ceramics increased as the size of the calcined powder decreased, which was controlled the size of the zirconia balls, and could be further increased by substituting 3 mol% La for Pb, as illustrated in Fig. 34.

A two-step sintering method for fabricating transparent La-doped PMN-0.25 P T ceramics from commercial powders was reported by Ruan et al. [346]. The ceramics prepared under the optimized conditions exhibited 65% in-line transmittance in the IR region, and had a relatively high quadratic electro-optic coefficient of 66×10^{-16} $(m/v)^2$. Wei et al. used a similar approach to develop transparent Er^{3+}-doped PMN–0.25 P T ceramics and found that the optical transparency of these ceramics was enhanced by doping with 0.5–2.0 mol% Er^{3+} [347].

More recently, Ji et al. studied the effect of sintering environment on the optical properties of transparent La-doped PMN-0.25 P T ceramics prepared by HP [348]. A modified HP process was developed to effectively promote densification, and this method consisted of four steps: (i) sintering at 800 °C for 2 h, first under vacuum and then in pure O_2; (ii) sintering in pure O_2 at 1150–1270 °C and 40 MPa for 8 h; (iii) replacing O_2 with CO_2 for 5 h to remove the closed pores; and (iv) switching CO_2 back to pure O_2 for another 5 h to eliminate the oxygen vacancies generated during the preceding step. The in-line transmittance of 0.35-mm thick samples of the transparent PMN-PT ceramics produced under optimized conditions was 64% at 632.8 nm; the authors explained the enhanced optical transparency by considering the defect chemistry of different sintering environments.

Zhang et al. prepared transparent La-doped PMN-0.25 P T ceramics using three methods: (i) uniaxial HP, (ii) O_2 atmosphere sintering, and (iii) two-stage sintering [349]. For the uniaxial HP method, the samples were sintered at 1200–1240 °C for 3–5 h under 100 MPa of uniaxial pressure. For O_2 sintering, the samples were sintered in O_2 at 1220–1260 °C for 3–5 h. For two-stage sintering, the samples were first sintered in O_2 at 1200–1250 °C for 3–5 h, and then sintered at 1200–1240 °C for 3–5 h under 60 MPa of uniaxial pressure. For the three methods, 3, 5, and 8 mol% of excess PbO was added to compensate for the loss of Pb during the sintering process, respectively. The two-stage sintering method was determined to be the most promising as the optical transmittance of the resultant ceramics was 70% at 900 nm, which was nearly the same as the theoretical value of 71%.

Transparent ferroelectric ceramics, $0.88Pb(Mg_{1/3}Nb_{2/3})O_3$-$0.12PbTiO_3$ (0.88PMN-0.12 P T), doped with different concentrations of La (0.5, 1.0, 1.5, and 2.0 mol%) have been prepared by combining the conventional solid-state reaction method with a two-stage sintering [350]. The La content strongly influenced the microstructural, electrical, and optical properties of the resultant ceramics and the 1.0 mol% La-0.88PMN-0.12 P T samples exhibited the highest optical transparency, with 65% in-line transmittance at 600 nm.

Single crystals of $Pb(Zn_{1/3}Nb_{2/3})O_3$ (PZN) have excellent dielectric and electrostrictive properties, as well as a very high electro-optic coefficient [351–354]. Unfortunately, phase-pure PZN ceramics cannot be produced because of their thermodynamic instability at room temperature. Therefore, other perovskite phases, such as PMN and PLZT, are combined with PZN to form solid solutions with the advantages of PZN. For example, transparent PZN-0.70PLZT (3/54/46) ferroelectric ceramics have been fabricated by HP sintering in O_2, using powders synthesized by the conventional solid-state reaction method as the precursors [355]. These PZN-PLZT ceramics had up to 60% in-line transmittance at 550 nm and exhibited very high optical transparency from the near-UV to IR regions.

Chu et al. also used HP to produce transparent $(Pb_{0.97}La_{0.02})[(Zn_{1/3}Nb_{2/3})_{0.3}(Zr_{0.53}Ti_{0.47})_{0.7}]O_3$ (PLZnNZT) ceramics from oxide precursors, adding 2 wt% excess PbO [356]. The final PLZnNZT ceramics had a dense perovskite structure with a distorted cubic-like symmetry and large grains, and this structure exhibited normal ferroelectric-like dielectric behavior with slightly diffuse ferroelectric characteristics. The maximum transmittance, 53%, was reached at 850 nm. In another study, Huang et al. used $BaTiO_3$ (BT) to stabilize PZN in a PZN-0.15BT solid solution [357]. The ceramics obtained under the optimal conditions of this study had 40% in-line transmittance from the visible region to the near-IR.

Lead-free transparent ferroelectric ceramics have also been reported in the open literature [358–362]. For example, Lin et al. prepared

SDC EX. 1018 - 30/66

transparent $NaNbO_3$ ceramics using the conventional solid-state reaction method [362]. These ceramics had a mixed state, consisting of both antiferroelectric *Pbcm* and ferroelectric *R3c* phases, and SEM results indicated that they were fully densified with a homogeneous microstructure. The samples were highly transparent, with 95% transmittance for UV light and as high as 97% transmittance for visible light > 450 nm. Li et al. developed transparent ceramics of bismuth-modified potassium sodium niobate, $K_{0.48}Na_{0.52}Nb_{1-x}Bi_xO_3$ (x = 0.05–0.15), using HP [360], and a similar method was used to prepare transparent $(K_{0.5}Na_{0.5})_{1-x}Li_xNb_{1-x}Bi_xO_3$ ceramics [361].

Furthermore, Wu et al. developed transparent Er^{3+}-doped $(K_{0.5}Na_{0.5})_{1-x}Li_xNb_{1-x}Bi_xO_3$ ($0.05 \le x \le 0.08$) ceramics in order to study their photoluminescence (PL), electro-optic response, and piezoelectric properties [363]. These ceramics exhibited high transparency, 50% and 75% in the NIR and mid-IR regions, respectively, and green and red up-conversion PL emissions of Er^{3+} were clearly observed. Strong electro-optic (EO) effects were evidenced by high effective linear EO coefficients of 128–184 pm/V. Moreover, the ceramics possessed fairly large piezoelectric coefficients, 70–90 pC/N, a relatively high dielectric constant, 1400, and a relatively low dielectric loss, 0.03; thus, these ceramics have potential applications as visible displays, mid-IR solid lasers, and optical attenuators.

Using a pressure-less sintering process, Yang et al. fabricated transparent ferroelectric ceramics of $(1-x)(K_{0.37}Na_{0.63})NbO_3$-xCa$(Sc_{0.5}Nb_{0.5})O_3$ with x = 0.050, 0.070, 0.090, 0.095, and 0.100 [364]. Commercial powders of Na_2CO_3, K_2CO_3, $CaCO_3$, Nb_2O_5, and Sc_2O_3 were thoroughly mixed and calcined at 950 °C for 5 h. The calcined powders were compacted and sintered in sealed alumina crucibles at 1220 °C for 4 h in order to embed the samples during the sintering process. As the $Ca(Sc_{0.5}Nb_{0.5})O_3$ content was increased, the phase of the materials changed first from an orthorhombic to tetragonal structure, and then to a pseudo-cubic structure. The $0.91(K_{0.37}Na_{0.63})NbO_3$-$0.09Ca(Sc_{0.5}Nb_{0.5})O_3$ ceramics had 60% in-line transmittance in the near-IR region.

Tanaka et al. prepared transparent $Sr_{0.6}Ba_{0.4}Nb_2O_6$ (SBN60) ceramics with anisotropic structures by combining a colloidal process at high magnetic fields with vacuum sintering and HIP [365]. The SBN60 ceramics had c-axis orientation wherein the degree of orientation was approximately 1.0 when expressed as the Lotgering factor. The in-line transmittance of the crystal-oriented SBN60 ceramics was 50% at 1500 nm, and optical phase modulation was observed, which confirms the presence of an electro-optic effect.

2.1.7. Mullite

Mullite is an aluminum silicate, $3Al_2O_3{\cdot}2SiO_2$ or $Al_6Si_2O_{13}$, and is one of the most popular engineering ceramics because it has sufficiently high strength at high temperatures, strong resistance to thermal shock, and relatively low dielectric constants [366]. Since mullite has high temperature stability, it can be used as window materials for high temperature applications in the mid-IR range. Fully dense, translucent mullite was achieved nearly fifty years ago by HP at 1500–1650 °C and 30–50 MPa [367]. Phase-pure oxide powders were synthesized by the hydrolytic decomposition of mixed metal alkoxides, and mullite powder was formed by calcining at 1200 °C. The optimal HP parameters were determined to be 5 kpsi and 1500 °C for 0.5 h.

Prochazka and Plug prepared IR-transparent mullite ceramics with 72 wt% and 76 wt% Al_2O_3 using HP and HIP at 1630 and 1650 °C, respectively [368]. To prepare mullite powders, A1 isopropoxide and ethylsilicate were dissolved separately in cyclohexane to form 1 M solutions, these solutions were mixed to obtain the desired Al_2O_3-SiO_2 compositions, and t-butylalcohol was added to form thin gels. After ageing and filtration, the solvent was evaporated from the gels at room temperature. The residue was dried at 120 °C, which produced white fluffy powders that were calcined at the appropriate temperatures to obtain mullite powders. Hot pressing was performed at 55 MPa and 1550–1750 °C while HIP was performed in Ar at 175 MPa and 1650 °C for 80 min.

A similar HIP process was used by Schneider to prepare translucent mullite ceramics from a commercial fused-mullite precursor [369]. The samples were presintered at 1700 °C for 4 h, followed by HIP at 120 MPa and 1650 °C for 30 min. The final mullite ceramics had uniform microstructures with grain sizes in the range of 5–10 μm, and their in-line transmittance was 40% in the visible range and as high as 80% in the NIR range. These optically translucent mullite ceramics are good candidates for optical windows in the visible–NIR range.

Fang et al. utilized microwave sintering to fabricate transparent mullite ceramics from a diphasic aerogel-derived powder, and they compared these to ceramics prepared by conventional sintering at 1320 °C [370]. To prepare the diphasic aerogel, boehmite (AlOOH) was dispersed in DI water at room temperature, the pH was adjusted to 2.0 by adding concentrated HNO_3 solution, and the mixture was refluxed overnight at 95 °C to achieve hydrolysis. The boehmite sol was then mixed with an ammonium-stabilized colloidal silica sol at room temperature to obtain an Al/Si molar ratio of 3:2. The sol mixture was heated at 60 °C to remove water and thus the diphasic mullite gel was obtained. The diphasic gels were converted to xerogels by further drying at 110 °C, followed by denitration at 550 °C. Microwave sintering was conducted in a microwave furnace set to 2.45 GHz and 900 W. The samples were rapidly heated from room temperature to 1300 °C and held at temperature for 10 min. While the conventionally-sintered samples were still amorphous, the mullite phase was readily formed by the microwave sintering process.

Mullite ceramics that are IR-transparent and translucent to visible light were fabricated by Ohashi et al. by vacuum sintering at 1750 °C [371]. Commercial mullite powders were calcined at 1250 °C for 1 h and then compacted by CIP at 200 MPa. The compacted samples were sintered at 1600–1800 °C for up to 8 h under a 10^{-3}–10^{-4} Pa vacuum, and the samples were heated and cooled at 10 and 20 °C/min, respectively. Samples were prepared with one of three compositions – 71.8, 75.2, and 76.5 wt% Al_2O_3 – and of these, the samples with 75.2 wt% Al_2O_3 had the highest optical transmittance after sintering at 1750 °C for 1 h.

Spark plasma sintering has also been used to develop transparent mullite ceramics from monophasic gels synthesized with aluminum nitrate nanohydrate (ANN) and TEOS [372,373]. The gels were dried at 110 °C and calcined at 800–1400 °C for 2 h. The samples were then sintered at 1450–1600 °C for 5–20 min; the SPS heating rate was 100 °C/min under vacuum and 30 MPa. The in-line transmittance of the samples processed at optimum conditions was 75–82% at 2.5–4.3 μm.

2.1.8. Other oxide ceramics

2.1.8.1. Pyrochlore oxide ceramics. Recently, various other oxide ceramics have emerged in the open literature. For example, transparent ceramics of spinel without Mg, have been fabricated, e.g., zinc spinel ($ZnAl_2O_4$) [374–378]. Complex oxide transparent ceramics with a pyrochlore crystal structure, such as $Lu_2Ti_2O_7$ [379–381], $Lu_2Zr_2O_7$ [382,383], $Y_2Ti_2O_7$ [384], $Y_2Hf_2O_7$ [385], $LaGdZr_2O_7$ [386,387], $LaYZr_2O_7$ [388], Lu_3NbO_7 [389,390], and Ga_3TaO_7 [391], have been obtained by SPS and vacuum-sintering techniques. For example, transparent lanthanum silicate oxyapatite ($La_{9.33}Si_6O_{26}$), which is ion-conductive, was prepared using SPS [392], and translucent $Sr_2Y_8(SiO_4)_6O_2$ oxyapatite ceramics were made from high-purity powder using SPS and ball milling [393]. However, it is necessary to mention that these transparent ceramics cannot be prepared by normal processing methods.

Transparent Eu^{3+}-doped $La_{0.8}Gd_{1.2}Hf_2O_7$ ceramics with different Eu^{3+} concentrations were fabricated by Wang et al. using vacuum sintering [394]. The Eu^{3+}-doped $La_{0.8}Gd_{1.2}Hf_2O_7$ powders were prepared from high-purity $La(NO_3)_3{\cdot}6H_2O$, Gd_2O_3, Eu_2O_3, $Hf(OH)_4$, and glycine precursor powders. First, aqueous solutions were prepared by dissolving $La(NO_3)_3{\cdot}6H_2O$ in DI water, and separately dissolving Gd_2O_3, $Hf(OH)_4$, and Eu_2O_3 in concentrated HNO_3 to obtain $Gd(NO_3)_3$, Hf

SDC EX. 1018 - 31/66

Fig. 35. Photographs of the as-sintered (above) and thermally annealed (below) Eu^{3+}-doped $La_{0.8}Gd_{1.2}Hf_2O_7$ ceramics. Reused from [394], Copyright © 2017, Elsevier.

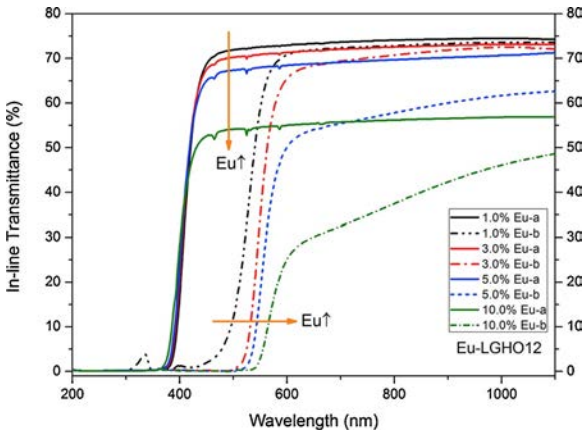

Fig. 36. In-line transmittance curves of 1-mm thick samples of the Eu^{3+}-doped $La_{0.8}Gd_{1.2}Hf_2O_7$ ceramics: (a) annealed (solid lines) and (b) unannealed (dash lines). Reused from [394], Copyright © 2017, Elsevier.

$(NO_3)_4$, and $Eu(NO_3)_3$ solutions. Mixtures of the nitrate solutions were prepared according to the composition of $La_{0.8}Gd_{1.2}Hf_2O_7$ with 1–10 at % Eu^{3+}, and glycine was added to the mixtures. Dilute aqueous ammonia solution was also added to the mixed solutions to maintain pH ~ 4. When the solutions were heated on a hot plate, sol-gel transition occurred as the water was evaporated, and eventual combustion yielded white fluffy powders. After calcining at 800 °C for 2 h and ball-milling for 20 h, the powders were compacted and treated with CIP at 200 MPa. The samples were then presintered in air at 1000 °C for 3 h, vacuum-sintered at 1830 °C for 6 h, and finally post-annealed at 1500 °C for 5 h in the ambient environment. Fig. 35 shows optical photos of the transparent Eu^{3+}-doped $La_{0.8}Gd_{1.2}Hf_2O_7$ ceramics before and after the final thermal annealing process, and the in-line transmittance profiles are illustrated in Fig. 36.

Qi et al. reported a SPS process for fabricating submircon transparent $Gd_2Zr_2O_7$ ceramics from nanocrystalline powders that were synthesized by a combination of coprecipitation and solvothermal treatment [395]. Because high heating and cooling rates (50 °C/min) and high pressures (up to 70 MPa) were used, the transparent $Gd_2Zr_2O_7$ ceramics had an average grain size of approximately 0.205 μm after sintering at 1400 °C for 5 min. The optimal transmittance of these ceramics was approximately 70% at 2000 nm.

Gui et al. also adopted a combined coprepication-solvothermal method to synthesize high-quality $LaGdZr_2O_7$ powders, which they used to produce transparent $LaGdZr_2O_7$ ceramics by vacuum sintering [387]. In this synthesis, the calcination temperature had a strong effect on the cation distribution and morphology of the $LaGdZr_2O_7$ powders, which indirectly influenced the microstructure and optical quality of the final $LaGdZr_2O_7$ ceramics. As the thermal treatment temperature

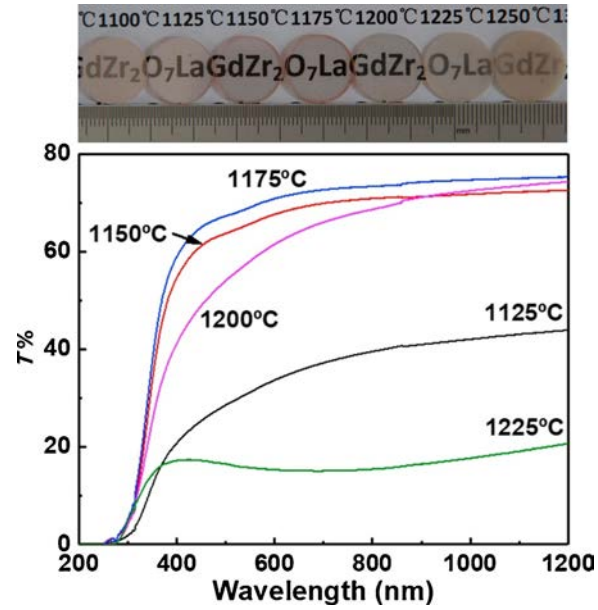

Fig. 37. Photographs and in-line transmittance curves of 1-mm thick samples of the $LaGdZr_2O_7$ ceramics prepared from powders calcined at different temperatures and sintered at 1800 °C for 10 h. Reproduced from [387]. Copyright © 2018, Elsevier.

was increased from 1000 to 1300 °C, both the domain and particle sizes increased while the ordering degree of the cations $[(La_{1/2}Gd_{1/2})^{3+}$-$Zr^{4+}]$ was enhanced. The $LaGdZr_2O_7$ powders calcined at 1150–1200 °C exhibited the lowest agglomeration and thus the highest sinterability, which resulted in ceramics with optimal optical properties. After vacuum sintering at 1800 °C for 10 h, the $LaGdZr_2O_7$ ceramics had 73–75% in-line transmittance at 1200 nm. Photographs and in-line transmittance curves of selected samples are shown in Fig. 37.

2.1.8.2. Transparent ceramics from glasses. Recent studies have indicated that transparent ceramics could be derived from glasses simply by thermal annealing at appropriate temperatures in air. Successful examples of such transparent ceramics include $BaAl_4O_7$ [396], $Sr_3Al_2O_6$ [397], $Sr_{1+x/2}Al_{2+x}Si_{2-x}O_8$ ($0 \le x \le 0.4$) [398,399], and $Ln_{1+x}Sr_{1-x}Ga_3O_{7+\delta}$ (Ln = Eu, Gd, or Tb) [400]. As an early example, Allix et al. proved that transparent barium aluminate ($BaAl_4O_7$) ceramics with micrometer-sized grains could be obtained from glass of the same composition [396]. The glass was made from high-purity $BaCO_3$ and Al_2O_3 using an aerodynamic levitator and two CO_2-lasers; glass beads were formed as the mixed powder pellets became molten at high temperature (2100 °C) and were then rapidly cooled. Transparent ceramics were obtained by annealing the glass beads in air at temperatures determined by differential scanning calorimetry (DSC).

Similarly, $Sr_3Al_2O_6$ and $Sr_3Ga_2O_6$ ceramics were made from glasses of the same composition by thermal annealing at 840 °C for 5 h [397]. Both glasses were prepared by melting mixtures of high-purity $SrCO_3$, Al_2O_3, and Ga_2O_3, and the transparent ceramics could be doped with Eu^{3+}, Er^{3+}, Ho^{3+}, and Ce^{3+}. The Eu^{3+}:$Sr_3Al_2O_6$ and Er^{3+}:$Sr_3Al_2O_6$ ceramics exhibited promising luminescence properties, with strong emissions in the visible and IR regions, while the Ce^{3+}:$Sr_3Al_2O_6$ ceramics exhibited scintillation behavior after X-ray excitation.

This method was further applied to $Sr_{1+x/2}Al_{2+x}Si_{2-x}O_8$ with x = 0–0.4 [398]. Glasses were formed by mixing $SrCO_3$, Al_2O_3, and SiO_2 powders in rhodium/platinum crucibles and melting the mixtures in an electric furnace. The samples were heated to 1700 °C, held for 10 min, heated to 1750 °C, held for 10 min, and then returned to 1700 °C and held for 30 min. After melting, the samples were removed

SDC EX. 1018 - 32/66

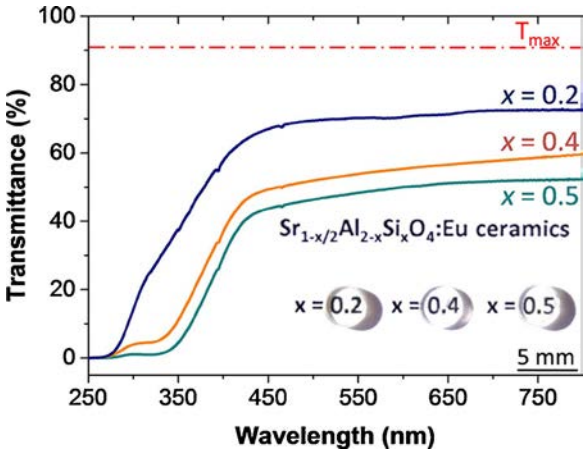

Fig. 38. Transmittance curves of 1.1-mm thick samples of the Eu-doped $Sr_{1-x/2}Al_{2-x}Si_xO_4$ (x = 0.2, 0.4, and 0.5) ceramics. Reused from [399], Copyright © 2017, American Chemical Society.

from the furnace and rapidly cooled in the ambient environment, which produced glass samples that were annealed in air at 1020 °C for 3 h to obtain transparent ceramics.

Transparent Eu-doped $Sr_{1-x/2}Al_{2-x}Si_xO_4$ (x = 0.2, 0.4, and 0.5) ceramics were recently developed by Fernandez-Carrion et al. [399]. In this study, glasses were prepared using aerodynamic levitation and a laser-heating method. The $Sr_{1-x/2}Al_{2-x}Si_xO_4$ glass samples were thermally annealed in air at 930 °C (6 h), 985 °C (7 h), and 1010 °C (7 h) in order to obtain ceramics with x = 0.2, 0.4, and 0.5, respectively; the heating and cooling rates were both 5 °C/min for all ceramics. After thermal annealing, the resultant ceramics were highly transparent to visible light, as shown in Fig. 38.

More recently, Boyer et al. reported a group of non-stoichiometric $Ln_{1+x}Sr_{1-x}Ga_3O_{7+\delta}$ (Ln = Eu, Gd, and Tb) melilite ceramics produced by crystallizing glasses [400]. The glasses were made from high-purity powders of $SrCO_3$, Ln_2O_3, and Ga_2O_3 by combining the aerodynamic levitator method with CO_2 laser heating, which allowed the samples to be cooled from the glass forming temperature (approximately 1650 °C) at approximately 300 °C/s by turning off the laser. The glass beads were crystallized to ceramics by annealing in air at 720 °C for 2 h. As shown in Fig. 39, the glass transition of the samples occurred near 760 °C, and

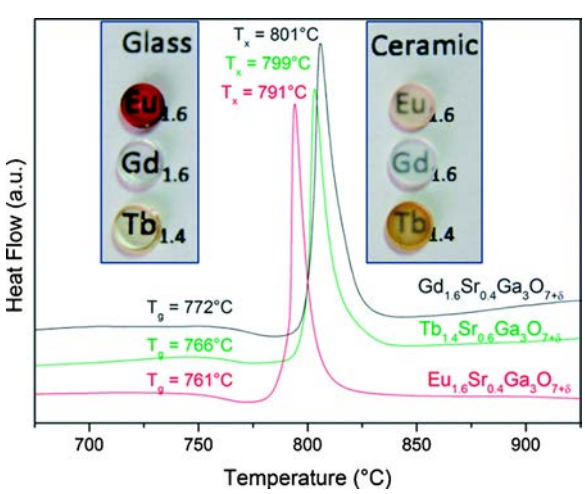

Fig. 39. Differential scanning calorimetry (DSC) curves of the $Ln_{1+x}Sr_{1-x}Ga_3O_{7+\delta}$ (Ln = Eu, Gd, and Tb) glasses; T_g and T_x are the glass transition and crystallization temperatures, respectively. Photographs show the $Ln_{1+x}Sr_{1-x}Ga_3O_{7+\delta}$ (Ln = Eu, Gd, and Tb) glasses (left) and the corresponding ceramics prepared by crystallizing the glasses at 720 °C for 2 h (right). Reused from [400], Copyright © 2018, Royal Society of Chemistry.

a crystallization peak was observed at approximately 790 °C. The presence of a single peak confirmed that the congruent crystallization process produced dense and phase-pure melilite ceramics, and the resultant ceramics retained relatively high transparency after crystallization. Furthermore, these transparent ceramics were the first to exhibit a bulk oxygen ionic conductivity of > 0.02 S cm^{-1} at 500 °C.

2.2. Non-oxide ceramics

2.2.1. Aluminum oxynitride (AlON) and aluminum nitride (AlN)

Aluminum oxynitride (AlON) – $Al_{(64+x)/3}O_{32-x}N_x$ ($2 \le x \le 5$) – has a defective cubic spinel structure as the rhombohedral structure of Al_2O_3 is altered by the incorporation of a small fraction of nitrogen. The optical transmittance of ALON is ≥ 80% from the near-UV region to the NIR region, and AlON also exhibits promising mechanical strength. Therefore, the fabrication of transparent AlON ceramics has a long history [401], and various synthetic strategies have been developed [402,403].

As with the oxide ceramics discussed in Section 2.1.8.1, AlON ceramics have also been produced by several advanced sintering technologies, such as pressure-less sintering [404–406], microwave processing [407], HP [408], HIP [404,409–411], and SPS [412]. Firstly, the fabrication of transparent AlON ceramics requires AlON powder. Several methods have been used to synthesize AlON powders, including Al_2O_3–AlN chemical reaction, Al_2O_3 carbothermal reduction, solid-state reactions, the plasma arc method, and high temperature rapid self-propagating combustion [413]. Carbothermal reduction and solid-state reactions are more popular than other methods because they are cost-effective and relatively simple; nevertheless, the synthesis of phase-pure AlON powders is still a challenge [414]. Once AlON powder has been obtained, sintering should be conducted in N_2 at temperatures > 1850 °C for at least 20 h.

A two-step approach to preparing transparent AlON ceramics using Al_2O_3 and AlN nanopowders as the precursors was adopted by Qi et al. [415]. Single-phase AlON powder was obtained from the direct reaction of Al_2O_3 and AlN nanopowders at 1750 °C for 4 h in N_2. After ball milling, the powder consisted of micron particles and demonstrated high densification behavior. Transparent AlON ceramics were produced by sintering in N_2 at 1880 °C for 20 h. While the IR-transmittance of the ceramics was promising, visible transmittance was not sufficiently high.

Yuan et al. employed MgO and Y_2O_3 as co-sintering aids to develop transparent AlON ceramics by reactive sintering [416]. The sintering aids and sintering time influenced the densification and allowed the optical performance of the AlON ceramics to be effectively optimized. Moreover, co-doping with MgO and Y_2O_3 promoted densification more efficiently than single-doping with either MgO or Y_2O_3. After sintering in N_2 at 1950 °C for 12 h, 1-mm thick samples of the AlON ceramics doped with 1 wt% MgO and 0.08 wt% Y_2O_3 exhibited 60% in-line transmittance at 600 nm.

Yuan et al. also reported using a hybrid method, combining carbothermal reduction and solid-state reaction, to synthesize high-quality γ-AlON powders [417]. In this study, organic sucrose was used as the reducing agent rather than carbon black. Sucrose was dissolved in DI water, γ-Al_2O_3 nanopowder was added to the solution, and the suspension was dried at 70 °C for a whole day prior to being thermally treated. During thermal treatment, the temperature was raised to 900 °C at 10 °C/min and held for 1 h while the pressure was held at 0.1 MPa and the N_2 flow rate was 0.5 L/min. The solid-state reaction was then conducted at 1500 °C and 0.1 MPa for 4 h in N_2 (2 L/min), and the resultant powder was calcined at 700 °C for 6 h to remove excess carbon.

Direct nitridation has been identified as one of the most effective strategies for synthesizing AlON powders for transparent AlON ceramics [418–421]. Jin et al. developed a two-step carbothermal nitridation process to obtain high-quality AlON powder, which they used to fabricate transparent AlON ceramics by pressure-less sintering [418]. The precursor powders were derived from a mixture of core-shell

SDC EX. 1018 - 33/66

structured Al_2O_3/C, which was prepared by the pyrolysis of an Al_2O_3/urea-formaldehyde-resin nanocomposite. A layer of amorphous carbon on the surface of the Al_2O_3 particles effectively prevented agglomeration and grain growth during the carbothermal nitridation process, and the resultant AlON powder had a bimodal particle size distribution centered at 0.2 and 0.7 μm, with a maximum particle size < 0.9 μm. At optimal conditions, the final AlON samples had 80% in-line transmittance from the visible to IR regions.

Su et al. reported a similar synthesis route for producing AlON powder from commercial powders of Al_2O_3 and Al [419]. The homogeneously mixed powders were thermally nitridized at 1750 °C for 3 h in N_2, which yielded AlON powder. Then, MgO (0.10 wt%), Y_2O_3 (0.08 wt%), and La_2O_3 (0.025 wt%) were added to the powder to promote densification. After sintering in N_2 at 1950 °C for 12 h, the in-line transmittance of 2-mm thick samples of AlON ceramics was 77.1% and 80.6% at 400 nm and 1100 nm, respectively.

Alternatively, Liu et al. synthesized AlON powder using commercial powders of γ-Al_2O_3 and carbon black, fabricated transparent AlON ceramics by pressure-less sintering with 0.25 wt% MgO and 0.04 wt% Y_2O_3 as sintering aids [420]. Phase-pure AlON powder was readily derived from γ-Al_2O_3/C mixture after calcination at 1550 °C for 1 h and thermal treatment at 1750 °C for 2 h. The ball milling parameters controlled the morphology and particle size of the AlON powders, which influenced the microstructure and optical transmittance of the final transparent AlON ceramics. Fig. 40 shows photographs and in-line transmittance curves of AlON ceramics sintered at 1850 °C for 6 h; the ceramic sample fabricated from powder that was ball milled for 12 h was foggy whereas the sample from powder that was ball milled for 24 h exhibited 79.4% and 83.3% in-line transmittance at 600 nm and 2000 nm, respectively.

More recently, transparent MgAlON ceramics were obtained using a similar synthetic route and sintering technique [421]. The MgAlON powder was prepared from a mixture of black carbon, γ−Al_2O_3, and MgO nanopowders, and the mixture was ball milled with absolute alcohol at 120 rpm for 24 h. The milled sample was calcined in N_2 (2 L/min) at 1500–1600 °C and 1 MPa for 2 h. Pellet samples were prepared by uniaxial pressing and treated with CIP at 250 MPa, followed by calcination under vacuum (700 °C and < 5 × 10^{-3} Pa for 2 h) in order to eliminate excess organic substances. Sintering was conducted in static N_2 at 1850 °C and 0.1 MPa for 20 h. The resultant ceramic sample had 86.59% and 82.37% in-line transmittance at 3700 nm and 600 nm, respectively.

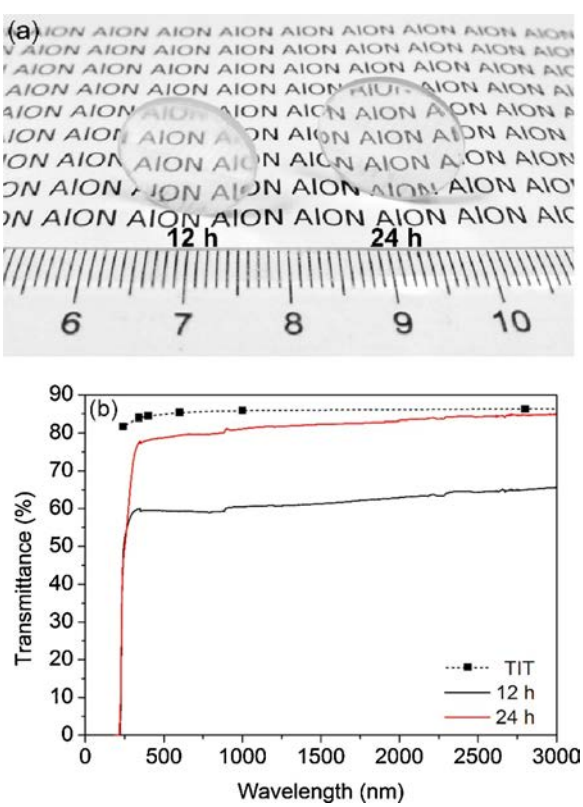

Fig. 40. (a) Photographs and (b) in-line transmittance curves of 1-mm thick samples of the transparent AlON ceramics derived from powders milled for 12 h and 24 h and sintered at 1850 °C for 360 min. Reused from [420], Copyright © 2016, Elsevier.

Zheng et al. combined vacuum sintering and HIP to fabricate transparent MgAlON ceramics that had an average grain size of 10 μm and displayed high mechanical strength and high optical transparency [422]. These transparent MgAlON ceramics were derived from mixtures of MgO, AlN, and Al_2O_3 powders, which were reactively sintered at 1650 °C for 15 h and HIP-treated at 1670 °C and 180 MPa for 5 h; the temperatures used in this study were lower than those reported for similar materials by 150–200 °C. The densification of the mixed powder was mainly attributed to the solute drag effect of Al_2O_3 before the solid solution was entirely formed at 1650 °C, which effectively suppressed grain growth. The in-line transmittance and flexural strength of the optimal samples were 86.1% at 3.7 μm and 386 MPa, respectively. The mechanical strength of the transparent MgAlON ceramics was higher than previously reported by approximately 40%, which was attributed to the synergistic effect of the Hall-Petch effect (finer grains) and the twin lamella strengthening mechanism. These transparent MgAlON ceramics could be promising candidates for high-performance IR domes, and may be an alternative to AlON ceramics and sapphires.

Cheng et al. attempted to use microwave sintering to fabricate transparent AlON ceramics [407]. The AlON powder was synthesized from α-Al_2O_3 and AlN powders, and a small quantity of Y_2O_3 (0.5 wt%) was added to promote densification of the AlON powder and enhance optical performance of the final ceramics. The mixed powder was compacted, treated with CIP at 250 MPa for 5 min, and sintered in a microwave set to 2.45 GHz, single mode, in a flowing N_2 atmosphere at ambient pressure. The temperature was increased at approximately 100 °C/min by controlling the power of the incident microwaves. After sintering at 1800 °C for 1 h, the resultant AlON ceramics had an average in-line transmittance of 60% for 0.6-mm thick samples.

Jiang et al. used pressure-less presintering and HIP to obtain AlON ceramics with high optical transparency [411]. The AlON powder was uniaxially compacted and further pressed by CIP at 200 MPa. The samples were presintered in high-purity N_2 at 1775–1875 °C and 0.1 MPa for 360 min, followed by HIP post-treatment in Ar at 1825 °C and 200 MPa for 180 min. After HIP, the AlON ceramics presintered at 1800 °C had an average grain size of 47.9 μm and an in-line transmittance of 84.8% at 600 nm and 86.1% at 2000 nm. For comparison, the in-line transmittance of the as-presintered samples was 63.6% and 75.4% at 600 nm and 2000 nm, respectively.

Zhang et al. developed highly transparent LiAlON ceramics (Φ57 × 6 mm) from commercial powders of AlN, Al_2O_3, and $LiAl_5O_8$ by reactive sintering at 1750 °C for 20 h and HIP post-treatment at 1850 °C and 180 MPa for 3 h [423]. By studying the sintering mechanisms, the authors reached three conclusions: (i) $LiAl_5O_8$ promoted the reaction that formed LiAlON at relatively high temperatures, (ii) Al_2O_3 enhanced densification before it was eliminated as the result of the solid solubility, and (iii) all residual pores were eliminated after HIP. By completely eliminating the Al_2O_3 secondary phase and residual pores, the samples were transparent across the visible and mid-IR regions, with a maximum in-line transmittance of 85.5%. Moreover, the flexural strength and Vickers hardness of these LiAlON ceramics were 303 MPa and 15.0 GPa, respectively.

Aluminum nitride can be stable in inert atmospheres at extremely high temperatures (> 2000 °C) and its high thermal conductivity, as compared to those of other ceramics, is an important property. Therefore, transparent AlN ceramics may have unique applications in

SDC EX. 1018 - 34/66

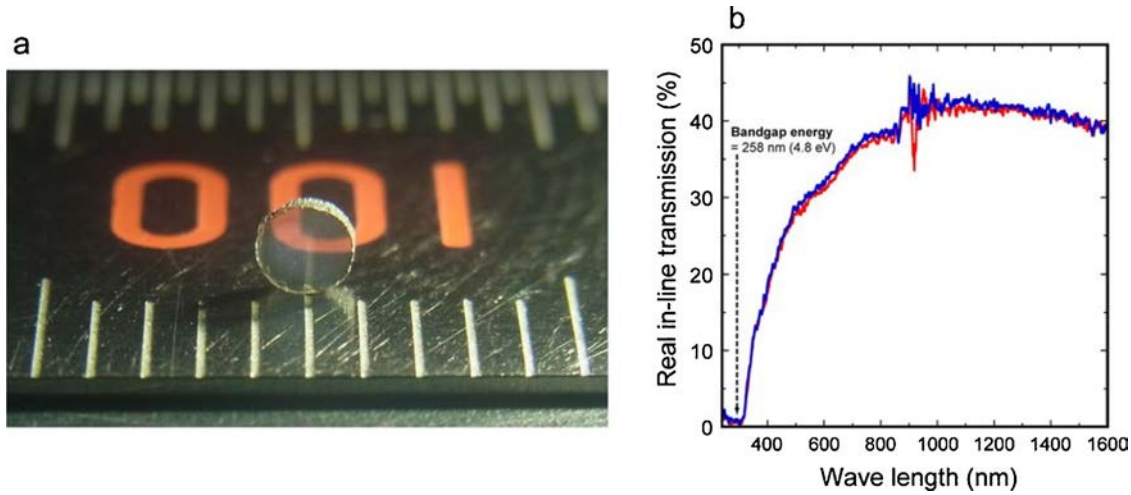

Fig. 41. (a) Photograph of the c-Si_3N_4 ceramics fabricated at 15.6 GPa and 1800 °C; the division of the ruler is 1 mm and sample thickness is 0.464 mm. (b) Real in-line transmittance curves of two representative c-Si_3N_4 ceramic samples (red and blue lines). Reused from [440], Copyright © 2017, Nature Publishing Group (For interpretation of the references to colour in this figure legend, the reader is referred to the web version of this article).

optics, lighting, electronics, and renewable energy. However, the fabrication of highly transparent AlN ceramics remains a challenge; currently, only translucent or low-transmittance transparent AlN ceramics have been reported [424–426]. Recently, Xiang et al. used HP to prepare highly transparent AlN ceramics from nanopowders that were prepared using a hydrothermal method [427]. First, $Al(NO_3)_3{\cdot}9H_2O$, urea, and sucrose were used to obtain the Al_2O_3/C precursor, which was then converted to AlN by calcining at 1500 °C for 4 h through the carbothermal nitridation method; the as-obtained powder was thermally treated at 700 °C for 60 min to eliminate excess carbon. Hot pressing was performed in flowing N_2 at 1800 °C and 30 MPa for 180 min, and the heating rate was 5 °C/min.

2.2.2. Sialon and Silicon Nitride (Si_3N_4)

While Sialon ceramics were named for their silicon (Si), aluminum (Al), oxygen (O), and nitrogen (N) contents, they are actually solid solutions of silicon nitride (Si_3N_4). Sialon ceramics are important engineering ceramics because of their high strength over a wide range of temperatures, high thermal shock resistance, and relatively high chemical stability, and advanced sintering technologies have been used to fabricate translucent and even transparent Sialon ceramics [428–436].

Li et al. used HP to fabricate transparent Er^{3+}-doped α-Sialon ceramics in order to study their up-conversion (UC) luminescence properties [437]. The samples were $Me_{m/v}Si_{12-(m+n)}Al_{m+n}O_nN_{16-n}$ with Me = Er, m = n = 0.9, m = n = 1, and m = n = 1.1. Powders of α-Si_3N_4, Al_2O_3, AlN, Er_2O_3, and Yb_2O_3 were thoroughly mixed by wet milling in absolute ethanol for 24 h and then dry milling for half a day; the mixtures contained 9.03, 10.00, and 10.92 wt% Er_2O_3, and Yb_2O_3 was added as a stabilizer. The powders were transferred to graphite moulds that were 2-mm thick and had an inner diameter of 50 mm, which were then subject to HP in a flow of N_2 at 1900 °C and 30 MPa for 120 min. During hot pressing, the samples were heated to 1050 °C at 20 °C/min, and then heated to the desired sintering temperature at 10 °C/min. After hot pressing, the samples were cooled from 1900 °C to 1050 °C at 10 °C/min, and then left to naturally cool to room temperature. The optimal transparency of these ceramics was approximately 60% in the visible light region.

Joshi et al. fabricated transparent yellow phosphor Sialon ceramics doped with Eu_2O_3 by HP [438]. The starting powders were ball milled in ethanol for 24 h using high-purity Si_3N_4 balls. Hot pressing was conducted at 1850 °C and 30 MPa of uniaxial pressure for 1 h in N_2 at 0.1 MPa. The samples consisted of a α-Sialon major phase and β-Sialon minor phase, with an average grain size < 500 nm. Moreover, AlN polytypoids were also observed as a minor phase. When excited by light in the UV to blue range, the Eu^{2+}-doped Sialon ceramics displayed yellow luminescence at approximately 570 nm, and white light was generated when the Sialon ceramic was coupled with a blue LED (455 nm). Furthermore, the samples doped with a small amount of Y_2O_3 exhibited substantially higher luminescence intensities than the samples that were only doped with Eu_2O_3.

Similarly, translucent Si_3N_4 ceramic samples have been produced by SPS [439]. In the study by Yang et al., Y_2O_3, MgO, and Al_2O_3 were used as sintering aids in order to increase the densification of Si_3N_4. Commercial powders of Si_3N_4 (> 95% α-phase, < 0.5 μm), MgO (10 nm), Y_2O_3 (0.7 μm), and Al_2O_3 (0.5 μm) were mixed by ball milling in alcohol for one day. The mixtures were then sintered by SPS with a pulse sequence of 12 on/2 off. The SPS was performed in N_2 at 1850 °C and 50 MPa for 5 min, and the heating and cooling rates were 100 °C/min and 350 °C/min, respectively. Fully dense ceramics were achieved when either Y_2O_3 or MgO was added as a single dopant; Al_2O_3 alone could not ensure full densification. The sintered samples consisted mainly of β-Si_3N_4, with grain sizes ranging from 0.29 μm to 0.37 μm, and the optical performance was closely related to the refractive indices of the additives and the thickness of the grain boundaries. The hardness and fracture toughness of the final translucent Si_3N_4 ceramics ranged from 12.6 GPa to 15.5 GPa and 6.2 MPa $m^{1/2}$ to 7.2 MPa $m^{1/2}$, respectively.

More recently, Nishiyama et al. developed highly transparent cubic silicon nitride (c-Si_3N_4) ceramics by sintering at extremely high pressures [440]. Commercial α-Si_3N_4 powder (> 95 wt%) was vacuum-dried at 8 Pa and 200 °C for 12 h and then enclosed in a sample capsule consisting of a Pt sleeve and disks that were embedded in an outer MgO sleeve with MgO lids; before the sample was loaded into the crucible, the platinum–MgO parts were heated at 1000 °C for approximately 10 min. Once the sample was loaded, the whole sample capsule was vacuum-dried at 150 °C for another 2 h. The apparatus used to conduct the high-pressure and high-temperature experiments could apply a maximum force of 1000 tons, and its second stage anvils were made of WC cubes with a truncated edge length of 7 mm. The pressure transmitting medium was an octahedron of MgO doped with Cr_2O_3 that had an edge length of 14 mm, and a cylindrical $LaCrO_3$ furnace was used to heat the sample capsule.

After being heated to 1800 °C, the sample had a transparent pale gray appearance, as shown in Fig. 41a. The in-line transmission curve shows that the sample had 18–38% transmittance over 400–800 nm (Fig. 41b). A representative bright-field TEM image of the sintered c-Si_3N_4 ceramics shows that they had an equigranular texture and an average grain size of 143 ± 59 nm (Fig. 42a). No residual pores or

SDC EX. 1018 - 35/66

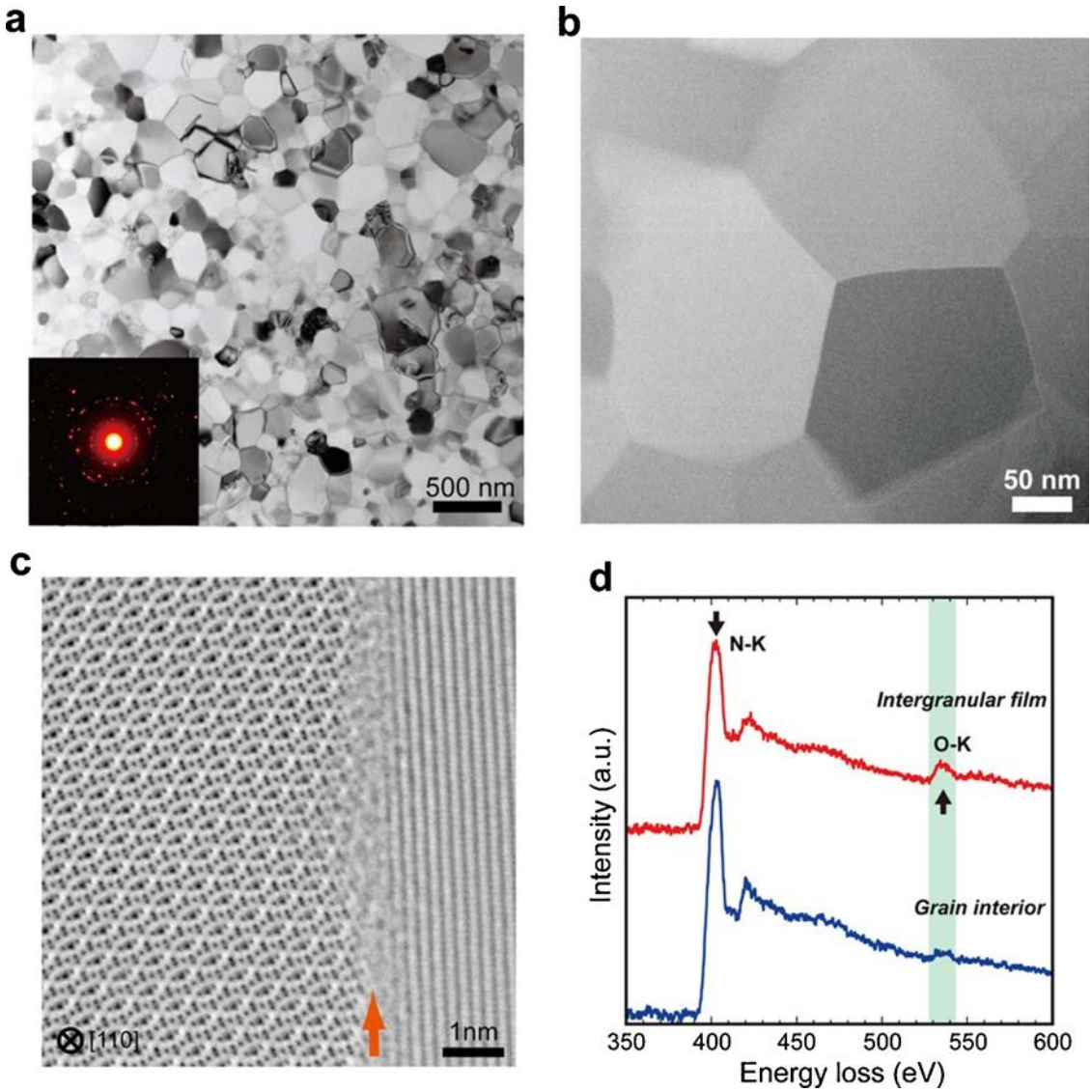

Fig. 42. (a) Representative bright-field TEM photographs of the c-Si_3N_4 obtained at 15.6 GPa and 1800 °C, which had an average grain size of 143 nm and a maximum grain size of 400 nm; the inset is the electron diffraction pattern that confirms the random orientation of the grains. (b) Low-angle annular dark-field scanning transmission electron microscopy (LAADF–STEM) photograph of a triple junction showing no pores or triple pockets. (c) Annular bright-field scanning transmission electron microscopy (ABF-STEM) image of a disordered/amorphous intergranular film between two grains, with the left grain viewed along the [110] orientation. (d) EELS spectra at an intergranular film (top) and grain interior (bottom). Reused from [440], Copyright © 2017, Nature Publishing Group.

triple pockets were observed at the multi-grain junctions, as illustrated in Fig. 42b, which confirms that the ceramics were fully densified. Moreover, the grain boundaries were mostly straight without dislocations. As shown in Fig. 42c, a very thin (< 1 nm thick) disordered/amorphous intergranular layer was observed, and electron energy-loss spectroscopy (EELS) of the intergranular film and grains indicated the segregation of oxygen (Fig. 42d). Because the high temperature metastability of c-Si_3N_4 in air is more advantageous than those of diamond and cubic BN, transparent c-Si_3N_4 ceramics could be used as window materials when there are harsh conditions.

2.2.3. Fluorides

Fluoride-based transparent ceramics have various advantages over oxide ceramics, including wide optical transmittance windows at wavelengths up to 7 μm, low phonon frequency cut-offs, low linear and non-linear refractive indices, as well as relatively low processing temperatures. The development of transparent CaF_2 ceramics has a long history as the first example, Dy^{2+}:CaF_2, was fabricated by HP in 1964 for solid laser applications [441]. Since then, this group of transparent ceramics has been extensively studied.

Samuel et al. studied the spectroscopic performance of transparent Eu-doped CaF_2 ceramics derived from hydrothermal powders and processed with pressure-less presintering and HIP [442]. Aubry et al. synthesized Yb-doped CaF_2 nanopowders for the fabrication of transparent ceramics using three methods: (i) mechanical alloying, (ii) reverse micelle reaction, and (iii) chemical coprecipitation [443]. The powder produced by mechanical alloying had an average particle size of 20 nm, whereas those produced by reverse micelle reaction and co-precipitation required calcination in order to eliminate the impurities adsorbed to the particle surfaces. The co-precipitation powder was used to fabricate transparent Yb:CaF_2 ceramics by combining vacuum presintering with HIP post-treatment.

For mechanical alloying, commercial powders of CaF_2 and YbF_3 were thoroughly mixed to obtain a 20 g mixture with a 9:1 M ratio. The mixture was high-energy ball milled using a FRITSCH Pulverisette 6 machine with 30 ZrO_2 balls (10 mm diameter) as the milling media; the powder was milled under Ar at 600 rpm for 17 h in an 80 mL container. For the wet-chemical, reverse micelle reaction, high-purity hydrated

SDC EX. 1018 - 36/66

calcium nitrate and hydrated ytterbium nitrate were used as the precursors, and 40 wt% HF was used as the fluorine source. An Igepal/cyclohexane/water system was prepared for the reverse micelle reaction by dissolving Igepal (CO-520) in cyclohexane to form microemulsions. After the mixtures were homogenized, an aqueous cationic salt solution was slowly added to the mixture, followed by ethanol, which acted as a co-surfactant; fluoride microemulsions were formed as the aqueous cationic salt solution was replaced with the HF solution. The mixtures were centrifuged at 13,000 rpm for 1 h in order to collect the nanopowders, which were then calcined in Ar at 400 °C for 4 h.

In the coprecipitation synthesis, the nitrate salts were dissolved in DI water to form cationic precursor solutions, and HF solution was added dropwise with constant stirring. The resultant Yb:CaF_2 nanopowders were collected by high-speed centrifugation at 13,000 rpm for 30 min, washed, dried at 110 °C, and thermally annealed in Ar at 400 °C for 4 h. All powders were compacted by uniaxial molding and CIP treatment. The pellet samples were presintered under a 0.1 Pa vacuum at 900 °C for 1 h, followed by HIP in Ar at 950 °C and 160 MPa for 40 min. The resultant ceramics had an average grain size of 24 μm and an optimal IR-transmittance of 55% at 1.2 μm. Lyberis et al. also prepared Yb^{3+}:CaF_2 nanopowder using a similar coprecipitation method, and used the powder to fabricate transparent ceramics by HP; their objective was to study the origin of light scattering when these ceramics were used for solid laser applications [444].

When doping with lanthanide ions, HP is the most popular sintering technology for fabricating transparent CaF_2 ceramics [445–459]. For example, Liu et al. synthesized CaF_2 nanopowder doped with different concentrations of Er^{3+} using a coprecipitation method and fabricated highly transparent ceramics by hot pressing in a vacuum [449]. The CaF_2 nanopowders were prepared by dissolving commercial chemicals – calcium nitrate (0.5 M Ca^{2+}), erbium nitrate (0.5 M Er^{3+}), and $KF{\cdot}2H_2O$ (1.2 M F^-) – in DI water to form solutions. To facilitate the coprecipitation reaction, the cationic solutions were added to the anionic solution in order to obtain $Ca_{1-x}Er_xF_{2+x}$ with x = 1, 5, 7, and 10 mol%. The mixed solutions were stirred for 30 min to complete the reaction, kept at room temperature for 24 h, and centrifuged at 11,000 rpm for 20 min to recover the precipitates. The recovered powders were then thoroughly washed with DI water, dried at 80 °C for 24 h, and HP at 30 MPa. Both the size and morphology of the CaF_2 powder were dependent on the Er^{3+} concentration while the microstructure and thus optical performance of the transparent Er:CaF_2 ceramics were dependent on the Er^{3+} concentration and sintering temperature. The sample that was doped with 5 mol% Er^{3+} and hot-pressed at 800 °C exhibited optimal optical properties; the 2-mm thick sample had 90% in-line transmittance in the near-IR region. Photographs and in-line transmittance curves of the transparent Er:CaF_2 ceramics are shown in Fig. 43.

Li et al. used HP to fabricate high-quality transparent 2 at% Ho:CaF_2 ceramics, which exhibited a strong emission peak at approximately 2030 nm when excited with 640 nm light [460]. The Ho:CaF_2 ceramics by sintering nanopowder at 800 °C for 1 h had an average grain size of 0.5 μm and an in-line transmittance of 89% at 1300 nm; the transmittance decreased in the NIR range because of the residual pores in the ceramics.

Transparent CaF_2 ceramics have also been fabricated using SPS technology [461–463]. Li et al. used SPS at relatively low temperatures to obtain transparent Yb^{3+}:CaF_2 ceramics from nanopowders with an average particle size of 50 nm, which were synthesized by chemical coprecipitation [461]. The samples were treated with SPS at 600 °C for 5 min, and the heating and cooling rates were 100 °C/min and 10 °C/min, respectively. The resultant Yb^{3+}:CaF_2 ceramics had 83% in-line transmittance at 1200 nm, which is only slightly lower than that of the samples processed with HP.

Wang et al. found that the contamination of transparent CaF_2 ceramics processed by the SPS graphite die could be avoided by using Mo foil to prevent direct contact between samples and the dies [462].

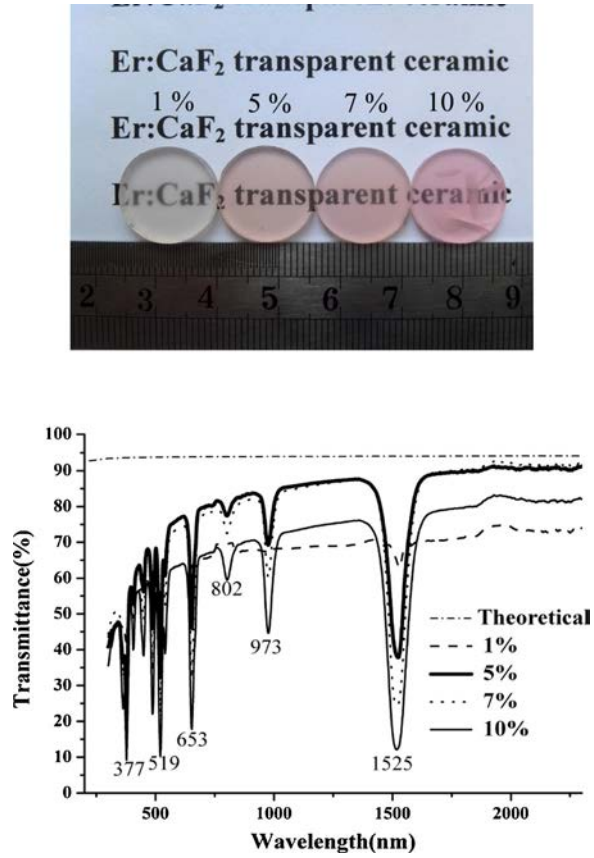

Fig. 43. Photograph and in-line transmittance curves of 2-mm thick samples of the transparent CaF_2 ceramics doped with different concentrations of Er and sintered at 800 °C for 2 h. Reused from [449], Copyright © 2015, Elsevier.

By using Mo foils, discoloration of the ceramics was effectively prevented and the transmittance was increased from 8% to 54% and 63% to 86% at 300 nm and 1100 nm, respectively. The Mo foils substantially enhanced the grain growth of the final CaF_2 ceramics which was responsible for the improved optical performance; after sintering at 1100 °C, the average grain size of the samples processed with a graphite sheet was 16 μm while the samples processed with Mo foil had grains as large as 260 μm.

Fluorides of other alkaline earth metals (Mg, Sr, and Ba) could also be used to fabricate transparent ceramics, although only limited information about these ceramics is available in the open literature. Nakamura et al. reported a series of studies on MgF_2-based transparent ceramics, which investigated SPS methods, their optical properties, and potential applications in scintillation, thermally-stimulated luminescence (TSL), optically-stimulated luminescence (OSL), and radio-photoluminescence (RPL) [464–467]. High-purity commercial MgF_2 powder was used as the starting material, and SPS was performed at the desired uniaxial pressures [466]. Both the temperature and pressure were used to control the microstructure and properties of the MgF_2 ceramics. In most cases, the temperature was increased to 500 °C at 100 °C/min and 6 MPa, held at 500 °C for 10 min, increased to 650 °C at 10 °C/min while the pressure was increased to 70 MPa, and held at 650 °C for 15 min. However, the optical transparency of these MgF_2 ceramics was still much lower than that of their single-crystal counterparts.

There have also been reports of SrF_2-based transparent ceramics [468–470]. For example, Li et al. prepared transparent Yb:SrF_2 ceramics from nanopowders synthesized by chemical co-precipitation [469].The authors employed high-speed centrifugation to remove the large agglomerated particles and retain the fine particles with high

SDC EX. 1018 - 37/66

sintering activity; the suspensions were centrifuged at 11,000 rpm for 20 min, and after thorough washing, the precipitates at the bottom and top of the centrifugal tube were collected separately. Both precipitates were used to fabricate Yb:SrF_2 ceramics by HP at 800 °C and 40 MPa for 1 h. The samples obtained from the fine powders exhibited 77% in-line transmittance at 1200 nm, which was much higher than that of the samples obtained from the agglomerated powders collected from the bottom of the tubes.

Similar studies have investigated transparent BaF_2 ceramics [471–473]. For example, Luo et al. prepared transparent Ce:BaF_2 ceramics with luminescence and scintillation properties. Barium nitrate and KF were separately dissolved in DI water to form solutions, Ce$(NO_3)_3 \cdot 6H_2O$ and PEG2000 were dissolved in the $Ba(NO_3)_2$ solution, and then the KF solution was slowly added; the final composition of the solution corresponded to $Ce_{0.001}Ba_{0.999}F_{2.001}$. The precipitates were collected, thoroughly washed, and dried at 100 °C overnight. The dried powders were compacted under 200 MPa of uniaxial pressure and further densified by CIP at 200 MPa for 3 min. The green bodies were sintered under a 10^{-3} Pa vacuum; the temperature was held at 1000 °C and 1300 °C for 2 h and 6 h, respectively, and the heating rate was 10 °C/min. The resultant transparent Ce:BaF_2 ceramics displayed promising luminescence and scintillation properties.

A solid solution of SrF_2-CaF_2 was prepared by Zhu et al. from CaF_2–SrF_2–NdF_3 nanopowders [474]. The nanopowders were obtained by chemical co-precipitation, which yielded a single phase with an average particle size of 20 nm, and the transparent CaF_2–SrF_2–NdF_3 ceramics were obtained by HP at 800 °C and 30 MPa. The transparent ceramics were fully densified with an average grain size of 0.5 μm, and 2-mm thick samples had an in-line transmittance of 86% at 250–1400 nm.

3. Potential applications

3.1. Applications in solid-state lasers

3.1.1. Conventional ceramic solid-state lasers

3.1.1.1. Nd^{3+}-doped ceramic lasers. The Nd^{3+} ion has very interesting spectroscopic and emission dynamic characteristics, and it has been used as a lasing material because its emissions cover a relatively wide range of temporal regimes, from continuous wave (CW) to very short pulses less than a picosecond. Moreover, Nd^{3+} has transitions from the two Stark levels of the $^4F_{3/2}$ manifold to the Stark levels of the $^4I_{9/2}$, $^4I_{11/2}$, and $^4I_{13/2}$ manifolds, which have emissions with large cross-sections near 0.9 μm, 1.0 μm, and 1.3 μm, respectively. Transparent ceramics with a cubic crystal structure, such as garnets and sesquioxides, are suitable to host the laser emission of Nd^{3+}, and thus are dominant ceramic laser materials that have been extensively studied in the open literature. The structure of this section is illustrated in Fig. 44.

Solid-state lasers based on transparent Nd^{3+}-doped garnet ceramics have five emission types: (i) 1.0 μm laser emissions, (ii) 1.3 μm laser emissions, (iii) 0.9 μm laser emissions, (iv) laser emissions at multiple wavelengths, and (v) CW laser emissions with sensitization. Transparent Nd:YAG ceramics have multiple lines with emission cross-sections that are sufficiently large for laser applications, especially the $^4F_{3/2}$ (R_i) → $^4I_{11/2}$ (Y_j) transition at room temperature [475]. Ikesue et al. were the first to report Nd:YAG ceramic lasers with CW laser emissions; these 1.1 at% Nd-doped YAG ceramics were fabricated using a solid-state reaction process [35]. The efficiency of these lasers was comparable to that of single-crystal lasers, and their performance could be further improved if the Nd^{3+} concentration was increased by using starting powders synthesized by other chemical processing routes [14,476,477]. For example, Lu et al. created 1.5 kW CW lasers by diode laser pumping with garnet ceramic rods that were sufficiently large and had fine grains [478]. Overall, the lasing performance of Nd:YAG ceramics has been comparable to that of single crystals [479–483].

Quasi-continuous wave (QCW) lasers have been constructed with composite ceramic rods that had a Nd:YAG core coated with Sm:YAG [484]. The lasing behavior of these lasers was largely enhanced compared to rods that have a uniform distribution of dopants and rods clad with pure YAG. A 100 kW Nd:YAG laser array with seven coherently coupled master oscillator power amplifiers (MOPA) has also been reported [485], as well as a system with low-duty regime, which had six modules paired and connected to thin Nd:YAG ceramic plates in a single-aperture power oscillator [486]. In the latter, the laser beam path had a zig-zag shape; thus, the concept was called thin ZAG. A burst-mode high aperture heat capacity laser that emits 67 kW of power has also been constructed using Nd:YAG [487].

A 1.02-kW QCW (1 kHz) laser was assembled with three 1 at% Nd:YAG rods in a 808.5-nm transverse diode-pumped MOPA structure and the Nd:YAG ceramics were directly pumped with Ti:sapphire or diode lasers at 885 nm [488]. Other studies have demonstrated that lasing characteristics were improved when the laser rods were not clad [489–491]. Furthermore, if the ceramic quality was enhanced and an anti-reflection (AR) coating was added, the lasing performance could approach the quantum defect limit. Improvements to CW laser performance have been ascribed to reduced heat generation and improved beam quality; for example, Frede et al. fabricated an efficient 250-W laser pumped with a diode laser [492].

Yagi et al. constructed a 1064-nm flash-lamp-pumped Nd:YAG ceramic laser that operated in the QCW free-generation regime [493]. When the Xe lamp was used, the pulse excitation of this laser was 5 ms at 20 Hz. The Nd:YAG ceramic rod was ϕ8.3 × 152 mm and contained 1.1 at% Nb^{3+}. A Sm-doped flow glass tube was used to filter the UV radiation. The average power of this laser was 387 Wand the lasing performance was superior to similar single-crystal lasers. Wang et al. went on to build a 1064-nm diode-side-pumped QCW laser using two Nd:YAG ceramic rods, which were arranged to form a symmetrical

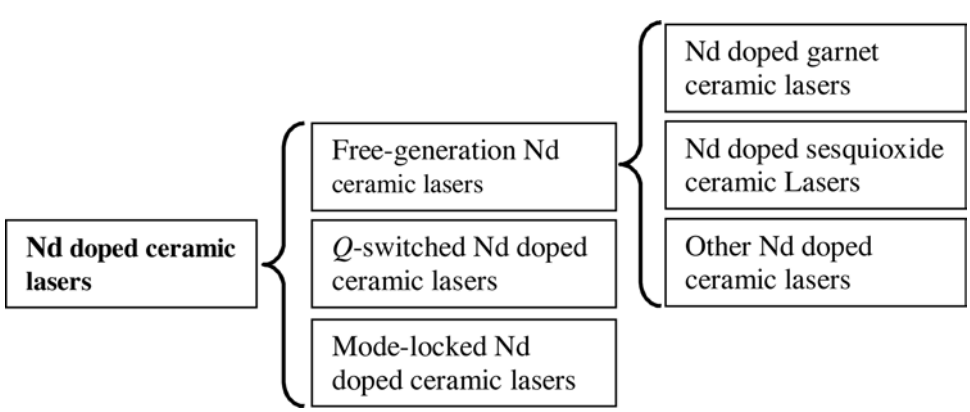

Fig. 44. Structure of the discussion of Nd-doped ceramic lasers.

SDC EX. 1018 - 38/66

convex-convex cavity [494]. The output power of this laser was as high as 961 W and the optical-to-optical conversion efficiency was 38.3% while the slope efficiency was 45.3%.

The Nd:YAG emission transition near 1.0 μm can be harnessed once competing transitions are reduced by wavelength selecting optics to levels below the laser threshold. For example, the emission and repetition rates of a high-efficiency QCW laser constructed in this way were 180 μs and 1.1 kHz, respectively, and the optical slope efficiency was 24.7% at 1123 nm [495–498]. Pumping was achieved using a 1000-W diode laser and the competitive transitions were suppressed using coating technology. A similar 1052-nm Nd:YAG ceramic laser has been described in the open literature [499].

Neodymium-YAG ceramic lasers with emissions at 1.3 μm and 0.9 μm have been widely reported. Lu et al. developed a Nd:YAG ceramic laser at 1.3 μm [500]; the emission cross-section of the $^4F_{3/2}(2) \rightarrow {}^4I_{13/2}(1)$ transition at 1319 nm was approximately 0.8×10^{-19} cm^2 at room temperature, and the slope efficiency was approximately 35%. Strohmaier et al. developed a CW Nd:YAG laser at 946 nm, which corresponds to the $^4F_{3/2}(2) \rightarrow {}^4I_{9/2}(5)$ transition, and the laser performance was similar to that of single-crystal lasers [501].

Laser emissions at multiple discrete wavelengths can be achieved using broad-band optics or multiple dichroic resonator mirrors once the pumping transitions reach the threshold. For example, Guo et al. obtained simultaneous emission at 1319 nm and 1338 nm with a Nd:YAG ceramic-based laser [502]. Duan et al. compared the dual-wavelength operation of Nd:YAG ceramic-based and single-crystal lasers at 1319 and 1338 nm; they found that the single-crystal lasers worked better at 1319 nm, but the ceramic-based lasers oscillated at 1338 nm, which implies that the $^4F_{3/2}$–$^4I_{13/2}$ transition of Nd^{3+} was different in the two media [503]. Furthermore, tri-wavelength laser emission at 1064, 1319, and 1338 nm was reported by Chen et al. [504]. Such multi-wavelength lasers can be used in non-linear processes, such as mixing and frequency multiplication, in order to generate radiation from visible to terahertz bands.

High-performance lamp-pumped Nd:YAG ceramic lasers have been developed by multi-component doping; for example, (Cr^{3+}, Nd^{3+}):YAG ceramics are widely available and thus have been widely reported [505–510]. When a 4 m^2 Fresnel lens collector was used with solar pumping, the doped Nd:YAG ceramic lasers reached 80 W of CW laser emission, which corresponds to 4.3% solar–laser power conversion efficiency [511–513]. Moreover, Dinh et al. demonstrated a 120-W CW solar-pumped laser that was assembled with (Cr, Nd):YAG rods and a liquid light-guided lens [514]. Based on these studies, (Cr, Nd):YAG ceramics are promising materials for highly efficient lamp-pumped and solar-pumped lasers.

The optimized sensitizing effect of (Ce, Cr, Nd):YAG ceramics has been evaluated for solar-pumped solid-state laser applications [515]. The YAG-based powders used to fabricate these ceramics were synthesized by a sol–gel process. Based on a parameter mapping survey of the sensitizing effects of Ce^{3+} and Cr^{3+} when Nd:YAG is exposed to sunlight, the optimal composition of the (Ce, Cr, Nd):YAG ceramics was determined to be 0.9 at% Ce^{3+}, 8.0 at% Cr^{3+}, and 1.0 at% Nd^{3+}. In this study, the sensitizing effect of the (Ce, Cr, Nd):YAG ceramics was four times greater than that of the (Cr, Nd):YAG ceramics; therefore, Ce^{3+} was an effective sensitizer for Nd^{3+}. Multi-dopant approaches could produce YAG-based ceramics for lasers that have applications in space solar power systems.

The efficiency of Nd-doped oxide ceramic lasers is closely related to their residual losses [113,516,517]. Oxide-based ceramics other than Nd:YAG have also been used to construct high-efficiency lasers; for example, high-performance 1-μm CW lasers under pumping with diode lasers have been developed from Nd:Y_2O_3 [518] and Nd:Lu_2O_3 [519] ceramics with fine microstructures. The large crystal-field splitting of these ceramics was due to the energy of the lowest Stark component at room temperature; therefore, the emission cross-sections of these transitions were larger than those of Nd:YAG. Furthermore, the strongest transitions of these ceramics terminated at the two lowest Stark components of the $^4I_{11/2}$ manifold, which have a difference of approximately 35 cm^{-1} but have similar emission cross-sections. Thus, both ceramics exhibited dual CW laser emissions: 1074.6 and 1078.6 nm for Y_2O_3 and 1075.9 and 1080 nm for Lu_2O_3.

Transparent 0.4 at% Nd^{3+}:Y_2O_3 ceramics have been used to construct dual-wavelength solid-state lasers with emissions at 946 and 1074 nm [520]. The fluorescence and radiative lifetimes of the $^4F_{3/2}$ manifold were 283 and 328 μs, respectively. With the laser diode pumping at 808 nm, the laser performance was measured using a plano-concave resonating cavity. At 1074 nm, the maximum output power was 3.5 W for an absorbed power of 13.0 W, and the optical-optical efficiency and slope efficiency were 26.9% and 31.1%, respectively. At 946 nm, the maximum output power was 1.0 W for an absorbed power of 13.0 W, and the optical-optical efficiency and slope efficiency were 7.9% and 12.4%, respectively.

If disordered Nd-doped ceramics are used for lasers, both the absorption and emission bands will be very broad; therefore, these ceramics could have various useful applications, such as tunable emissions, multi-wavelength emissions, and ultra-short pulse generation. For example, a laser made from transparent Ba(Zr,Mg,Ta)O_3 ceramics, which have a disordered cubic perovskite structure [521]. Similarly, lead lanthanum zirconate titanate ($Pb_{1-x}La_xZr_{1-y}Ti_yO_3$) has also been used for solid-state laser applications. For example, CW laser emission at 1064.4 nm was reported for PLZT 10/65/35 ceramics doped with 1 at% Nd pumped with a 100-ms pulsed CW diode laser at 805 nm [522,523].

Transition metal (TM) ions are generally used for the passive *Q*-switching of IR solid-state lasers; for example, Cr^{4+}, V^{3+}, and Co^{2+} have been used for 1.3–1.6 μm, 0.940–1.100 μm, and 1.30–1.35 μm, respectively. These ions can be incorporated in ceramics with a cubic crystal structure; however, only Cr^{4+}:YAG ceramics have been reported as ceramic saturable absorber (SA) *Q*-switches to date [511,524–526]. Because the laser and *Q*-switch components have the same host ceramic – e.g., Nd:YAG lasers passively *Q*-switched by Cr^{4+}:YAG – the two items should have comparable refractive indices in order to minimize reflections at the interface.

According to both theoretical predictions and experimental results, SAs are used for passive *Q*-switching in solid-state lasers, they should have low initial transmittance in order to enhance the lasing energy and reduce the pulse duration. Furthermore, the transmission of the out-coupling mirror should be increased and the laser resonator should be shortened [527–532]. For example, Kalisky et al. studied a passively *Q*-switched diode-pumped Yb:YAG laser with Cr^{4+}:YAG, Cr^{4+}:LuAG, and Cr^{4+}:GSGG saturable absorbers in order to check the repetitive modulation in the kilohertz frequency domain [531]; the experimental results were very close to the numerical model predictions.

Repetition rate is significantly affected by pumping intensity, which has a minimal effect on the energy and duration of the pulses. The Nd-doped ceramic lasers with Cr^{4+}:YAG SA passive *Q*-switches that have been reported are mainly CW diode-pumped lasers. For example, the most popular 808-nm diode lasers and *Q*-switched 1064-nm Nd:YAG ceramic lasers with Cr^{4+}:YAG SAs have pulse energies on the scale of millijoules, with peak powers up to tens of kilowatts; however, their durations are on the scale of tens of nanoseconds [533–536]. Feng et al. reported passively *Q*-switched Nd:YAG ceramic lasers with Cr^{4+}:YAG SAs [536]. When these lasers were pumped by a 1-W CW laser diode, the optical-optical efficiency could reach 22% if the Cr^{4+}:YAG had an initial transmittance of 79–94%; this performance is similar to that of devices based on single crystals.

Huss et al. found that if end-pumped Nd:YAG ceramic lasers were clad with a layer of Sm:YAG ceramics, the stability of passive Cr^{4+}:YAG *Q*-switched emissions could be increased [484]. Moreover, the peak power of efficient, passively *Q*-switched Nd:YAG ceramic lasers with Cr^{4+}:YAG SAs could be > 20 kW at 1052 and 1064 nm, and the pulse energies could approach tens of millijoules with pulsed pumping at 1.0 μm [493,537]. For example, as a YAG ceramic rod with 1 at% Nd^{3+}

SDC EX. 1018 - 39/66

was doped with 0.1 at% Cr^{3+}, the absorption was enhanced and the passively *Q*-switched YAG ceramic lasers exhibited flash-lamp pumping at 5 Hz [538].

Hybrid active–passive *Q*-switching for single-crystal lasers has also been adopted for ceramic lasers, and has been used to obtain giant pulses for flash-lamp-pumped (Cr, Nd):YAG ceramic lasers. For example, Pavel et al. reported 2.4-mJ pulse emission, 2.8-MW peak power, and repetition rates of 5–100 Hz under the pumping of an 807-nm QCW diode laser [539]. Omatsu et al. achieved passive *Q*-switching of a 1.3-μm Nd:YAG ceramic bounce laser with a V^{3+}:YAG SA [540]. The ground-state absorption cross-section of this laser was 7.2×10^{-18} cm^2, but the excited state absorption was nearly negligible. Similar diode end-pumped lasers have reported 128-ns pulses at a repetition rate of 230 kHz, with 9% slope efficiency [541,542]. The self-*Q*-switching properties of single-crystal lasers, such as (Cr^{4+}, Nd/Yb):YAG crystals, have been used to fabricate single-mode microchip lasers [543,544], and this function can be extended to ceramic lasers, such as (Cr^{4+}, Nd):YAG ceramics [545,546].

Mode-locking can be applied in three ways: (i) passive saturable absorptions, (ii) effective saturable absorptions, and (iii) controlled mirror reflections. The pulse duration of solid-state lasers can be effectively reduced using either passive or active mode-locking techniques; for example, acousto-optic modulators are used for active mode-locking. Moreover, losses in resonators with real or effective SAs could be controlled by the intra-cavity intensity while the reflectivity of mirrors could be modified by non-linear processes, both of which are representative passive approaches. However, using active mode-locking to generate stable regular trains with picosecond pulses is more successful in CW pumped Nd-doped single-crystal lasers than in Nd-doped ceramic lasers [547–550]; therefore, more research should investigate mode-locking in ceramic lasers.

Nanocarbon materials with semiconducting behavior, such as semiconducting single-walled carbon nanotubes (SWCNTs) [551] and graphene nanosheets [552], have been employed as SAs for mode-locking in ceramic lasers. For example, a single-layer graphene nanosheet has been demonstrated to absorb 2.3% of incident light [552]. Graphene is insensitive to the wavelength of light, recovers quickly, and graphene films can be prepared to have different transparencies; therefore, mode-locking SAs made of graphene can be readily manipulated.

Certain modifying methods have been used to achieve mode-locking by controlling the reflectivity of the rear mirror in lasers; semiconductor saturable absorption mirrors (SESAMs) are used for this type of mode-locking [553,554]. Furthermore, *Q*-switching stability can be increased by adjusting the modulation depth of the SESAM and controlling the length of the laser resonators; this has been demonstrated in SESAM mode-locked Nd:YAG ceramic lasers [555].

Compositional inhomogeneity usually occurs in solid solution ceramics and garnet ceramics that have an intrinsically disordered ion distribution; thus, these ceramics have emission lines that exhibit broadening behavior. When this line broadening is used for mode-locking, pulses can be effectively shortened [556]; for example, a sub-picosecond solid-state laser was constructed with solid solutions of GSAG–YSGG doped with Nd^{3+}, and achieved a 5.3-nm linewidth [557]. Because the bandwidth was much broader than that of Nd:YAG, the duration of the mode-locked pulses was on the scale of sub-picoseconds.

Neodymium:LuAG ceramics doped with 0.8 at% Nd^{3+} exhibited photoluminescence at 1063.5 nm and the fluorescence lifetime of this $^4F_{3/2}$ transition was 240 μs [558]. When the pumping-beam diameter was 300 μm and the reflectivity of the output coupler was 25%, the slope efficiency and optical–optical efficiency of the laser were 43.45% and 39.3%, respectively. As the pumping power was increased, an annulus isogyre pattern was observed instead of a four leaf-like pattern.

Moreover, 2 at% Nd:LuAG ceramics have been used to develop solid-state lasers with CW lasing at 1064 nm, under diode-laser pumping at 808 nm [559]. Both the fluorescence lifetime and radiative lifetime of the $^4F_{3/2}$ manifold were measured, the inter-Stark energy levels of the $4I_{J'}$ manifolds were derived, and the peak emission cross-sections of the $^4F_{3/2} \rightarrow 4I_{J'}$ intermanifold transitions were obtained; the total emission cross-sections of the $^4F_{3/2} \rightarrow {}^4I_{9/2}$, $^4F_{3/2} \rightarrow {}^4I_{11/2}$, and $^4F_{3/2} \rightarrow {}^4I_{13/2}$ transitions were determined to be 7.41×10^{-20} cm^2, 29.83×10^{-20} cm^2, and 10.53×10^{-20} cm^2, respectively. Based on the results, the quantum efficiency was estimated to be 80.4%.

Short pulse generation and passive mode-locking have been demonstrated by Nd^{3+}-doped calcium niobium gallium garnet (CNGG) ceramic lasers with a SESAM [560,561]. These lasers have achieved 101-mW output power, 2.0-ps pulse duration, 1.2-nm spectral bandwidth, and 88.4-MHz repetition rate. Similarly, a passively mode-locked hybrid laser was constructed with composite Nd:CNGG/Nd:calcium lithium niobium gallium garnet (CLNGG) crystals [562]; the pulse width was 534 fs and the effective FWHM was 2.2 nm.

3.1.1.2. Ho-doped ceramic lasers. The $^5I_7$ manifold of the Ho^{3+} ion has a quasi-three-level emission at 2.0 μm under direct pumping, which can be used for efficient CW lasing. Zhang et al. studied a Ho:YAG ceramic laser, doped with 1 at% Ho, that had a 2.09 μm laser emission under 1.91 μm pumping with a Tm:YLF laser [196]. The slope efficiency of this laser was 44.2% and the threshold was approximately 2.3 W. A maximum laser output power of 1.95 W was achieved when the Tm:YLF pump power was 6.7 W, and there is still room to improve the laser performance to be comparable to that of single crystals.

Chen et al. used 1.5 at% Ho:YAG ceramics to assemble a ceramic laser with 2097-nm CW radiation [563]. This laser exhibited a power of 21 W, a slope efficiency of 63.3%, and an optical efficiency of 61% when it was pumped with a 1907-nm Tm fiber laser. Zhao et al. studied the laser behavior of Ho:YAG ceramics with different Ho^{3+} concentrations [564]. The 0.8 at% Ho:YAG ceramic laser with 15.1-W pump power at 1907 nm had an output coupler with 6% transmission, an output power of 9.4 W at 2097 nm, and a slope efficiency of 64.0%.

Holmium:YAG ceramics have also been used for an IR lasers [565]. These Ho:YAG ceramics were derived from nanopowders, 1 at% Ho:Y_2O_3 and Al_2O_3, which were synthesized by laser ablation processing. The optical transmittance of the resultant ceramics was approximately 82% in the IR region. The Ho:YAG samples contained scattering centers (30 ppm vol.), which were distributed in the depth direction; the number of defects was estimated by collinear two-photon inter-band photoexcitation and by directly counting the defects shown in optical microscopy images. The laser was constructed with 1-mm thick Ho:YAG ceramics and intra-cavity pumping was used to determine its slope efficiency: 40% at 1.85 μm.

Yuan et al. developed a high-power dual-end-pumped passively *Q*-switched Ho:YAG ceramic laser with a Cr^{2+}:ZnS SA [566]. The performance of the *Q*-switched laser was influenced by the beam diameter passing through the SA, which was placed far away from the laser beam waist. The maximum pulse energy of the laser was 0.94 mJ, the peak power was 33.5 kW, the pulse width was 28 ns, and the pulse repetition frequency was 28.8 kHz. Moreover, the average output power of the CW Ho:YAG ceramic laser was 30.3 W and the maximum output power was 40.4 W. Fig. 45 shows a schematic diagram of the experimental setup.

Duan et al. reported a CW mode-locked Ho:YAG ceramic laser that used an acousto-optic modulator [567]. The 1 at% Ho:YAG ceramics in the laser were $40 \times 6 \times 1.5$ mm^3, and the pump source was a 1.91-μm Tm-fiber laser. With an incident pump power of 11.4 W, the maximum output power approached 1.84 W at 2122.1 nm in the CW mode-locked regime. A short-duration pulse of 241.5 ps was observed at a repetition rate of 82.15 MHz, with a beam quality factor (M^2) of 1.2 and a maximum single-pulse energy of 22.4 nJ.

A passively mode-locked Ho:YAG ceramic laser at 2.1 μm was constructed using a GaSb-based near-surface SESAM as the SA [568]. Stable self-starting mode-locked operation was achieved across the entire tuning range, 2059–2121 nm, the oscillator was operated at a repetition rate of 82 MHz, and the maximum output power was 230 mW

SDC EX. 1018 - 40/66

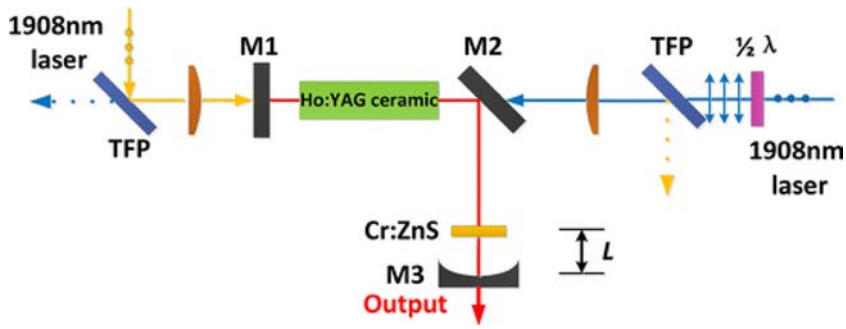

Fig. 45. Schematic diagram of the high-power dual-end-pumped passively *Q*-switched Ho:YAG ceramic laser experimental setup. Reused from [566], Copyright © 2015, Springer.

at 2121 nm. The shortest pulse was 2.1 ps, which was observed at 2064 nm. The 1 at% Ho:YAG ceramics were fabricated using a solid-state reaction and vacuum sintering method with high-purity, commercially available oxide powders.

Yttrium aluminum garnet ceramics doped with Ho^{3+}, Cr^{3+}, and Tm^{3+} were used to assemble IR solid-state lasers [569]. Laser emission at 2.09 μm was obtained by excitation at 430 nm, which corresponds to a transition from Cr^{3+} to Ho^{3+} with Tm^{3+} as the intermediate media. The efficiency ratio of the $^3F_4 \rightarrow {}^5I_7$ ($Tm^{3+} \rightarrow Ho^{3+}$) transfer and back-transfer was 7.87, which is very close to those observed for YAG single crystals and YLF ceramics.

A *Q*-switched Ho:LuAG ceramic laser with a polycrystalline Cr^{2+}:ZnS SA was developed by Zhang et al. [570]. A diode-pumped Tm:YLF laser emitting at 1907.5 nm was employed as the pump source, and the laser was operated in both CW mode and passive *Q*-switching (PQS) mode. The maximum PQS output power was 2.67 W and the slope efficiency of 26.4%. As the absorbed pump power was increased from 4.78 W to 10.8 W, the pulse width of the T = 2%, T = 10%, and T = 25% output couplers decreased from 102.9 ns to 89.2 ns, 147.1 ns to 127.6 ns, and 173 ns to 150 ns while the repetition frequency increased from 10.2 kHz to 20.1 kHz, 9.3 kHz to 18.3 kHz, and 8.45 kHz to 16.66 kHz, respectively. The central wavelength was maintained at 2100.64 nm as the output couplers and operation modes were varied. Moreover, beam quality factor of the output laser was $M^2 = 1.1$.

Zhao et al. reported a high-power Ho:Y_2O_3 ceramic laser in-band pumped with a Tm-doped all-fiber MOPA at 1941 nm [571]. The Ho:Y_2O_3 ceramics were fabricated by vacuum sintering and HIP. The in-band pumping approach resulted in a 2117-nm laser with 24.6 W of output power, which was higher than those of other ceramics by nearly an order of magnitude. Therefore, Ho-doped sesquioxide ceramics are promising candidates for high-power solid-state lasers.

Spectroscopic profiles of Ho:$(Lu,Sc)_2O_3$ ceramics with 1.4 at% and 3 at% Ho^{3+} were evaluated according to Judd-Ofelt theory, which yielded intensity parameters of $\Omega_2 = 7.863$, $\Omega_4 = 1.843$, and $\Omega_6 = 0.531 \times 10^{-20}\,cm^2$ [572]. The $^5I_7$ state had a radiative lifetime of 10.63 ms, and the maximum emission cross-section (σ_{SE}) at > 2 μm was $3.41 \times 10^{-21}\,cm^2$, which corresponded to 2.101 μm. Under GaSb diode-pumping at 1.929 μm, the 1.4 at% Ho:$(Lu,Sc)_2O_3$ ceramic laser exhibited a 187-mW QCW output at 2.114–2.135 μm with 7.6% slope efficiency. When pumped with a 1.946-μm Tm^{3+} laser, 20.5-mW CW output power and 25% slope efficiency could be achieved. These Ho:$(Lu,Sc)_2O_3$ ceramics could be used to fabricate 2.1-μm lasers with broadband tunability and ultra-short pulses.

Transparent 2 at% Ho:CaF_2 ceramics exhibited five distinct absorption peaks at 448 nm, 536 nm, 642 nm, 1152 nm, and 1940 nm, which correspond to transitions from the $^5I_8$ ground state to the $^5G_5$, $^5S_2$, $^5F_5$, $^5I_6$, and $^5I_7$ excited states, respectively [460]. According to the emission spectrum at 640 nm, the $^5I_7 \rightarrow {}^5I_8$ transition is responsible for the major Ho^{3+} emission band at 2.03 μm, which was within the absorption bands between 1800 nm to 2100 nm. These transparent Ho:CaF_2 ceramics had a self-absorption process and thus could be used for 2.0-μm solid-state lasers.

3.1.1.3. Er-doped ceramic lasers. Transparent Er-doped ceramics have very low levels of quantum defects; thus, their laser behavior is due to the $^4I_{13/2} \rightarrow {}^4I_{15/2}$ and $^4I_{11/2} \rightarrow {}^4I_{13/2}$ IR transitions at 1.5 μm and 3 μm, respectively. For example, the strong absorption of Er:YAG at 1532.2 nm has been triggered by InP diode-laser pumping, which has adjacent hot-band transitions: $^4I_{15/2}(2) \rightarrow {}^4I_{13/2}(1)$ at 1532.1 nm and $^4I_{15/2}(4) \rightarrow {}^4I_{13/2}(3)$ at 1532.3 nm. Laser emission at 1647 nm with 7 W of output power was obtained using Er:YAG composite ceramic rods under QCW fiber-laser pumping at 1532 nm [573]. The device was constructed with three segments, which had 0 at%, 0.25 at%, and 0.5 at % Er^{3+}. The slope efficiency was 56.9% while the pulse width was 10 ms and the duty cycle was 5%. Shen et al. developed a similar solid-state laser with 1 at% Er:YAG ceramic rods; their device produced 1645 nm radiation with 13.8 W of output power and a slope efficiency of 54.5% [574]. Zhang et al. reported a 0.5 at% Er:YAG ceramic laser that exhibited CW emission at 1617 nm and had a slope efficiency of 51.7% [575].

A tunable Er:YAG ceramic laser was built using a volume Bragg grating with a relatively wide tuning range that covered three sections: (i) 1614.2 nm–1621.5 nm, (ii) 1629.3 nm–1635.1 nm, and (iii) 1639.2 nm–1649.2 nm [576]. A resonantly pumped eye-safe laser has also been made with transparent 0.5 at% Er:YAG ceramics, which were prepared using a combined SPS + HIP process [577]. The maximum slope efficiency of this laser was 31% and the optical-optical efficiency was 20%.

Dai et al. presented actively *Q*-switched CW Er:YAG ceramic lasers, which were resonantly dual-end-pumped by a 1532-nm fiber-coupled laser diode [578]. The maximum CW output power at 1645.3 nm was 1.48 W, the absorbed pump power was 12.72 W, and the slope efficiency was 19.2%. The device exhibited a maximum pulse energy of 0.84 mJ in the *Q*-switching regime when the pulse repetition rate was 100 Hz, the pulse duration was 48.03 ns, and the absorbed pump power was 10.51 W.

Huang et al. reported a fiber laser resonantly pumped *Q*-switched mode-locked Er:YAG ceramic laser with a graphene SA, which emitted 1645 nm [579]. The lasing parameters included mode-locked pulses with an average output power of 320 mW, *Q*-switching envelope temporal width of 10 μs, and mode-locking repetition rate of 83 MHz. The same authors also developed a Er:YAG ceramic laser that was passively *Q*-switched using a Cr:ZnSe crystal as the SA [580]. This laser produced 28.8-ns pulses at 1617 nm when the initial transmission of the SA was 80% and the laser was pumped with a 1532-nm Er,Yb-doped fiber laser with a maximum power of 12.4 W. The maximum power of the Er:YAG ceramic laser was 11.3 kW when the repetition rate was 2.17 kHz.

Transparent Er:Y_2O_3 ceramics have been used to develop a passively *Q*-switched 2.7-μm laser [581]. The average output power could reach 0.88 W when the absorbed pump power was 9.5 W, and the pulse

SDC EX. 1018 - 41/66

energy, pulse duration, and pulse peak power were 17.4 μJ, 63 ns, and 0.27 kW, respectively. When a SESAM with a modulation depth of 2.4% was used, the ceramic laser could generate 63-ns-wide pulses, which approached the limit imposed by the cavity length. As the modulation depth of the SESAM was increased, the pulse duration could be shortened to 29 ns. This was the first report of sub-100 ns pulses for continuously pumped 3-μm passively *Q*-switched lasers.

Wang et al. reported highly stable self-pulsed operation of a 2.74-μm Er:Lu_2O_3 ceramic laser pumped with a wavelength-locked narrow bandwidth laser diode at 976 nm [582]. Based on the pump power, the operating pulse repetition rate could be continuously tuned over the range of 126–270 kHz; when the absorbed diode pump power was 12.3 W, the repetition rate was 270 kHz for 183-ns pulses and the average output power approached 820 mW. The pulse-to-pulse amplitude fluctuation was maintained at < 0.7%. In the CW mode, the laser displayed an output power of > 1.3 W, and the slope efficiency was 11.9% with respect to the pump power at 976 nm.

In a separate study, Wang et al. demonstrated that 2.7-μm CW Er:Lu_2O_3 and Er:Y_2O_3 ceramic lasers with diode end-pumping can operate at room temperature [583]. These lasers exhibited maximum output powers of 320 mW and 611 mW, and slope efficiencies of 6.5% and 7.6%, respectively. The ceramic lasers displayed a red-shift in lasing wavelength. Under laser-diode pumping at 967 and 976 nm, the performance of the 15 at% Er:Lu_2O_3 ceramics was better than that of the Y_2O_3 ceramics.

A highly efficient 2.8-μm CW laser was also assembled with transparent Er:Lu_2O_3 ceramics [584]; the Er^{3+} concentration of these ceramics was 11 at% Er^{3+}. As this laser was pumped at 2.3 W, the slope efficiency was 29% and the output power was 2.3 W; this is the best performance that has been reported for 2.8-μm Er:Lu_2O_3 ceramic lasers to date. Furthermore, a passively *Q*-switched solid-state laser at 2.7 μm was constructed with Er:Lu_2O_3 ceramics [585] This study used a semiconductor saturable mirror based on a low non-saturable loss Bragg-reflector to achieve *Q*-switching. Pulses with a pulse-width of 70 ns could be generated and the average power was 692 mW, which corresponded to a pulse energy of approximately 9.8 μJ. The pulse-width could be shortened to 32 ns if the resonator design was modified to decrease the round-trip time.

3.1.1.4. Tm-doped ceramic lasers. The lasing emission of Tm^{3+} is in the range of 2.0 μm, when the host is YAG. Lasing can be achieved by pumping with a Ti:sapphire or diode laser, and is the result of the down-conversion from ($^3H_4$, $^3H_6$) to ($^3F_4$, $^3F_4$). To ensure efficient down-conversion energy transfer, the concentration of Tm^{3+} should be at least 6 at%. While the intrinsic quantum defect of this excitation process will damage the performance of the Tm:YAG ceramic lasers, the down-conversion efficiency and quasi-three-level scheme of the laser emission are critical factors for lasing performance. Nevertheless, slope efficiencies in the range from 20% to 42% have been achieved by CW Tm:YAG ceramic lasers at 2012 and 2015 nm [586–588].

A CW actively *Q*-switched laser was constructed with Tm:YAG ceramics [589]. When pumped with a fiber-coupled laser diode at 792 nm, the maximum output power of the device was 5.21 W with a slope efficiency of 46.1%, which was due to the improved beam quality. The pulse width was very short (107 ns), the pulse repetition frequency (PRF) was 0.5 kHz, the pulse energy was 1.44 mJ, and the peak power was 13.42 kW. Similarly, resonant pumping of 4 at% and 6 at% Tm:YAG ceramics with a 1617-nm Er:YAG laser generated CW emission at 2015 nm [590].

Transparent ceramics of $(Y_{3-x}Tm_x)Al_5O_{12}$ solid solutions were examined for laser applications [197]; specifically, a 5 × 5 × 3.5 mm^3 sample of $(Y_{2.82}Tm_{0.18})Al_5O_{12}$, which corresponds to 6 at% Tm, was tested. When the sample was end-pumped by a 785-nm Ti:sapphire laser, the maximum output power of the material was 725 mW at 2012 nm. Moreover, 36.2% slope efficiency and 19.9% optical-to-optical efficiency were observed.

Han et al. reported a passively mode-locked laser based on 6 at% Tm:YAG ceramics that were 2.7 mm long [591]. Stable mode-locked pulses were observed at a 109-MHz repetition rate when a semiconductor SA was used. The maximum output power was 116.5 mW at 2007 nm, the central wavelength, and the pulse duration was 55 ps. These experimental results suggest that Tm:YAG ceramics could be promising candidates for ultrafast lasers with high power densities and high efficiency outputs.

Liu et al. used 4 at% Tm:YAG ceramics to develop a high-efficiency narrow-band 2000-nm ceramic laser that combined the advantages of in-band pumping at 1617 nm and using a volume Bragg grating for wavelength selection [592]. When an output coupler with 10% transmission was used, the maximum output power was 1.64 W at 1999.9 nm with an incident pump power of 4.56 W, which corresponded to a slope efficiency of 50%; this is the highest slope efficiency that has been reported for 2000 nm Tm:YAG lasers to date.

Highly controllable optical bistability was observed in a *x* at% Tm:YAG ceramic laser, and was attributed to thermal-induced variation in the stability of the resonator [593]. The width of the bistable region could be altered over 0.8–6.3 W. With a nearly semi-confocal cavity configuration, the bistable region had a second lasing emission with a modulated shape and a broadened laser spectrum. The performance of the bistable laser was dependent on temperature.

Zhu et al. assembled an efficient diode-end-pumped CW Tm:YAG ceramic laser at 1962 nm by using a compact two-mirror cavity [594]. The laser oscillated at 1962 nm when the cavity loss was increased at 2016 nm, so as to limit the oscillation with the strongest laser gain. The study compared two output couplers by constructing single-wavelength lasers at 1962 and 2016 nm. At 6.59 W of absorbed pump power, the laser could achieve 2.06 W of output power at 1962 nm when it was kept at 15 °C; however, the maximum output power at 2016 nm was only 3.47 W. Furthermore, the 1962-nm laser had a slope efficiency of 37.8% and a conversion efficiency of 31.3%. The authors concluded that the 1962-nm laser could be a promising candidate for the applications measuring CO_2 and HBr gaseous molecules.

A diode-pumped CW (Tm, Ho):YAG ceramic laser reported by Liu et al. had dual-wavelength emission at 2090 and 2096 nm [595]. They achieved a maximum output power of ~1.2 W and a beam quality factor M^2 = 1.19 by using YAG ceramics doped with 3 at% Tm and 0.5 at% Ho. Moreover, the corresponding slope efficiency was 16.7% with respect to the absorbed pump power. When the absorbed pump power and transmittance of the output coupler were increased, the ceramic laser exhibited a gradual blue-shift in the emission wavelengths.

Transparent 2 at% Tm:Lu_2O_3 ceramics with fine grains (550 nm diameter) have been used for solid-state ceramic lasers [596], and Saarinen et al. studied a 1.97-μm ceramic disk laser based on 2 at% Tm:Lu_2O_3 ceramics [597]. The 2 at% Tm:Lu_2O_3 ceramic disk was a commercial product with a diameter of 3 mm and a thickness of 260 μm. The thinness of the gain disk resulted in inefficient pump light absorption. This issue has previously been addressed by using a complex multi-pass pump configuration, but Saarinen et al. tackled the problem by intracavity pumping with a 1.2-μm semiconductor disk laser. The proposed disk laser concept led to enhanced pump absorption and fully utilized the wide wavelength coverage of the semiconductor disk laser; however, the output power at 1.97 μm only reached 250 mW because of the heat spreader-less mounting scheme of the ceramic gain disk.

Wang et al. demonstrated a diode-pumped *Q*-switched Tm:Y_2O_3 ceramic laser with CW emission at 2050 nm and compared the lasing performance of Tm:Y_2O_3 ceramics doped with 1 at%, 2 at%, and 3 at% Tm^{3+} [598]. The ceramic lasers had optimal properties when the Tm^{3+} concentration was 2 at%. The maximum output power of the optimal laser was 7.25 W, the slope efficiency was 40% for CW operation, and the shortest pulse width was 115 ns at a 1-kHz repetition rate.

Jing et al. synthesized transparent "mixed" sesquioxide ceramics – $(Lu_{2/3}Sc_{1/3})_2O_3$ doped with 4.76 at% Tm – and used them to develop

SDC EX. 1018 - 42/66

ceramic lasers [599]. The maximum stimulated emission cross-section of the $^3F_4 \rightarrow {}^3H_6$ transition at 1951 nm was 7.15×10^{-21} cm^2, and the $^3F_4$ state had a radiative lifetime of 4.01 ms. Under diode pumping at 802 nm, the microchip Tm:$(Lu,Sc)_2O_3$ ceramic laser created 1 W of power at 2100 nm with a slope efficiency of 24%. The spectroscopic and laser properties of the Tm:$(Lu,Sc)_2O_3$ ceramics were compared to those of a Tm:$LuScO_3$ single crystal; the ceramics displayed much broader and flatter gain cross sections than the single crystal, which makes them more suitable for generating ultrashort pulses.

The same authors used "mixed" Tm:$(Lu_{2/3}Sc_{1/3})_2O_3$ to develop a ceramic laser that was mode-locked at approximately 2 μm using an InGaAsSb quantum-well semiconductor SA and chirped mirrors to compensate the dispersion [600]. A maximum average output power of 175 mW was observed for a 230-fs pulse and a 78.9-MHz repetition rate, with an output coupler of 3%. If a 0.2% output coupler was applied, 63-fs pulses could be generated at 2057 nm.

3.1.1.5. Yb-doped ceramic lasers. The spectroscopic properties of Yb^{3+}-doped ceramics ensure roughly pure four-level emissions by the $^2F_{5/2}(1) \rightarrow {}^2F_{7/2}(4)$ transition and quasi-three-level emissions by the very intense $^2F_{5/2}(1) \rightarrow {}^2F_{7/2}(3)$ transition. The laser emissions based on these transitions can be readily manipulated by controlling either the surrounding temperature or the temperature inside the pumped laser media, i.e., controlling the amount of heat that can be generated. Heat generation depends on the absorbed pump power and the transmission of the output mirror, which also influenced the intracavity intensity. For example, when the temperature is sufficiently low, the $f_t(3)$ coefficient can be decreased to the level generated by the four-level transition of $^2F_{5/2}(1) \rightarrow {}^2F_{7/2}(3)$.

Generally, Yb^{3+}-doped ceramic lasers with diode-laser pumping suffer from small absorption cross-sections in the broad $^2F_{7/2}(1) \rightarrow {}^2F_{5/2}(2)$ absorption band near 940 nm. The absorption line of $^2F_{7/2}(1) \rightarrow {}^2F_{5/2}(1)$ has a strong peak with a large cross-section, which could generate a low quantum defect laser emission. If the Yb^{3+}-doped ceramics are highly ordered, the absorption line would be very sharp and low temperatures would cause the absorption line to narrow. Therefore, diode-laser pumping is difficult; however, with the advancement of stabilized diode lasers, pumping this transition is possible at room temperature for many ceramic lasers made of transparent Yb^{3+}-doped ceramics. The small absorption cross-sections of Yb^{3+}-doped ceramic lasers can be enlarged by using ceramics with high concentrations of Yb^{3+} and/or increasing the path of pump radiation inside the laser media. Spectroscopic studies have revealed that the $^2F_{7/2}(1) \rightarrow {}^2F_{5/2}(1)$ absorption line can be broadened by adopting highly disordered transparent ceramics; however, this would inevitably decrease the peak absorption cross-section.

Because the electronic structure of Yb^{3+} is not complicated, lasers based on Yb^{3+}-doped ceramics have minimal issues with de-excitation. However, these lasers could potentially suffer from a reduction in emission lifetime and emission quantum efficiency. Moreover, the interaction between two excited Yb^{3+} ions may lead to cooperative processes if the ion concentration is sufficiently high. Such parasitic de-excitation processes generate extra heat, which could be substantially higher than the heat generated by quantum defects [601].

The first diode-end-pumped Yb:YAG ceramic laser was reported by Takaichi et al. [602]. The transparent Yb:YAG ceramics were prepared using vacuum sintering. The ceramic laser exhibited a CW output power of 345 mW with a slope efficiency of 26%. These results confirmed that transparent Yb:YAG ceramics could be used as highly efficient high-power diode-pumped solid-state lasers. The efficiency of these ceramic lasers could be further enhanced by optimizing the concentration of Yb^{3+}, the thickness of the gain medium, and the output coupling efficiency of the devices.

Dong et al. demonstrated a low-threshold highly efficient CW solid-state laser that was assembled with transparent Yb:YAG ceramics, and the beam quality of this laser approached the diffraction limit at room temperature [603]. Dual-wavelength operation at 1030 and 1049 nm with 5% transmission of the output coupler was obtained by varying the pump power intensity. Under CW laser-diode pumping, the 1-mm thick plate of 9.8 at% Yb:YAG had slope efficiencies of 79% and 67% at 1030 and 1049 nm, respectively. This study also evaluated the effect of pump power on the emission spectra of the lasing device under dual-wavelength operation. The outstanding performance of the laser suggested that Yb:YAG ceramics are potential candidates for high-power solid-state lasers.

Nakamura et al. assembled an efficient Yb:YAG ceramic laser with high power at room temperature [604]. The Yb^{3+} concentration of the Yb:YAG ceramic was 9.8 at% and a 1-mm thick sample was used as the gain medium. The ceramic laser had a pumping power of 13.8 W, an output coupler of T = 10%, and a cavity length of 20 mm; with these parameters, the CW output power was 6.8 W and the slope efficiency was 72%. This Yb:YAG ceramic laser was the first tunable solid-state laser based on transparent Yb:YAG ceramics to be reported; it was continuously tunable over 1020.1–1083.6 nm, with 63.5-nm spectral tunability for T = 1% at a maximum output power of 1.6 W.

A high-power CW laser based on transparent Yb:YAG ceramics was also developed by Hao et al. [605]. This laser was pumped at 968 nm by a fiber-pigtailed laser diode with a fiber core diameter of 400 μm. The transparent Yb:YAG ceramics were prepared by a solid-state reaction at 1780 °C and vacuum sintering, using commercial powders of Al_2O_3, Y_2O_3, and Yb_2O_3 as the precursors and adding MgO and TEOS as sintering aids. The performance of different Yb^{3+} concentrations was evaluated using a conventional end-pump laser cavity that consisted of two flat mirrors with output couplers of different transmissions. The optimal Yb^{3+} concentration was determined to be 5 at%; the laser based on this ceramic achieved a CW laser output with an average power of 40 W and an M^2 factor of 5.8 at an incident pump power of 120 W.

Zhou et al. proposed a highly efficient diode-end-pumped femtosecond laser based on transparent Yb:YAG ceramics [606]. When this device was pumped with a 968-nm fiber-coupled diode laser, a 1.9-W mode-locked output power was achieved at a 64.27-MHz repetition rate and an absorbed pump power of 3.5 W, which corresponded to a slope efficiency of 76%. Furthermore, a 418-fs pulse was observed at the central wavelength, 1048 nm.

Pirri et al. studied the lasing performance of two solid-state Yb:YAG lasers (10 at% and 20 at% Yb^{3+}) under QCW laser pumping [607]. The laser behavior was closely related to the density of Yb^{3+} at the excited level, and both the maximum output power and efficiency were nearly independent of the Yb^{3+} concentration at the low population inversion density. The device based on the 20 at% Yb:YAG ceramics exhibited a high output power, 8.9 W, which corresponded to a slope efficiency of 52% relative to the incident pump power. However, at high population inversion density, the laser output of the 20 at% device abruptly decreased with increasing pump power, which was ascribed to the onset of a nonlinear loss mechanism. The experimental observations were analyzed using numerical simulations to elucidate the inversion density and temperature distribution profile. Luo et al. went on to achieve CW lasing at 1030 nm using Yb:YAG ceramics by pumping with a 940-nm fiber-coupled laser diode; the slope efficiency of this laser was relatively high, 62.7% [608].

Agnesi et al. compared the spectroscopic properties and laser performance of transparent Yb:YAG ceramics (5 at% and 10 at% Yb^{3+}) and single crystals (6 at% Yb^{3+}) [609]. The Yb:YAG ceramics had similar laser performance to the single crystals. Pumped with a fiber-coupled diode at 940 nm and 15.5-W absorbed power, the Yb:YAG ceramic laser offered a maximum output power of 5.1 W, which corresponded to 44.3% slope efficiency in CW operation. When using passive *Q*-switching with a Cr:YAG SA, 7-ns pulses with 4.4 W of power and a 48-kHz repetition rate could be generated.

The effects of temperature and dopant concentration on the thermal properties and laser performance of transparent Yb:YAG ceramics were

SDC EX. 1018 - 43/66

studied by Tang et al. [610]. In terms of optical properties, the absorption edge experienced a gradual red-shift while both the absorption coefficient of Yb^{3+} and fluorescence lifetime increased as the Yb^{3+} concentration was increased. For the samples with 5 at% Yb^{3+}, the fluorescence intensity decreased and the peaks broadened as the temperature was increased from 100 K to room temperature. At room temperature, the thermal conductivity of the 5 at% sample was 10.7 W/m·K, and thermal conductivity decreased as the dopant concentration was increased. Both the 5 at% and 10 at% ceramics exhibited optimum emission at 1030 nm. When pumped with a 940-nm diode laser, the slope efficiency of the 5 at% Yb:YAG ceramic laser was as high as 49%, which was 41% of the efficiency of the 10 at% Yb:YAG ceramic.

Zhu et al. presented a diode-pumped (Er, Yb):YAG ceramic laser with 1.6-μm eye-safe emission and evaluated the effects of ceramic length, co-doping concentration, and operating temperature on the performance of the ceramic lasers [611]. At optimized conditions, the device exhibited a maximum output power of 222 mW when the absorbed pump power was 8.1 W; thus, the conversion efficiency was 2.74%. Moreover, the relationship between the laser emission at 1.05 μm and the transition of the Yb^{3+} ion was also examined, and the results suggested that there was resonant energy transfer from Yb^{3+} to Er^{3+}.

Luo et al. were the first to synthesize Yb^{3+}-doped yttrium gadolinium aluminum garnet (Yb:GdYAG) laser ceramics, which they obtained using solid-state reactive vacuum sintering [612]. The output power of the CW 5 at% Yb:GdYAG ceramic laser was 4.27 W, with a slope efficiency of 26.7%. Passive mode-locking was attempted by using a SESAM, and stable mode-locked pulses with a 4.4-ps pulses and a maximum output power of 3.75 W at 1030.4 nm were effectively produced. Xu et al. went on to use the these Yb:GdYAG ceramics to achieve passive mode-locking of diode-pumped ceramic lasers with a near isotropic cavity [613]. Mode-locking was observed in the two orthogonal principal polarization directions of the cavity, and mode-locked pulses exhibited similar characteristics for both polarization directions. Moreover, the pulses were temporally synchronized in a near-perfect manner.

Xu et al. developed Yb:LuAG ceramic lasers [614]. Lasers with uncoated Yb:LuAG ceramics had a maximum output power of 7 W for 13 W of absorbed pump power, which corresponded to 63% slope efficiency. Because the thermal conductivity of Yb:LuAG is higher than that of Yb:YAG, Yb:LuAG ceramics could be promising candidates for laser gain media in high-power solid-state lasers. The same authors also studied the effect of Yb^{3+} concentration on the laser performance of devices made of similar Yb:LuAG ceramics [256]. These ceramics had a large emission cross-section, 2.7×10^{-20} cm^2 at 1030 nm, and CW laser operation exhibited an output power of 7.2 W with a slope efficiency of 65%.

Zhu et al. further explored the applications of transparent Yb:LuAG (2.5 at% and 15 at% Yb^{3+}) ceramics for solid-state lasers [615]. With diode-pumping, the maximum output power of the CW lasers was 1.86 W, which corresponded to 53.6% slope efficiency. The CW laser emission could be tuned between 1030–1096 nm by inserting a prism in the cavity. With the aid of a SESAM, passive mode-locking was achieved and generated sub-picosecond pulses (933 fs) with an average power of 532 mW at a 90.35-MHz repetition rate.

Pirri et al. characterized the spectroscopic characteristics and laser behavior of transparent Yb:LuAG ceramics doped with 5 at%, 10 at%, and 20 at% Yb^{3+} [616]. The optimal Yb^{3+} concentration was 10 at%, which had a maximum output power of 8.7 W at 1029 nm. Furthermore, the 10 at% Yb:LuAG ceramic laser achieved 90.1% slope efficiency and demonstrated relatively large tunability. Conversely, the 20 at% Yb:LuAG ceramic laser could only deliver a maximum output power of 7.2 W at 1047.6 nm, and the slope efficiency was merely 47.4%. The reduced output power of the high Yb^{3+} ceramics was attributed to its high pump power, which was mainly caused by a nonlinear loss mechanism.

The optical properties and laser characteristics of transparent Yb:YAG and Yb:LuAG ceramics prepared by vacuum sintering have been compared by Ma et al. [617]. Comparing the optical transmittance spectra of the as-sintered samples, absorption peaks of the Yb:LuAG ceramics were blue-shifted in the visible region relative to those of the Yb:YAG ceramics. The emission intensity gradually decreased as temperature was increased. According to the fitting results of fluorescence decay curves, the Yb^{3+} lifetimes of the Yb:YAG and Yb:LuAG samples were 1.23 and 1.50 ms at 1030 nm, respectively. When pumped with a 970-nm diode laser, the slope efficiency of the 5.0 at% Yb:LuAG ceramic laser was 33% as the maximum laser output was 881 mW for 3.3 W of absorbed pump power. Comparatively, the 5.0 at% Yb:YAG device exhibited a relatively low slope efficiency of 24%. This result confirmed the above statements.

Ma et al. employed transparent Yb:$Y_3ScAl_4O_{12}$ (Yb:YSAG) ceramics to assemble a solid-state laser that could generate sub-100-fs pulses by using diode-pumped passive mode-locking [618]. Specifically, the laser device had a maximum output power of 51 mW and delivered stable mode-locked pulses that were 96 fs at the central wavelength, 1052 nm, with a 102-MHz repetition rate; these are the shortest pulses reported for mode-locked ceramic lasers to date.

More recently, Pirri et al. published a comprehensive study of the microstructure, spectroscopic properties, and laser performance of 10 at % Yb^{3+}-doped YSAG (Yb:$Y_3Sc_xAl_{5-x}O_{12}$, $x = 1.5$) ceramics [619]. The authors demonstrated that the absorption and emission bands of Yb^{3+} were broader in YSAG than in YAG; thus, Yb:YSAG is a superior material for solid-state lasers because it offers more flexible tunability and is capable of ultrafast pulse generation. Specifically, when pumped in a QCW regime at 936 nm, the Yb:YSAG ceramic laser exhibited a maximum output power of 6.3 W, which corresponded to 67.8% slope efficiency; in a CW regime, the maximum output power approached 5 W and the slope efficiency was 52.7%. With the given output coupler transmissions, the laser emission wavelengths were 1051 and 1031 nm in a free-running regime. Furthermore, laser emission was available between 991.5–1073 nm in a tunable cavity; this 81.5-nm range is the broadest tuning range ever reported for this material to the best of our knowledge.

Kong et al. reported a diode-pumped Yb:Y_2O_3 ceramic laser in 2003 [620]. This laser offered a CW lasing output of 0.75 W at 1078 nm when pumped with 11 W at 937 nm. The laser threshold was 4.7 W and the slope efficiency was 12.6% when using an output coupler of $R = 98\%$. Furthermore, a diode-end-pumped passively mode-locked solid-state laser based on Yb:Y_2O_3 ceramics has also been reported [621]. This laser achieved stable CW mode-locking, using GaAs wafers as both the SA and output coupler. The pulse width was 1.0 ps at a repetition rate of 125 MHz, and the average output power was 1.14 W at a pump power of 17.7 W.

Room temperature CW laser oscillations in the TEM_{00} mode at 1030 and 1075 nm were achieved by Yb:Y_2O_3 ceramic lasers with laser-diode pumping [622]. The maximum extraction efficiencies at 1030 and 1075 nm were 45% and 72%, respectively. Kong et al. also constructed a high-efficiency diode-end-pumped Yb:Y_2O_3 ceramic laser [623]. When this device was pumped with a 976-nm laser diode bar at 2.8 W of absorbed pump power, the CW output power was 0.73 and 1.74 W at 1040 and 1078 nm, respectively, which corresponded to slope efficiencies of 57.1% and 82.4%.

A similar solid-state laser made of 2.5 at% Yb:Sc_2O_3 ceramics fabricated by vacuum sintering was reported by Lu et al. [624]. Continuous-wave laser oscillations were observed at 1041 and 1094 nm, which corresponded to relatively broadband absorption. The combination of this broad absorption and the fluorescence spectra make Yb:Sc_2O_3 a promising candidate for short pulse generation using a laser-diode pump source.

Transparent Yb:CaF_2 ceramics have also been used to develop solid-state lasers [445]. The slope efficiency of the devices made with $Ca_{0.95}Yb_{0.05}F_{2.05}$ was 35% in the pulsed mode of laser operation and as

SDC EX. 1018 - 44/66

the concentration of Yb^{3+} was reduced to 3 at%, the thermal conductivity increased to 4.5 W/m·K while the decrease in slope efficiency could be neglected. This study was the first to demonstrate that hot-pressed Yb:CaF_2 ceramics could be used for solid-state lasers. Aballea et al. went on to examine the laser performance of solid-state lasers based on Yb:CaF_2 ceramics that were fabricated by a simple green synthetic route [625]. When the 4 at% Yb:CaF_2 ceramic laser was diode-pumped, the output power was 1.6 W, the optical-to-optical efficiency reached 25%, the slope efficiency was 43%, the gain was 1.4, and could be tuned between 1015–1060 nm.

3.1.2. Composite ceramic lasers

Conventional technologies are unable to further improve the performance of ceramic lasers; hence, composite ceramic lasers have been proposed. The performance and functionality of reported composite lasers are superior to those of conventional single-element lasers [539,544,626–633]. Composite lasers were initially fabricated by bonding single crystals with different compositions, and diffusion bonding is the most popular method. However, this approach can only bond components with flat surfaces and the resultant bonded structure is not sufficiently strong for some applications. Polycrystalline ceramics offer more flexibility when designing composite lasers because they are fabricated from powders, which allows their composition can be easily adjusted [2].

There are five categories of composite ceramic lasers: layered structures, cylindrical structures, waveguide types, core-shell fibers, and gradient types [634]. Layered structures and waveguide types have flat interfaces, which can be bonded in a similar fashion as conventional crystal composite lasers. The three other groups do not have flat bonding interfaces; therefore, lasers with these structures must be developed using new strategies. This section will discuss various composite ceramic lasers.

Liu et al. fabricated composite ceramic slabs of YAG/1.0 at% Nd:YAG/YAG using a solid-state reaction and vacuum sintering [635]. High-purity commercial powders of Al_2O_3, Y_2O_3, and Nd_2O_3 were used as the precursors and TEOS and La_2O_3 were added as sintering aids. At optimal conditions, the YAG and 1.0 at% Nd:YAG ceramics could be fully densified at the same temperature, which allowed the composite ceramics to be obtained directly without a bonding step. To fabricate the composite ceramics through one-step sintering, the Nd:YAG section was doped with 0.8 wt% TEOS whereas the pure YAG section was doped with 1.0 wt% TEOS and 0.8 wt% La_2O_3. The resultant composite sample had a uniform microstructure and there was a continuous transition region between the pure YAG and Nd:YAG whereas an interface is always present in single-crystal composites obtained by the conventional diffusing bonding method. After sintering at 1750 °C for 50 h, the composite ceramic samples had an average grain size of 10 μm and > 81% in-line transmittance at 400 nm. The composite ceramic rod (Ø3 mm × 82 mm) achieved an output power of 20.3 W for a pump power of 201 W, which corresponded to an optical-to-optical conversion efficiency of 10.1%.

Ma et al. produced Nd:YAG-based sandwich composite ceramics that demonstrated planar waveguide laser output [636]. These composite ceramics were prepared by tape casting and vacuum sintering; the fabrication process is illustrated in Fig. 46. The core layer was 2 at% Nd:YAG that was 0.1-mm thick, and the samples were highly transparent: > 80% in-line transmittance at 632 nm. Near-perfect bonding between the YAG and Nd:YAG layers was achieved by using a sintering aid to control the sintering behavior of the two components, as shown in Fig. 47. By using the quasi-monolithic Fabry–Perot cavity configuration, the composite ceramic laser achieved a maximum slope efficiency of 63% in the CW operation mode; the maximum output power and threshold absorbed pump power were 804 mW and 0.16 W, respectively.

Jia et al. constructed a diode-pumped composite ceramic disk laser from a YAG/Nd:YAG disk with 4-mm thick YAG layers on a 2-mm thick 1.0 at% Nd:YAG layer [637]. The maximum slope efficiency of the composite ceramic disk laser was 36.6%, which corresponded to a maximum optical-to-optical efficiency of 29.2%. Moreover, the device could deliver an average power output of 340 W at the absorbed pump power of 1.29 kW.

Li et al. reported both the theoretical design and experiment validation of YAG/Nd:YAG/YAG composite ceramic slab laser amplifiers [638]. Numerical analysis results were used as a reference to design the YAG/Nd:YAG/YAG composite ceramic slabs with two doping concentrations. The composite ceramic slab laser amplifier exhibited a double-pass extracted power of 7.08 kW and a high optical-to-optical conversion efficiency, 39.2%, at a total diode pump power of 18.06 kW. At the double-pass extracted power of 7.08 kW, depolarization of single-pass transmission was 3.2% and the peak and valley of the transmission wave-front distortion in the center 26.1-mm region were both less than 0.5 μm in the width direction of the laser slab.

Fu et al. fabricated sandwich structured YAG/Nd:YAG/YAG ceramics by dry pressing and vacuum sintering a mixture of oxide powders [558]. The Nd^{3+}-doped core components were either 1-mm or 5-mm long, and the doping concentrations were either 1 or 2 at%. The 5-mm long, 2 at% Nd:YAG sample had the smallest average grain size of the prepared ceramics. The optimal transmissions of the output coupler were 10% and 19% for the 1-mm and 5-mm long samples, respectively. The slope efficiencies were 12.9% and 24.4% when the 1-mm long samples were doped with 1 at% and 2 at% Nd^{3+}, respectively, and the slope efficiencies of the 5-mm long samples were 31.5% and 36.2% for 1 at% and 2 at%. Moreover, the devices with longer cores were subject to the thermal lens effect, which substantially reduced the beam quality. The length effect also manifested as thermally induced depolarization of the beam pattern.

Tsunekane and Taira developed a diode edge-pumped composite Yb:YAG microchip laser with high-power operation [639]. The composite microchip, which had a diameter of 5 mm and thickness of 0.3 mm, consisted of a single crystal Yb:YAG core covered with an undoped transparent ceramic pump light-guide with the same thickness. The high-reflection coated face of the microchip was bonded to a water-cooled heat sink with a thermally conductive glue to ensure efficient heat dissipation, and the pump light from a four-fold diode stack was directly coupled to the light-guide. When the input pump power was 866 W, the maximum output powers obtained at room temperature were 410 W (peak) and 285 W, which correspond to QCW (10 ms at 10 Hz) and CW operations, respectively.

Wang et al. designed a diode-pumped passively mode-locked laser using YAG/Yb:YAG composite ceramics [640]. Theoretical calculations predicted that the thermal effect problem could be reduced by the composite structure. When using a SESAM mode-locked laser at room temperature, 1.35-ps pulses with a maximum output power of 475 mW were generated. Moreover, a maximum laser output power of 240 W was achieved by a master oscillator power amplifier system that used the mode-locked YAG/Yb:YAG ceramic laser as the seeding oscillator.

Similarly, Esposito et al. synthesized two multi-layered YAG/Yb:YAG composite ceramics: YAG/10 at% Yb:YAG or YAG/10 at% Yb:YAG/YAG [641]. These compositions were selected in order to eliminate deformation and stresses in the composite structures, and thus reduce the thermal lensing effect of the final ceramic lasers. The samples were assembled using a linear lamination method, and were then treated with CIP and co-sintered under vacuum. Diffusion of Yb^{3+} ions across the interface of the doped and undoped sections was observed, which negatively affected the output power of the composite ceramic lasers; however, this was not quantitatively examined. The in-line transmittance of the composite approached 96% of the theoretical value, and the composite ceramic lasers exhibited a maximum output power of 5 W with a slope efficiency as high as 74.3%.

Tang et al. developed a composite ceramic laser with fifteen layers of YAG/Yb:YAG/YAG, which were prepared by tape casting and vacuum sintering [642]. The authors concluded that the optical

SDC EX. 1018 - 45/66

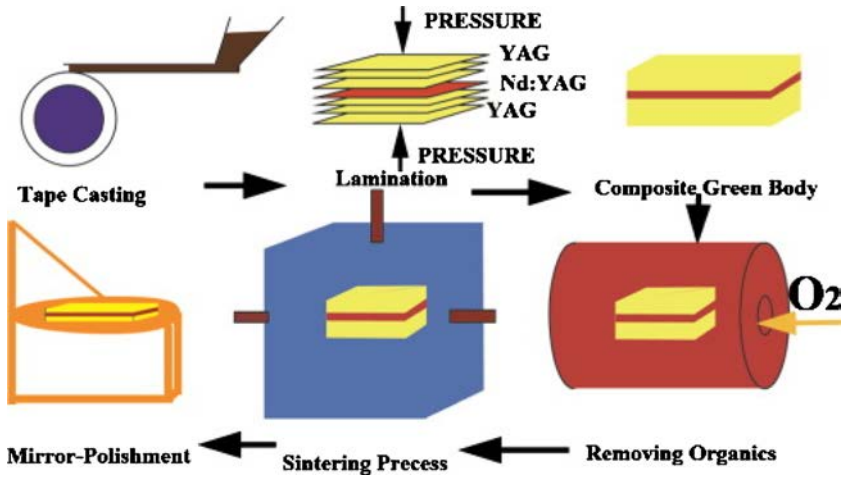

Fig. 46. Schematic diagram of the YAG/Nd:YAG/YAG fabrication process. Reused from [636], Copyright © 2015, Elsevier.

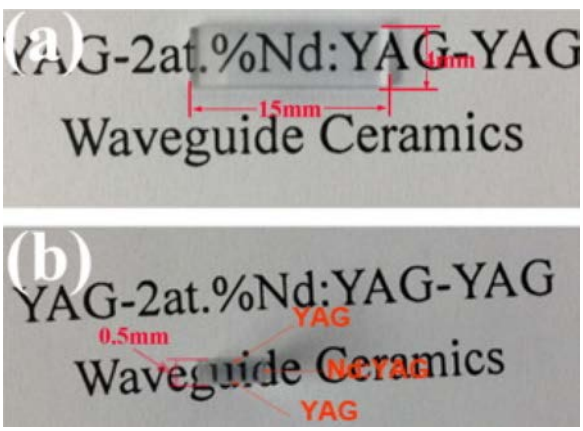

Fig. 47. Photographs of the Nd:YAG-based sandwich composite ceramic that demonstrated planar waveguide laser output: (a) top face and (b) side face. Reused from [636], Copyright © 2015, Elsevier.

transmittance of the multi-layered ceramics was improved by thermally annealing in O_2, which eliminated the lattice distortion. The composite ceramic laser had a threshold pump power of 5.5 W, an output coupler transmission of 6%, and a slope efficiency of 12%. When the absorbed pump power was 10 W, the maximum output power was 0.53 W.

Efficient laser-diode pumped picosecond self-*Q*-switched all-ceramic composite Yb:YAG/Cr^{4+}:YAG microchip lasers with 720-kW peak power have been developed by Dong et al. [643]. These composite ceramic lasers oscillated at stable single- and multi-longitudinal-modes with nearly diffraction-limited beam quality ($M^2 < 1.09$) because of the combined etalon effects in the Yb:YAG and Cr^{4+}:YAG components. The gain medium was a plane-parallel coated Yb:YAG/Cr^{4+}:YAG composite ceramic, and the Yb:YAG and Cr^{4+}:YAG layers were 1.2-mm and 1.5-mm thick, respectively.

Liu et al. designed and fabricated slabs of Yb:YAG ceramics clad with Cr^{4+}:YAG layers at the edges [644]. During fabrication of the composite ceramics, CaO was added as a charge compensator and the Cr:Ca molar ratio was 1:3; however, the addition of CaO resulted in abnormal grain growth and the formation of residual pores. The resultant ceramic had a lasing wavelength at 1030 nm, which was within the broad absorption of Cr^{4+} over 900–1100 nm, and the intensity of the Cr^{4+} absorption peak increased almost monotonically with the concentration of Cr^{4+}; the optimal concentration of Cr^{4+} was 0.35 at%. The composite ceramics had no interfacial issues and their optical transparency was comparable to that of their single-crystal counterparts.

Tang et al. also used tape casting to fabricate composite ceramics, YAG/RE:YAG/YAG (RE = Yb or Nd), for laser applications [642,645]. The composition of these composite ceramics could be easily adjusted and $(RE_xY_{1-x})_3Al_5O_{12}$ (x = 0.02 for RE = Nd and x = 0.2 for RE = Yb) was determined to be the optimal composition. All starting materials were commercial powders, which were made into casting slurries. The lasing emission of the YAG/Yb:YAG/YAG composite ceramic lasers was 1030 nm; the threshold absorbed pump power was 4.33 W, which corresponded to 12% slope efficiency and an output coupler transmission of 2.3%. The lasing emission of the YAG/Nd:YAG/YAG composite ceramic laser was 1064 nm. Compared to YAG/Yb:YAG/YAG, the YAG/Nd:YAG/YAG composite had a higher slope efficiency and output coupler transmission: 38% and 10%, respectively.

A colloidal co-casting process was developed by Kupp et al. to prepare multi-segment composite ceramic lasers [646]. A three-segment transparent composite rod (6.2-cm long with a diameter of 0.3 cm) was composed of (i) YAG, (ii) 0.25 at% Er:YAG, and (iii) 0.5 at % Er:YAG. At the segment-segment interfaces, the Er^{3+} concentration profile was sharp and the Er^{3+} concentration within the individual segment was not compromised. The in-line transmittance of the composite ceramic rod was 84% at the lasing wavelength, 1645 nm, which corresponded to a scattering loss as low as 0.4% cm^{-1}. The lasing performance of this Er:YAG composite ceramic rod was comparable to that of the Er:YAG single crystal rod.

Yao et al. observed efficient guided laser action of a diode-pumped YAG/Tm:YAG/YAG ceramic planar waveguide, which was prepared by nonaqueous tape casting and solid-state reactive sintering [647]. The maximum output power of the waveguide device was 173 mW at the center wavelength, 2013.76 nm, when the incident pump power was 10.3 W; thus, the slope efficiency was 3.0%. The beam quality measured in the horizontal direction at the highest output power was $M^2 = 1.5$.

Zhang et al. examined the spatial distribution of ions near the bonding interface of transparent YAG/Nd:LuAG composite ceramics obtained using a thermal bonding process [648]. The Lu^{3+} and Y^{3+} ions were substituted in the place of the other in dodecahedral symmetry sites near the bonding interface. According to X-ray photoelectron spectroscopy (XPS) and energy dispersive spectroscopy (EDS), the diffusion distance of Y^{3+} into the LuAG segment was approximately 35 μm, while that of Lu^{3+} into the YAG segment was approximately 5 μm; therefore, the diffusion coefficients of Y^{3+} and Lu^{3+} at 1750 °C (the sintering temperature) were estimated to be $D_Y = 2.43 \times 10^{-10}\ cm^2/s$ and $D_{Lu} = 0.56 \times 10^{-10}\ cm^2/s$, respectively. Furthermore, a solid solution of $Y_xLu_{3-x}Al_5O_{12}$ formed in the bonded area, which confirms coherent strong bonding between LuAG and YAG. Moreover, there was no obvious Nd^{3+} diffusion in the composite ceramics. However, this study did not investigate laser performance.

SDC EX. 1018 - 46/66

A more detailed study of transparent YAG/Nd:LuAG/YAG composite ceramics with a sandwich structure, prepared by tape casting and vacuum sintering, was conducted by Ma et al. [649]. The CW laser behavior was evaluated under both perpendicular and longitudinal diode-laser pumping at 808 nm. When using perpendicular pumping, the maximum output power was 1.13 W for the 17-W incident pump power, and the optical-to-optical efficiency was 6.6%. For longitudinal pumping, the CW laser output power increased linearly with the incident pump power, while the optical-to-optical efficiency was approximately 0.4%. Therefore, this planar ceramic waveguide could be a promising candidate for high-power scaling when using longitudinal pumping.

Ma et al. also developed a transparent YAG/15 at% Yb:LuAG/YAG composite ceramic planar waveguide [650]. Under 970-nm diode-laser pumping, the absorption efficiency of the waveguide was 85.4%. Moreover, the waveguide exhibited efficient CW laser operation at 1030.7 nm, with high beam quality and a Gaussian spatial profile. The maximum output power of the waveguide was 288 mW at the pump power of 4.69 W, and the slope efficiency and optical-to-optical conversion efficiencies were 9% and 5%, respectively. Based on these results, composite ceramic lasers are expected to be designed and fabricated combining and optimizing various transparent ceramics.

3.2. Lighting applications

3.2.1. Brief introduction

Transparent ceramics have found applications as envelopes in focused-beam short-arc lamps that use fillers because of their unique thermal and mechanical characteristics. Working temperatures are continuously increasing and conventional quartz cannot withstand these high temperatures; thus, transparent ceramics are promising candidates to replace quartz in this special application. Initially, coarse-grain translucent polycrystalline alumina (PCA) ceramics were used as envelopes in discharge lamps [651–653], and translucent PCA ceramics doped with MgO have been used by the lighting industry since the 1960s [654,655]. The translucent alumina ceramics used in metal-halide lamps are typically cylindrical or spherical-like tubes [656,657]. As discussed in Section 2.1.1, transparent PCA ceramics with fine grains can be obtained using the HIP sintering technique; thus, the illumination performance of PCA ceramics has significantly improved [49,651,652,658]. Furthermore, transparent ceramics based on other materials have also been used for lighting applications, such as AlON, YAG, Y_2O_3, and Dy_2O_3 [659–662]; these ceramics will be described in the upcoming sections.

Polycrystalline alumina ceramics could be transferred to single crystals (i.e., sapphire) using solid-state crystal conversion (SSCC) technology [663,664]. At sufficiently high temperatures, PCA samples doped with a certain concentration of MgO would undergo a microstructural transition from polycrystalline (multiple grains) to a single crystal (single grain), and thus from translucent to transparent. However, the residual pores in sapphires converted from PCA cannot be entirely removed; therefore, the conversion of PCA ceramics to sapphires that are of comparable quality to those grown from melts is still a technical difficulty that requires further research.

3.2.2. Fine-grained transparent Al_2O_3 ceramics

Polycrystalline alumina ceramics with submicron grain sizes and sufficiently high optical transparencies have been used in metal halide lamps [665]. The visible transparency of such PCA ceramics is approximately 70% of that of single crystal sapphire because of physical limitations [666]; however, the mechanical properties of these PCA ceramics are comparable to those of sapphires and PCA ceramics have high toughness because of their fine grains [49]. Moreover, PCA ceramics can adopt various shapes that cannot be obtained using sapphires; hence, PCA ceramics will eventually replace sapphires in lamp envelopes.

For lamp envelopes, the basic requirement of transparent ceramics is to possess high total and high in-line transmittances. While total transmittance is dependent on the absorption of the arc tubes, which is critical to the total lumen output, in-line transmittance is mainly determined by the scattering of the materials, which directly influences the luminance or brightness of the arcs. Therefore, a device could suffer from low total transmittance even if the in-line transmittance of the transparent ceramics is sufficiently high [667]. The total transmittance is usually characterized by placing a small light pipe inside the body of the lamp and recording the total integrated flux of light travelling through the tube walls.

Discharge vessels made of HIP-sintered Al_2O_3 ceramics with submicron grain sizes can have a total transmittance as high as 77.7%. This transmittance is much lower than that of the samples sintered with conventional techniques, which had an average grain size of 15 μm and a total transmittance of 99%. Nevertheless, the total transmittance of the HIP-sintered Al_2O_3 ceramics can be enhanced by post-annealing; for example, the total transmittance of HIP-sintered ceramic vessels was increased to 90.5% when the samples were thermally annealed in air at 1025–1150 °C for up to 4 h.

3.2.3. AlON ceramics

Aluminum oxynitride ceramics with high optical transparencies have been widely reported in the open literature [416,668–674]. These AlON ceramics have similar mechanical and thermal properties to PCA ceramics and their in-line transmittance in the visible region is comparable to that of single crystal sapphire [675]; thus, AlON ceramics are also suitable for applications in metal halide lamps. Unfortunately, the stability region of the AlON phase relative to the N_2 partial pressure is very narrow above 1640 °C, which limits the viability of AlON ceramics for these applications. However, this issue can be mitigated by doping with MgO, which stabilizes the AlON phase [676–678]. In order to use AlON ceramics in projection lamps, the oxidation of AlON in air at temperatures ≥ 1200 °C should be addressed [677].

3.2.4. YAG ceramics

Transparent YAG ceramics have advantages for applications in lamp envelopes, such as outstanding optical transparency and high mechanical strengths [659,660]. However, YAG ceramics have lower corrosion resistance to the rare earth halide fillers than PCA ceramics; for example, YAG may react with rare earth halides (ReI_3), such as TmI_3, after prolonged use. Once YI_3 is formed, there would be emission lines of yttrium and there would be a color shift and voltage drop in the lamps. Therefore, less corrosive fillers must be available if transparent YAG ceramics are to be used in arc lamps.

3.2.5. Rare earth oxide (Re_2O_3) ceramics

Transparent rare earth oxide ceramics have potential as tube materials for beamer lamps; for example, Dy_2O_3 is much less reactive with metal halide fillers than YAG ceramics, they are highly transparent, and they have high mechanical strength as well as high thermal stability [662]. Compared with PCA ceramics, Dy_2O_3 has relatively low emissivity and high efficacy because of its long infrared cutoff; the intrinsic absorption bands of Dy_2O_3 are between 275–450 nm. Since Dy_2O_3 has a similar free energy of formation as Tm_2O_3, Dy_2O_3 is relatively stable when in contact with molten salts.

3.2.6. Solid-state phosphors

Inorganic materials that emit red light were first discovered more than 50 years ago and a large number of color sources have been developed since [679]. The first bright blue light-emitting diode (LED) was invented in 1993 by Nakamura, who became a Nobel Prize laureate in Physics in 2014. When a blue LED based on gallium nitride (GaN) is covered with a yellow phosphor, white light is emitted; this combination is similar to UV-emitting fluorescent tubes and compact fluorescent lamps that are coated with a phosphor, which generates white light.

SDC EX. 1018 - 47/66

Such white LEDs can last for as long as 100 kilo-hours, and the best white LEDs have an efficiency of 30% and an efficacy of 100 Lm/W. The market value of GaN-based LEDs was over $4 billion in 2014 and is expected to continue increasing [680].

However, non-thermal efficiency "droop" occurs when the LED current density is continuously increased. This efficiency droop limits the output power per unit area, which has become a challenging issue for solid-state white lighting applications. Because high efficiency operation requires low current densities, there must be a large number of device dies in order for the high-power white light illumination systems to operate at peak efficiency. In contrast to LEDs, the efficiency of laser diodes (LDs) does not suffer from non-thermal droop above a certain current density threshold. Therefore, LDs can achieve high efficiencies at very high current densities, which results in very high output power per unit area [681]. Thus, LD white lighting is widely acknowledged to be the next generation of lighting technology, although it is still at its infant stage.

As the power density of LD excitation is increased, the lighting device will generate more and more heat. Conventional powder phosphors cannot be used in this case because of their low thermal conductivities and the reduction in internal quantum efficiency that results from the increase in temperature. Complex cooling strategies can be used to limit the temperature; however, this limits the power of the LDs. Furthermore, non-oxide-based powder phosphors irreversibly degrade as the temperature is increased, which limits their practical applications in many areas [682].

Bulk phosphors have been used to address these temperature problems because of their superior temperature behavior. Firstly, bulk phosphors have high thermal conductivity, which promotes cooling efficiency, prevents overheating, and thus enables size shrinkage and cost reduction. Furthermore, the "droop" in quantum efficiency caused by the rise in temperature is avoided; the efficiency of LDs with bulk phosphors can exceed 0.9 up to 300 °C. Therefore, bulk transparent phosphors offer much brighter and more powerful lighting sources compared to conventional powdery phosphors, and are expected to be the next generation of white-light phosphors. Two types of bulk transparent phosphors are candidates for white-light devices: (i) single crystals and (ii) transparent ceramics. As discussed throughout this review, ceramics offer many advantages over single crystals.

Nishiura et al. studied the properties of transparent Ce:YAG ceramics for use as phosphors for white LEDs [683]. The $Ce_{0.003}Y_{2.997}Al_5O_{12}$ phosphors were derived from powder that was synthesized by chemical coprecipitation, and the in-line transmittance of these Ce:YAG ceramics was 70–87% at 800 nm. The samples exhibited a broad emission band centered at 530 nm, which was ascribed to the 5d → 4f transition of Ce^{3+}, and both the absorption coefficient and emission intensity of Ce^{3+} increased with increasing thickness of the Ce:YAG ceramics. As the sample thickness was gradually increased, the Ce:YAG ceramic phosphors experienced a color shift from blue to yellow under 465-nm LED excitation; thus, their emissions crossed the theoretical white point in the chromaticity diagram. White light was produced by Ce:YAG samples what were 0.4–0.6 mm thick, and the luminous efficacy of the white LED device reached 73.5 Lm/W when complemented with the blue light emitted by InGaN LEDs. The performance of this device was similar to that of commercial white LEDs.

Wei et al. used transparent $(Y_{1-x}Ce_x)_3Al_5O_{12}$ (x = 0.0005–0.0020) ceramics to generate white light through excitation with commercial blue LEDs [684]. The photoluminescence properties and color emission of the ceramic phosphors were strongly dependent on the Ce^{3+} concentration. and the color emission also depended on the thickness of the ceramic phosphor. At optimal conditions, the maximum luminous efficacy exceeded 93 Lm/W at a low correlated color temperature (CCT) of 4600 K. This luminous efficacy was superior to that of devices fabricated with commercial phosphor powders, which demonstrates that transparent ceramics have a bright future as solid-state phosphors for lighting applications.

The influences of Ce^{3+} concentration and sample thickness on the white-LED performance of transparent Ce:YAG ceramics were evaluated by Hu et al. [685]. Both factors can be used to tailor the CIE color coordinates of LED devices in order to obtain white light. The color rendering index (CRI) of the LED devices increased as the Ce^{3+} concentration and sample thickness were reduced. Moreover, the effect of Ce^{3+} concentration on CRI was more pronounced than that of sample thickness. This observation offered a useful reference for modifying the luminescence properties of transparent ceramic phosphors and improving the CRI of white LEDs.

Zheng et al. demonstrated that transparent (Dy^{3+}, Ce^{3+}):YAG ceramics can also be used as white-light phosphors [686]. The transparent (Dy^{3+}, Ce^{3+}):YAG ceramics – $(Dy_{0.03}Ce_xY_{0.97-x})_3Al_5O_{12}$, with x = 0, 0.0001, 0.001, and 0.01 – were prepared by vacuum sintering commercial oxide powders. A commercial UV-LED chip (365–370 nm) was used for electroluminescence characterization; the dimensions of the LED package were 10 × 10 × 2 mm^3, and the LED module was mounted on a metal slug for heat dissipation. When the samples were directly excited with the UV-LED, they emitted light that could be tuned from pure white to slightly yellow by varying the Ce^{3+} content.

The $(Dy_{0.03}Ce_{0.0001}Y_{0.9699})_3Al_5O_{12}$ ceramics were pore-free microstructures with high optical transparency. The luminescence color of the transparent $(Dy_{0.03}Ce_xY_{0.97-x})_3Al_5O_{12}$ ceramics was related to the spectral energy distribution of the emitted light; the CIE color coordinates calculated from the emission spectra are shown Fig. 48a and b. The results indicated that the color coordinates were dependent on both the Ce^{3+} concentration and the excitation wavelength. As the Ce^{3+} concentration was increased, the luminescence color shifted from white to yellow as the energy transfer between Dy^{3+} and Ce^{3+} became gradually increased. Photographs of the $(Dy_{0.03}Ce_xY_{0.97-x})_3Al_5O_{12}$ phosphors on the UV-LED chips are shown in Fig. 48c (1–4), and photographs of the ceramics illuminated by the LED chip are shown in Fig. 48c (5–8). The photoluminescence quantum yields of the optimal $(Dy_{0.03}Ce_{0.0001}Y_{0.9699})_3Al_5O_{12}$ samples were 32% for white light (x = 0.0001) and 62% for yellow light (x = 0.001). This study concluded that transparent (Dy^{3+}, Ce^{3+}):YAG ceramics can be used to produce white–yellow light when combined with commercial UV-LEDs, and the color of the light can be controlled by the Ce^{3+} content.

Feng et al. studied the spectroscopic properties of transparent Ce:YAG ceramics codoped with Pr^{3+} and Cr^{3+}, and evaluated their potential for white LED applications [687]. The Pr^{3+} and Cr^{3+} dopants were added to expand the spectrum of Ce:YAG and the resultant ceramics had a high CRI as the luminescence spectrum ranged from 500 to 750 nm, covering nearly the whole visible light region. Furthermore, the ceramics had a high luminous efficiency. By optimizing the concentrations of Ce^{3+}, Pr^{3+}, and Cr^{3+} – YAG:Ce/Pr/Cr ($Y_{2.9865}Ce_{0.006}Pr_{0.0075}Al_{4.9875}Cr_{0.0125}O_{12}$) – high-quality white light was generated when the ceramic phosphor was excited by commercial blue LED chips. Under 450-nm LED excitation, the color coordinates of the YAG:Ce/Pr/Cr ceramics varied from cold white light to warm white light, and the maximum luminous efficiency, 89.3 Lm/W, was achieved when the CRI approached 80. Energy transfers from $Ce^{3+} \rightarrow Pr^{3+}$ and $Ce^{3+} \rightarrow Cr^{3+}$ were observed in this triple-doped ceramic phosphor. The transparent luminescent ceramics developed in this study are promising for high-power white-LED applications.

Hu et al. studied the luminescence characteristics of transparent Ce^{3+}-doped Gd^{3+}-admixed YAG ceramics [688]. Samples of Ce^{3+}-doped (Gd, Y)$_3Al_5O_{12}$ with 0–80 mol% Gd^{3+} were prepared by combining the conventional solid-state reaction method with vacuum sintering. The introduction of Gd^{3+} had a strong effect on the band structure of the crystals and the energy state of Ce^{3+} in the ceramics. The ceramic phosphors with optimal Gd^{3+} content exhibited outstanding color coordinates and CRI, which are promising for the generation of warm white light.

Zhang et al. prepared high-quality Ce:YAG ceramics by tape casting and vacuum sintering in order to enhance light extraction from high-

SDC EX. 1018 - 48/66

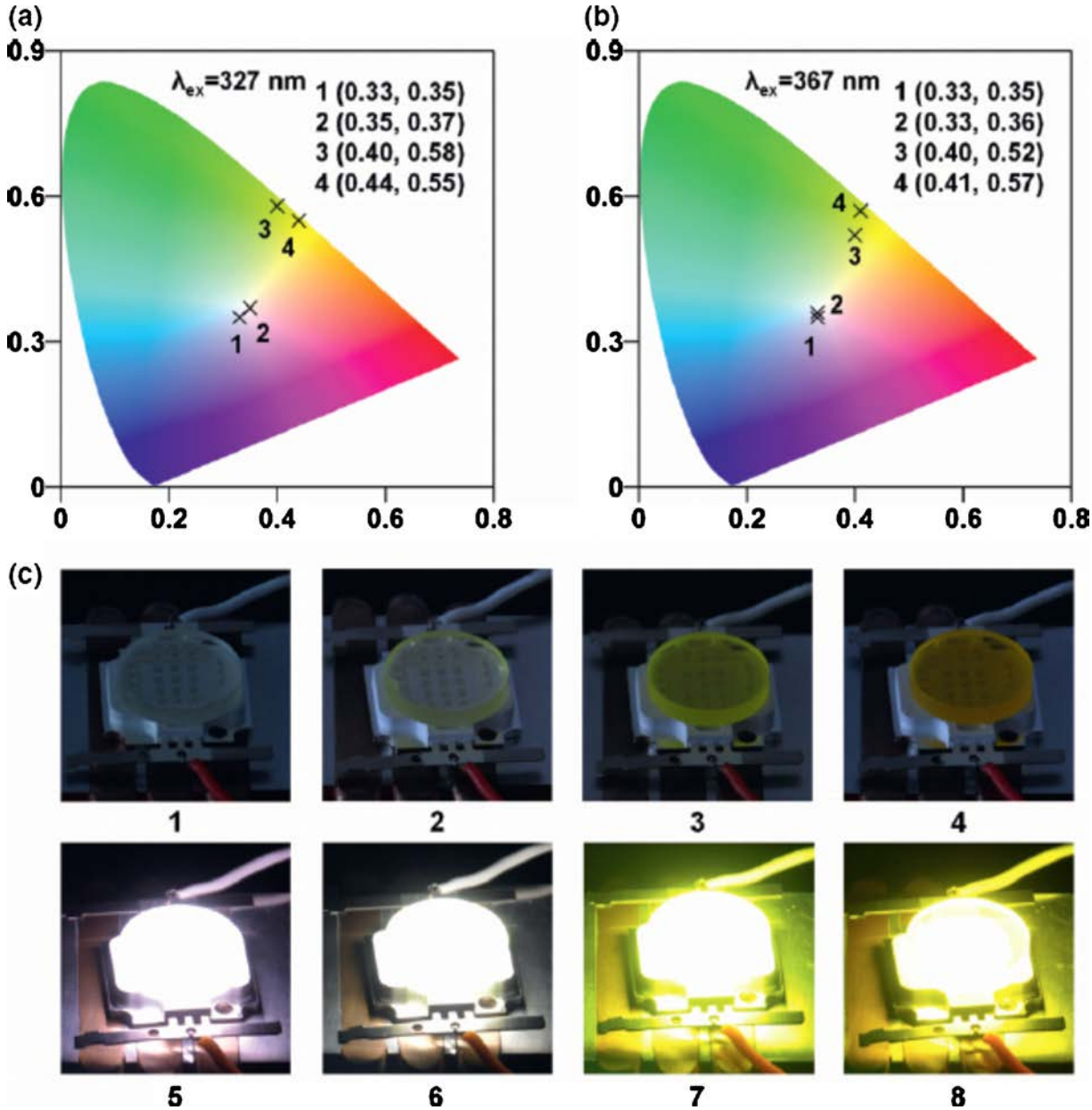

Fig. 48. CIE chromaticity coordinates of the $(Dy_{0.03}Ce_xY_{0.97-x})_3Al_5O_{12}$ ceramics under two excitation wavelengths: (a) λ_{ex} = 327 nm and (b) λ_{ex} = 367 nm. (c) Photographs of the transparent ceramic phosphors and resultant UV-LEDs. The marks and images labeled (1, 5), (2, 6), (3, 7), and (4, 8) represent the samples with x = 0, 0.0001, 0.001, and 0.01, respectively; the images labeled 5, 6, 7, and 8 depict the UV-excited samples (365–370 nm). Reused from Ref. [686]. Copyright © 2015, John Wiley & Sons.

power LED chips [689]. Several factors, including surface texture, sample thickness, and the assembly mode, affected the lighting performance of these ceramics. The ceramics were fully densified, with a pore-free microstructure and an average grain size of 5.4 μm. Surface texture was formed by convex and concave impressions, which enhanced the photoluminescence by approximately six times. The forward light extraction was enhanced by 22.5% as the result of the light trapping effect and the reduced total internal reflection (TIR) effect in the SP-Up mode assembled device. Using a 0.6-mm thick sample of the Ce:YAG ceramic, the resultant color coordinates were (0.3393, 0.3512), which were close to white light. High efficacy (93.0 Llm/W) and low CCT (4144 K) were achieved in the simple remote mode when the ceramic sample was 0.8-mm thick.

The extraction efficacy and emission color were improved by using planar transparent Ce:YAG ceramics with special surface texture and assembly mode, and the resultant ceramics exhibited great potential for large-scale industrial applications of high-power white LEDs. While the development of a simple approach to enhance the forward light extraction of optical devices is still a challenge, these planar transparent Ce:YAG ceramics could be promising candidates for the next generation of high-power white LEDs because of their excellent optical properties and high thermal conductivity.

Ueda et al. utilized transparent Ce^{3+}/Cr^{3+}-doped $Y_3Al_{5-x}Ga_xO_{12}$ (x = 2.5, 3.0, 3.5) ceramics as bright persistent phosphors with green luminescence (i.e., 5d → 4f of Ce^{3+}) under blue-light excitation [690]. After blue-light excitation for 5 min, the (Ce^{3+}, Cr^{3+}):$Y_3Al_2Ga_3O_{12}$ (YAGG) ceramics demonstrated persistent luminance that was approximately 3900 times stronger than that of their Ce^{3+}:YAGG counterparts and even stronger than that reported for typical compact (Eu^{2+}, Dy^{3+}):$SrAl_2O_4$ powders. The superior performance of these (Ce^{3+}, Cr^{3+}):YAGG ceramic phosphors was readily attributed to the generation of efficient carrier traps and effective excitation of the

SDC EX. 1018 - 49/66

interior material. Therefore, these garnet ceramics would be suitable persistent phosphors for solid-state lighting applications.

The photoionization threshold between the $5d_1$ energy level of Ce^{3+} and the bottom of the conduction band (CB) with photo-stimulation can be reduced by substituting the [B] and (C) sites of the $< A >_3[B]_2(C)_3O_{12}$ garnet matrix with Ga^{3+}, where < A >, [B], and (C) represent the cations in the dodecahedral, octahedral, and tetrahedral sites, respectively [691]. The Cr^{3+} ions can serve as an electron trap with an ideal trap depth to facilitate persistent luminescence at room temperature. Moreover, the trap depth, i.e., the energy gap between the bottom of the CB and the electron trap, can be adjusted by controlling the concentration of Ga^{3+}.

The same authors monitored the effect of ceramic thickness on the luminescence performance of transparent (Ce^{3+}, Cr^{3+}):YAGG ceramics [692]. They confirmed that the transparent phosphors delivered much brighter persistent luminescence than their opaque counterparts because of the volumetric transparency effect of transparent materials. Specifically, the persistent luminescence intensity of the transparent (Ce^{3+}, Cr^{3+}):YAGG ceramic phosphor approached 2 mcd/m^2, which is almost two times that of the compacted pellet made of (Eu^{2+},Dy^{3+}):$SrAl_2O_4$ commercial powder.

Ueda et al. also synthesized transparent (Ce^{3+}, Cr^{3+}):$Gd_3Al_2Ga_3O_{12}$ ceramics from oxide powders using the conventional solid-state reaction, and these ceramics demonstrated yellow persistent phosphor performance [693]. The color coordinate of the persistent luminescence was (0.394, 0.557), which correspond to an authentic yellow color. This yellow persistent luminescence was attributed to the 5d → 4f transition of Ce^{3+} under blue-light excitation at 460 nm and UV excitation, and the luminance intensities after blue excitation for 1, 5, and 30 min were 731, 63, and 8 mcd/m^2, respectively. The persistent luminance of the transparent (Ce^{3+}, Cr^{3+}):$Gd_3Al_2Ga_3O_{12}$ ceramics was much stronger than that of opaque ceramics because the effective excitation of the phosphor interior was directly enabled by the high optical transparency.

The spectroscopic characteristics and energy resolution of transparent Ce:LuAG ceramics were studied by Ma et al. in order to determine whether they have potential as green-yellow LEDs [694]. The XPS spectra revealed the co-presence of Ce^{3+} and Ce^{4+} ions in the ceramics and energy level splitting of Ce^{3+} in the LuAG host was monitored using the broad band emission over 500–700 nm, which is caused by electron transitions from $5d^1$ excited levels (^2D) to the 4f ground state ($^2F_{5/2}$, $^2F_{7/2}$). The fluorescence lifetimes of these samples were 50–60 ns at 540 nm while the energy resolution was 12% at ^{22}Na (511 keV). When coupled with InGaN-GaN LED chips, a maximum CRI of 55.8 and a relatively high luminous efficacy of 223.4 lm/W could be achieved, which suggests that the transparent Ce:LuAG ceramics could be used for white LEDs.

Boyer et al. investigated transparent $SrREGa_3O_7$ (RE = Eu, Gd, Tb, Dy, Ho, Er, Tm, Yb, and Y) melilite ceramics as potential phosphors for tunable solid-state lighting applications [695]. The transparent $SrREGa_3O_7$ melilite ceramics were converted from glasses through congruent crystallization at an appropriate temperature. The transparent $SrGdGa_3O_7$ ceramics doped with Dy^{3+} or Tb^{3+}/Eu^{3+} demonstrated white light emission under UV excitation. The method developed in this study offers a new, cost-effective opportunity for obtaining transparent ceramics for phosphor applications.

Sun et al. prepared transparent $(Pr_xY_{0.9-x}La_{0.1})_2O_3$ (x = 0.005, 0.01, and 0.05) ceramics with potential applications as white LEDs as well as scintillators [696]. In this ceramic, the Pr^{3+} ion was able to down-convert UV light to blue emissions, and the strong excitation band at 430–520 nm, which was accessed by emissions of InGaN blue chips with λ_{em} = 450–470 nm, generated bright red emission at 630 nm. The overall luminescence characteristics suggested that the transparent $(Pr_xY_{0.9-x}La_{0.1})_2O_3$ ceramic phosphor with x = 0.005 was the most promising as UV-based InGaN blue chip white light-emitting diodes.

Wen et al. fabricated and characterized Pr^{3+}-doped Ba(Sn,Zr,Mg,Ta)O_3 (Pr:BMT) transparent ceramic phosphor [697]. The obtained Pr:BMT ceramics had 59% in-line transmittance at 650 nm and emitted red light at 650 nm when excited with blue light at 447 nm. More importantly, the ceramic could still be used at 110 °C and the luminous intensity at this temperature was greater than 70% of its room temperature intensity, which indicates high thermal stability. The activation energy of this ceramic phosphor was 0.17 eV and its efficiency was two times that of its powder counterpart. These characteristics make Pr:BMT ceramics promising phosphors for white-LED applications.

Li et al. developed a transparent MgAlON ceramic phosphor activated with Mn^{2+} for green emissions [698]. The ceramic composition was 3 at% Mn:$Mg_{0.21}Al_{2.57}O_{3.80}N_{0.20}$ (Mn:MgAlON), which was derived from the precursor powder by combining pressure-less sintering and HIP treatment. The Mn^{2+} ions were entirely incorporated into the spinel lattice by occupying the tetrahedral sites. The ceramics were highly transparent in the UV–vis region, their in-line transmittance was 82% at 800 nm, and they had a strong green emission at 513 nm under excitation at 445 nm. Moreover, this ceramic phosphor possessed higher green color purity, higher internal quantum efficiency (47%), and lower thermal quenching than its powder counterpart. Therefore, this unique green solid phosphor could be a potential candidate for high color rendering and high-power white light-emitting diodes.

Li et al. proposed a Al_2O_3–Ce:YAG ceramic phosphor in which yellow-emitting Ce:YAG particles were distributed in a non-luminescent Al_2O_3 matrix with a relatively high thermal conductivity [699]. Because the thermal conductivity of the Al_2O_3 matrix was 18.5 W/m·K, the ceramic phosphor had a fairly high thermal stability. Moreover, the highly crystallized Ce:YAG particles (5–20 μm) demonstrated a high external quantum efficiency of 76% under 460-nm excitation while the fine Al_2O_3 grains (0.5–2 μm) minimized scattering related to birefringence and thus ensured a sufficiently high in-line transmittance of 55% at 800 nm. When the phosphor was excited with 445-nm blue laser diodes, no luminescence saturation was observed at power densities up to 50 W/mm^2; hence, these ceramic phosphors are suitable for high-power solid-state laser lighting applications.

Wieg et al. explored transparent Ce:AlN ceramics for potential solid-state laser lighting, taking the high thermal conductivity of AlN into account [700]. The Ce:AlN ceramics displayed overlapping photoluminescence emissions across the majority of the visible range, which resulted in white light emission under 375-nm excitation without color mixing. The photoluminescence was ascribed to the synergistic effect of intrinsic defect complexes in the AlN matrix and the electronic transitions of Ce^{3+}. Furthermore, the peak intensity could be changed by controlling the Ce^{3+} concentration as well as the processing parameters.

3.3. Scintillating applications

Scintillators are luminescent materials that are mainly used to detect radiation and thus have applications in high-energy physics research, astrophysics, spectrometers, medical imaging machines, industrial nondestructive detection facilities, oil-well logging, and land security monitoring, to name a few [701–711]. In these applications, scintillators act as primary radiation sensors as they emit visible light when they are excited by high-energy photons. Solid scintillators are reflectively coated to direct the emitted light onto photodiodes or photomultiplier tubes, wherein they are photoelectrically converted to electrical signals. In order for a material to be an efficient and effective scintillator, it must satisfy various requirements.

In terms of materials, there are six groups of scintillators: (i) single-crystal scintillators [712–718], (ii) ceramic scintillators [719,720], (iii) glass scintillators [721–724], (iv) powdery scintillators [725–728], (v) polymeric plastic scintillators [729–734], and (vi) inert gaseous scintillators [735,736]. Scintillating materials should be selected based on the application. For example, ceramic scintillators such as Eu:

SDC EX. 1018 - 50/66

$(Y,Gd)_2O_3$, Lu_2O_3 and $Lu_3Ga_{5-x}In_xO_{12}$ are mainly used as X-ray detectors in medical and industrial CT-scanning facilities. Ceramic scintillators are highly sensitive and their quantitative detection accuracy is less than 10^{-3}. Ceramic scintillators can be fabricated by controlling the phosphor composition and doping with suitable additives [113,703,737]; for example, Pr_2O_3 can be added as a dopant to decrease the X-ray-induced luminescent afterglow [703,738–741].

The performance of ceramic scintillators is related to several factors when they are used for high-energy detection, including their (i) optical qualities, (ii) X-ray stopping capabilities, (iii) lighting output, (iv) primary speed and afterglow, and (v) radiation damage resistance. Firstly, a ceramic scintillator should have high optical transmittance so that the visible scintillation photon can be transferred to the photodetector as efficiently as possible. After reflection at the surface and scattering both at the surface and within the material, the isotropically emitted scintillation light is transported to the photodetector. Ideally, all incident X-rays should be directed onto and absorbed by the ceramic scintillator [738,742–744].

Generally, the total energy level of the scintillated light is determined by the photoelectric absorption and Compton scattering; thus, the transmitted flux can be reduced by increasing the thickness of the ceramic scintillator. Moreover, the ceramic scintillator material should be as dense as possible; hence, transparent ceramics for scintillating applications should contain elements with high atomic weights. Various processes follow the photoelectric absorption of X-ray photons in order to leave luminescent centers for excited states, and the energy of mobile electrons is released through ionization and the generation of secondary electrons [745–748].

Relative light output, which is characterized by the current that flows out of the diodes connected to the scintillator component, is not an intrinsic property of ceramic scintillators; however, energy quantum efficiency is an intrinsic property of all ceramic scintillators. Energy quantum efficiency is defined as the ratio of photon energy emitted from the luminescent sites to the total energy trapped at the sites [725–728].

The efficiency of an X-ray detector equipped with ceramic scintillators is closely related to the coupling between the scintillator and the photodiode, which should be taken into account by practical applications. A wide range of high-density ceramics can be used to alter the internal crystal fields of the activators in order to ensure that they emit at the desired wavelengths [749–754]. The 3d levels of transition element activators interact with the crystal fields in the surrounding region; for example, because $Cr:Gd_3Ga_5O_{12}$ has a weak crystal field, its $^4T_2 \rightarrow {}^4A_2$ transitions emits at 730 nm, which matches the efficiency peak of Si-based photodiodes [755–757].

The primary speed is determined by the decay time, which is the reciprocal of the probability per unit time, as the activator undergoes a radiative transition from an excited state to the ground state; for example, the decay time of Ce^{3+} ions in $BaHfO_3$ is 20 ns. The probability is dependent on the symmetry state and spin state of the activators, as well as the local crystal field [749,750,753]. Because activators can occupy multiple sites, the Eu^{3+} ions in $Eu:(Y,Gd)_2O_3$ can occupy both the symmetric S_6 site and the non-symmetric C_2 site [758–760].

When the intensity of the visible scintillator emissions are higher than the theoretical prediction, the emissions are called an afterglow. The duration of afterglow emissions can exceed the decay time by three orders of magnitude. When scintillators are used in an integrated format, the afterglow has a positive effect on the signal, which is true even if the detector encounters a sudden decrease in X-ray flux intensity [761]. In photon-counting applications, afterglow can reduce the signal-to-noise ratio and thus increase the dead time of the detector [762].

Afterglow occurs when mobile electrons or holes are trapped at the intrinsic and/or extrinsic defect sites in ceramic scintillator materials. The release of the electrons and holes back to the conduction and valence bands requires thermal energy corresponding to the binding energy of the trapping processes. Hence, if the process is assumed to be first order and both the trapping and releasing of charge carriers are due to a single defect before it is trapped by the emitting ions, the emission decay is strongly dependent on temperature. When the temperature is low, all traps are occupied and thus will contribute to afterglow emissions when the temperature reaches the required level; the traps are quickly emptied at this temperature, which results in a short decay time. The afterglow decay is the sum of all emissions from defect traps [760]; therefore, the afterglow can be readily addressed by controlling the doping ion distribution [737]. Nearly all applications require ceramic scintillators to be sufficiently stable and reproductive [762].

Another advantage to using transparent ceramics as scintillators is that the concentration and homogeneity of their activators can be superior to those of single crystals. For example, Cherepy et al. developed a new gamma spectroscopy scintillator that exhibited relatively high light yields and outstanding phase stability using Ce^{3+}-doped gadolinium garnet (Ce:GYGAG) ceramics, which demonstrated that the scintillation performance of Ce:GYGAG-based scintillators is comparable to that of single crystals [763]. These authors also developed a radiography scintillator based on transparent $Eu:Lu_2O_3$ ceramics [763,764]. Moreover, various other transparent ceramics, including Lu_2O_3 [170,765–768], Ga_2O_3 [769] Ce:YAG [770], and LuAG [708,771–773], have been used as scintillators and discussed in the open literature.

Zych et al. compared the scintillation performance of Ce:YAG ceramics and single crystals [774]. When these ceramics and single crystals were excited with gamma radiation, their dominant decay times were both approximately 85 ns; however, the ceramic samples exhibited an additional fast component of 20 ns, which was not observed for the single crystals. Furthermore, the scintillation output of the ceramic scintillator was roughly half that of the single-crystal scintillator because the deformed lattice structure at the ceramic grain boundaries resulted in unusual loss, which diminished the scintillation effect. A phenomenological model was established to account for the lattice deformation, and this model satisfactorily explained the kinetic data.

Mihokova et al. demonstrated that both Ce:YAG ceramics and single crystals exhibited radio-luminescence with comparable intensity, which corresponded to the Ce^{3+} band at 550 nm [775]. The ceramics did not exhibit the host band at 300–350 nm because they did not have the Y_{Al} antisite defect, in which Y is present at the Al site; this antisite defect is the origin of the UV emission as it contains luminescence centers [776]. This defect is usually formed at high temperatures, but the ceramics were processed at a relatively low temperature; thus, Y_{Al} antisite defects were not generated [478]. Based on their overall performance, the Ce:YAG ceramics could be used to replace high-quality industrial single crystals as scintillating materials.

Osipov et al. presented a systematic study of the optical and scintillation properties of transparent Ce:YAG ceramics [777]. The samples were prepared from mixtures of $Ce_{2x}Y_{2-2x}O_3$ (x = 0.001, 0.01, 0.03, and 0.05) and Al_2O_3 nanopowders using solid-state reactive sintering, and the in-line transmittance of 2-mm thick samples was 72–82% at 550–900 nm. The transparent Ce:YAG ceramics exhibited intensive luminescence with a maximum at 525–545 nm, and the absolute light yields were 18–21 ph/MeV and 5 ph/MeV for samples with 1–5 at% and 0.1 at% Ce^{3+}, respectively. The energy resolution of the 2-mm thick samples was 10–15% under excitation with 662-keV γ-rays. The scintillation decay curves had two decay components and the decay times depended on the Ce^{3+} concentration; for example, the main fast component of the 5 at% Ce:YAG ceramics was characterized by a decay time of 26 ns. The scintillation performance of the Ce:YAG ceramics was comparable to that of commercial Ce:YAG and CsI:Tl single crystal scintillators. Moreover, a comprehensive discussion of the effect of Ce^{3+} concentration on the optical, luminescence, and scintillation properties offered important guidance for the development of ceramic scintillators.

SDC EX. 1018 - 51/66

The scintillation behavior of Ce:LuAG ceramics has been intensively studied [9,10,20,778]. Li et al. fabricated Ce:LuAG ceramics with an average grain size of 6 μμm by calcining at 1000 °C for 2 h and vacuum sintering at 1800 °C for 10 h without sintering aids [20]. The resultant Ce:LuAG ceramics had 65% in-line transmittance in the visible light region and a broad band in their radioluminescence spectrum at 480–650 nm. The ceramics exhibited two emissions, which corresponded to Ce^{3+} transitions from the lowest 5d excited state to the 4f ground state; these emissions were similar to those of the Ce:LuAG single crystals [708,779].

Liu et al. described the scintillation performance of 5 at% Ce:LuAG ceramics prepared by the conventional solid-state reaction method and vacuum sintering [772]. Post-sintering thermal annealing in air was used to improve the scintillation behavior of the ceramics and resulted in a steady-state scintillation efficiency under X-ray excitation that was much higher than that of the conventional $Bi_4Ge_3O_{12}$ (BGO) single crystal. Moreover, thermal annealing increased the light yield (^{137}Cs, 662 keV) of the ceramic by approximately two times. The radiation hardness of the Ce:LuAG ceramic scintillator was studied under a 2×10^5 Gy dose of ^{60}Co gamma radiation delivered at approximately 1×10^4 Gy/h and radiation-induced absorption was observed at approximately 380 nm and 610 nm. This absorption was separate from the Ce:LuAG emission band, which indicates that these ceramics are suitable for applications in high-energy physics.

Yanagida reported the scintillation properties of transparent 0.2–1.0 at% Pr:LuAG ceramics prepared by vacuum sintering [780]. The optical and scintillation properties of these Pr:LuAG ceramics were compared to those of single crystals grown by the Czochralski method. Although the overall performance of the ceramics was lacking compared to that of single crystals, the light yield of the sample with 0.25 at % Pr^{3+} was higher than that of single crystals by approximately 20% under gamma radiation. Moreover, both the slow scintillation decay components and the defect-related host emission were absent in the Pr:LuAG ceramics.

Seeley et al. developed a Ce:GYGAG ceramic scintillator for gamma spectroscopy detectors: $Gd_{1.49}Y_{1.49}Ce_{0.02}Ga_{2.2}Al_{2.8}O_{12}$ [781]. The light yield and energy resolution of the ceramic scintillator were closely related to the processing parameters of powder preparation, compaction, and sintering. Furthermore, the sublimation of Ga during vacuum sintering generated compositional gradients in the ceramic samples, which degraded the energy resolution. Although Ga sublimation could be prevented by sintering the Ce:GYGAG ceramics in an O_2 environment, sintering in O_2 altered the oxygen vacancy concentration of the ceramics and thus changed the distribution of the electron trap state, which reduced the afterglow, light yield, and energy resolution accordingly. Alternatively, a bed of coarse Ce:GYGAG powder was applied during vacuum sintering to create a relatively high Ga partial pressure, which ensured compositional homogeneity without compromising the trap state distribution and thus improved the scintillation performance. This study is a useful reference when using materials with similar limitations.

Mori et al. studied 0.8 at% Ce^{3+}-doped (Y, Gd, Lu)$_3Al_2Ga_3O_{12}$ (Ce:YAGG, Ce:GAGG, and Ce:LuAGG) transparent ceramics and compared their photoluminescence and scintillation properties [782]. These ceramics all had strong, broad photoluminescence over 470–600 nm because of the 5d → 4f transitions of the Ce^{3+} ions. The photoluminescence curves had two components while the scintillation decay curves consisted of three exponential components; in both cases, the primary components were present between 35–43 ns. Furthermore, the features of the X-ray excited scintillation spectra were very similar to those of the photoluminescence spectra. Based on the X-ray induced afterglow results, Ce:LuAGG demonstrated the weakest afterglow intensity of the three ceramics. Photoabsorption peaks were clearly observed in the pulse height spectra of the ceramic samples. Furthermore, Ce:LuAGG displayed a scintillation light yield of 18,700 ph/MeV, which was the highest of the three samples.

In a separate study, Li et al. compared the optical properties and scintillation behavior of transparent Ce:LuAG and Ce:YAG ceramics that both contained 0.9 at% Ce^{3+} [783]. The Ce:LuAG ceramics had higher light yield than the Ce:YAG ceramics under UV and X-ray excitation whereas the Ce:YAG ceramics had higher light yield under γ–ray excitation. The Ce:YAG ceramics also had better energy resolution, which was attributed to the fact that the Ce:LuAG ceramics contained more slow emissions (38.5%) and was less transparent. It is worth mentioning that results of comparison studies reported by other researchers could differ because ceramic processing involves several steps with various influential parameters; therefore, these results should only be used as a reference.

The scintillation performance of ceramic scintillators can be enhanced by co-doping. For example, co-doping with Ce^{3+} effectively mitigated the afterglow of a (Cr, Ce):$Gd_3Ga_5O_{12}$ ceramic scintillator because the holes at the Ce^{3+} ion sites were efficiently captured through the conversion of $Ce^{3+} \rightarrow Ce^{4+}$ [703,784]. Moreover, co-doping Eu:(Y,Gd)$_2O_3$ with Pr^{3+} suppressed the nonradiative recombination of migrating electrons and/or temporary Eu^{2+} centers. Furthermore, the trapping states in the forbidden gap related to the grain boundary interfaces could be removed or passivated by thermal annealing in controlled environments.

Theoretical predictions of the temporal dependence of X-ray excited scintillation in Eu:Lu_2O_3 ceramics has been supported by experimental observations, which included the decay waveforms recorded between 100 ns and 5 min [766]. The kinetic data were in good agreement with the analytic model of the temporal behavior, which predicted that the trap depths had two overlapping Gaussian distributions, with values in the range of 0.58–1.0 eV, that could potentially cause afterglow. The ceramics were evaluated in terms of their scintillating performance and the thermoluminescence excited by heavy gamma irradiation, and the experimental thermoluminescence glow profile matched the theoretical model of afterglow [767]. Because the effect of carrier trapping on scintillation efficiency cannot be accurately evaluated using only the thermoluminescence data and the absolute light output cannot be quantitatively obtained, the effect of carrier trapping was characterized using the branching ratio of electron–hole pairs responsible for the thermoluminescence or scintillation performance [785,786]. In 2004, Nagarkar et al. developed (Eu^{3+}, Tb^{3+}):Lu_2O_3 ceramics as a new group of scintillating ceramics because the 4f → 4f transitions of rare earth ions are relatively slow [787]. The authors concluded that these ceramics could be used to produce large screens up to 16 × 16 cm^2.

Retot et al. characterized the scintillation behavior of Eu:Lu_2O_3 and Eu:$(Lu_{0.5}Gd_{0.5})_2O_3$ ceramics and determined that the optical transparency and light yield of the two ceramics were very similar [788]. However, the afterglow of Eu:$(Lu_{0.5}Gd_{0.5})_2O_3$ was approximately one order of magnitude less than that of Eu:Lu_2O_3 in the range of 3–300 ms. The reduced afterglow was evidenced by the thermally stimulated luminescence peaks as the intensities of the Eu:$(Lu_{0.5}Gd_{0.5})_2O_3$ peaks were significantly less than those of the Eu:Lu_2O_3 peaks, which suggests that the Eu:$(Lu_{0.5}Gd_{0.5})_2O_3$ ceramics contained much fewer charge trapping defects. Using low-temperature selective excitation of Eu^{3+}, the location and behavior of the Eu^{3+} ions at the C_2 and S_6 sites of the Lu_2O_3 and $(Lu_{0.5}Gd_{0.5})_2O_3$ crystal lattices were comprehensively examined. The 4f–4f lifetime of Eu^{3+} at both sites was shorter in Eu:$(Lu_{0.5}Gd_{0.5})_2O_3$ than Eu:Lu_2O_3 while $(Lu_{0.5}Gd_{0.5})_2O_3$ was more suitable for hosting Eu^{3+} ions in the C_2 sites. The preferential occupation of the C_2 sites by Eu^{3+} in Eu:$(Lu_{0.5}Gd_{0.5})_2O_3$ resulted in the relatively short decay times of Eu:$(Lu_{0.5}Gd_{0.5})_2O_3$ (3–20 ms).

Yanagida et al. reported the scintillator performance of transparent $(Yb_xLu_{1-x})_2O_3$ (x = 0.001–1.0) ceramics prepared by a wet-chemical method [170]. The in-line transmittance of the ceramics was 60–80% at > 240 nm, and absorption bands near 970 nm corresponded to the 4f → 4f transition of Yb^{3+}. For photoluminescence and X-ray induced radioluminescence, the charge transfer luminescence of Yb^{3+} was observed at 330 and 490 nm, and the photoluminescence and scintillation

SDC EX. 1018 - 52/66

decay times of the charge transfer luminescence were in the range of 0.5–1.5 ns. The light yield of the fast component was obtained from the ^{137}Cs-excited pulse height spectrum and the sample with $x = 0.003$ displayed the maximum light yield: approximately 500 ph/MeV.

Yanagida et al. also demonstrated that Yb^{3+}-doped RE_2O_3 sesquioxide ceramics exhibited ultrafast scintillation behavior because of the special charge-transfer luminescence of Yb^{3+} [789]. A series of Yb^{3+}-doped transparent ceramics, including Y_2O_3, Sc_2O_3, Lu_2O_3, and Yb_2O_3, were fabricated by vacuum sintering. When the sesquioxide ceramics were irradiated with γ-rays and X-rays, the pulse height spectra exhibited a photoabsorption peak with an ultrafast scintillation decay of just 1 ns. The scintillation performance of these ceramics could be further enhanced by optimizing the fabrication process for ultrafast scintillator applications.

Futami et al. prepared transparent Sc_2O_3, Y_2O_3, and Lu_2O_3 ceramics for scintillator applications using the SPS technique [768]. The optical transmittance of the as-prepared ceramics ranged from 10% to 40% at 500 nm. The X-ray induced emission spectra each exhibited a broad emission peak centered at 335 nm, and at this wavelength, the scintillation decay times of Y_2O_3 and Sc_2O_3 were 22 and 48 ns, respectively. The light yields of the Sc_2O_3, Y_2O_3, and Lu_2O_3 ceramics derived from the α-ray induced pulse height spectra were 16200, 2600, and 200 ph/5.5 MeV-alpha, respectively. The γ-ray induced light yield of Sc_2O_3 was 11,500 ph/MeV, which was approximately 1.4 times higher than that of the conventional BGO single crystal scintillator. This study was the first to report the light yield non-proportionality and energy resolution of Sc_2O_3 ceramics.

Transparent ceramics with perovskite structures have formed a new family of ceramic scintillators, which includes $Ba(ZrMgTa)O_3$ [$Ba(Zr_{0.25}Mg_{0.25}Ta_{0.5})O_3$ and $Ba(Yb_{0.1}Zr_{0.2}Mg_{0.2}Ta_{0.5})O_3$] and $(LaSr)(AlTa)O_3$ [$(La_{0.5}Sr_{0.5})(Al_{0.8}Ta_{0.2})O_3$ and $(Yb_{0.1}La_{0.5}Sr_{0.4})(Al_{0.8}Ta_{0.2})O_3$] [790]. These ceramics exhibit in-line transmittances in the range of 50–70% in the visible light region. Specifically, $Ba(ZrMgTa)O_3$ and $(LaSr)(AlTa)O_3$ display strong emissions at 470 nm and 500 nm when excited by 284 nm and 324 nm photons, respectively, and the corresponding photoluminescence decay times are 14 and 16 μs. Moreover, the charge transfer transition of Yb^{3+} has been demonstrated to trigger rapid and intensive emissions [791,792]. Experimental results have indicated that most ceramic scintillators could provide fast and strong emissions at room temperature now that the challenges posed by strong thermal quenching have been addressed [793–795].

Kato et al. reported a comparative study of the optical, scintillation, and dosimeter properties of transparent MgO ceramics and single crystals [796]. The transparent MgO ceramics were prepared using the SPS technique. Although the ceramics and single crystals had the same composition, the ceramics predominantly exhibited photoluminescence near 450 nm while the dominant single-crystal emissions were in the NIR region. The photoluminescence lifetime of the emission at 450 nm was approximately 10 ns, whereas it was typically 50 ns for emissions of the F^+ center in MgO. The scintillation spectra of the ceramics were similar to the photoluminescence spectra; however, the scintillation lifetimes were on the scale of microseconds. The thermally stimulated luminescence (TSL) glow curves of the MgO ceramics had a main peak at approximately 140 °C and broad emission bands at 300–400 nm, 600 nm, and 750 nm, which were in agreement with the scintillation spectra. Both the ceramics and single crystals exhibited a TSL response that was linear with respect to the irradiation dose over the dose range of 0.1–1000 mGy. Moreover, the dosimeter properties of the ceramics were evaluated for X-ray detection.

The effect of Mn^{2+} on the photoluminescence, scintillation, and TSL dosimeter properties of the transparent MgO ceramics has also been studied [797]. The MgO ceramics doped with 0.001, 0.01, 0.1, and 1.0% Mn^{2+} were prepared by SPS. Each of these ceramics displayed photoluminescence emission near 730 nm, and the emission intensity increased with the doping concentration. The photoluminescence decay-time constants were on the scale of milliseconds, which is typical for Mn^{2+}. Moreover, the X-ray excited scintillation spectra exhibited additional emissions at 340, 620, and 760 nm. However, the TSL profiles and responses of the Mn^{2+}-doped samples were similar to those of undoped MgO ceramics.

Nakamura et al. studied the scintillation, dosimeter, and photoluminescence properties of transparent $Eu:CaF_2$ ceramics doped with 0.01, 0.02, 0.05, and 0.10 at% Eu^{2+} and fabricated by SPS [798]. Under X-ray irradiation, each ceramic exhibited emissions at 300 and 430 nm because of self-trapped excitons (STE) and the 5d → 4f transition of Eu^{2+}, respectively. Furthermore, weak emissions related to the 4f → 4f transitions of Eu^{3+} were observed at 570, 590, 615, and 625 nm for all samples. Under ^{137}Cs irradiation, the light yields of the samples doped with 0.01, 0.02, 0.05, and 0.10 at% Eu^{2+} were approximately 16400, 15400, 17700, and 14,300 ph/MeV, respectively. The TSL glow curves of all samples had glow peaks at 100 and 180 °C, and their intensities increased linearly as the X-ray dose was increased from 0.1 to 1000 mGy. Moreover, the transparent $Eu:CaF_2$ ceramics also exhibited optically stimulated luminescence (OSL).

Transparent $Nd:CaF_2$ ceramics with different concentrations of Nd^{3+} have been developed using a similar method in order to be used for scintillation and dosimeter applications [463]. As expected, these samples had absorption peaks in the visible and NIR regions because of the 4f → 4f transitions of Nd^{3+}; these peaks were present at 860 and 1064 nm under X-ray irradiation. Under 160-nm vacuum-UV excitation, photoluminescence was confirmed by emissions corresponding to the 5d → 4f transitions of Nd^{3+}. Furthermore, the transparent $Nd:CaF_2$ ceramics exhibited TSL glow peaks at 100, 150, and 380 °C. The samples with 5 at% Nd^{3+} had optimal sensitivity and could be used to measure radiation doses in the range of 0.1–1000 mGy as they have the desirable linear relationship between scintillation and radiation.

The same authors also developed transparent MgF_2 ceramics for scintillation and dosimeter applications, and compared their properties to those of single crystals [466]. Under X-ray irradiation, the transparent ceramics had broad scintillation emissions across 300–600 nm with decay times of 310 and 1940 μs, while no such emissions were produced by the single crystal. Moreover, the MgF_2 ceramics exhibited radio-photoluminescence (RPL) as a new luminescence center was produced by the ionizing radiation. This RPL was characterized by two emission bands centered near 415 and 700 nm when the ceramic was excited at 340 ± 40 nm. While measuring the RPL, the intensity of the emission band at 415 nm increased for > 50 s, which implies that the RPL was a "building-up" effect. Based on the photoluminescence characteristics and decay time, the authors deduced that the RPL peak at 415 nm corresponded to the $M(C_{2h})$ center. Transparent MgF_2 ceramics doped with Eu^{2+} and Gd^{3+} have also been studied for scintillator applications [465,467].

Similarly, photoluminescence emission of transparent BaF_2 ceramics has been observed near 500 nm [473]. Under X-ray irradiation, emissions at 190 and 220 nm were caused by the auger-free luminescence (AFL) of the ceramics. The light yield of these transparent BaF_2 ceramics was approximately 6000 ph/MeV under irradiation with ^{137}Cs γ-rays. Moreover, the afterglow of the ceramics was lower than that of their single crystal counterpart. These ceramics also exhibited TSL glow peaks at 50, 105, 140, 205, 280, and 420 °C.

3.4. Electro-optic (EO) Ceramics and devices

Various devices have been designed using transparent EO ceramics, such as variable optical attenuation devices (VOA), polarization controllers (PC), sinusoidal filters, dynamic gain flattening filters, tunable optical filters, and *Q*-switches [799]. Light is an electromagnetic wave and thus has two field components: electric and magnetic components. These components are perpendicular to each other as well as the direction of propagation; hence, light has a polarized electromagnetic field. Since light is distinctively oriented in space and its propagation through a medium is influenced by the direction of polarization, the

SDC EX. 1018 - 53/66

rate of transmission in dense wavelength division multiplexing (DWDM) systems is impeded; examples of impeded transmission include polarization dependent loss (PDL) and polarization mode dispersion (PMD). This issue could be solved by proper polarization management; for example, dynamic polarization controllers (PCs) could serve to compensate for polarization mode dispersion, scramble polarization, manipulate polarization multiplexing, and generate polarization [799].

Ferroelectric PLZT ceramics are representative EO ceramics as they have an intrinsic optical uniaxial anisotropy at the microscopic scale and an extrinsic optical uniaxial anisotropy at the macroscopic scale if they are polarized or activated by an external electric field. Ferroelectric transparent ceramics such as PLZT have a unique symmetry axis because the optic axis is colinear with the ferroelectric polarization vector and has optical properties that are different from those of the other two orthogonal axes. Therefore, light travels in the direction of the optic axis and vibrates in the perpendicular direction. This means that the index of refraction (n_0) of light with polarization perpendicular to the optic axis – an ordinary ray – is different from that of light with polarization perpendicular to the ordinary ray (n_e). The difference between these two indices is called birefringence: $\Delta n = |n_e - n_0|$. The birefringence, Δn, of as-prepared ferroelectric ceramics is zero. After poling, the material will have a non-zero Δn, which is dependent on the composition of the material and the degree of poling. Relaxor ferroelectric ceramics only have non-zero values of Δn when they are subject to external electric fields [799,800].

When linearly polarized white light is incident on electrically activated ceramics, it will be split into two components with orthogonal polarization. The polarization directions are determined by the crystallographic axes of the ceramic materials, and the axes are dependent on the direction of the applied electric fields. Because of the difference between n_e and n_0, the two light components have different propagation velocities as they travel through the ferroelectric ceramics, which results in a phase shift that is called optical retardation.

Qiao et al. published a systematic study of the EO properties of transparent PMN-PT EO ceramics [338]. The EO switch was polarization independent and constructed according to the structure of a fiber Sagnac interferometer (FSI). The polarization orientation of the incident light had a negative effect on the EO performance of the switch, but this could be effectively suppressed by incorporating an initial π-shift into the Sagnac loop. The optical signal between the reflection and transmission ports could be switched using an electrically controllable PMNT phase retarder. The switching behavior of the devices, as well as their thermal characteristics and switching frequency response, were theoretically analyzed. The PMN-PT EO ceramics had a relatively high refractive index (n = 2.465); thus, that they are suitable for Fabry–-Perot (FP) resonators, which can be used to measure electric hysteresis and thermo-optic coefficients.

Fernando et al. attempted to prepare $(Pb_{1-x}La_x)TiO_3$ ceramics ($0.18 \leq x \leq 0.23$) using the solid-state reaction method [801]. The $Pb_{0.79}La_{0.21}TiO_3$ sample was optically transparent. Based on EO measurements, linear and quadratic EO behaviors were observed for the relationship between birefringence and electric field. At room temperature, the calculated quadratic (R) and the linear coefficients (r) at 632 nm were 0.5×10^{-16} m^2/V^2 and 1.9×10^{-10} m/V, respectively. These ceramics showed potential for EO device applications.

Li and Kwok reported the EO effect of lead-free transparent ceramics, $(K_{0.5}Na_{0.5})_{0.9}Li_{0.1}Nb_{0.9}Bi_{0.1}O_3$, obtained using pressure-less sintering [802]. The inclusion of Li and Bi resulted in ceramics with diffuse phase transition behavior, i.e., the ceramics exhibited relaxor-like characteristics because of the presence of polar nanoregions. The addition of excessive Bi_2O_3 further modified the crystal structure and dielectric properties of the ceramics to be more cubic-like and more relaxor-like, respectively; thus, adding excessive Bi_2O_3 increased the optical transparency. The in-line transmittance of samples with 4–6 mol % excessive Bi_2O_3 was 60–70% in the NIR region. Moreover, these lead-free ceramics had effective EO coefficients in the range of 30–40 pm/V.

Zeng et al. investigated the EO properties of Dy:PLZT ceramics: $Pb_{0.9}(La_{1-x}Dy_x)_{0.1}(Zr_{0.65}Ti_{0.35})_{0.975}O_3$, with x = 0–0.06 [324]. The authors found that the coercive field of the PLZT ceramics was reduced by doping with Dy, which significantly improved the optical transparency and EO performance of the ceramics. Furthermore, the half-wave retardation voltage was effectively decreased by doping with Dy; thus, the working voltage of the EO devices was reduced.

The EO effects, microstructure, and optical transparency of La-doped $0.75Pb(Mg_{1/3}Nb_{2/3})O_3$-$0.25PbTiO_3$ (PLMNT) transparent ceramics were reported by Ji et al. [803]. These ceramics were prepared using the columbite precursor method and excessive PbO (10, 15, and 20 mol%). The phase composition of the samples was not influenced by the amount of excessive PbO whereas the average grain size increased with the PbO content and the optical transparency decreased with the PbO content. The sample with 10 mol% excess PbO had 62% in-line transmittance at 632.8 nm. The EO coefficients of the samples were derived from the birefringence and electric field; the EO coefficients increased with the concentration of excess PbO, and the maximum EO coefficient, 40.6×10^{-16} $(m/V)^2$, corresponded to the sample with 20 mol% excess PbO.

3.5. Optical lenses

With the rapid advancement of digital cameras and mobile phones, compact and miniaturized lens systems are in high demand. Transparent ceramics could play an important role in these systems because of their high refractive indices and high Abbe numbers. Generally, the refractive indices of glasses are in the range of n = 1.50–1.85, while the refractive indices of polycrystalline ceramics are usually > 2 [804–806]. Moreover, ceramics exhibit much higher mechanical strengths than their glass counterparts, which is especially important when the materials need to be scratch-free and impact resistant [807].

Peuchert et al. studied transparent ZrO_2 ceramics obtained by combining a solid-state reaction process with vacuum sintering and HIP [100]. The refractive index (n_d) of these ZrO_2 opto-ceramics was 2.10–2.20 at 630 nm, and could be modulated by controlling the concentration of the sintering aid, TiO_2. The presence of TiO_2 caused competition between optical transparency and uniformity. Transparent cubic ZrO_2 ceramics do not have anisotropic optical properties in any specific directions; however, if the sintering aid and/or stabilizing phases precipitate at the grain boundaries, the optical properties of the transparent ceramics will be inhomogenized and birefringence properties will emerge, as has been reported for the ZrO_2–Y_2O_3–TiO_2 ceramics [100]. The application of transparent ceramics to optical lenses deserves further investigation and development as this application has yet to be comprehensively studied.

3.6. Transparent ceramic windows and domes

Transparent armors are used for personnel protection, such as face shields, visors, windows of military vehicles, and lookdown windows in aircrafts. The glass transparent windows that are currently available are very thick in order to resist multi-hit ballistic impact. In order to meet required weight limits without compromising the ballistic resistance, transparent ceramics have been increasingly considered for such applications. Moreover, some of the multimode weapon systems that are required to withstand harsh environment conditions also require relatively large windows and domes [808–810].

Strength and hardness are important properties in these applications, which significantly narrows the range of materials that can be used. For example, the mechanical strengths of the transparent fluoride ceramics that are typically used as laser windows are not sufficient for military applications [811,812]. Therefore, the potential candidates for these applications include single crystals (e.g., sapphire) [813] and

SDC EX. 1018 - 54/66

transparent ceramics such as AlON [814–818] and $MgAl_2O_4$ [294,668–670,819–822]. Although windows based on transparent ceramics are still less popular than those based on single crystal sapphire [823–832], it is very likely that transparent ceramics will be the ideal materials because of the advantages discussed in this review.

Because of the relationship between polycrystallinity and toughness, some transparent ceramics are more suitable for armor applications than single crystals, such as $MgAl_2O_4$ [814–818] and AlON [668–670,819]. Spinel is highly transparent over the visible and mid-IR regions (0.25–5.5 μm); thus, it can be used as windows and domes in EO and IR sensors used by defense systems that work in extreme environments. The mechanical properties of ceramic materials are largely dependent on their grain size; generally, the smaller the grain size, the stronger the ceramics. Borrero-Lopez et al. studied the effect of grain size on the mechanical strengths of transparent $MgAl_2O_4$ ceramics [815], and Beyer et al. evaluated AlON ceramics as materials for canon windows [819]. When using laser ignition in large caliber cannons, the window admitting the laser to the cannon chamber is a crucial component; therefore, this window must be able to withstand repeated impact by combustion products from the gun propellant at pressures as high as 440 MPa. Aluminum oxynitride ceramics have been intensively examined for such applications.

Conventional transparent armors consist of glasses and polycarbonate backers [833], but transparent ceramics with higher mechanical strength have been acknowledged to be the next generation of armor materials. Since testing transparent ceramics is quite expensive, modeling and simulations are generally used to predict their mechanical performance and ballistic testing is conducted to evaluate armor designs. The protective strength of transparent ceramics has been studied using ballistic testing methods as well as visualization techniques, which can be used to understand the interaction mechanisms between the tested samples and the high speed projectiles [834]. The dynamic responses of some transparent ceramics have been characterized for armor applications [835]. Real ceramic armor is in fact an assembly of ceramic/polycarbonate laminates, and the failure probability of the ceramic portion can be simulated by considering the ceramic defects [836,837].

Salem conducted a systematic study of the mechanical properties of transparent AlON and $MgAl_2O_4$ ceramics, and thoroughly evaluated whether they can be used for spacecraft windows [809]. The window materials used in spacecrafts (e.g., the NASA space shuttle) must be able to meet numerous requirements, including maintaining cabin pressure according to the design of the vehicle, withstanding the thermal shock caused by alternative rapid heating and cooling, resisting high impact at different velocities, retaining high optical performance in various harsh environments, in order to avoid catastrophic failures. Therefore, the optical, thermal, and mechanical properties of the window materials must be well-characterized to ensure that they satisfy the stringent requirements. A database for the design and characterization of transparent ceramics for such special applications should include the following characteristic parameters: (i) elastic constants, (ii) texture and grain sizes, (iii) fracture toughness, (iv) strength and slow crack growth, (v) failure sources, and (vi) residual stress [838].

3.7. Biomedical applications

Since normal bioceramic materials are opaque, the direct observation of cells with a light microscope in the transmission mode is not possible. To address this problem, John et al. used transparent hydroxyapatite (tHA) ceramics to directly observe living cells and complete time-lapse studies as the optical transparency of the tHA ceramics facilitated the visualization of cellular events under transmitted light [839]. This system was used to monitor the interactions of different types of bone cells with the tHA ceramics; for example, rat calvaria osteoblasts (RCO) were cultured on the transparent tHA ceramics using transmission light microscopy, which revealed the high cytocompatibility of the bioceramic materials. Furthermore, osteogenic-induced human bone marrow stromal cells (hBMSCs) were microscopically analyzed on the tHA ceramics and their lactate dehydrogenase (LDH) activities were quantitatively characterized at different times during the culture. The results of these analyses confirmed favorable proliferation as the enhanced alkaline phosphatase (ALP) activity demonstrated the differentiation of osteogenic-induced hBMSCs towards the osteoblastic lineage. Moreover, the differentiation of human monocytes from the osteoclast-like cells was observed on the tHA samples, and further confirmed by fluorescent microscopy imaging of the multinucleated cells on the transparent ceramics.

Bodhak et al. studied the potential biomedical applications of commercial $MgAl_2O_4$ and AlON® transparent ceramics [840]. The biomedical evaluation tests investigated in-vitro cytotoxicity, material-cell interactions, and tribological behavior, all of which are important for implant applications. The hardness of the transparent ceramics was in the range of 1334–1543 HV and their in-vitro wear rates were $5.3–10 \times 10^{-6}\ mm^3 \cdot Nm^{-1}$ against an Al_2O_3 ball at a load of 20 N. An in-vitro biocompatibility experiment with hFOB cells indicated that the transparent ceramics have no toxicity, and material-cell interaction testing confirmed that both the $MgAl_2O_4$ and AlON® transparent ceramics were even more biocompatible than the commercial CP-Ti product. The mechanical properties and material-cell interactions of the $MgAl_2O_4$ ceramics were superior to those of the AlON® ceramics. The $MgAl_2O_4$ ceramics also demonstrated stronger cellular adhesion and proliferation because the surface energy of their polar component had a positive effect on their mechanical characteristics.

Recently, the viability of transparent $MgAl_2O_4$ ceramics as esthetic orthodontic brackets was evaluated [841]. The biomaterial-oral mucosa interface is generally used to characterize the biocompatibility of a new candidate for dental applications, and this study experimentally confirmed that transparent $MgAl_2O_4$ ceramics have outstanding biocompatibility. Moreover, the physico-chemical, mechanical, and optical properties of $MgAl_2O_4$ ceramics meet the requirements of orthodontic brackets, which face in-vivo biological attacks, chemical corrosion and thermal stress [842]. Nevertheless, the application of transparent ceramics in biomedical field is still in its infancy, and thus requires further investigation.

4. Conclusions and perspectives

Transparent ceramics are a new category of materials that can be used in the development of high temperature technologies. Various processing strategies have been developed to obtain transparent ceramics with a wide range of compositions and properties in order to satisfy the needs of different potential applications. Firstly, not all materials can be used to make transparent ceramics. According to intrinsic requirements of transparency, potential candidates for transparent ceramics should have highly symmetric crystal structures, i.e., cubic, tetragonal, and hexagonal.

Secondly, transparent ceramics cannot be obtained using the conventional ceramic process. The most popular strategy for fabricating transparent ceramics is vacuum sintering. High-pressure sintering, HP, and HIP are also important techniques for developing transparent ceramics. However, HIP requires expensive high-quality equipment while HP has issues with contamination because the die is usually made of graphite and is in direct contact with the sintered samples; therefore, diffusion of carbon into the samples is inevitable at high temperatures. Spark plasma sintering is a new sintering technique for fabricating transparent ceramics. One of the main advantages of SPS is that it requires relatively low sintering temperatures and shorter sintering times and HP or HIP because an electric field is applied during sintering. However, SPS has similar contamination issues to HP. Furthermore, neither HP nor SPS can be used to prepare large samples because of the limitations of the equipment. Microwave sintering also has short sintering times, like SPS, and can produce large samples, like vacuum

SDC EX. 1018 - 55/66

sintering; however, information about preparing transparent ceramics by microwave sintering is still scarce in the open literature. Hence, microwave sintering should be an important topic in future studies.

Transparent ceramics were initially developed for solid-state lasers, which are still their primary application. However, various other applications are being investigated, including scintillation, lighting, optical lenses, electro-optical devices, transparent armors, windows, and biomaterials. Solid-state phosphors are expected to be the next generation of white lighting and thus a hot topic in the near future as there is a global research trend in new materials and new energies. Moreover, high-efficiency LEDs and LDs are set to become the main domestic and industrial lighting sources. The key requirement of these applications is the availability of high-quality solid-state phosphors, i.e., transparent ceramics doped with luminescent elements. Furthermore, low-cost transparent ceramics with strong mechanical properties have the potential to replace glasses as smartphone screens, which is a huge market given that the smartphone is an indispensable item in our daily life.

Transparent ceramics have recently been derived from glasses and Si_3N_4 ceramics. If conventional glass technology can be applied to transparent ceramics with compositions that can be made into glasses, the production of transparent ceramics will be revolutionized. The advantages of the glass crystallization process can be readily incorporated into the production of these transparent ceramics and thus has substantially increased the scope of transparent ceramic materials. Although the processing conditions used to obtain transparent Si_3N_4 ceramics are relatively stringent (extremely high temperature and high pressure), this achievement has inspired the investigation of transparent ceramics derived from materials with low-symmetry crystal structures. Moreover, this achievement will encourage manufacturers to design and create equipment that is more powerful than the equipment currently available in the market.

Transparent ceramics have higher thermal stability and stronger mechanical properties than other optical materials, such as glasses and polymers; thus, they can be used at higher temperatures and harsher conditions. Transparent ceramics also have advantages as scintillators. Transparent armors made from transparent ceramics are much thinner and lighter than those made from other materials, and transparent ceramics also exhibit potential for biomedical applications. However, the applications of transparent ceramics in areas other than solid-state lasers are still in their infancy, which implies that they are many opportunities in these areas, and more possible applications are expected to be explored. Therefore, transparent ceramic research is expected to have a bright future in materials science and engineering.

Ultimately, the detailed processes used to fabricate transparent ceramics must be characterized and monitored. For example, the slurry concentration of Y_2O_3 powder during preparation could critically affect the optical transparency of the final ceramics; however, the differences in the properties of powders and slurries with different solid contents have not been elucidated. This indicates that the optical properties of ceramics are more sensitive to their microstructural characteristics than their other properties, such as mechanical strength, electrical conductivity, and dielectric constant. Therefore, the relationship between the microstructure, process parameters, and optical transparency of transparent ceramics requires further investigation. To this end, new methods and strategies should be developed to characterize transparent ceramics that have similar or even identical microstructures but significantly different optical transparencies.

Declaration of Competing Interest

The authors have no conflicts of interest to declare.

Acknowledgement

This work was supported by the National Natural Science Foundation of China (51762023 and 51962013), the Natural Science Foundation of Jiangxi, China (20192ACB20018), and Key R&D Program of Jiangxi Province (20171BBE50006, 20192ACB80007, and 20192ACB80004). Ling Bing Kong would like acknowledge Shenzhen Technology University (SZTU) for financial support through a Start-up Grant (2018) and grant from the Natural Science Foundation of Top Talent of SZTU (grant no. 2019010801002).

References

[1] S.F. Wang, J. Zhang, D.W. Luo, F. Gu, D.Y. Tang, Z.L. Dong, et al., Prog. Solid State Chem. 41 (2013) 20–54.
[2] A. Ikesue, Y.L. Aung, Nat. Photonics 2 (2008) 721–727.
[3] J. Sanghera, S. Bayya, G. Villalobos, W. Kim, J. Frantz, B. Shaw, et al., Opt. Mater. 33 (2011) 511–518.
[4] J. Sanghera, W. Kim, G. Villalobos, B. Shaw, C. Baker, J. Frantz, et al., Materials 5 (2012) 258–277.
[5] J. Sanghera, W. Kim, G. Villalobos, B. Shaw, C. Baker, J. Frantz, et al., Opt. Mater. 35 (2013) 693–699.
[6] A. Krell, T. Hutzler, J. Klimke, J. Eur. Ceram. Soc. 29 (2009) 207–221.
[7] M.N. Rahaman, Ceramic Processing and Sintering, 2nd ed., CRC Press, New York, 2003.
[8] A. Ikesue, I. Furusato, K. Kamata, J. Am. Ceram. Soc. 78 (1995) 225–228.
[9] H.L. Li, X.J. Liu, L.P. Huang, J. Am. Ceram. Soc. 88 (2005) 3226–3228.
[10] H.L. Li, X.J. Liu, L.P. Huang, J. Inorg. Mater. 21 (2006) 1161–1166.
[11] J. Li, Q. Chen, L.L. Yang, G.Y. Feng, W.J. Wu, F.S. Zheng, et al., Ferroelectrics 411 (2011) 62–68.
[12] N.L. Wang, X.Y. Zhang, H.T. Jiang, T.T. Dong, D. Yang, Mater. Chem. Phys. 135 (2012) 709–713.
[13] Y.S. Wu, J. Li, F.G. Qiu, Y.B. Pan, Q. Liu, J.K. Guo, Ceram. Int. 32 (2006) 785–788.
[14] J. Lu, M. Prabhu, J. Song, C. Li, J. Xu, K. Ueda, et al., Appl. Phys. B 71 (2000) 469–473.
[15] S. Arabgari, R. Malekfar, K. Motamedi, J. Nanoparticle Res. 13 (2011) 597–611.
[16] J.Y. Chen, Y. Shi, J.L. Shi, J. Mater. Res. 19 (2004) 3586–3591.
[17] Y.H. Huang, D.L. Jiang, J.X. Zhang, Q.L. Lin, Opt. Mater. 31 (2009) 1448–1453.
[18] Z.G. Huang, X.D. Sun, Z.M. Xiu, S.W. Chen, C.T. Tsai, Mater. Lett. 58 (2004) 2137–2142.
[19] X.B. Ji, J.G. Deng, B. Kang, H. Huang, X. Wang, W. Jing, et al., J. Anal. Appl. Pyrolysis 104 (2013) 361–365.
[20] H.L. Li, X.J. Liu, R.J. Xie, Y. Zeng, L.P. Huang, J. Am. Ceram. Soc. 89 (2006) 2356–2358.
[21] T. Ikegami, J.G. Li, T. Mori, Y. Moriyoshi, J. Am. Ceram. Soc. 85 (2002) 1725–1729.
[22] J.G. Li, T. Ikegami, T. Mori, J. Mater. Res. 18 (2003) 1816–1822.
[23] K. Guo, H.H. Chen, X.G. Guo, X.X. Yang, F.F. Xu, J.T. Zhao, J. Alloys. Compd. 500 (2010) 34–38.
[24] D.Y. Li, Y. Hui, J.S. Lian, T.T. Xie, J. Rare Earths 23 (2005) 600–605.
[25] A. Biswas, K. Prabhakaran, N.M. Gokhale, S.C. Sharma, Mater. Res. Bull. 42 (2007) 609–617.
[26] K. Prabhakaran, D.S. Patil, R. Dayal, N.M. Gokhale, S.C. Sharma, Mater. Res. Bull. 44 (2009) 613–618.
[27] J. Su, J.H. Miao, L.H. Xu, Y.Q. Ji, C.Q. Wang, Mater. Res. Bull. 47 (2012) 1709–1712.
[28] N. Wang, X. Zhang, Z. Bai, H. Sun, Q. Liu, L. Lu, et al., Ceram. Int. 37 (2011) 3133–3138.
[29] B.T. Huang, Y.Q. Ma, S.B. Qian, D. Zou, G.H. Zheng, Z.X. Dai, Opt. Mater. 36 (2014) 1561–1565.
[30] C.A. Moore, C.D. McMillen, J.W. Kolis, Cryst. Growth Des. 13 (2013) 2298–2306.
[31] S. Qian, Y. Ma, F. Zan, D. Zou, Z. Dai, G. Zheng, et al., Micro Nano Lett. 8 (2013) 201–205.
[32] L. Mancic, V. Lojpur, B.A. Marinkovic, M.D. Dramicanin, O. Milosevic, Opt. Mater. 35 (2013) 1817–1823.
[33] Y.H. Sang, H.M. Qin, H. Liu, L.L. Zhao, Y.N. Wang, H.D. Jiang, et al., J. Eur. Ceram. Soc. 33 (2013) 2617–2623.
[34] A. Ikesue, K. Kamata, K. Yoshida, J. Am. Ceram. Soc. 79 (1996) 359–364.
[35] A. Ikesue, T. Kinoshita, K. Kamata, K. Yoshida, J. Am. Ceram. Soc. 78 (1995) 1033–1040.
[36] R. Pazik, P. Gluchowski, D. Hreniak, W. Strek, M. Ros, R. Fedyk, et al., Opt. Mater. 30 (2008) 714–718.
[37] K. Serivalsatit, B.Y. Kokuoz, B. Kokuoz, J. Ballato, Opt. Lett. 34 (2009) 1033–1035.
[38] R. Fedyk, D. Hreniak, W. Lojkowski, W. Strek, H. Matysiak, E. Grzanka, et al., Opt. Mater. 29 (2007) 1252–1257.
[39] B.Y. Kokuoz, K. Serivalsatit, B. Kokuoz, O. Geiculescu, E. McCormick, J. Ballato, J. Am. Ceram. Soc. 92 (2009) 2247–2253.
[40] K. Serivalsatit, J. Ballato, J. Am. Ceram. Soc. 93 (2010) 3657–3662.
[41] K. Serivalsatit, B. Kokuoz, B. Yazgan-Kokuoz, M. Kennedy, J. Ballato, J. Am. Ceram. Soc. 93 (2010) 1320–1325.
[42] J. Ballato, K. Serivalsatit, Laser Technol. Def. Security Vii (2011) 8039.
[43] R. Johnson, P. Biswas, P. Ramavath, R.S. Kumar, G. Padmanabham, Trans. Indian Ceram. Soc. 71 (2012) 73–85.
[44] A. Goldstein, J. Eur. Ceram. Soc. 32 (2012) 2869–2886.
[45] M.R. du Merac, H.J. Kleebe, M.M. Muller, I.E. Reimanis, J. Am. Ceram. Soc. 96 (2013) 3341–3365.
[46] A. Goldstein, A. Krell, J. Am. Ceram. Soc. 99 (2016) 3173–3197.
[47] L. Pauling, S.B. Hendricks, J. Am. Chem. Soc. 47 (1925) 781–790.
[48] X.H. Jin, L. Gao, J. Sun, J. Am. Ceram. Soc. 93 (2010) 1232–1236.
[49] A. Krell, P. Blank, H.W. Ma, T. Hutzler, M.P.B. van Bruggen, R. Apetz, J. Am.

SDC EX. 1018 - 56/66

Ceram. Soc. 86 (2003) 12–18.
[50] A. Krell, J. Klimke, J. Am. Ceram. Soc. 89 (2006) 1985–1992.
[51] K. Watzig, T. Hutzler, A. Krell, CFI-Ceram. Forum Int. 86 (2009) E47-E9.
[52] A. Krell, G. Baur, C. Dahne, R.W. Tustison (Ed.), Window and Dome Technologies VIII, SPIE-Int Soc Optical Engineering, Bellingham, 2003, pp. 199–207.
[53] A. Krell, D. Bray, The effects of load, grain size, and grain boundaries on the hardness of alumina, 22nd Annual Conference on Composites, Advanced Ceramics, Materials, and Structures: B, (1998), pp. 159–168.
[54] H. Mizuta, K. Oda, Y. Shibasaki, M. Maeda, M. Machida, K. Ohshima, J. Am. Ceram. Soc. 75 (1992) 469–473.
[55] R. Apetz, M.P.B. van Bruggen, J. Am. Ceram. Soc. 86 (2003) 480–486.
[56] B.N. Kim, K. Hiraga, K. Morita, H. Yoshida, Scr. Mater. 57 (2007) 607–610.
[57] B.N. Kim, K. Hiraga, K. Morita, H. Yoshida, T. Miyazaki, Y. Kagawa, Acta Mater. 57 (2009) 1319–1326.
[58] B.N. Kim, K. Hiraga, K. Morita, H. Yoshida, J. Eur. Ceram. Soc. 29 (2009) 323–327.
[59] J. Petit, P. Dethare, A. Sergent, R. Marino, M.H. Ritti, S. Landais, et al., J. Eur. Ceram. Soc. 31 (2011) 1957–1963.
[60] M. Trunec, K. Maca, R. Chmelik, J. Eur. Ceram. Soc. 35 (2015) 1001–1009.
[61] K. Drdlikova, R. Klement, D. Drdlik, T. Spusta, D. Galusek, K. Maca, J. Eur. Ceram. Soc. 37 (2017) 2695–2703.
[62] M. Suarez, A. Fernandez, J.L. Menendez, R. Torrecillas, Scr. Mater. 61 (2009) 931–934.
[63] I. Alvarez-Clemares, G. Mata-Osoro, A. Fernandez, S. Lopez-Esteban, C. Pecharroman, J. Palomares, et al., Adv. Eng. Mater. 12 (2010) 1154–1160.
[64] M. Stuer, Z. Zhao, U. Aschauer, P. Bowen, J. Eur. Ceram. Soc. 30 (2010) 1335–1343.
[65] N. Roussel, L. Lallemant, B. Durand, S. Guillemet, J.Y.C. Ching, G. Fantozzi, et al., Ceram. Int. 37 (2011) 3565–3573.
[66] S. Grasso, C.F. Hu, G. Maizza, B.N. Kim, Y. Sakka, J. Am. Ceram. Soc. 94 (2011) 1405–1409.
[67] M. Schehl, L.A. Diaz, R. Torrecillas, Acta Mater. 50 (2002) 1125–1139.
[68] J.N. Chen, P.Y. Shen, Scr. Mater. 37 (1997) 1287–1294.
[69] K.C. Yang, P. Shen, D. Gan, J. Eur. Ceram. Soc. 28 (2008) 1169–1176.
[70] S. Grasso, H. Yoshida, H. Porwal, Y. Sakka, M. Reece, Ceram. Int. 39 (2013) 3243–3248.
[71] N. Nishiyama, T. Taniguchi, H. Ohfuji, K. Yoshida, F. Wakai, B.N. Kim, et al., Scr. Mater. 69 (2013) 362–365.
[72] S. Ghanizadeh, S. Grasso, P. Ramanujam, B. Vaidhyanathan, J. Binner, P. Brown, et al., Ceram. Int. 43 (2017) 275–281.
[73] T. Ashikaga, B.N. Kim, H. Kiyono, T.S. Suzuki, J. Eur. Ceram. Soc. 38 (2018) 2735–2741.
[74] X.J. Mao, S.W. Wang, S. Shimai, J.K. Guo, J. Am. Ceram. Soc. 91 (2008) 3431–3433.
[75] H.L. Yi, X.J. Mao, G.H. Zhou, S. Chen, X.Q. Zou, S.W. Wang, et al., Ceram. Int. 38 (2012) 5557–5561.
[76] D. Godlinski, M. Kuntz, G. Grathwohl, J. Am. Ceram. Soc. 85 (2002) 2449–2456.
[77] Y. Yang, Y. Wu, J. Mater. Res. 29 (2014) 2312–2317.
[78] C.L. Zhou, B.X. Jiang, J.T. Fan, X.J. Mao, L.J. Pan, Y.G. Jiang, et al., Ceram. Int. 42 (2016) 1648–1652.
[79] Z. Feng, J.Q. Qi, Y. Han, T.C. Lu, Ceram. Int. 44 (2018) 1059–1065.
[80] D. Drdlik, K. Drdlikova, H. Hadraba, K. Maca, J. Eur. Ceram. Soc. 37 (2017) 4265–4270.
[81] F.M. Liu, D.W. He, Q. Wang, W. Ding, J. Liu, Y.J. Liu, Scr. Mater. 122 (2016) 54–58.
[82] R.W. Rice, J. Am. Ceram. Soc. 54 (1971) 205–207.
[83] T. Ikegami, S.I. Matsuda, H. Suzuki, J. Am. Ceram. Soc. 57 (1974) 507.
[84] D.Y. Chen, E.H. Jordan, M. Gell, Scr. Mater. 59 (2008) 757–759.
[85] Y. Fang, D. Agrawal, G. Skandan, M. Jain, Mater. Lett. 58 (2004) 551–554.
[86] W.H. Rhodes, D.J. Sellers, Am. Ceram. Soc. Bull. 46 (1967) 469.
[87] P.E. Hart, J.A. Pask, J. Am. Ceram. Soc. 54 (1971) 315–316.
[88] A. Kan, T. Moriyama, S. Takahashi, H. Ogawa, J. Appl. Phys. 50 (2011) 09NF2.
[89] K. Itatani, T. Tsujimoto, A. Kishimoto, J. Eur. Ceram. Soc. 26 (2006) 639–645.
[90] R. Chaim, Z.J. Shen, M. Nygren, J. Mater. Res. 19 (2004) 2527–2531.
[91] N. Jiang, R.J. Xie, Q. Liu, J. Li, J. Eur. Ceram. Soc. 37 (2017) 4947–4953.
[92] F.W. Vahldiek, J. Less-Common Metals 13 (1967) 530–540.
[93] Mazdiyas Ks, C.T. Lynch, J.S. Smith, J. Am. Ceram. Soc. 50 (1967) 532–537.
[94] K. Tsukuma, J. Mater. Sci. Lett. 5 (1986) 1143–1144.
[95] P. Duran, P. Recio, J.R. Jurado, C. Pascual, C. Moure, J. Am. Ceram. Soc. 72 (1989) 2088–2093.
[96] V.V. Srdic, M. Winterer, H. Hahn, J. Am. Ceram. Soc. 83 (2000) 729–736.
[97] V.V. Srdic, M. Winterer, H. Hahn, J. Am. Ceram. Soc. 83 (2000) 1853–1860.
[98] U. Anselmi-Tamburini, J.N. Woolman, Z.A. Munir, Adv. Funct. Mater. 17 (2007) 3267–3273.
[99] S.R. Casolco, J. Xu, J.E. Garay, Scr. Mater. 58 (2008) 516–519.
[100] U. Peuchert, Y. Okano, Y. Menke, S. Reichel, A. Ikesue, J. Eur. Ceram. Soc. 29 (2009) 283–291.
[101] J.E. Alaniz, F.G. Perez-Gutierrez, G. Aguilar, J.E. Garay, Opt. Mater. 32 (2009) 62–68.
[102] H.B. Zhang, B.N. Kim, K. Morita, H. Yoshida, J.H. Lim, K. Hiraga, J. Alloys. Compd. 508 (2010) 196–199.
[103] K. Tsukuma, I. Yamashita, T. Kusunose, J. Am. Ceram. Soc. 91 (2008) 813–818.
[104] H. Zhang, B.-N. Kim, K. Morita, H.Y.K. Hiraga, Y. Sakka, Sci. Technol. Adv. Mater. 12 (2011) 055003.
[105] L.W. Lei, Z.Y. Fu, H. Wang, S.W. Lee, K. Niihara, Ceram. Int. 38 (2012) 23–28.
[106] Y. Nigara, J. Appl. Phys. 7 (1968) 404–408.
[107] A. Fukabori, T. Yanagida, J. Pejchal, S. Maeo, Y. Yokota, A. Yoshikawa, et al., J. Appl. Phys. 107 (2010) 073501.
[108] A. Pirri, G. Toci, B. Patrizi, M. Vannini, Ieee J. Sel. Top. Quantum Electron. 24 (2018) 1602108.
[109] X.R. Hou, S.M. Zhou, T.T. Jia, H. Lin, H. Teng, Phys. B Condensed Matter 406 (2011) 3931–3937.
[110] A.L. Micheli, D.F. Dungan, J.V. Mantese, J. Am. Ceram. Soc. 75 (1992) 709–711.
[111] J. Iwasawa, R. Nishimizu, M. Tokita, M. Kiyohara, K. Uematsu, J. Am. Ceram. Soc. 90 (2007) 2327–2332.
[112] R.A. Lefever, J. Matsko, Mater. Res. Bull. 2 (1967) 865–869.
[113] C. Greskovich, J.P. Chernoch, J. Appl. Phys. 44 (1973) 4599–4606.
[114] W.H. Rhodes, J. Am. Ceram. Soc. 64 (1981) 13–19.
[115] N. Saito, S. Matsuda, T. Ikegami, J. Am. Ceram. Soc. 81 (1998) 2023–2028.
[116] T. Ikegami, T. Mori, Y. Yajima, S. Takenouchi, T. Misawa, Y. Moriyoshi, J. Ceram. Soc. Jpn. 107 (1999) 297–299.
[117] Y.H. Huang, D.L. Jiang, J.X. Zhang, Q.L. Lin, J. Am. Ceram. Soc. 92 (2009) 2883–2887.
[118] L.L. Jin, G.H. Zhou, S. Shimai, J. Zhang, S.W. Wang, J. Eur. Ceram. Soc. 30 (2010) 2139–2143.
[119] J. Zhang, L.Q. An, M. Liu, S. Shimai, S.W. Wang, J. Eur. Ceram. Soc. 29 (2009) 305–309.
[120] J. Wang, Y.G. Zhao, D. Yin, P. Liu, J. Ma, Y. Wang, et al., J. Eur. Ceram. Soc. 38 (2018) 1986–1989.
[121] X.R. Hou, S.M. Zhou, T.T. Jia, H. Lin, H. Teng, J. Lumin. 131 (2011) 1953–1958.
[122] S.R. Podowitz, R. Gaume, R.S. Feigelson, J. Am. Ceram. Soc. 93 (2010) 82–88.
[123] L. Gan, Y.J. Park, H. Kim, J.M. Kim, J.W. Ko, J.W. Lee, Opt. Mater. 71 (2017) 109–116.
[124] H. Eilers, J. Eur. Ceram. Soc. 27 (2007) 4711–4717.
[125] J. Mouzon, A. Maitre, L. Frisk, N. Lehto, M. Oden, J. Eur. Ceram. Soc. 29 (2009) 311–316.
[126] L. Gan, Y.J. Park, H. Kim, J.M. Kim, J.W. Ko, J.W. Lee, Ceram. Int. 41 (2015) 9622–9627.
[127] Z.Y. Wang, L. Zhang, H. Yang, J. Zhang, L.X. Wang, Q.T. Zhang, Ceram. Int. 42 (2016) 4238–4245.
[128] A. Kruk, A. Wajler, M. Bobruk, A. Adamczyk, M. Mrozek, W. Gawlik, et al., J. Eur. Ceram. Soc. 37 (2017) 4129–4140.
[129] J. Wang, J. Ma, J. Zhang, P. Liu, D.W. Luo, D.L. Yin, et al., Opt. Mater. 71 (2017) 117–120.
[130] L.L. Zhu, Y.J. Park, L. Gan, S.I. Go, H.N. Kim, J.M. Kim, et al., J. Mater. Sci. Mater. Electron. 28 (2017) 7854–7861.
[131] X.K. Li, Y.Y. Xu, X.J. Mao, Q.Q. Zhu, J.X. Xie, M.H. Feng, et al., Ceram. Int. 44 (2018) 1362–1369.
[132] H. Yoshida, K. Morita, B.-N. Kim, K. Hiraga, K. Yamanaka, K. Soga, et al., J. Am. Ceram. Soc. 94 (2011) 3301–3307.
[133] L.Q. An, A. Ito, T. Goto, J. Eur. Ceram. Soc. 32 (2012) 1035–1040.
[134] H. Furuse, S. Nakasawa, H. Yoshida, K. Morita, T.S. Suzuki, B.N. Kim, et al., J. Am. Ceram. Soc. 101 (2018) 694–702.
[135] B. Ahmadi, S.R. Reza, M. Ahsanzadeh-Vadeqani, M. Barekat, Ceram. Int. 42 (2016) 17081–17088.
[136] M. Hajizadeh-Oghaz, R.S. Razavi, M. Barekat, M. Naderi, S. Malekzadeh, M. Rezazadeh, J. Solgel Sci. Technol. 78 (2016) 682–691.
[137] R.S. Razavi, M. Ahsanzadeh-Vadeqani, M. Barekat, M. Naderi, S.H. Hashemi, A.K. Mishra, Ceram. Int. 42 (2016) 7819–7823.
[138] M. Ahsanzadeh-Vadeqani, R.S. Razavia, M. Barekat, G.H. Borhani, A.K. Mishra, J. Eur. Ceram. Soc. 37 (2017) 2169–2177.
[139] Z.W. Hu, X.D. Xu, J. Wang, P. Liu, D.Z. Li, X.D. Wan, et al., Ceram. Int. 43 (2017) 12057–12060.
[140] C.W. Park, J.H. Lee, S.H. Kang, J.H. Park, H.M. Kim, H.S. Kang, et al., J. Ceram. Process. Res. 18 (2017) 183–187.
[141] Z.W. Hu, X.D. Xu, J. Wang, P. Liu, D.Z. Li, X.D. Wang, et al., J. Eur. Ceram. Soc. 38 (2018) 1981–1985.
[142] H. Yoshida, K. Morita, B.N. Kim, K. Soga, T. Yamamoto, J. Eur. Ceram. Soc. 38 (2018) 1972–1980.
[143] L.L. Zhu, Y.J. Park, L. Gan, H.N. Kim, J.W. Ko, H.D. Kim, J. Eur. Ceram. Soc. 39 (2018) 3255–3260.
[144] H.B. Zhang, B.N. Kim, K. Morita, H. Yoshida, K. Hiraga, Y. Sakka, J. Am. Ceram. Soc. 94 (2011) 3206–3210.
[145] L. Wen, X.D. Sun, Q. Lu, G.X. Xu, X.Z. Hu, Opt. Mater. 29 (2006) 239–245.
[146] Y.H. Huang, D.L. Jiang, J.X. Zhang, Q.L. Lin, Z.R. Huang, Ceram. Int. 37 (2011) 3523–3529.
[147] L.L. Zhu, Y.J. Park, L. Gan, S.I. Go, H.N. Kim, J.M. Kim, et al., Ceram. Int. 43 (2017) 13127–13132.
[148] K. Majima, N. Niimi, M. Watanabe, S. Katsuyama, H. Nagai, J. Jpn. Inst. Met. 57 (1993) 1221–1226.
[149] X.R. Hou, S.M. Zhou, Y.K. Li, W.J. Li, Opt. Mater. 32 (2010) 920–923.
[150] Q. Yi, S. Zhou, H. Teng, H. Lin, X. Hou, T. Jia, J. Eur. Ceram. Soc. 32 (2012) 381–388.
[151] K.J. Ning, J. Wang, D.W. Luo, J. Ma, J. Zhang, Z.L. Dong, et al., Opt. Mater. 50 (2015) 21–24.
[152] K.J. Ning, J. Wang, D.W. Luo, J. Zhang, Z.L. Dong, L.B. Kong, et al., J. Eur. Ceram. Soc. 36 (2016) 253–256.
[153] Y.H. Huang, D.L. Jiang, J.X. Zhang, Q.L. Lin, Z.G. Huang, J. Am. Ceram. Soc. 93 (2010) 2964–2967.
[154] J. Wang, J. Zhang, D.W. Luo, H. Yang, D.Y. Tang, L.B. Kong, J. Eur. Ceram. Soc. 35 (2015) 1011–1019.
[155] C. Gheorghe, A. Lupei, V. Lupei, L. Gheorghe, A. Ikesue, J. Appl. Phys. 105 (2009) 123110.

SDC EX. 1018 - 57/66

[156] Z.F. Dai, Q. Liu, D. Hreniak, J.W. Dai, W. Wang, J. Li, Opt. Mater. 75 (2018) 673–679.
[157] Z.F. Dai, Q. Liu, G. Toci, M. Vannini, A. Pirri, V. Babin, et al., J. Eur. Ceram. Soc. 38 (2018) 1632–1638.
[158] J.G. Li, T. Ikegami, T. Mori, J. Am. Ceram. Soc. 88 (2005) 817–821.
[159] J.G. Li, T. Ikegami, T. Mori, Y. Yajima, J. Am. Ceram. Soc. 87 (2004) 1008–1013.
[160] S. Kuck, L. Fornasiero, E. Mix, G. Huber, J. Lumin. (2000) 87-9:1122-5.
[161] L. Fornasiero, E. Mix, V. Peters, K. Petermann, G. Huber, Cryst. Res. Technol. 34 (1999) 255–260.
[162] A. Lupei, V. Lupei, C. Gheorghe, A. Ikesue, J. Lumin. 128 (2008) 918–920.
[163] L. Longuet, A.C. Bravo, D. Autissier, P. Vissie, J.L. Longuet, S. Lambert, V. Dierolf, Y. Fujiwara, U. Hommerich, P. Ruterana, J.M. Zavada (Eds.), Rare-Earth Doping of Advanced Materials for Photonic Applications, Materials Research Society, Warrendale, 2009, pp. 161–166.
[164] J.G. Li, T. Ikegami, T. Mori, J. Mater. Res. 19 (2004) 733–736.
[165] Y. Wang, B. Lu, X. Sun, T. Sun, H. Xu, Adv. Appl. Ceram. 110 (2011) 95–98.
[166] Q. Liu, Z.F. Dai, D. Hreniak, S.S. Li, W.B. Liu, W. Wang, et al., Opt. Mater. 72 (2017) 482–490.
[167] L.Q. An, A. Ito, T. Goto, J. Eur. Ceram. Soc. 31 (2011) 1597–1602.
[168] Y. Shi, Q.W. Chen, J.L. Shi, Opt. Mater. 31 (2009) 729–733.
[169] Z.F. Wang, W.P. Zhang, L. Lin, B.G. You, Y.B. Fu, M. Yin, Opt. Mater. 30 (2008) 1484–1488.
[170] T. Yanagida, Y. Fujimoto, H. Yagi, T. Yanagitani, Opt. Mater. 36 (2014) 1044–1048.
[171] C. Ma, X.D. Li, S.H. Liu, Q. Zhu, D. Huo, J.G. Li, et al., Ceram. Int. 41 (2015) 9577–9584.
[172] N.L. Wang, X.Y. Zhang, P.H. Wang, J. Alloys. Compd. 652 (2015) 281–286.
[173] N.L. Wang, X.Y. Zhang, P.H. Wang, Mater. Lett. 94 (2013) 5–7.
[174] Q.W. Chen, Y. Shi, L.Q. An, J.Y. Chen, J.L. Shi, J. Am. Ceram. Soc. 89 (2006) 2038–2042.
[175] K. Serivalsatit, T. Wasanapiarnpong, C. Kucera, J. Ballato, Opt. Mater. 35 (2013) 1426–1430.
[176] X.B. Qiao, H.T. Huang, H. Yang, L. Zhang, L. Wang, D.Y. Shen, et al., J. Alloys. Compd. 640 (2015) 51–55.
[177] R.N. Maksimov, V.A. Shitov, A.S. Yurovskikh, Mater. Lett. 211 (2018) 208–211.
[178] Q. Liu, J.B. Li, J.W. Dai, Z.W. Hu, C. Chen, X.P. Chen, et al., Ceram. Int. 40 (2018) 11635–11643.
[179] Z.M. Seeley, J.D. Kuntz, N.J. Cherepy, Opt. Mater. 33 (2011) 1721–1726.
[180] Q. Liu, J.B. Li, J.W. Dai, Z.W. Hu, C. Chen, X.P. Chen, et al., Ceram. Int. 44 (2018) 11635–11643.
[181] W.F. Xie, J. Wang, M.Q. Cao, Z.W. Hu, Y.G. Feng, X.P. Chen, et al., Opt. Mater. 80 (2018) 22–29.
[182] M. Prakasam, O. Viraphong, D. Michau, A. Largeteau, Ceram. Int. 40 (2014) 1859–1864.
[183] R. Boulesteix, R. Epherre, S. Noyau, M. Vandenhende, A. Maitre, C. Salle, et al., Scr. Mater. 75 (2014) 54–57.
[184] M. Guzik, J. Pejchal, A. Yoshikawa, A. Ito, T. Goto, M. Siczek, et al., Cryst. Growth Des. 14 (2014) 3327–3334.
[185] G. Alombert-Goget, Y. Guyot, M. Guzik, G. Boulon, A. Ito, T. Goto, et al., Opt. Mater. 41 (2015) 3–11.
[186] G. Toci, M. Vannini, M. Ciofini, A. Lapucci, A. Pirri, A. Ito, et al., Opt. Mater. 41 (2015) 12–16.
[187] A. Ito, L.Q. An, T. Goto, J. Ceram. Soc. Jpn. 124 (2016) 313–320.
[188] C.W. Xu, C.D. Yang, H. Zhang, Y.M. Duan, H.Y. Zhu, D.Y. Tang, et al., Opt. Express 24 (2016) 20571–20579.
[189] L.Q. An, A. Ito, T. Goto, J. Am. Ceram. Soc. 94 (2011) 695–698.
[190] M. Prakasam, O. Viraphong, D. Michau, P. Veber, M. Velazquez, K. Shimamura, et al., Ceram. Int. 39 (2013) 1307–1313.
[191] G.G. Xu, X.D. Zhang, W. He, H. Liu, H. Li, R.I. Boughton, Mater. Lett. 60 (2006) 962–965.
[192] A. Ikesue, I. Furusato, K. Kamata, J. Am. Ceram. Soc. 78 (1995) 225–228.
[193] X.D. Zhang, H. Liu, W. He, J.Y. Wang, X. Li, R.I. Boughton, J. Cryst. Growth 275 (2005) E1913-E7.
[194] J. Li, Y.S. Wu, Y.B. Pan, W.B. Liu, Y. Zhu, J.K. Guo, J. Ceram. Soc. Jpn. 116 (2008) 572–577.
[195] X.D. Li, J.G. Li, Z.M. Xiu, D. Huo, X.D. Sun, J. Am. Ceram. Soc. 92 (2009) 241–244.
[196] W.X. Zhang, J. Zhou, W.B. Liu, J. Li, L. Wang, B.X. Jiang, et al., J. Alloys. Compd. 506 (2010) 745–748.
[197] W.X. Zhang, Y.B. Pan, J. Zhou, W.B. Liu, J. Li, Y.W. Zou, et al., Ceram. Int. 37 (2011) 1133–1137.
[198] J. Liu, Q. Liu, J. Li, X.W. Ba, W.B. Liu, H.M. Kou, et al., Phys. Status Solidi C: Curr. Top. Solid State Phys. 10 (6) (2013) 933–939.
[199] Q.X. Meng, B.Y. Liang, H.Y. Li, C.H. Su, S.Z. Jin, Int. J. Mater. Res. 104 (2013) 207–209.
[200] Y.L. You, L.H. Qi, H.Z. Miao, W. Pan, Rare Met. Mater. Eng. 42 (2013) 348–350.
[201] X.T. Chen, T.C. Lu, N. Wei, Z.W. Lu, L.J. Chen, Q.H. Zhang, et al., Opt. Mater. 49 (2015) 330–336.
[202] T.Y. Zhou, L. Zhang, Z. Li, S. Wei, J.D. Wu, L.X. Wang, et al., Ceram. Int. 43 (2017) 3140–3146.
[203] L. Zhang, T.Y. Zhou, F.A. Selim, H. Chen, J. Am. Ceram. Soc. 101 (2018) 703–712.
[204] T.Y. Zhou, L. Zhang, S. Wei, L.X. Wang, H. Yang, Z.X. Fu, et al., J. Eur. Ceram. Soc. 38 (2018) 687–693.
[205] J.G. Li, T. Ikegami, J.H. Lee, T. Mori, J. Am. Ceram. Soc. 83 (2000) 961–963.
[206] J.G. Li, J.H. Lee, T. Mori, Y. Yajima, S. Takenouchi, T. Ikegami, J. Ceram. Soc. Jpn. 108 (2000) 439–444.
[207] J.G. Li, T. Ikegami, J.H. Lee, T. Mori, Y. Yajima, J. Eur. Ceram. Soc. 20 (2000) 2395–2405.
[208] L. Wen, X.D. Sun, Z. Xiu, S.W. Chen, C.T. Tsai, J. Eur. Ceram. Soc. 24 (2004) 2681–2688.
[209] T. Tachiwaki, M. Yoshinaka, K. Hirota, T. Ikegami, O. Yamaguchi, Solid State Commun. 119 (2001) 603–606.
[210] Q. Liu, J. Liu, J. Li, M. Ivanov, A. Medvedev, Y.P. Zeng, et al., J. Alloys. Compd. 616 (2014) 81–88.
[211] J. Liu, X.N. Cheng, J. Li, T.F. Xie, M. Ivanov, X.W. Ba, et al., J. Eur. Ceram. Soc. 35 (2015) 3127–3136.
[212] E. Zych, C. Brecher, J. Lumin. 90 (2000) 89–99.
[213] H.M. Wang, J.G. Qi, Z.W. Lu, T.C. Lu, Q.Y. Wang, Scr. Mater. 142 (2018) 126–128.
[214] A. Ikesue, K. Kamata, J. Am. Ceram. Soc. 79 (1996) 1927–1933.
[215] S.H. Lee, S. Kochawattana, G.L. Messing, J.Q. Dumm, G. Quarles, V. Castillo, J. Am. Ceram. Soc. 89 (2006) 1945–1950.
[216] S.H. Lee, E.R. Kupp, A.J. Stevenson, J.M. Anderson, G.L. Messing, X. Li, et al., J. Am. Ceram. Soc. 92 (2009) 1456–1463.
[217] L. Chretien, L. Bonnet, R. Boulesteix, A. Maitre, C. Salle, A. Brenier, J. Eur. Ceram. Soc. 36 (2016) 2035–2042.
[218] S.S. Li, P. Ma, X.W. Zhu, N. Jiang, M. Ivanov, C.Y. Li, et al., Ceram. Int. 43 (2017) 10013–10019.
[219] R. Chaim, R. Marder-Jaeckel, J.Z. Shen, Mater. Sci. Eng. A 429 (2006) 74–78.
[220] R. Chaim, M. Kalina, J.Z. Shen, J. Eur. Ceram. Soc. 27 (2007) 3331–3337.
[221] P. Palmero, B. Bonelli, G. Fantozzi, G. Spina, G. Bonnefont, L. Montanaro, et al., Mater. Res. Bull. 48 (2013) 2589–2597.
[222] R.R. Wang, Y.C. Wang, Z.Y. Fu, H. Wang, W.M. Wang, J.Y. Zhang, et al., J. Eur. Ceram. Soc. 36 (2016) 2153–2156.
[223] X.R. Zhang, G.F. Fan, W.Z. Lu, Y.H. Chen, X.F. Ruan, J. Eur. Ceram. Soc. 36 (2016) 2767–2772.
[224] A. Katz, E. Barraud, S. Lemonnier, E. Sorrel, M. Eichhorn, S. d'Astorg, et al., Ceram. Int. 43 (2017) 15626–15634.
[225] Z.H. Chen, J.T. Li, Z.G. Hu, J.J. Xu, J. Inorg. Mater. 23 (2008) 130–134.
[226] J. Li, Q. Chen, G.Y. Feng, W.J. Wu, D.Q. Xiao, J.G. Zhu, Ceram. Int. 38 (2012) S649-S52.
[227] X.X. Li, B.Y. Zheng, T. Odoom-Wubah, J.L. Huang, Ceram. Int. 39 (2013) 7983–7988.
[228] J. Zhou, W.X. Zhang, L.A. Wang, Y.Q. Shen, J. Li, W.B. Liu, et al., Ceram. Int. 37 (2011) 119–125.
[229] G. Dewith, H.J.A. Vandijk, Mater. Res. Bull. 19 (1984) 1669–1674.
[230] W. Liu, J. Li, B. Jiang, D. Zhang, Y. Pan, J. Alloys. Compd. 512 (2012) 1–4.
[231] H. Yang, X. Qin, J. Zhang, J. Ma, D. Tang, S. Wang, et al., Opt. Mater. 34 (2012) 940–943.
[232] K.A. Appiagyei, G.L. Messing, J.Q. Dumm, Ceram. Int. 34 (2008) 1309–1313.
[233] A.J. Stevenson, X. Li, M.A. Martinez, J.M. Anderson, D.L. Suchy, E.R. Kupp, et al., J. Am. Ceram. Soc. 94 (2011) 1380–1387.
[234] R. Boulesteix, L. Bonnet, A. Maitre, L. Chretien, C. Salle, J. Am. Ceram. Soc. 100 (2017) 945–953.
[235] S.J. Pandey, M. Martinez, J. Hostasa, L. Esposito, M. Baudelet, R. Gaume, Opt. Mater. Express 7 (2017) 1666–1671.
[236] W.B. Liu, W.X. Zhang, J. Li, H.M. Kou, D. Zhang, Y.B. Pan, J. Eur. Ceram. Soc. 31 (2011) 653–657.
[237] Y.K. Li, S.M. Zhou, H. Lin, X.R. Hou, W.J. Li, H. Teng, et al., J. Alloys. Compd. 502 (2010) 225–230.
[238] P.L. Chen, I.W. Chen, J. Am. Ceram. Soc. 79 (1996) 3129–3141.
[239] L. Esposito, A. Piancastelli, J. Eur. Ceram. Soc. 29 (2009) 317–322.
[240] W.B. Liu, W.X. Zhang, J. Li, H.M. Kou, Y.H. Shen, L. Wang, et al., J. Alloys. Compd. 503 (2010) 525–528.
[241] X.T. Chen, T.C. Lu, N.A. Wei, Z.W. Lu, L.J. Chen, Q.H. Zhang, et al., J. Alloys. Compd. 653 (2015) 552–560.
[242] M. Serantoni, A. Piancastelli, A.L. Costa, L. Esposito, Opt. Mater. 34 (2012) 995–1001.
[243] W.B. Liu, W.X. Zhang, J. Li, D. Zhang, Y.B. Pan, Ceram. Int. 38 (2012) 259–264.
[244] E. Cavalli, L. Esposito, J. Hostasa, M. Pedroni, J. Eur. Ceram. Soc. 33 (2013) 1425–1434.
[245] J. Li, F. Chen, W.B. Liu, W.X. Zhang, L. Wang, X.W. Ba, et al., J. Eur. Ceram. Soc. 32 (2012) 2971–2979.
[246] L. Zhang, Y.Z. Li, X.Y. Li, H. Yang, X.B. Qiao, T.Y. Zhou, et al., J. Alloys. Compd. 639 (2015) 244–251.
[247] L. Zhang, H. Yang, X.B. Qiao, T.Y. Zhou, Z.Y. Wang, J. Zhang, et al., J. Eur. Ceram. Soc. 35 (2015) 2391–2401.
[248] L. Zhang, T.Y. Zhou, H. Yang, X.B. Qiao, Z.Y. Wang, J. Zhang, et al., J. Inorg. Mater. 30 (2015) 487–492.
[249] W. Jing, F. Li, Ji X.B. Yu SQ, T. Xu, J. Zhang, et al., J. Eur. Ceram. Soc. 38 (2018) 2454–2461.
[250] Y. Rabinovitch, C. Bogicevic, F. Karolak, D. Tetard, H. Dammak, J. Mater. Process. Technol. 199 (2008) 314–320.
[251] H. Gong, D.Y. Tang, H. Huang, J. Ma, J. Am. Ceram. Soc. 92 (2009) 812–817.
[252] H. Gong, J. Zhang, D.Y. Tang, G.Q. Xie, H. Huang, J. Ma, J. Nanoparticle Res. 13 (2011) 3853–3860.
[253] B.X. Jiang, X. Lu, Y.P. Zeng, S.P. Liu, J. Li, W.B. Liu, et al., Phys. Status Solidi C 10 (2013) 958–961.
[254] Y.K. Liao, D.Y. Jiang, T. Feng, N. Zhang, J. Mater. Sci. 42 (2007) 5406–5410.
[255] D.W. Luo, J. Zhang, C.W. Xu, H. Lin, H. Yang, H.Y. Zhu, et al., Phys. Status Solidi C 10 (2013) 967–968.
[256] D.W. Luo, J. Zhang, C.W. Xu, H. Yang, H. Lin, H.Y. Zhu, et al., Opt. Mater. Express 2 (2012) 1425–1431.
[257] A. Pirri, M. Vannini, V. Babin, M. Nikl, G. Toci, Laser Phys. (2013) 23.

SDC EX. 1018 - 58/66

[258] Y.Q. Shen, X.Q. Feng, V. Babin, M. Nikl, A. Vedda, F. Moretti, et al., Ceram. Int. 39 (2013) 5985–5990.
[259] N. Wagner, B. Herden, T. Dierkes, J. Plewa, T. Justel, J. Eur. Ceram. Soc. 32 (2012) 3085–3089.
[260] W.X. Zhang, J. Li, W.B. Liu, Y.B. Pan, J.K. Guo, Ceram. Int. 35 (2009) 2927–2931.
[261] S. Hu, X.P. Qin, C.H. Lu, G.H. Zhou, Z.Z. Xu, S.W. Wang, J. Am. Ceram. Soc. 98 (2015) 1714–1716.
[262] P.D. Zhang, B.X. Jiang, J.T. Fan, X.J. Mao, L. Zhang, Opt. Mater. Express 5 (2015) 2209–2216.
[263] Y.L. Fu, J. Li, C. Wang, T.F. Xie, W.X. Li, L.X. Wu, et al., J. Alloys. Compd. 664 (2016) 595–601.
[264] C.Y. Ma, F. Tang, J.F. Zhu, Yuan X.Y. Du MM, Y. Yu, et al., J. Am. Ceram. Soc. 99 (2016) 3267–3272.
[265] D. Zhou, Y. Shi, L.C. Fan, D.B. Lin, Z.Q. Sun, J.Y. Xu, J. Inorg. Mater. 31 (2016) 1099–1102.
[266] C.Y. Li, T.F. Xie, Z. Ye, B.Q. Yao, H.M. Kou, Y.B. Pan, et al., J. Am. Ceram. Soc. 100 (2017) 2081–2087.
[267] C.Y. Ma, J.F. Zhu, K. Liu, Z.C. Wen, R. Ma, J.Q. Long, et al., Opt. Mater. 69 (2017) 190–195.
[268] H. Kimura, T. Numazawa, M. Sato, J. Jpn. Inst. Met. 60 (1996) 295–300.
[269] X. Dong, G.Y. Zhang, W.S. Xia, Y.J. Huang, F. Hu, Acta Phys. Sin. 64 (2015) 177502.
[270] J.W. Dai, Y.B. Pan, H.H. Chen, T.F. Xie, H.M. Kou, J. Li, Ceram. Int. 43 (2017) 14457–14463.
[271] J.W. Dai, Y.B. Pan, W. Wang, W. Luo, T.F. Xie, H.M. Kou, et al., Opt. Mater. 73 (2017) 38–44.
[272] X.P. Chen, Z.W. Hu, M.Q. Cao, C. Hu, S.P. Liu, H.H. Chen, et al., J. Eur. Ceram. Soc. 38 (2018) 3246–3254.
[273] M.R. du Merac, H.J. Kleebe, M.M. Muller, I.E. Reimanis, J. Am. Ceram. Soc. 96 (2013) 3341–3365.
[274] I. Ganesh, Int. Mater. Rev. 58 (2013) 63–112.
[275] J.L. Sepulveda, R.O. Loutfy, S.Y. Chang, S. Ibrahim, R.W. Tustison (Ed.), Window and Dome Technologies and Materials XII, SPIE, 2011, p. 801604.
[276] R.J. Bratton, J. Am. Ceram. Soc. 57 (1974) 283–286.
[277] J.G. Li, T. Ikegami, J.H. Lee, T. Mori, J. Am. Ceram. Soc. 83 (2000) 2866–2868.
[278] A.F. Dericioglu, Y. Kagawa, J. Eur. Ceram. Soc. 23 (2003) 951–959.
[279] I. Reimanis, H.J. Kleebe, J. Am. Ceram. Soc. 92 (2009) 1472–1480.
[280] A.F. Dericioglu, A.R. Boccaccini, I. Dlouhy, Y. Kagawa, Mater. Trans. 46 (2005) 996–1003.
[281] C. Wang, Z. Zhao, Scr. Mater. 61 (2009) 193–196.
[282] K. Morita, B.N. Kim, K. Hiraga, H. Yoshida, Scr. Mater. 58 (2008) 1114–1117.
[283] S. Meir, S. Kalabukhov, N. Froumin, M.P. Dariel, N. Frage, J. Am. Ceram. Soc. 92 (2009) 358–364.
[284] N. Frage, S. Cohen, S. Meir, S. Kalabukhov, M.P. Dariel, J. Mater. Sci. 42 (2007) 3273–3275.
[285] M. Sokol, S. Kalabukhov, M.P. Dariel, N. Frage, J. Eur. Ceram. Soc. 34 (2014) 4305–4310.
[286] B.-N. Kim, K. Morita, J.-H. Lim, K. Hiraga, H. Yoshida, J. Am. Ceram. Soc. 93 (2010) 2158–2160.
[287] K. Morita, B.-N. Kim, H. Yoshida, K. Hiraga, J. Am. Ceram. Soc. 92 (2009) 1208–1216.
[288] Y.T. Zou, D.W. He, X.K. Wei, Lu T.C. Yu RC, X.H. Chang, et al., Mater. Chem. Phys. 123 (2010) 529–533.
[289] K. Tsukuma, J. Ceram. Soc. Jpn. 114 (2006) 802–806.
[290] G.R. Villalobos, J.S. Sanghera, I.D. Aggarwal, J. Am. Ceram. Soc. 88 (2005) 1321–1322.
[291] L. Esposito, A. Piancastelli, S. Martelli, J. Eur. Ceram. Soc. 33 (2013) 737–747.
[292] L. Esposito, A. Piancastelli, P. Miceli, S. Martelli, J. Eur. Ceram. Soc. 35 (2015) 651–661.
[293] S.S. Balabanov, R.P. Yavetskiy, A.V. Belyaev, E.M. Gavrishchuk, V.V. Drobotenko, I.I. Evdokimov, et al., Ceram. Int. 41 (2015) 13366–13371.
[294] A. Krell, T. Hutzler, J. Klimke, A. Potthoff, J. Am. Ceram. Soc. 93 (2010) 2656–2666.
[295] Z. Yuan, H. Wang, B.T. Tu, X. Liu, C.L. Xu, W.M. Wang, et al., J. Inorg. Mater. 30 (2015) 843–847.
[296] K. Waetzig, A. Krell, J. Am. Ceram. Soc. 99 (2016) 946–953.
[297] P. Biswas, P. Ramavath, C.S. Kumbhar, D.S. Patil, T.K. Chongdar, N.M. Gokhale, et al., Adv. Eng. Mater. 19 (2017) 1700111.
[298] C. Gajdowski, J. Bohmler, Y. Lorgouilloux, S. Lemonnier, S. d'Astorg, E. Barraud, et al., J. Eur. Ceram. Soc. 37 (2017) 5347–5351.
[299] W. Luo, P. Ma, T.F. Xie, J.W. Dai, Y.B. Pan, H.M. Kou, et al., Opt. Mater. 69 (2017) 152–157.
[300] D. Han, J. Zhang, P. Liu, G. Li, L.Q. An, S.W. Wang, Ceram. Int. 44 (2018) 3189–3194.
[301] A. Rothman, S. Kalabukhov, N. Sverdlov, M.P. Dariel, N. Frage, Int. J. Appl. Ceram. Technol. 11 (2014) 146–153.
[302] P. Fu, Y. Xu, H.H. Shi, B.H. Zhang, X.F. Ruan, W.Z. Lu, Opt. Mater. 36 (2014) 1232–1237.
[303] P. Fu, Y. Xu, X.H. Wang, W.Z. Lu, W. Lei, X.F. Ruan, Int. J. Appl. Ceram. Technol. 12 (2015) 116–123.
[304] R. Boulesteix, A. Maitre, K. Lemanski, P.J. Deren, J. Alloys. Compd. 722 (2017) 358–364.
[305] H. Shahbazi, H. Shokrollahi, M. Tataei, Ceram. Int. 44 (2018) 4955–4960.
[306] G. Bernard-Granger, N. Benameur, C. Guizard, M. Nygren, Scr. Mater. 60 (2009) 164–167.
[307] H.J. Kleebe, I.E. Reimanis, R.L. Cook, C.B. DiAntonio, Processing and microstructure characterization of transparent spinel monoliths, Characterization and Modeling to Control Sintered Ceramic Microstructures and Properties, (2005), pp. 61–68.
[308] A. Goldstein, A. Goldenberg, Y. Yeshurun, M. Hefetz, J. Am. Ceram. Soc. 91 (2008) 4141–4144.
[309] A.C. Sutorik, G. Gilde, J.J. Swab, C. Cooper, R. Gamble, E. Shanholtz, Int. J. Appl. Ceram. Technol. 9 (2012) 575–587.
[310] M. Suarez, V. Rocha, A. Fernandez, J.L. Menendez, R. Torrecillas, Ceram. Int. 40 (2014) 4065–4069.
[311] I.E. Reimanis, K. Rozenburg, H.J. Kleebe, R.L. Cook, R.W. Tustison (Ed.), Window and Dome Technologies and Materials IX, 2005, pp. 48–55.
[312] I.E. Reimanis, H.-J. Kleebe, Int. J. Mater. Res. 98 (2007) 1273–1278.
[313] K. Rozenburg, I.E. Reimanis, H.J. Kleebe, R.L. Cook, J. Am. Ceram. Soc. 90 (2007) 2038–2042.
[314] K. Rozenburg, I.E. Reimanis, H.-J. Kleebe, R.L. Cook, J. Am. Ceram. Soc. 91 (2008) 444–450.
[315] M.R. du Merac, I.E. Reimanis, C. Smith, H.-J. Kleebe, M.M. Mueller, Int. J. Appl. Ceram. Technol. 10 (2013) E33–E48.
[316] A. Goldstein, J. Raethel, M. Katz, M. Berlin, E. Galun, J. Eur. Ceram. Soc. 36 (2016) 1731–1742.
[317] A.C. Sutorik, G. Gilde, C. Cooper, J. Wright, C. Hilton, J. Am. Ceram. Soc. 95 (2012) 1807–1810.
[318] A.C. Sutorik, G. Gilde, J.J. Swab, C. Cooper, R. Gamble, E. Shanholtz, J. Am. Ceram. Soc. 95 (2012) 636–643.
[319] D. Han, J. Zhang, P. Liu, G. Li, S.W. Wang, J. Eur. Ceram. Soc. 38 (2018) 3261–3267.
[320] J.A. Wollmershauser, B.N. Feigelson, E.P. Gorzkowski, C.T. Ellis, R. Goswami, S.B. Qadri, et al., Acta Mater. 69 (2014) 9–16.
[321] G.H. Haertling, J. Am. Ceram. Soc. 82 (1999) 797–818.
[322] J.J. Choi, J. Ryu, H.E. Kim, J. Am. Ceram. Soc. 84 (2001) 1465–1469.
[323] Y. Abe, K. Kakegawa, J. Am. Ceram. Soc. 85 (2002) 473–475.
[324] X. Zeng, X.Y. He, W.X. Cheng, P.S. Qiu, B. Xia, Ceram. Int. 40 (2014) 6197–6202.
[325] G.H. Hertling, J. Am. Ceram. Soc. 54 (1971) 303–309.
[326] P. Sun, C.N. Xu, M. Akiyama, T. Watanabe, J. Am. Ceram. Soc. 82 (1999) 1447–1450.
[327] L.B. Kong, J. Ma, W. Zhu, O.K. Tan, J. Mater. Sci. Lett. 21 (2002) 197–199.
[328] L.B. Kong, J. Ma, T.S. Zhang, R.F. Zhang, J. Mater. Res. 17 (2002) 929–932.
[329] L.B. Kong, J. Ma, H.T. Huang, W. Zhu, O.K. Tan, Mater. Lett. 50 (2001) 129–133.
[330] L.B. Kong, J. Ma, W. Zhu, O.K. Tan, Mater. Res. Bull. 36 (2001) 1675–1685.
[331] L.B. Kong, J. Ma, W. Zhu, O.K. Tan, J. Alloys. Compd. 322 (2001) 290–297.
[332] L.B. Kong, T.S. Zhang, J. Ma, F. Boey, Prog. Mater. Sci. 53 (2008) 207–322.
[333] L.T. Nie, X.Y. He, C.K. Chang, X. Zeng, P.S. Qiu, W.X. Cheng, et al., Opt. Mater. Express 6 (2016) 3565–3573.
[334] Y.J. Wu, J. Li, R. Kimura, N. Uekawa, K. Kakegawa, J. Am. Ceram. Soc. 88 (2005) 3327–3331.
[335] C. Huang, J.M. Xu, Z. Fang, D. Ai, W. Zhou, L. Zhao, et al., J. Alloys. Compd. 723 (2017) 602–610.
[336] X.Y. Chen, R.M. Chen, Z.Y. Chen, J.P. Chen, K.K. Shung, Q.F. Zhou, Ceram. Int. 42 (2016) 18554–18559.
[337] E.V. Colla, E.Y. Koroleva, N.M. Okuneva, S.B. Vakhrushev, Phys. Rev. Lett. 74 (1995) 1681–1684.
[338] L. Qiao, Q. Ye, J.L. Gan, H.W. Cai, R.H. Qu, Opt. Commun. 284 (2011) 3886–3890.
[339] V.V. Shvartsman, A.L. Kholkin, A. Orlova, D. Kiselev, A.A. Bogomolov, A. Sternberg, Appl. Phys. Lett. 86 (2005) 202937.
[340] V.V. Shvartsman, A.L. Kholkin, C. Verdier, D.C. Lupascu, J. Appl. Phys. 98 (2005) 094109.
[341] S.E. Park, T.R. Shrout, J. Appl. Phys. 82 (1997) 1804–1811.
[342] L.S. Kamzina, W. Ruan, G.R. Li, J.T. Zeng, Phys. Solid State 54 (2012) 2024–2029.
[343] L.S. Kamzina, R. Wei, J.T. Zeng, G.R. Li, Phys. Solid State 53 (2011) 1608–1613.
[344] X.L. Tong, K. Lin, D.J. Lv, M.H. Yang, Z.X. Liu, D.S. Zhang, Appl. Surf. Sci. 255 (2009) 7995–7998.
[345] I. Fujii, R. Yoshida, T. Imai, S. Yamazoe, T. Wada, J. Am. Ceram. Soc. 96 (2013) 3782–3787.
[346] W. Ruan, G.R. Li, J.T. Zeng, J.J. Bian, L.S. Kamzina, H.R. Zeng, et al., J. Am. Ceram. Soc. 93 (2010) 2128–2131.
[347] Z.H. Wei, Y.L. Huang, T. Tsuboi, Y. Nakai, J.T. Zeng, G.R. Li, Ceram. Int. 38 (2012) 3397–3402.
[348] W.L. Ji, X.Y. He, X. Zeng, D.Z. Sun, W.X. Cheng, P.S. Qiu, et al., Ferroelectrics 490 (2016) 196–202.
[349] Y.C. Zhang, Z.Z. Song, M.J. Lv, B.L. Yang, L. Wang, C. Chen, et al., J. Mater. Sci. 28 (2017) 15612–15617.
[350] Z.M. Ma, Y.C. Zhang, C.J. Lu, Y.L. Qin, Z.L. Lv, S.J. Lu, J. Mater. Sci. 29 (2018) 6985–6990.
[351] S. Ganesamoorthy, G. Singh, I. Bhaumik, A.K. Karnal, V.S. Tiwari, K. Kitamura, et al., Ferroelectrics 326 (2005) 19–23.
[352] S. Wan, C.S. Lynch, Characterization of PZN Single Crystals, (2001).
[353] L.S. Kamzina, N.N. Krainik, Phys. Solid State 40 (1998) 485–488.
[354] M.L. Mulvihill, L.E. Cross, W.W. Cao, K. Uchino, J. Am. Ceram. Soc. 80 (1997) 1462–1468.
[355] Q.R. Yin, A.L. Ding, X.S. Zheng, P.S. Qiu, M.R. Shen, W.W. Cao, J. Mater. Res. 19 (2004) 729–732.
[356] K.B. Chu, Y. Shi, K. Li, B.J. Fang, J.N. Ding, J. Phys. Chem. Solids 81 (2015) 10–14.
[357] L.Z. Huang, J.T. Zeng, W. Ruan, W. Zhao, K.Y. Zhao, G.R. Li, Ceram. Int. 39 (2013) S171-S4.
[358] Y.H. Huang, D.L. Jiang, J.X. Zhang, Q.L. Lin, Ceram. Int. 36 (2010) 1615–1619.
[359] Y. Kintaka, S. Kuretake, N. Tanaka, K. Kageyama, H. Takagi, J. Am. Ceram. Soc. 93

SDC EX. 1018 - 59/66

(2010) 1114–1119.
[360] K. Li, F.L. Li, Y. Wang, K.W. Kwok, H.L.W. Chan, Mater. Chem. Phys. 131 (2011) 320–324.
[361] F.L. Li, K.W. Kwok, J. Eur. Ceram. Soc. 33 (2013) 123–130.
[362] X. Lin, Z.F. Li, L.F. Shu, J. Ceram. Sci. Technol. 8 (2017) 209–212.
[363] X. Wu, S.B. Lu, K.W. Kwok, J. Alloys. Compd. 695 (2017) 3573–3578.
[364] D. Yang, C. Ma, Z.P. Yang, L.L. Wei, X.L. Chao, Z.Y. Yang, et al., Ceram. Int. 42 (2016) 4648–4657.
[365] S. Tanaka, T. Takahashi, K. Uematsu, J. Eur. Ceram. Soc. 34 (2014) 3723–3728.
[366] H. Schneider, J. Schreuer, B. Hildmann, J. Eur. Ceram. Soc. 28 (2008) 329–344.
[367] K.S. Mazdiyasni, L.M. Brown, J. Am. Ceram. Soc. 55 (1972) 548–552.
[368] S. Prochazka, F.J. Klug, J. Am. Ceram. Soc. 66 (1983) 874–880.
[369] H. Schneider, M. Schmucker, K. Ikeda, W.A. Kaysser, J. Am. Ceram. Soc. 76 (1993) 2912–2914.
[370] Y. Fang, R. Roy, D.K. Agrawal, D.M. Roy, Mater. Lett. 28 (1996) 11–15.
[371] M. Ohashi, H. Tabata, O. Abe, S. Kanzaki, S. Mitachi, T. Kumazawa, J. Mater. Sci. Lett. 6 (1987) 528–530.
[372] G.M. Zhang, Y.C. Wang, Z.Y. Fu, H. Wang, W.M. Wang, J.Y. Zhang, et al., J. Eur. Ceram. Soc. 29 (2009) 2705–2711.
[373] L. Ren, Z.Y. Fu, Y.C. Wang, F. Zhang, J.Y. Zhang, W.M. Wang, et al., Mater. Des. 83 (2015) 753–759.
[374] A. Goldstein, Y. Yeshurun, M. Vulfson, H. Kravits, J. Am. Ceram. Soc. 95 (2012) 879–882.
[375] B.N. Kim, K. Hiraga, A. Jeong, C. Hu, T.S. Suzuki, J.D. Yun, et al., J. Ceram. Soc. Jpn. 122 (2014) 784–787.
[376] Y. Xu, P. Fu, B.H. Zhang, J. Gao, L. Zhang, X.H. Wang, Mater. Lett. 123 (2014) 142–144.
[377] A.V. Belyaev, I.I. Evdokimov, V.V. Drobotenko, A.A. Sorokin, J. Eur. Ceram. Soc. 37 (2017) 2747–2751.
[378] P. Fu, Z.Y. Wang, Z.D. Lin, Y.Q. Liu, V.A.L. Roy, J. Mater. Sci. 28 (2017) 9589–9595.
[379] L. An, A. Ito, T. Goto, Ceram. Int. 38 (2012) 4973–4977.
[380] L. An, A. Ito, T. Goto, J. Eur. Ceram. Soc. 31 (2011) 237–240.
[381] L.Q. An, A. Ito, T. Goto, J. Am. Ceram. Soc. 94 (2011) 3851–3855.
[382] L.Q. An, A. Ito, T. Goto, T. Goto, T. Akatsu (Eds.), Advanced Engineering Ceramics and Composites, Trans Tech Publications Ltd, Stafa-Zurich, 2011, pp. 135–138.
[383] L.Q. An, A. Ito, T. Goto, Opt. Mater. 35 (2013) 817–819.
[384] X.J. Wang, J.J. Xie, Z.J. Wang, G.H. Zhou, Y. Shi, S.W. Wang, et al., Ceram. Int. 44 (2018) 9514–9518.
[385] G.H. Zhou, Z.J. Wang, B.Z. Zhou, Y. Zhao, G.J. Zhang, S.W. Wang, Opt. Mater. 35 (2013) 774–777.
[386] Z.J. Wang, G.H. Zhou, X.P. Qin, Y. Yang, G.J. Zhang, Y. Menke, et al., J. Eur. Ceram. Soc. 33 (2013) 643–646.
[387] D.Y. Gui, Z.K. Cao, W. Han, J.Q. Qi, T.C. Lu, Y. Zou, et al., Ceram. Int. 44 (2018) 7006–7012.
[388] H.L. Yi, Z.J. Wang, G.H. Zhou, J. Zhang, S.W. Wang, Ceram. Int. 42 (2016) 2070–2073.
[389] L.Q. An, A. Ito, T. Goto, Ceram. Int. 39 (2013) 383–387.
[390] L. An, A. Ito, T. Goto, Mater. Lett. 65 (2011) 3167–3169.
[391] C.F. Chen, R.A. Synowicki, M.J. Brand, E.L. Tegtmeier, J.D. Montalvo, J. Ivy, et al., J. Am. Ceram. Soc. 101 (2018) 1847–1856.
[392] A. Chesnaud, C. Bogicevic, F. Karolak, C. Estournes, G. Dezanneau, Chem. Commun. (2007) 1550–1552.
[393] Y. Shen, J. Xu, A. Tok, D. Tang, K.A. Khor, Z. Dong, J. Am. Ceram. Soc. 93 (2010) 3060–3063.
[394] Z.J. Wang, G.H. Zhou, J. Zhang, X.P. Qin, S.W. Wang, Opt. Mater. 71 (2017) 5–8.
[395] J.Q. Qi, Z.Y. Huang, M. Zhou, S.T. Peng, N.N. Ma, T.C. Lu, J. Eur. Ceram. Soc. 38 (2018) 2256–2258.
[396] M. Allix, S. Alahrache, F. Fayon, M. Suchomel, F. Porcher, T. Cardinal, et al., Adv. Mater. 24 (2012) 5570–5575.
[397] S. Alahrache, K. Al Saghir, S. Chenu, E. Veron, D.D.S. Meneses, A.I. Becerro, et al., Chem. Mater. 25 (2013) 4017–4024.
[398] K. Al Saghir, S. Chenu, E. Veron, F. Fayon, M. Suchomel, C. Genevois, et al., Chem. Mater. 27 (2015) 508–514.
[399] A.J. Fernandez-Carrion, K. Al Saghir, E. Veron, A.I. Becerro, F. Porcher, W. Wisniewsld, et al., Inorg. Chem. 56 (2017) 14446–14458.
[400] M. Boyer, X.Y. Yang, A.J.F. Carrion, Q.C. Wang, E. Veron, C. Genevois, et al., J. Mater. Chem. A 6 (2018) 5276–5289.
[401] J.W. McCauley, P. Patel, M.W. Chen, G. Gilde, E. Strassburger, B. Paliwal, et al., J. Eur. Ceram. Soc. 29 (2009) 223–236.
[402] J.W. McCauley, N.D. Corbin, J. Am. Ceram. Soc. 62 (1979) 476–479.
[403] Y.W. Kim, B.H. Park, H.C. Park, Y.B. Lee, K.D. Oh, F.L. Riley, Br. Ceram. Trans. 97 (1998) 97–104.
[404] N. Zhang, B. Liang, X.Y. Wang, H.M. Kan, K.W. Zhu, X.J. Zhao, Mater. Sci. Eng. A 528 (2011) 6259–6262.
[405] Y.C. Shan, J.X. Xu, G. Wang, X.N. Sun, G.H. Liu, J.J. Xu, et al., Ceram. Int. 41 (2015) 3992–3998.
[406] Y.C. Shan, Z.H. Zhang, X.N. Sun, J.J. Xu, Q.H. Qin, J.T. Li, J. Eur. Ceram. Soc. 36 (2016) 671–678.
[407] J.P. Cheng, D. Agrawal, Y.J. Zhang, R. Roy, J. Mater. Sci. Lett. 20 (2001) 77–79.
[408] D. Zientara, M.M. Bucko, J. Lis, J. Eur. Ceram. Soc. 27 (2007) 4051–4054.
[409] D. Clay, D. Poslusny, M. Flinders, S.D. Jacobs, R.A. Cutler, J. Eur. Ceram. Soc. 26 (2006) 1351–1362.
[410] R.S. Kumar, K. Rajeswari, B. Praveen, U.N.S. Hareesh, R. Johnson, J. Am. Ceram. Soc. 93 (2010) 429–435.
[411] N. Jiang, Q. Liu, T.F. Xie, P. Ma, H.M. Kou, Y.B. Pang, et al., J. Eur. Ceram. Soc. 37 (2017) 4213–4216.
[412] F.C. Sahin, H.E. Kanbur, B. Apak, J. Eur. Ceram. Soc. 32 (2012) 925–929.
[413] D. Zientara, M.M. Bucko, J. Lis, J. Eur. Ceram. Soc. 27 (2007) 775–779.
[414] W. Rafaniello, I.B. Cutler, J. Am. Ceram. Soc. 64 (1981) C128-C.
[415] J.Q. Qi, Y.Z. Wang, T.C. Lu, Y. Yu, L. Pan, N.A. Wei, et al., Metallurg. Mater. Trans. A 42A (2011) 4075–4079.
[416] X.Y. Yuan, F. Zhang, X.J. Liu, Z. Zhang, S.W. Wang, J. Inorg. Mater. 26 (2011) 499–502.
[417] X.Y. Yuan, X.J. Liu, F. Zhang, S.W. Wang, J. Am. Ceram. Soc. 93 (2010) 22–24.
[418] X.H. Jin, L. Gao, J. Sun, Y.Q. Liu, L.H. Gui, J. Am. Ceram. Soc. 95 (2012) 2801–2807.
[419] M.Y. Su, Y.F. Zhou, K. Wang, Z.F. Yang, Y.G. Cao, M.C. Hong, J. Eur. Ceram. Soc. 35 (2015) 1173–1178.
[420] Q. Liu, N. Jiang, J. Li, K. Sun, Y.B. Pan, J.K. Guo, Ceram. Int. 42 (2016) 8290–8295.
[421] B.Y. Ma, Y.Z. Wang, W. Zhang, Q.Y. Chen, J. Alloys. Compd. 745 (2018) 617–623.
[422] R.S. Zhang, H. Wang, M. Tian, Y.Z. Wang, M.Y. Liu, H.M. Wang, et al., Ceram. Int. 44 (2018) 17383–17390.
[423] R.S. Zhang, Y.Z. Wang, M. Tian, H. Wang, J. Eur. Ceram. Soc. 38 (2018) 5252–5256.
[424] Y.P. Zhou, D.F. Wang, H.R. Zhuang, S.L. Wen, J.K. Guo, J. Inorg. Mater. 13 (1998) 256-.
[425] L.D. Merkle, A.C. Sutorik, T. Sanamyan, L.K. Hussey, G. Gilde, C. Cooper, et al., Opt. Mater. Express 2 (2012) 78–91.
[426] Y. Xiong, H. Wang, Z.Y. Fu, J. Eur. Ceram. Soc. 33 (2013) 2199–2205.
[427] M. Xiang, Y.F. Zhou, W.T. Xu, X.Q. Li, K. Wang, W. Pan, J. Ceram. Soc. Jpn. 126 (2018) 241–245.
[428] X.L. Su, P.L. Wang, W.W. Chen, B. Zhu, Y.B. Cheng, D.S. Yan, J. Am. Ceram. Soc. 87 (2004) 730–732.
[429] Y. Xiong, Z.Y. Fu, H. Wang, Y.C. Wang, J.Y. Zhang, Q.J. Zhang, Mater. Sci. Eng. A 488 (2008) 475–481.
[430] B. Joshi, H.H. Lee, Y.H. Kim, Z. Fu, K. Niihara, S.W. Lee, Mater. Lett. 80 (2012) 178–180.
[431] B. Joshi, G. Gyawali, H. Wang, T. Sekino, S.W. Lee, J. Alloys. Compd. 557 (2013) 112–119.
[432] Y. Shan, G. Wang, G. Liu, X. Sun, J. Xu, J. Li, Ceram. Int. 40 (2014) 11743–11749.
[433] B. Joshi, B. Li, Y.K. Kshetri, H. Wang, S.W. Lee, Ceram. Int. 40 (2014) 13041–13047.
[434] B. Joshi, Y.K. Kshetri, R. Adhikari, S.W. Lee, Ceram. Int. 41 (2015) 6455–6462.
[435] Y.K. Kshetri, B. Joshi, S.W. Lee, J. Eur. Ceram. Soc. 36 (2016) 4215–4224.
[436] Y.K. Kshetri, B. Joshi, L.A. Diaz-Torres, S.W. Lee, J. Am. Ceram. Soc. 100 (2017) 224–234.
[437] B. Li, B. Joshi, Y.K. Kshetri, R. Adhikari, R. Narro-Gracia, S.W. Lee, Opt. Mater. 39 (2015) 239–246.
[438] B. Joshi, Y.K. Kshetri, G. Gyawali, S.W. Lee, J. Alloys. Compd. 631 (2015) 38–45.
[439] W.W. Yang, J. Hojo, N. Enomoto, Y. Tanaka, M. Inada, J. Am. Ceram. Soc. 96 (2013) 2556–2561.
[440] N. Nishiyama, R. Ishikawa, H. Ohfuji, H. Marquardt, A. Kurnosov, T. Taniguchi, et al., Sci. Rep. 7 (2017) 44755.
[441] S.E. Hatch, R.J. Weagley, W.F. Parsons, Appl. Phys. Lett. 5 (1964) 153–154.
[442] P. Samuel, H. Ishizawa, Y. Ezura, K.I. Ueda, S.M. Babu, Opt. Mater. 33 (2011) 735–737.
[443] P. Aubry, A. Bensalah, P. Gredin, G. Patriarche, D. Vivien, M. Mortier, Opt. Mater. 31 (2009) 750–753.
[444] A. Lyberis, G. Patriarche, P. Gredin, D. Vivien, M. Mortier, J. Eur. Ceram. Soc. 31 (2011) 1619–1630.
[445] M.S. Akchurin, T.T. Basiev, A.A. Demidenko, M.E. Doroshenko, P.P. Fedorov, E.A. Garibin, et al., Opt. Mater. 35 (2013) 444–450.
[446] Z.D. Liu, B.C. Mei, J.H. Song, W.W. Li, J. Am. Ceram. Soc. 97 (2014) 2506–2510.
[447] G. Lu, B.C. Mei, J.H. Song, W.W. Li, R.Z. Xing, Mater. Lett. 115 (2014) 162–164.
[448] Z.D. Liu, B.C. Mei, J.H. Song, W.W. Li, J. Eur. Ceram. Soc. 34 (2014) 4389–4394.
[449] Z.D. Liu, B.C. Mei, J.H. Song, D. Yuan, Z. Wang, J. Alloys. Compd. 646 (2015) 760–765.
[450] Z.C. Sun, B.C. Mei, W.W. Li, Z.D. Liu, L.B. Su, J. Am. Ceram. Soc. 99 (2016) 4039–4044.
[451] X.Y. Liu, B.C. Mei, W.W. Li, Z.C. Sun, Z.D. Liu, L.B. Su, Ceram. Int. 42 (2016) 13285–13290.
[452] W.W. Li, Z.D. Liu, Z.W. Zhou, J.H. Song, B.C. Mei, L.B. Su, J. Eur. Ceram. Soc. 36 (2016) 3481–3486.
[453] W.W. Li, H.J. Huang, B.C. Mei, J.H. Song, Ceram. Int. 43 (2017) 10403–10409.
[454] Z.C. Sun, B.C. Mei, W.W. Li, X.Y. Liu, L.B. Su, Opt. Mater. 71 (2017) 35–40.
[455] F. Xiong, J.H. Song, W.W. Li, B.C. Mei, L.B. Su, Mater. Res. Bull. 95 (2017) 138–145.
[456] W.W. Li, H.J. Huang, B.C. Mei, J.H. Song, X.D. Xu, J. Alloys. Compd. 747 (2018) 359–365.
[457] X.Y. Xie, B.C. Mei, J.H. Song, W.W. Li, L.B. Su, Opt. Mater. 76 (2018) 111–116.
[458] G.Q. Yi, W.W. Li, J.H. Song, B.C. Mei, Z.W. Zhou, L.B. Su, Mater. Res. Bull. 102 (2018) 304–310.
[459] J. Sarthou, P. Aballea, G. Patriarche, H. Serier-Brault, A. Suganuma, P. Gredin, et al., J. Am. Ceram. Soc. 99 (2016) 1992–2000.
[460] W.W. Li, H.J. Huang, B.C. Mei, J.H. Song, G.Q. Yi, X.S. Guo, Mater. Lett. 207 (2017) 37–40.
[461] W.W. Li, B.C. Mei, J.H. Song, W.B. Zhu, G.Q. Yi, J. Alloys. Compd. 660 (2016) 370–374.
[462] P. Wang, M.J. Yang, S. Zhang, R. Tu, T. Goto, L.M. Zhang, J. Eur. Ceram. Soc. 37 (2017) 4103–4107.

SDC EX. 1018 - 60/66

[463] F. Nakamura, T. Kato, G. Okada, N. Kawaguchi, K. Fukuda, T. Yanagida, J. Eur. Ceram. Soc. 37 (2017) 4919–4924.
[464] F. Nakamura, T. Kato, G. Okada, N. Kawaguchi, K. Fukuda, T. Yanagida, Opt. Mater. 72 (2017) 470–475.
[465] F. Nakamura, T. Kato, G. Okada, N. Kawaguchi, K. Fukuda, T. Yanagida, J. Alloys. Compd. 726 (2017) 67–73.
[466] F. Nakamura, T. Kato, G. Okada, N. Kawaguchi, K. Fukuda, T. Yanagida, Ceram. Int. 43 (2017) 7211–7215.
[467] F. Nakamura, T. Kato, G. Okada, N. Kawano, N. Kawaguchi, K. Fukuda, et al., Mater. Res. Bull. 98 (2018) 83–88.
[468] W.W. Li, B.C. Mei, J.H. Song, Z. Wang, Mater. Lett. 159 (2015) 210–212.
[469] W.W. Li, H.J. Huang, B.C. Mei, J.H. Song, Opt. Mater. 75 (2018) 7–12.
[470] J. Liu, P. Liu, J. Wang, X.D. Xu, D.Z. Li, J. Zhang, et al., Materials (2018) 11.
[471] J.M. Luo, S. Sahi, M. Groza, Z.Q. Wang, L. Ma, W. Chen, et al., Opt. Mater. 58 (2016) 353–356.
[472] J.M. Luo, L.F. Ye, J.L. Xu, J. Nanosci. Nanotechnol. 16 (2016) 3985–3989.
[473] T. Kato, G. Okada, K. Fukuda, T. Yanagida, Radiat. Meas. 106 (2017) 140–145.
[474] C.H. Zhu, J.H. Song, B.C. Mei, W.W. Li, Z.D. Liu, Mater. Lett. 167 (2016) 115–117.
[475] A.A. Kaminskii, S.N. Bagaev, K. Ueda, A. Shirakawa, T. Tokurakawa, H. Yagi, et al., Laser Phys. Lett. 6 (2009) 682–687.
[476] S. Goldring, R. Lavi, Opt. Lett. 33 (2008) 669–671.
[477] I. Shoji, S. Kurimura, Y. Sato, T. Taira, A. Ikesue, K. Yoshida, Appl. Phys. Lett. 77 (2000) 939–941.
[478] J.R. Lu, K. Ueda, H. Yagi, T. Yanagitani, Y. Akiyama, A.A. Kaminskii, J. Alloys. Compd. 341 (2002) 220–225.
[479] V. Lupei, N. Pavel, T. Taira, IEEE J. Quantum Electron. 38 (2002) 240–245.
[480] V. Lupei, N. Pavel, T. Taira, Opt. Commun. 201 (2002) 431–435.
[481] H.F. Li, D.G. Xu, Y. Yang, Y.Y. Wang, R. Zhou, T.L. Zhang, et al., Chinese Phys. Lett. 22 (2005) 2565–2567.
[482] D. Kracht, D. Freiburg, R. Wilhelm, M. Frede, C. Fallnich, Opt. Express 14 (2006) 2690–2694.
[483] A. Ikesue, Y.L. Aung, Ieee J. Sel. Top. Quantum Electron. (2018) 24.
[484] R. Huss, R. Wilhelm, C. Kolleck, J. Neumann, D. Kracht, Opt. Express 18 (2010) 13094–13101.
[485] S.J. McNaught, H. Komine, S.B. Weiss, R. Simpson, A.M.F. Johnson, J. Machan, et al., 100 kW Coherently Combined Sab MOPAs, (2009).
[486] A. Mandl, D.E. Klimek, Textron's J-HPSSL 100 kW ThinZag (R) Laser Program, (2010).
[487] R.M. Yamamoto, J.M. Parker, K.L. Allen, R.W. Allmon, K.F. Alviso, C.P.J. Barty, et al., G.L. Wood, M.A. Dubindkii (Eds.), Laser Source Technology for Defense and Security III, 2007, p. 55205.
[488] C.Y. Li, Y. Bo, B.S. Wang, C.Y. Tian, Q.J. Peng, D.F. Cui, et al., Opt. Commun. 283 (2010) 5145–5148.
[489] V. Lupei, N. Pavel, T. Taira, Appl. Phys. Lett. 81 (2002) 2677–2679.
[490] V. Lupei, N. Pavel, T. Taira, Appl. Phys. Lett. (80) (2002) 4309–4311.
[491] V. Lupei, A. Lupei, S. Georgescu, T. Taira, Y. Sato, A. Ikesue, Phys. Rev. B 64 (2001) 092102.
[492] M. Frede, R. Wilhelm, D. Kracht, Opt. Lett. 31 (2006) 3618–3619.
[493] H. Yagi, T. Yanagitani, K. Takaichi, K. Ueda, A.A. Kaminskii, Opt. Mater. 29 (2007) 1258–1262.
[494] Y.B. Wang, B.S. Wang, Y. Bo, J.L. Xu, S. Song, Q.J. Peng, et al., Chinese Opt. Lett. 8 (2010) 1144–1146.
[495] S.S. Zhang, Q.P. Wang, X.Y. Zhang, Z.H. Cong, S.Z. Fan, Z.J. Liu, et al., Laser Phys. Lett. 6 (2009) 864–867.
[496] C.Y. Li, Y. Bo, F. Yang, Z.C. Wang, Y.T. Xu, Y.B. Wang, et al., Opt. Express 18 (2010) 7923–7928.
[497] C.Y. Li, Y. Bo, J.L. Xu, C.Y. Tian, Q.J. Peng, D.F. Cui, et al., Opt. Commun. 284 (2011) 4574–4576.
[498] C.Y. Li, Y. Bo, Y.T. Xu, F. Yang, Z.C. Wang, B.S. Wang, et al., Opt. Commun. 283 (2010) 2885–2887.
[499] Z.P. Wang, H. Liu, J.Y. Wang, Y.H. Lv, Y.H. Sang, R.J. Lan, et al., Opt. Express 17 (2009) 12076–12081.
[500] J.H. Lu, J.R. Lu, T. Murai, K. Takaichi, T. Uematsu, J.Q. Xu, et al., Opt. Lett. 27 (2002) 1120–1122.
[501] S.G.P. Strohmaier, H.J. Eichler, J.F. Bisson, H. Yagi, K. Takaichi, K. Ueda, et al., Laser Phys. Lett. 2 (2005) 383–386.
[502] L. Guo, R.J. Lan, H. Liu, Zhang H.J. Yu HH, J.Y. Wang, et al., Opt. Express 18 (2010) 9098–9106.
[503] Y.M. Duan, H.Y. Zhu, C.W. Xu, H. Yang, D.W. Luo, H. Lin, et al., Appl. Phys. Express 6 (2013) 012701.
[504] L.J. Chen, Z.P. Wang, H. Liu, S.D. Zhuang, Guo L. Yu HH, et al., Opt. Express 18 (2010) 22167–22173.
[505] H. Yagi, T. Yanagitani, H. Yoshida, M. Nakatsuka, K. Ueda, Jpn. J. Appl. Phys. 1 45 (2006) 133–135.
[506] T. Saiki, S. Motokoshi, K. Imasaki, K. Fujioka, H. Fujita, M. Nakatsuka, et al., J. Appl. Phys. 47 (2008) 7896–7902.
[507] T. Saiki, S. Motokoshi, K. Imasaki, K. Fujioka, H. Yoshida, H. Fujita, et al., Opt. Commun. 282 (2009) 1358–1362.
[508] T. Saiki, S. Motokoshi, K. Imasaki, M. Nakatsuka, C. Yamanaka, K. Fujioka, et al., Opt. Commun. 282 (2009) 936–939.
[509] T. Saiki, M. Nakatsuka, K. Fujioka, S. Motokoshi, K. Imasaki, Opt. Commun. 284 (2011) 2980–2984.
[510] H. Yagi, T. Yanagitani, H. Yoshida, M. Nakatsuka, K. Ueda, Opt. Laser Technol. 39 (2007) 1295–1300.
[511] T. Saiki, M. Nakatsuka, K. Imasaki, J. Appl. Phys. 49 (2010) 082702.
[512] T. Ohkubo, T. Yabe, K. Yoshida, S. Uchida, T. Funatsu, B. Bagheri, et al., Opt. Lett. 34 (2009) 175–177.
[513] T.H. Dinh, T. Ohkubo, T. Yabe, Appl. Opt. 53 (2014) 2711–2719.
[514] T.H. Dinh, T. Ohkubo, T. Yabe, H. Kuboyama, Opt. Lett. 37 (2012) 2670–2672.
[515] K. Fujioka, T. Saiki, S. Motokoshi, Y. Fujimoto, H. Fujita, M. Nakatsuka, J. Lumin. 143 (2013) 10–13.
[516] C. Greskovich, J.P. Chernoch, J. Appl. Phys. 45 (1974) 4495–4502.
[517] C. Greskovich, K.N. Woods, Am. Ceram. Soc. Bull. 52 (1973) 473–478.
[518] J.R. Lu, J.H. Lu, T. Murai, K. Takaichi, T. Uematsu, K. Ueda, et al., Jpn. J. Appl. Phys. 2 Lett. 40 (2001) L1277-L9.
[519] J. Lu, K. Takaichi, T. Uematsu, A. Shirakawa, M. Musha, K. Ueda, et al., Appl. Phys. Lett. 81 (2002) 4324–4326.
[520] S. Sattayaporn, G. Aka, P. Loiseau, A. Ikesue, Y.L. Aung, J. Alloys. Compd. 711 (2017) 446–454.
[521] H. Kurokawa, A. Shirakawa, M. Tokurakawa, K. Ueda, S. Kuretake, N. Tanaka, et al., Opt. Mater. 33 (2011) 667–669.
[522] J.W.W. Zhang, Y.Y.K. Zou, Q.S. Chen, R.F. Zhang, K.W.K. Li, H. Jiang, et al., Appl. Phys. Lett. 89 (2006) 061113.
[523] H. Zhao, X.D. Sun, J.W. Zhang, Y.K. Zou, K.W. Li, Y.Y. Wang, et al., Opt. Express 19 (2011) 2965–2971.
[524] A. Ikesue, K. Kamata, K. Yoshida, J. Am. Ceram. Soc. 78 (1995) 2545–2547.
[525] A. Ikesue, K. Yoshida, K. Kamata, J. Am. Ceram. Soc. 79 (1996) 507–509.
[526] H. Yagi, K. Takaichi, K. Ueda, T. Yanagitani, A.A. Karninskii, Opt. Mater. 29 (2006) 392–396.
[527] J.J. Degnan, IEEE J. Quantum Electron. 31 (1995) 1890–1901.
[528] Y. Kalisky, O. Kalisky, U. Rachum, G. Boulon, A. Brenier, Ieee J. Sel. Top. Quantum Electron. 13 (2007) 502–510.
[529] Y. Kalisky, Prog. Quantum Electron. 28 (2004) 249–303.
[530] Y. Kalisky, L. Kravchik, M.R. Kokta, Opt. Mater. 24 (2004) 607–614.
[531] Y. Kalisky, C. Labbe, K. Waichman, L. Kravchik, U. Rachum, P. Deng, et al., Opt. Mater. 19 (2002) 403–413.
[532] H. Sakai, H. Kan, T. Taira, Opt. Express 16 (2008) 19891–19899.
[533] K. Takaichi, J.R. Lu, T. Murai, T. Uematsu, A. Shirakawa, K. Ueda, et al., Jpn. J. Appl. Phys. 2 Lett. 41 (2002) L96-L8.
[534] R. Lan, Z. Wang, H. Liu, H. Yu, L. Guo, L. Chen, et al., Laser Phys. 20 (2010) 187–191.
[535] J. Kong, Z.Z. Zhang, D.Y. Tang, G.Q. Xie, C.C. Chan, Y.H. Shen, Laser Phys. 18 (2008) 1508–1511.
[536] Y. Feng, J.R. Lu, K. Takaichi, K. Ueda, H. Yagi, T. Yanagitani, et al., Appl. Opt. 43 (2004) 2944–2947.
[537] H.H. Yu, H.J. Zhang, Z.P. Wang, J.Y. Wang, Y.G. Yu, X.Y. Zhang, et al., Appl. Phys. Lett. 94 (2009) 041126.
[538] T. Saiki, S. Motokoshi, K. Imasaki, K. Fujioka, H. Yoshida, H. Fujita, et al., J. Appl. Phys. 48 (2009) 122501.
[539] N. Pavel, M. Tsunekane, T. Taira, Opt. Express 19 (2011) 9378–9384.
[540] T. Omatsu, A. Minassian, M.J. Damzen, Opt. Commun. 282 (2009) 4784–4788.
[541] P. Li, X.H. Chen, H.N. Zhang, Q.P. Wang, Laser Phys. 21 (2011) 1708–1711.
[542] T. Omatsu, K. Miyamoto, M. Okida, A. Minassian, M.J. Damzen, Appl. Phys. B 101 (2010) 65–70.
[543] J. Dong, K. Ueda, H. Yagi, A.A. Kaminskii, Opt. Rev. 15 (2008) 57–74.
[544] Y. Ren, J. Dong, Opt. Commun. 312 (2014) 163–167.
[545] J. Li, Y.S. Wu, Y.B. Pan, H.M. Kou, Y. Shi, J.K. Guo, Ceram. Int. 34 (2008) 1675–1679.
[546] J. Li, Y. Wu, Y. Pan, J. Guo, J. Non. Solids 352 (2006) 2404–2407.
[547] W.J. Ling, S.G. Zhang, M.X. Zhang, Z. Dong, K. Li, Y.Y. Zuo, et al., Chinese Phys. Lett. (2010) 27.
[548] A.S. Shcherbakov, A.Y. Kosarsky, P. Moreno Zarate, J. Campos Acosta, Y.V. Il'in, I.S. Tarasov, Optik 122 (2011) 136–141.
[549] A.K. Wojcik, P. Malara, R. Blanchard, T.S. Mansuripur, F. Capasso, A. Belyanin, Appl. Phys. Lett. (2013) 103.
[550] K. Yin, B.B. Zhang, W.Q. Yang, H. Chen, S.P. Chen, J. Hou, Opt. Lett. 39 (2014) 4259–4262.
[551] W.D. Tan, F. Chen, R.J. Knize, J. Zhang, D. Tang, L.-J. Li, Opt. Mater. 33 (2011) 679–683.
[552] W.D. Tan, C.Y. Su, R.J. Knize, G.Q. Xie, L.J. Li, D.Y. Tang, Appl. Phys. Lett. 96 (2010) 031106.
[553] L. Guo, W. Hou, H.B. Zhang, Z.P. Sun, D.F. Cui, Z.Y. Xu, et al., Opt. Express 13 (2005) 4085–4089.
[554] J.A. Wisdom, D.S. Hum, M.J.F. Digonnet, A. Ikesue, M.M. Fejer, R.L. Byer, S. Jiang, M.J.F. Digonnet (Eds.), Optical Components and Materials IV, 2007 C4690-C.
[555] E. Martin-Rodriguez, P. Molina, A. Benayas, L.E. Bausa, J. Garcia Sole, D. Jaque, Opt. Mater. 31 (2009) 725–728.
[556] Y. Sato, J. Saikawa, T. Taira, A. Ikesue, Opt. Mater. 29 (2007) 1277–1282.
[557] H. Okada, M. Tanaka, H. Kiriyama, Y. Nakai, Y. Ochi, A. Sugiyama, et al., Opt. Lett. 35 (2010) 3048–3050.
[558] Y.L. Fu, L. Ge, J. Li, Y. Liu, M. Ivanov, L. Liu, et al., Opt. Mater. 71 (2017) 90–97.
[559] C.Y. Ma, J.F. Zhu, Z.Q. Hu, Z.C. Wen, J.Q. Long, X.Y. Yuan, et al., IEEE Photonics J. (2017) 9.
[560] G.Q. Xie, D.Y. Tang, W.D. Tan, H. Luo, H.J. Zhang, H.H. Yu, et al., Opt. Lett. 34 (2009) 103–105.
[561] H. Luo, D.Y. Tang, G.Q. Xie, W.D. Tan, H.J. Zhang, H.H. Yu, Opt. Commun. 282 (2009) 291–293.
[562] G.Q. Xie, L.J. Qian, P. Yuan, D.Y. Tang, W.D. Tan, H.H. Yu, et al., Laser Phys. Lett. 7 (2010) 483–486.
[563] H. Chen, D.Y. Shen, J. Zhang, H. Yang, D.Y. Tang, T. Zhao, et al., Opt. Lett. 36 (2011) 1575–1577.

SDC EX. 1018 - 61/66

[564] T. Zhao, H. Chen, D.Y. Shen, Y. Wang, X.F. Yang, J. Zhang, et al., Opt. Mater. 35 (2013) 712–714.
[565] S.N. Bagayev, V.V. Osipov, S.M. Vatnik, V.A. Shitov, I.A. Vedin, V.V. Platonov, et al., Opt. Mater. 50 (2015) 47–51.
[566] J.H. Yuan, X.M. Duan, B.Q. Yao, J. Li, Z. Cui, Y.J. Shen, et al., Appl. Phys. B 119 (2015) 381–385.
[567] X.M. Duan, J.H. Yuan, Z. Cui, B.Q. Yao, T.Y. Dai, J. Li, et al., Appl. Opt. 55 (2016) 1953–1956.
[568] Y.C. Wang, R.J. Lan, X. Mateos, J. Li, C. Hu, C.Y. Li, et al., Opt. Express 24 (2016) 18003–18012.
[569] B.J. Fei, W. Guo, J.Q. Huang, Q.F. Huang, J. Chen, J.T. Li, et al., Opt. Mater. Express 3 (2013) 2037–2044.
[570] Y. Zhang, B.Q. Yao, Z. Cui, J. Li, H. Li, T.F. Xie, et al., Appl. Phys. B 123 (2017) 28.
[571] Y.G. Zhao, J. Wang, W.C. Yao, Z.H. Shao, C.F. Shen, D.L. Yin, et al., IEEE Photonics J. 10 (2018) 1502107.
[572] W. Jing, P. Loiko, J. Maria Serres, Y.C. Wang, E. Kifle, E. Vilejshikova, et al., J. Lumin. 203 (2018) 145–151.
[573] N. Ter-Gabrielyan, L.D. Merkle, E.R. Kupp, G.L. Messing, M. Dubinskii, Opt. Lett. 35 (2010) 922–924.
[574] D.Y. Shen, H. Chen, X.P. Qin, J. Zhang, D.Y. Tang, X.F. Yang, et al., Appl. Phys. Express 4 (2011) 052701.
[575] C. Zhang, D.Y. Shen, Y. Wang, L.J. Qian, J. Zhang, X.P. Qin, et al., Opt. Lett. 36 (2011) 4767–4769.
[576] X.Q. Zhang, D.Y. Shen, H.T. Huang, J. Liu, X. Liu, J.N. Zhang, et al., Opt. Express 22 (2014) 7154–7159.
[577] S. Bigotta, L. Galecki, A. Katz, J. Bohmler, S. Lemonnier, E. Barraud, et al., Opt. Express 26 (2018) 3435–3442.
[578] T.Y. Dai, Y. Deng, Y.L. Ju, B.Q. Yao, X.M. Duan, Y.Z. Wang, Quantum Elec. 45 (2015) 1098–1100.
[579] H.T. Huang, D.Y. Shen, J. Zhang, D.Y. Tang, J. Nonlinear Opt. Phys. Mater. 24 (2015) 1550001.
[580] X.Q. Zhang, D.Y. Shen, H.T. Huang, J. Liu, J. Zhang, D.Y. Tang, et al., Appl. Phys. B 120 (2015) 305–309.
[581] L. Wang, H.T. Huang, X.J. Ren, J. Wang, D.Y. Shen, Y.G. Zhao, et al., Ieee J. Sel. Top. Quantum Electron. 24 (2018) 1600906.
[582] L. Wang, H.T. Huang, D.Y. Shen, J. Zhang, H. Chen, D.Y. Tang, Laser Phys. Lett. 14 (2017) 045803.
[583] L. Wang, H.T. Huang, D.Y. Shen, J. Zhang, H. Chen, Y. Wang, et al., Opt. Express 22 (19495) (2014) -503.
[584] H. Uehara, S. Tokita, J. Kawanaka, D. Konishi, M. Murakami, S. Shimizu, et al., Opt. Express 26 (2018) 3497–3507.
[585] L. Wang, H.T. Huang, D.Y. Shen, J. Zhang, D.Y. Tang, Appl. Sci. Basel 8 (2018) 801.
[586] X.J. Cheng, J.Q. Xu, W.X. Zhang, B.X. Jiang, Y.B. Pan, Chinese Phys. Lett. 26 (2009) 074204.
[587] W.-X. Zhang, Y.-B. Pan, J. Zhou, W.-B. Liu, J. Li, B.-X. Jiang, et al., J. Am. Ceram. Soc. 92 (2009) 2434–2437.
[588] Y.W. Zou, Y.D. Zhang, X. Zhong, Z.Y. Wei, W.X. Zhang, B.X. Jiang, et al., Chinese Phys. Lett. 27 (2010) 074213.
[589] S.Y. Zhang, X. Wang, W.J. Kong, Q.L. Yang, J.Q. Xu, B.X. Jiang, et al., Opt. Commun. 286 (2013) 288–290.
[590] Y. Wang, D.Y. Shen, H. Chen, J. Zhang, X.P. Qin, D.Y. Tang, et al., Opt. Lett. 36 (2011) 4485–4487.
[591] M.J. Zhan, Y.W. Zou, Q.F. Lin, Z.H. Wang, H.N. Han, L. Lu, et al., Acta Phys. Sin. (2014) 63.
[592] X.L. Liu, H.T. Huang, D.Y. Shen, X. Liu, X.Q. Zhang, J. Liu, et al., Opt. Eng. (2014) 53.
[593] X. Liu, H.T. Huang, D.Y. Shen, H.Y. Zhu, J. Zhang, D.Y. Tang, Opt. Express 23 (2015) 7619–7629.
[594] H.Y. Zhu, Y.C. Zhang, J. Zhang, Y.J. Zhang, Y.M. Duan, X.K. Ruan, et al., IEEE Photonics J. 9 (2017) 1506607.
[595] P. Liu, L. Jin, X. Liu, H.T. Huang, J. Zhang, D.Y. Tang, et al., IEEE Photonics J. (2016) 8.
[596] O.L. Antipov, S.Y. Golovkin, O.N. Gorshkov, N.G. Zakharov, A.P. Zinovev, A.P. Kasatkin, et al., Quantum Elec. 41 (2011) 863–868.
[597] E.J. Saarinen, E. Vasileva, O. Antipov, J.P. Penttinen, M. Tavast, T. Leinonen, et al., Opt. Express 21 (2013) 23844–23850.
[598] H. Wang, H.T. Huang, P.A. Liu, L. Jin, D.Y. Shen, J. Zhang, et al., Opt. Mater. Express 7 (2017) 296–303.
[599] W. Jing, P. Loiko, J.M. Serres, Y.C. Wang, E. Vilejshikova, M. Aguilo, et al., Opt. Mater. Express 7 (2017) 4192–4202.
[600] Y.C. Wang, W. Jing, P. Loiko, Y.G. Zhao, H. Huang, X. Mateos, et al., Opt. Express 26 (2018) 10299–10304.
[601] S. Chenais, F. Druon, S. Forget, F. Balembois, P. Georges, Prog. Quantum Electron. 30 (2006) 89–153.
[602] K. Takaichi, H. Yagi, J. Lu, A. Shirakawa, K. Ueda, T. Yanagitani, et al., Phys. Status Solidi A 200 (2003) R5–R7.
[603] J. Dong, A. Shirakawa, Ueda K-i, H. Yagi, T. Yanagitani, A.A. Kaminskii, Appl. Phys. Lett. 89 (2006) 091114.
[604] S. Nakamura, H. Yoshioka, Y. Matsubara, T. Ogawa, S. Wada, Opt. Commun. 281 (2008) 4411–4414.
[605] Q. Hao, W. Li, H. Pan, X. Zhang, B. Jiang, Y. Pan, et al., Opt. Express 17 (2009) 17734–17738.
[606] B.B. Zhou, Z.Y. Wei, Y.W. Zou, Y.D. Zhang, X. Zhong, G.L. Bourdet, et al., Opt. Lett. 35 (2010) 288–290.
[607] A. Pirri, G. Toci, D. Alderighi, M. Vannini, Opt. Express 18 (2010) 17262–17272.
[608] D.W. Luo, J. Zhang, C.W. Xu, X.P. Qin, D.Y. Tang, J. Ma, Opt. Mater. 34 (2012) 936–939.
[609] A. Agnesi, L. Carra, F. Pirzio, G. Reali, S. Veronesi, J.T. Thomas, et al., Opt. Commun. 315 (2014) 208–212.
[610] F. Tang, W.C. Wang, X.Y. Yuan, C. Zhu, J.Q. Huang, C.Y. Ma, et al., J. Alloys. Compd. 593 (2014) 123–127.
[611] H.Y. Zhu, D.Y. Tang, Y.M. Duan, D.W. Luo, J. Zhang, Opt. Express 21 (2013) 26955–26961.
[612] D.W. Luo, C.W. Xu, J. Zhang, X.P. Qin, H. Yang, W.D. Tan, et al., Laser Phys. Lett. 8 (2011) 719–722.
[613] C.W. Xu, D.Y. Tang, H.Y. Zhu, J. Zhang, Laser Phys. Lett. 10 (2013) 095702.
[614] C.W. Xu, D.W. Luo, J. Zhang, H. Yang, X.P. Qin, W.D. Tan, et al., Laser Phys. Lett. 9 (2012) 30–34.
[615] J.F. Zhu, K. Liu, J. Li, J.L. Wang, Y. Yu, H.B. Wang, et al., Chinese Phys. B 26 (2017) 054213.
[616] A. Pirri, G. Toci, J. Li, T.F. Xie, Y.B. Pan, V. Babin, et al., Opt. Mater. 73 (2017) 312–318.
[617] C.Y. Ma, F. Tang, Z.C. Wen, Zhang J.T. Du MM, J.Q. Long, et al., Ceram. Int. 41 (2015) 14635–14640.
[618] J. Ma, J. Wang, D.Y. Shen, A. Ikesue, D.Y. Tang, Chinese Opt. Lett. 15 (2017) 121403.
[619] A. Pirri, G. Toci, J. Li, Y.G. Feng, T.F. Xie, Z.X. Yang, et al., Materials 11 (2018) 837.
[620] J. Kong, J. Lu, K. Takaichi, T. Uematsu, K. Ueda, D.Y. Tang, et al., Appl. Phys. Lett. 82 (2003) 2556–2558.
[621] J. Kong, D.Y. Tang, J. Lu, K. Ueda, H. Yagi, T. Yanagitani, Opt. Commun. 237 (2004) 165–168.
[622] K. Takaichi, H. Yagi, J.R. Lu, J.F. Bisson, A. Shirakawa, K. Ueda, et al., Appl. Phys. Lett. 84 (2004) 317–319.
[623] J. Kong, D.Y. Tang, C.C. Chan, J. Lu, K. Ueda, H. Yagi, et al., Opt. Lett. 32 (2007) 247–249.
[624] J. Lu, J.F. Bisson, K. Takaichi, T. Uematsu, A. Shirakawa, M. Musha, et al., Appl. Phys. Lett. 83 (2003) 1101–1103.
[625] P. Aballea, A. Suganuma, F. Druon, J. Hostalrich, P. Georges, P. Gredin, et al., Optica 2 (2015) 288–291.
[626] S.X. Li, G.Q. Li, S.Z. Zhao, X.M. Wang, K.J. Yang, D.C. Li, et al., Opt. Quantum Electron. 46 (2014) 1179–1186.
[627] S.Q. Zhu, Q. He, S.F. Wang, Z.Q. Chen, A.M. Li, H. Yin, et al., J. Laser Appl. (2014) 26.
[628] W. Jiang, S. Zhu, Z.Q. Chen, Q. He, Z. Chen, S. Wang, et al., J. Appl. Spectrosc. 80 (2013) 694–697.
[629] J.Y. Meng, H.X. Wang, Laser Phys. 21 (2011) 79–81.
[630] L. Yin, G.Q. Li, S.Z. Zhao, X. Li, K. Cheng, G. Zhang, Laser Phys. 21 (2011) 1151–1154.
[631] J. Ma, J. Dong, Ueda Ki, A.A. Kaminskii, Appl. Phys. B 105 (2011) 749–760.
[632] G. Salamu, A. Ionescu, C.A. Brandus, O. Sandu, N. Pavel, T. Dascalu, Laser Phys. 22 (2012) 68–73.
[633] F. Tang, Y.G. Cao, J.Q. Huang, W. Guo, H.G. Liu, W.C. Wang, et al., Laser Phys. Lett. 9 (2012) 564–569.
[634] A. Ikesue, Y.L. Aung, J. Am. Ceram. Soc. 89 (2006) 1936–1944.
[635] W.B. Liu, Y.P. Zeng, J. Li, Y. Shen, Y. Bo, N. Zong, et al., J. Alloys. Compd. 527 (2012) 66–70.
[636] C.Y. Ma, F. Tang, H.F. Lin, W.D. Chen, G. Zhang, Y.G. Cao, et al., J. Alloys. Compd. 640 (2015) 317–320.
[637] K. Jia, Y. Jiang, F. Yang, B. Deng, T.J. Hou, J.W. Guo, et al., Laser Phys. 26 (2016) 115801.
[638] M. Li, H. Hu, Q.S. Gao, J.T. Wang, J. Zhang, Y.C. Wu, et al., IEEE Photonics J. 9 (2017) 1503010.
[639] M. Tsunekane, T. Taira, Jpn. J. Appl. Phys. 2 Lett. 44 (2005) 1164–1167.
[640] C. Wang, W.X. Li, D.B. Bai, J. Zhao, J. Li, X.W. Ba, et al., Ieee Photonics Technol. Lett. 28 (2016) 433–436.
[641] L. Esposito, J. Hostasa, A. Piancastelli, G. Toci, D. Alderighi, M. Vannini, et al., J. Mater. Chem. C 2 (2014) 10138–10148.
[642] F. Tang, Y. Cao, J. Huang, H. Liu, W. Guo, W. Wang, J. Am. Ceram. Soc. 95 (2012) 56–59.
[643] J. Dong, Ueda K-i, A. Shirakawa, H. Yagi, T. Yanagitani, A.A. Kaminskii, Opt. Express 15 (2007) 14516–14523.
[644] W.B. Liu, J. Li, J. Liu, B.L. Liu, Y.L. Fu, Y.B. Pan, et al., Ceram. Int. 40 (2014) 8879–8883.
[645] F. Tang, Y.G. Cao, J.Q. Huang, W. Guo, H.G. Liu, Q.F. Huang, et al., J. Eur. Ceram. Soc. 32 (2012) 3995–4002.
[646] E.R. Kupp, G.L. Messing, J.M. Anderson, V. Gopalan, J.Q. Dumm, C. Kraisinger, et al., J. Mater. Res. 25 (2010) 476–483.
[647] B.Q. Yao, X.L. Li, T.Y. Dai, Z. Cui, S. Bai, H.Y. Yang, et al., Opt. Lett. 41 (2016) 254–256.
[648] P.D. Zhang, B.X. Jiang, Y.G. Jiang, G. Zhang, S.L. Chen, J.T. Fan, et al., J. Am. Ceram. Soc. 100 (2017) 5030–5037.
[649] C.Y. Ma, J.F. Zhu, X. Nan, Z.Q. Hu, Z.C. Wen, J.Q. Long, et al., J. Alloys. Compd. 727 (2017) 912–918.
[650] C.Y. Ma, J.F. Zhu, K. Liu, F. Tang, J.Q. Long, Z.C. Wen, et al., Opt. Lett. 41 (2016) 3317–3319.
[651] A. Krell, T. Hutzler, J. Klimke, CFI-Ceram. Forum Int. 84 (2007) E50-E6.
[652] A. Krell, T. Hutzler, J. Klimke, CFI-Ceram. Forum Int. 84 (2007) E41–E50.
[653] A. Krell, E. Strassburger, Am. Ceram. Soc. Bull. 86 (2007) 9201–9207.
[654] J.J. de Groot, J. van Vliet (Eds.), The High-Pressure Sodium Lamp. Macmillan, London, 1986.

SDC EX. 1018 - 62/66

[655] K.E. Brown, A.G. Chalmers, D.O. Wharmby, J. Illum. Eng. Soc. 11 (1982) 106–114.
[656] S. Carleton, P.A. Seinen, J. Stoffels, J. Illum. Eng. Soc. 26 (1997) 139–145.
[657] S. Jungst, D. Lang, M. Galvez, G. Zissis (Ed.), Light Sources 2004, 2004, pp. 115–124.
[658] K. Hayashi, O. Kobayashi, S. Toyoda, K. Morinaga, Mater. Trans. Jim 32 (1991) 1024–1029.
[659] G.C. Wei, J. Phys. D 38 (2005) 3057–3065.
[660] G.C. Wei, J. Eur. Ceram. Soc. 29 (2009) 237–244.
[661] G.C. Wei, G. Zissis (Ed.), Light Sources 2004, IOP Publishing Ltd, Bristol, 2004, pp. 169–170.
[662] G.C. Wei, W.P. Lapatovich, J. Browne, R. Snellgrove, J. Phys. D 41 (2008) 144014.
[663] C. Scott, M. Kaliszewski, C. Greskovich, L. Levinson, J. Am. Ceram. Soc. 85 (2002) 1275–1280.
[664] G.S. Thompson, P.A. Henderson, M.P. Harmer, G.C. Wei, W.H. Rhodes, J. Am. Ceram. Soc. 87 (2004) 1879–1882.
[665] W.P. Lapatovich, J.S. Cohen, S. Mazevet, D.P. Kilcrease (Eds.), Atomic Processes in Plasmas, 2004, pp. 255–264.
[666] K. Hayashi, O. Kobayashi, S. Toyoda, K. Morinaga, Mater. Trans. JIM 32 (1991) 1024–1029.
[667] G.C. Wei, et al., M. Matsui, S. Jahanmir, H. Mostaghaci, M. Naito, K. Uematsu, R. Wasche (Eds.), Improved Ceramics Through New Measurements, Processing, and Standards, 2002, pp. 135–144.
[668] L.M. Goldman, R. Foti, M. Smith, U. Kashalikar, S. Sastri, J.J. Swab (Ed.), Advances in Ceramic Armor V, 2010, pp. 225–232.
[669] L.M. Goldman, T.M. Hartnett, J.M. Wahl, R.J. Ondercin, K. Olson, R.W. Tustison (Ed.), Window and Dome Technologies and Materials VII, SPIE-Int Soc Optical Engineering, Bellingham, 2001, pp. 71–78.
[670] L.M. Goldman, R. Twedt, S. Balasubramanian, S. Sastri, Window Dome Technol. Mater. XII 8016 (2011) 801608.
[671] T.M. Hartnett, S.D. Bernstein, E.A. Maguire, R.W. Tustison, Infrared Phys. Technol. 39 (1998) 203–211.
[672] H.W. Jiang, Tian T.Y. Du HB, H. Wu, W. Pan, J.H. Gong (Eds.), Chinese Ceramics Communications, 2010, pp. 580–581.
[673] J.Q. Qi, Y.Z. Wang, T.C. Lu, Y. Yu, L. Pan, N. Wei, et al., Metallurg. Mater. Trans. A 42A (2011) 4075–4079.
[674] J.Q. Qi, J.C. Zhou, W. Pang, J.F. He, Y.Y. Su, Z.J. Liao, et al., Rare Met. Mater. Eng. 36 (2007) 88–91.
[675] J.W. McCauley, N.D. Corbin, J. Am. Ceram. Soc. 62 (1979) 476–479.
[676] H.X. Willems, Hendrix MMRM, G. de With, R. Metselaar, J. Eur. Ceram. Soc. 10 (1992) 327–337.
[677] H.X. Willems, Hendrix MMRM, G. de With, R. Metselaar, J. Eur. Ceram. Soc. 10 (1992) 339–346.
[678] H.X. Willems, G. Dewith, R. Metselaar, J. Eur. Ceram. Soc. 12 (1993) 43–49.
[679] N. Holonyak, S.F. Bevacqua, Appl. Phys. Lett. 1 (1962) 82–83.
[680] M. Cantore, N. Pfaff, R.M. Farrell, J.S. Speck, S. Nakamura, S.P. DenBaars, Opt. Express 24 (2016) A215-A21.
[681] S. Grzanka, P. Perlin, R. Czernecki, L. Marona, M. Bockowski, B. Lucznik, et al., Appl. Phys. Lett. 95 (2009) 071108.
[682] G. Ledru, C. Catalano, P. Dupuis, G. Zissis, AIP Adv. 4 (2014) 107134.
[683] S. Nishiura, S. Tanabe, K. Fujioka, Y. Fujimoto, Opt. Mater. 33 (2011) 688–691.
[684] N.A. Wei, T.C. Lu, F. Li, W. Zhang, B.Y. Ma, Z.W. Lu, et al., Appl. Phys. Lett. 101 (2012) 061902.
[685] S. Hu, C.H. Lu, G.H. Zhou, X.X. Liu, X.P. Qin, G.H. Liu, et al., Ceram. Int. 42 (2016) 6935–6941.
[686] R.L. Zheng, D.W. Luo, Y. Yuan, Z.Y. Wang, Y. Zhang, W. Wei, et al., J. Am. Ceram. Soc. 98 (2015) 3231–3235.
[687] S.W. Feng, H.M. Qin, G.Q. Wu, H.C. Jiang, J.T. Zhao, Y.F. Liu, et al., J. Eur. Ceram. Soc. 37 (2017) 3403–3409.
[688] S. Hu, X.P. Qin, G.H. Zhou, C.H. Lu, G.H. Liu, Z.Z. Xu, et al., Opt. Mater. Express 5 (2015) 2902–2910.
[689] L. Zhang, B.H. Sun, L.C. Gu, W. Bu, X.Z. Fu, R. Sun, et al., Appl. Surf. Sci. 455 (2018) 425–432.
[690] J. Ueda, K. Kuroishi, S. Tanabe, Appl. Phys. Lett. 104 (2014) 101904.
[691] J. Ueda, S. Tanabe, T. Nakanishi, J. Appl. Phys. 110 (2011) 053102.
[692] J. Xu, J. Ueda, K. Kuroishi, S. Tanabe, Scr. Mater. 102 (2015) 47–50.
[693] J. Ueda, K. Kuroishi, S. Tanabe, Appl. Phys. Express 7 (2014) 062201.
[694] C.Y. Ma, F. Tang, J.D. Chen, R. Ma, X.Y. Yuan, Z.C. Wen, et al., J. Eur. Ceram. Soc. 36 (2016) 4205–4213.
[695] M. Boyer, A.J.F. Carrion, S. Ory, A. Isabel Becerro, S. Villette, S.V. Eliseeva, et al., J. Mater. Chem. C 4 (2016) 3238–3247.
[696] Y. Sun, Q.H. Yang, H.Q. Wang, X.B. Jiang, B.F. Li, Z.F. Shi, J. Lumin. 194 (2018) 452–455.
[697] Z.C. Wen, C.Y. Ma, C. Zhao, F. Tang, Z.J. Cao, Z.Q. Cao, et al., Opt. Lett. 43 (2018) 2438–2441.
[698] K. Li, H. Wang, X. Liu, W.M. Wang, Z.Y. Fu, J. Eur. Ceram. Soc. 37 (2017) 4229–4233.
[699] S.X. Li, Q.Q. Zhu, D.M. Tang, X.J. Liu, G. Ouyang, L.L. Cao, et al., J. Mater. Chem. C 4 (2016) 8648–8654.
[700] A.T. Wieg, E.H. Penilla, C.L. Hardin, Y. Kodera, J.E. Garay, APL Mater. 4 (2016) 126105.
[701] R. Autrata, Scanning Microsc. 3 (1989) 739–763.
[702] G. Blasse, Chem. Mater. 6 (1994) 1465–1475.
[703] C. Greskovich, S. Duclos, Annu. Rev. Mater. Sci. 27 (1997) 69–88.
[704] R.L. Heath, R. Hofstadter, E.B. Hughes, Nucl. Instrum. Methods 162 (1979) 431–476.
[705] A. Knapitsch, P. Lecoq, Int. J. Mod. Phys. A (2014) 29.
[706] L. Nadaraia, N. Jalabadze, R. Chedia, L. Khundadze, Ceram. Int. 39 (2013) 2207–2214.
[707] M. Nikl, V.V. Laguta, A. Vedda, Phys. Status Solidi B 245 (2008) 1701–1722.
[708] M. Nikl, A. Yoshikawa, K. Kamada, K. Nejezchleb, C.R. Stanek, J.A. Mares, et al., Prog. Cryst. Growth Charact. Mater. 59 (2013) 47–72.
[709] P.A. Rodnyi, P. Dorenbos, C.W.E. Vaneijk, Phys Status Solidi B 187 (1995) 15–29.
[710] V.D. Ryzhkov, P.E. Stadnik, Y.A. Yakovlev, Instrum. Exp. Tech. 27 (1984) 1045–1056.
[711] C.W.E. van Eijk, Phys. Med. Biol. 47 (2002) R85–R106.
[712] J. Graichen, K. Maier, J. Schuth, A. Siepe, W. von Witsch, Nucl. Instr. Methods Phys. Res. Sec. A 485 (2002) 774–779.
[713] M. Picchio, A. Savi, M. Lecchi, C. Landoni, L. Gianolli, M. Brioschi, et al., Quart. J. Nucl. Med. 47 (2003) 90–100.
[714] V.V. Nagarkar, V. Gaysinskiy, E.E. Ovechkina, S.C. Thacker, S.R. Miller, C. Brecher, et al., IEEE Trans. Nucl. Sci. 54 (2007) 1378–1382.
[715] I. Valais, D. Nikolopoulos, N. Kalivas, A. Gaitanis, G. Loudos, I. Sianoudis, et al., Nucl. Instr. Methods Phys. Res. Sec. A 571 (2007) 343–345.
[716] L. Gironi, C. Arnaboldi, S. Capelli, O. Cremonesi, G. Pessina, S. Pirro, et al., Opt. Mater. 31 (2009) 1388–1392.
[717] L. Nagornaya, G. Onyshchenko, E. Pirogov, N. Starzhinskiy, I. Tupitsyna, V. Ryzhikov, et al., Nucl. Instr. Methods Phys. Res. Sec. A 537 (2005) 163–167.
[718] C. Zaldo, E. Moya, J. Phys. Cond. Matter 5 (1993) 4935–4944.
[719] C.D. Greskovich, D. Cusano, D. Hoffman, R.J. Riedner, Am. Ceram. Soc. Bull. 71 (1992) 1120–1130.
[720] T. Martin, P.A. Douissard, Z.M. Seeley, N. Cherepy, S. Payne, E. Mathieu, et al., IEEE Trans. Nucl. Sci. 59 (2012) 2269–2274.
[721] R.C. Placious, D. Polansky, H. Berger, C. Bueno, C.L. Vosberg, R.A. Betz, et al., Mater. Eval. 49 (1991) 1419–1421.
[722] C. Bueno, M.D. Barker, R.A. Betz, R.C. Barry, R.A. Buchanan, Nondestructive Evaluation of Aircraft Structures Using High-resolution Real-time Radiography, (1995).
[723] Y.P. Chen, D.L. Luo, J. Inorg. Mater. 27 (2012) 1121–1128.
[724] X.Y. Sun, M. Zhang, X.G. Yu, Int. J. Mater. Res. 102 (2011) 104–108.
[725] P.C. Sangway, R.E. Stapleton, J. Electrochem. Soc. 124 (1977) C110.
[726] K. Somaiah, M.V. Narayana, L.H. Brixner, Phys. Status Solidi A 117 (1990) K81-K4.
[727] V. Shanker, K. Ohmi, S. Tanaka, H. Kobayashi, Ieice Trans. Electron. E81C (1998) 1721–1724.
[728] S. Tao, Z.H. Gu, A. Nathan, J. Vacuum Sci. Technol. A Vacuum Surf. Films 20 (2002) 1091–1094.
[729] J.H. Timmer, T.L. van Vuure, V. Bom, C.W. van Eijk, J. de Haas, J.M. Schippers, Nucl. Instr. Methods Phys. Res. Sec. A 478 (2002) 98–103.
[730] J.M. Schippers, S.N. Boon, P. van Luijk, Nucl. Instr. Methods Phys. Res. Sec. A 477 (2002) 480–485.
[731] A.V. Klyachko, V. Moskvin, D.F. Nichiporov, K.A. Solberg, Nucl. Instr. Methods Phys. Res. Sec. A 694 (2012) 271–279.
[732] G.H.V. Bertrand, M. Hamel, S. Normand, F. Sguerra, Nucl. Instr. Methods Phys. Res. Sec. A 776 (2015) 114–128.
[733] G.H.V. Bertrand, M. Hamel, F. Sguerra, Chem. Eur. J. 20 (2014) 15660–15685.
[734] N.J. Cherepy, R.D. Sanner, P.R. Beck, E.L. Swanberg, T.M. Tillotson, S.A. Payne, et al., Nucl. Instr. Methods Phys. Res. Sec. A 778 (2015) 126–132.
[735] K. Boyer, B.D. Thompson, A. McPherson, C.K. Rhodes, J. Phys. B 27 (1994) 4373–4389.
[736] H. Kubo, A. Sasaki, K. Moribayashi, S. Higashijima, H. Takenaga, K. Shirnizu, et al., J. Nucl. Mater. 363 (2007) 1441–1445.
[737] S.J. Duclos, C.D. Greskovich, R.J. Lyons, J.S. Vartuli, D.M. Hoffman, R.J. Riedner, et al., Nucl. Instr. Methods Phys. Res. Sec. A 505 (2003) 68–71.
[738] W. Kostler, A. Winnacker, W. Rossner, B.C. Grabmaier, J. Phys. Chem. Solids 56 (1995) 907–913.
[739] I. Godmanis, W. Hohenau, Phys. Status Solidi A Appl. Res. 111 (1989) 335–343.
[740] T. Yanagida, Y. Fujimoto, T. Ito, K. Uchiyama, K. Mori, Appl. Phys. Express (2014) 7.
[741] T. Yanagida, H. Sato, Opt. Mater. 38 (2014) 174–178.
[742] W. Knupfer, E. Hell, D. Mattern, Nucl. Phys. B Proc. Suppl. 78 (1999) 610–615.
[743] H. Yamada, A. Suzuki, Y. Uchida, M. Yoshida, H. Yamamoto, Y. Tsukuda, J. Electrochem. Soc. 136 (1989) 2713–2716.
[744] J. Shimizu, H. Yamada, S. Murata, A. Tomita, M. Kitamura, A. Suzuki, Ieee Photonics Technol. Lett. 3 (1991) 773–776.
[745] P.A. Rodnyi, P. Dorenbos, C.W.E. Vaneijk, M.J. Weber, P. Lecoq, R.C. Ruchti, C. Woody, W.M. Yen, R.Y. Zhu (Eds.), Scintillator and Phosphor Materials, 1994, pp. 379–385.
[746] P.A. Rodnyi, P. Dorenbos, C.W.E. Vaneijk, Phys. Status Solidi B Basic Res. 187 (1995) 15–29.
[747] R. Devanathan, L.R. Corrales, F. Gao, W.J. Weber, Nucl. Instr. Methods Phys. Res. Sec. A 565 (2006) 637–649.
[748] S.M. Gruner, M.W. Tate, E.F. Eikenberry, Rev. Sci. Instrum. 73 (2002) 2815–2842.
[749] G.P. Morgan, T.J. Glynn, G.F. Imbusch, J.P. Remeika, J. Chem. Phys. 69 (1978) 4859–4866.
[750] G.P. Morgan, J.F. Treacy, T.J. Glynn, G.F. Imbusch, J.P. Remeika, J. Lumin. (1979) 18-9:175-8.
[751] C.J. Donnelly, T.J. Glynn, G.P. Morgan, G.F. Imbusch, J. Lumin. (1991) 48-9:283-7.
[752] B. Henderson, G.F. Imbusch, Contemp. Phys. 29 (1988) 235–272.
[753] G.F. Imbusch, J. Lumin. 53 (1992) 465–467.
[754] B.D. Maccraith, T.J. Glynn, G.F. Imbusch, C. McDonagh, J. Phys. C-Solid State Phys. 13 (1980) 4211–4216.

SDC EX. 1018 - 63/66

[755] M. Ilmer, J. Schneider, M. Ostertag, T. Berthold, L. Bohaty, B.C. Grabmaier, R. Delhez, E.J. Mittemeijer, Studies of structural and luminescent properties of $Gd_3Ga_5O_{12}$:Cr and corresponding solid solutions, Epdic 3, Pts 1 and 2: Proceedings of the 3rd European Powder Diffraction Conference, (1994), pp. 801–806.
[756] A. Yamaji, V.V. Kochurikhin, S. Kurosawa, A. Suzuki, Y. Fujimoto, Y. Yokota, et al., IEEE Trans. Nucl. Sci. 61 (2014) 320–322.
[757] G. Blasse, B.C. Grabmaier, M. Ostertag, J. Alloys. Compd. 200 (1993) 17–18.
[758] H. Forest, G. Ban, J. Electrochem. Soc. 116 (1969) 474–478.
[759] H. Forest, G. Ban, J. Electrochem. Soc. 118 (1971) 1999–2001.
[760] S.J. Duclos, C.D. Greskovich, C.R. Oclair, M.J. Weber, P. Lecoq, R.C. Ruchti, C. Woody, W.M. Yen, R.Y. Zhu (Eds.), Scintillator and Phosphor Materials, 1994, pp. 503–509.
[761] J. Hsieh, E. Williams, C. Shaughnessy, X.Y. Tang, B. Grekowicz, R. Nilsen, et al., U. Bonse (Ed.), Developments in X-Ray Tomography Iv, 2004, pp. 694–700.
[762] H. Grassmann, H.G. Moser, H. Dietl, G. Eigen, V. Fonseca, E. Lorenz, et al., Nucl. Instr. Methods Phys. Res. Sec. A 234 (1985) 122–124.
[763] N.J. Cherepy, J.D. Kuntz, Z.M. Seeley, S.E. Fisher, O.B. Drury, B.W. Sturm, et al., A. Burger, L.A. Franks, R.B. James (Eds.), Hard X-Ray, Gamma-Ray, and Neutron Detector Physics Xii, 2010.
[764] N.J. Cherepy, J.D. Kuntz, J.J. Roberts, T.A. Hurst, O.B. Drury, R.D. Sanner, et al., A. Burger, L.A. Franks, R.B. James (Eds.), Hard X-Ray, Gamma-Ray, and Neutron Detector Physics X, Spie-Int Soc Optical Engineering, Bellingham, 2008.
[765] A. Lempicki, C. Brecher, P. Szupryczynski, H. Lingertat, V.V. Nagarkar, S.V. Tipnis, et al., Nucl. Instr. Methods Phys. Res. Sec. A 488 (2002) 579–590.
[766] C. Brecher, R.H. Bartram, A. Lempicki, J. Lumin. 106 (2004) 159–168.
[767] R.H. Bartram, A. Lempicki, L.A. Kappers, D.S. Hamilton, J. Lumin. 106 (2004) 169–176.
[768] Y. Futami, T. Yanagida, Y. Fujimoto, J. Pejchal, M. Sugiyama, S. Kurosawa, et al., Radiat. Meas. 55 (2013) 136–140.
[769] Y. Hui, X. Sun, J. Chen, X. Li, D. Huo, S. Liu, et al., IEEE Trans. Nucl. Sci. 61 (2014) 367–372.
[770] T. Yanagida, T. Roh, H. Takahashi, S. Hirakuri, M. Kokubun, K. Makishima, et al., Nucl. Instr. Methods Phys. Res. Sec. A 579 (2007) 23–26.
[771] N.J. Cherepy, J.D. Kuntz, T.M. Tillotson, D.T. Speaks, S.A. Payne, B.H.T. Chai, et al., Nucl. Instr. Methods Phys. Res. Sec. A 579 (2007) 38–41.
[772] S.P. Liu, X.Q. Feng, Y. Shi, L.X. Wu, J.L. Luo, W. Wang, et al., Opt. Mater. 36 (2014) 1973–1977.
[773] T. Yanagida, Adv. Sci. Technol. 98 (2017) 44–53.
[774] E. Zych, C. Brecher, A.J. Wojtowicz, H. Lingertat, J. Lumin. 75 (1997) 193–203.
[775] E. Mihokova, M. Nikl, J.A. Mares, A. Beitlerova, A. Vedda, K. Nejezchleb, et al., J. Lumin. 126 (2007) 77–80.
[776] Y. Zorenko, V. Gorbenko, I. Konstankevych, A. Voloshinovskii, G. Stryganyuk, V. Mikhallin, et al., J. Lumin. 114 (2005) 85–94.
[777] V.V. Osipov, A.V. Ishchenko, V.A. Shitov, R.N. Maksimov, K.E. Lukyashin, V.V. Platonov, et al., Opt. Mater. 71 (2017) 98–102.
[778] H.L. Li, X.J. Liu, R.J. Xie, G.H. Zhou, N. Hirosaki, X.P. Pu, et al., J. Appl. Phys. 47 (2008) 1657–1661.
[779] M. Nikl, J.A. Mares, N. Solovieva, H.L. Li, X.J. Liu, L.P. Huang, et al., J. Appl. Phys. 101 (2007) 033515.
[780] T. Yanagida, Y. Fujimoto, K. Kamada, D. Totsuka, H. Yagi, T. Yanagitani, et al., IEEE Trans. Nucl. Sci. 59 (2012) 2146–2151.
[781] Z.M. Seeley, N.J. Cherepy, S.A. Payne, J. Cryst. Growth 379 (2013) 79–83.
[782] M. Mori, J. Xu, G. Okada, T. Yanagida, J. Ueda, S. Tanabe, J. Ceram. Soc. Jpn. 124 (2016) 569–573.
[783] J. Li, S. Sahi, M. Groza, Y. Pan, A. Burger, R. Kenarangui, et al., J. Am. Ceram. Soc. 100 (2017) 150–156.
[784] R. Hupke, C. Doubrava, Phys. Med. 15 (1999) 315–318.
[785] R.H. Bartram, D.S. Hamilton, L.A. Kappers, A. Lempicki, J. Lumin. 75 (1997) 183–192.
[786] R.H. Bartram, D.S. Hamilton, L.A. Kappers, A. Lempicki, J. Glodo, J.S. Schweitzer, et al., Radiat. Eff. Defects Solids 150 (1999) 11–14.
[787] V.V. Nagarkar, S.R. Miller, S.V. Tipnis, A. Lempicki, C. Brecher, H. Lingertat, Nucl. Instr. Methods Phys. Res. Sec. B 213 (2004) 250–254.
[788] H. Retot, S. Blahuta, A. Bessiere, B. Viana, B. LaCourse, E. Mattmann, J. Phys. D Appl. Phys. 44 (2011) 235101.
[789] T. Yanagida, Y. Fujimoto, S. Kurosawa, K. Watanabe, H. Yagi, T. Yanagitani, et al., Appl. Phys. Express 4 (2011) 126402.
[790] T. Yanagida, Y. Fujimoto, Y. Yokota, A. Yoshikawa, S. Kuretake, Y. Kintaka, et al., Opt. Mater. 34 (2011) 414–418.
[791] R. Chipaux, M. Cribier, C. Dujardin, N. Garnier, N. Guerassimova, J. Mallet, et al., Nucl. Instr. Methods Phys. Res. Sec. A 486 (2002) 228–233.
[792] N. Guerassimova, C. Dujardin, N. Garnier, C. Pedrini, A.G. Petrosyan, I.A. Kamenskikh, et al., Nucl. Instr. Methods Phys. Res. Sec. A 486 (2002) 278–282.
[793] P. Antonini, S. Belogurov, G. Bressi, G. Carugno, P. Santilli, Nucl. Instr. Methods Phys. Res. Sec. A 488 (2002) 591–603.
[794] S. Belogurov, G. Bressi, G. Carugno, Y. Grishkin, Nucl. Instr. Methods Phys. Res. Sec. A 516 (2004) 58–67.
[795] S. Belogurov, G. Bressi, G. Carugno, M. Moszynski, W. Czarnacki, M. Kapusta, et al., Nucl. Instr. Methods Phys. Res. Sec. A 496 (2003) 385–389.
[796] T. Kato, G. Okada, T. Yanagida, Ceram. Int. 42 (2016) 5617–5622.
[797] T. Kato, G. Okada, T. Yanagida, J. Ceram. Soc. Jpn. 124 (2016) 559–563.
[798] F. Nakamura, T. Kato, G. Okada, N. Kawaguchi, K. Fukuda, T. Yanagida, Ceram. Int. 43 (2017) 604–609.
[799] H. Jiang, Y.K. Zou, Q. Chen, K.K. Li, R. Zhang, Y. Wang, et al., H. Ming, X.P. Zhang, M.Y. Chen (Eds.), Optoelectronic Devices and Integration, Pts 1 and 2, Spie-Int Soc Optical Engineering, Bellingham, 2005, pp. 380–394.
[800] Q.W. Song, X.M. Wang, R. Bussjager, J. Osman, Appl. Opt. 35 (1996) 3155–3162.
[801] F.A. Londono, J.A. Eiras, D. Garcia, Opt. Mater. 34 (2012) 1310–1313.
[802] F.L. Li, K.W. Kwok, J. Am. Ceram. Soc. 96 (2013) 3557–3562.
[803] W.L. Ji, X.Y. He, W.X. Cheng, P.S. Qiu, X. Zeng, B. Xia, et al., Ceram. Int. 41 (2015) 1950–1956.
[804] B.R. Peters, P.J. Reardon, J.K. Wong, G.C. Righini, S. Honkanen (Eds.), Integrated Optics Devices V, Spie-Int Soc Optical Engineering, Bellingham, 2001, pp. 242–248.
[805] T. Tatebayashi, T. Yamamoto, H. Sato, Appl. Opt. 30 (1991) 5049–5055.
[806] T. Tatebayashi, T. Yamamoto, H. Sato, Appl. Opt. 31 (1992) 2770–2775.
[807] G. Staudigl, H. Benien, R. Suchentrunk, Materialwissenschaft Werkstofftechnik 31 (2000) 360–364.
[808] M. Grujicic, W.C. Bell, B. Pandurangan, Mater. Des. 34 (2012) 808–819.
[809] J.A. Salem, J. Am. Ceram. Soc. 96 (2013) 281–289.
[810] G. Subhash, Exp. Mech. 53 (2013) 1–2.
[811] C.A. Klein, Appl. Phys. Lett. 87 (2005) 231117.
[812] C.A. Klein, J. Appl. Phys. 100 (2006) 083101.
[813] A. Krell, E. Strassburger, T. Hutzler, J. Klimke, J. Am. Ceram. Soc. 96 (2013) 2718–2721.
[814] M.C.L. Patterson, A.A. DiGiovanni, L. Fehrenbacher, D.W. Roy, R.W. Tustison (Ed.), Window and Dome Technologies VIII, SPIE-Int Soc Optical Engineering, Bellingham, 2003, pp. 71–79.
[815] O. Borrero-Lopez, A.L. Ortiz, A.D. Gledhill, F. Guiberteau, T. Mroz, L.M. Goldman, et al., J. Eur. Ceram. Soc. 32 (2012) 3143–3149.
[816] T. Mroz, L.M. Goldman, A.D. Gledhill, D.S. Li, N.P. Padture, Int. J. Appl. Ceram. Technol. 9 (2012) 83–90.
[817] T.J. Mroz, T.M. Hartnett, J.M. Wahl, L.M. Goldman, J. Kirsch, W.R. Lindberg, R.W. Tustison (Ed.), Window and Dome Technologies and Materials IX, SPIE-Int Soc Optical Engineering, Bellingham, 2005, pp. 64–70.
[818] M. Ramisetty, S. Sastri, U. Kashalikar, L.M. Goldman, N. Nag, Am. Ceram. Soc. Bull. 92 (2013) 20–25.
[819] R.A. Beyer, H. Kerwien, R.W. Tustison (Ed.), Window and Dome Technologies and Materials VI, 1999, pp. 113–118.
[820] A. Krell, A. Bales, Int. J. Appl. Ceram. Technol. 8 (2011) 1108–1114.
[821] A. Krell, J. Klimke, T. Hutzler, J. Eur. Ceram. Soc. 29 (2009) 275–281.
[822] S. Bayya, G. Villalobos, W. Kim, J. Sanghera, G. Chin, M. Hunt, et al., Mater. Technol. Appl. Optics Structures Components Sub-Systems (2013) 8837.
[823] B. Pazol, P. McGuire, R. Gentilman, J. Locher, J. Askinazi, A.J. Marker, E.G. Arthurs (Eds.), Inorganic Optical Materials II, 2000, pp. 52–58.
[824] J. Askinazi, R.V. Wientzen, C.P. Khattak, R.W. Tustison (Ed.), Window and Dome Technologies and Materials VII, 2001, pp. 1–11.
[825] J. Askinazi, J.W. Tuttle (Ed.), Tactical Infrared Systems, 1991, pp. 100–109.
[826] J. Askinazi, G.W. Wilkerson (Ed.), Passive Materials for Optical Elements II, 1993, pp. 149–158.
[827] J. Askinazi, R.W. Tustison (Ed.), Window and Dome Technologies and Materials V, 1997, pp. 214–225.
[828] M.R. Borden, J. Askinazi, R.W. Tustison (Ed.), Window and Dome Technologies and Materials V, 1997, pp. 246–249.
[829] R. Gentilman, P. McGuire, D. Fiore, K. Ostreicher, J. Askinazi, R.W. Tustison (Ed.), Window and Dome Technologies VIII, 2003, pp. 12–17.
[830] R. Gentilman, P. McGuire, D. Fiore, K. Ostreicher, J. Askinazi, R.W. Tustison (Ed.), Window and Dome Technologies VIII, 2003, pp. 54–60.
[831] R. Gentilman, P. McGuire, B. Pazol, J. Askinazi, R. Steindl, J. Locher, R.W. Tustison (Ed.), Window and Dome Technologies and Materials VI, 1999, pp. 282–287.
[832] P. McGuire, B. Pazol, R. Gentilman, J. Askinazi, J. Locher, R.W. Tustison (Ed.), Window and Dome Technologies and Materials VII, 2001, pp. 12–19.
[833] J.M. Sands, C.G. Fountzoulas, G.A. Gilde, P.J. Patel, J. Eur. Ceram. Soc. 29 (2009) 261–266.
[834] E. Strassburger, J. Eur. Ceram. Soc. 29 (2009) 267–273.
[835] J.W. McCauley, E. Strassburger, P. Patel, B. Paliwal, K.T. Ramesh, Exp. Mech. 53 (2013) 3–29.
[836] M.S. Vysotsky, E.K. Pochtenny, M.I. Gorbatsevich, Doklady Akademii Nauk Belarusi 36 (1992) 511–514.
[837] M.S. Vysotsky, E.K. Pochtenny, M.I. Gorbatsevich, A.V. Kurban, Doklady Akademii Nauk Belarusi 35 (1991) 334–337.
[838] T. Benitez, S.Y. Gomez, A.P. Novaes de Oliveira, N. Travitzky, D. Hotza, Ceram. Int. 43 (2017) 13031–13046.
[839] A. John, H.K. Varma, S. Vijayan, A. Bernhardt, A. Lode, A. Vogel, et al., Biomed. Mater. 4 (2009) 015007.
[840] S. Bodhak, V.K. Balla, S. Bose, A. Bandyopadhyay, U. Kashalikar, S.K. Jha, et al., J. Mater. Sci. Mater. Med. 22 (2011) 1511–1519.
[841] M. Krishnan, B. Tiwari, S. Seema, N. Kalra, P. Biswas, K. Rajeswari, et al., J. Mater. Sci. Mater. Med. 25 (2014) 2591–2599.
[842] D.F. Williams, Biomaterials 29 (2008) 2941–2953.
[843] L.Q. An, A. Ito, T. Goto, J. Eur. Ceram. Soc. 32 (2012) 1035–1040.
[844] P.D. Zhao, H.Z. Zhao, J. Yu, H. Zhang, H.J. Gao, Q. Chen, Ceram. Int. 44 (2018) 1356–1361.
[845] N. Peng, C.J. Deng, H.X. Zhu, J. Li, S.H. Wang, Ceram. Int. 41 (2015) 5513–5524.
[846] E.G. Fu, Y. Fang, M.J. Zhuo, S.J. Zheng, Z.X. Bi, Y.Q. Wang, et al., Acta Mater. 64 (2014) 100–112.
[847] A. Mondal, S. Ram, Ceram. Int. 30 (2004) 239–249.
[848] E. Djurado, P. Bouvier, G. Lucazeau, J. Solid State Chem. 149 (2000) 399–407.
[849] M. Aghazadeh, A.A.M. Barmi, H.M. Shiri, S. Sedaghat, Ceram. Int. 39 (2013) 1045–1055.

SDC EX. 1018 - 64/66

[850] S.V. Ovsyannikov, E. Bykova, M. Bykov, M.D. Wenz, A.S. Pakhomova, K. Glazyrin, et al., J. Appl. Phys. (2015) 118.
[851] J. Zeler, L.B. Jerzykiewicz, E. Zych, Materials 7 (2014) 7059–7072.
[852] J. Li, Y.B. Pan, F.G. Qiu, Y.S. Wu, W.B. Liu, J.K. Guo, Ceram. Int. 33 (2007) 1047–1052.
[853] S. Takahashi, A. Kan, H. Ogawa, J. Eur. Ceram. Soc. 37 (2017) 1001–1006.
[854] I.A. Aksay, D.M. Dabbs, M. Sarikaya, J. Am. Ceram. Soc. 74 (1991) 2343–2358.
[855] H. Yoshida, K. Morita, B.N. Kim, K. Hiraga, K. Yamanaka, K. Soga, et al., J. Am. Ceram. Soc. 94 (2011) 3301–3307.
[856] A. Ikesue, K. Kamata, J. Am. Ceram. Soc. 79 (1996) 1927–1933.
[857] W. Zhang, T.C. Lu, B.Y. Ma, N. Wei, Z.W. Lu, F. Li, et al., Opt. Mater. 35 (2013) 2405–2410.
[858] A. Katz, E. Barraud, S. Lemonnier, E. Sorrel, J. Boehmler, A. Blanc, et al., Ceram. Int. 43 (2017) 10673–10682.

Dr Zhuohao Xiao received his PhD degree from Central South University, China, in 2009. He is currently a Professor in Jingdezhen Ceramic Institute. His research interests include optical materials, glass-ceramics, glass materials and other functional materials. He serves as referees for various international and domestic journals. He is a Member of Chinese Ceramic Society, Chinese Mechanical Engineering Society, and China Instrument and Control Society.

Dr Shijin Yu got his PhD degree from Huazhong University of Science and Technology, China, in 2009. His research interest focuses on design and fabrication of nanomaterials for energy applications. He serves as referees for *Nuclear Instruments and Methods in Physics Research A, Journal of the Chinese Ceramic Society*. He is a Member of Committee on Industrial, Scientific and Medical RF Equipment.

Dr Yueming Li is current a Professor, at the School of Materials Science and Engineering, Jingdezhen Ceramics Institute, China. He got his PhD degree from Wuhan University of Technology, China, in 2004. His research interests include transparent ceramics, ferroelectric/piezoelectric ceramics and lead-free piezoelectric ceramics. He is one of the directors of the Chinese Ceramic Society and the China Instrument and Control Society.

Dr Shuangchen Ruan is currently a professor at the Shenzhen Technology University, China. He received his BS and MS degrees from the Northwest University in China in 1986 and 1989, respectively. He got his PhD degree from Tianjin University in 2004. He worked in Imperial College London from 1993 to 1994. He was promoted as a Full Professor in 1994. His research interests focus on solid state laser, fiber laser, ultrafast pulse generation and carbon-based nanomaterials. He has published more than 200 journal papers in leading journals of related areas.

Dr Ling Bing Kong got his PhD degree from Xi'an Jiaotong University, China, in 1997. He then moved to Nanyang Technological University, Singapore, as Posdoc Fellow and Research Fellow. Since 2002, he worked in Temasek Laboratories, National Univeristy of Singapore. In 2012, he returned Nanyang Technological University. He joined Shenzhen Technology University in 2018. His reseaerch interests included funcational ceramics, composites and nanomaterials for energy applications. He serves as referees for more than 50 internal journals and Member of Editorial Board, Guest Editors of several journals.

Dr Kun Zhou is an Associate Professor at the School of Mechanical & Aerospace Engineering, Nanyang Technological University, Singapore. His research interests focus on micro/nano mechanics of materials and structures, novel computational methods for modeling material behaviour, and sustainable energy and green technologies. He serves as an Editor of Journal of Micromechanics and Molecular Physics (World Scientific), an Associate Editor of Mechanics Research Communications (Elsevier), and Editorial Board Members of International Journal of Applied Mechanics (World Scientific), Virtual and Physical Prototyping (Taylor & Francis) and Materials Physics and Mechanics (Russian Academy of Sciences). He is also on the Elasticity Technical Committee of American Society of Civil Engineers (ASCE). So far, he has published 10 book chapters and over 190 papers in refereed journals including Progress in Materials Science, Physical Review Letters, Advanced Materials, ACS Nano, JMPS, Acta Materialia, CMAME and IJNME.

Dr. Haibin Su is an Associate Professor at The Hong Kong University of Science and Technology. He graduated from Stony Brook University, while performing his thesis projects in Center for Data Intensive Computing at Brookhaven National Laboratory. Then, he went to California Institute of Technology, taking a three-year PostDoc position in Professor William A. Goddard's research center. His research interest includes development and application of theoretical and computational physical science, i.e., quantum-mechanical and classical simulations and modeling of the structural, kinetic and dynamic properties of complex functional systems, in particular emergent collective properties at multiple spatial and temporal scales.

Zhengjun Yao is currently a Professor in the College of Materials and Technologies, Nanjing University of Aeronautics and Astronautics, China. He got his PhD degree from Nanjing University of Aeronautics ad Astronautics in 2004. He has published about 200 journal papers, 2 textbooks and more than 30 patents. His research interests include functional materials, materials and surface engineering, composite materials, materials analysis and simulations.

Wenxiu Que is currently a Professor at Xi'an Jiaotong University. He got his PhD degree from Xi'an Jiaotong University in 1995. His research interests cover transparent laser ceramics, organic-inorganic hybrid materials based on organically modified silanes for photonic applications, oxide semiconductor nanostructured arrays/polymer organic-inorganic nanocomposite materials for clean energy and environment applications, semiconductor compound and organic thin film solar cells, as well as organic-inorganic perovskite solar cells, etc.

SDC EX. 1018 - 65/66

Yin Liu is currently a Professor at the Anhui University of Science and Technology. His research interests include inorganic functional materials, magnetic nanomaterials, functional ceramics, new energy materials and resource recycling. He has published > 100 papers, 1 book and 3 textbooks. He has been granted > 20 patents.

Tianshu Zhang is current the CEO of Anhui Advanced Target Co Ltd, Anhui, China, since he set up the company in 2013. He got his PhD degree from Nanyang Technological University, Singapore, in 2003. His research interest is on sintering mechanism of functional ceramics and development of ceramic products. He has published more than 180 scientific articles in international journals, 40 conference papers, 4 books and 10 book chapters.

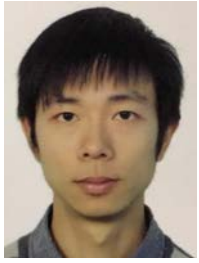

Dr Jun Wang was received his Bachelor's and Master's degrees from the Department of Electronic Science and Technology, Huazhong University of Science and Technology, China, in 2008 and 2011, respectively. He received his PhD degree from the School of Electrical and Electronic Engineering (EEE), Nanyang Technological University (NTU), Singapore, in 2017. He is currently a Research Fellow with the School of EEE, NTU. His research interests include fabrication, characterization and laser application of rare-earth doped sesquioxide and garnet transparent laser ceramics. He has published more than 10 papers in leading journals of ceramics and laser materials, including J. Am. Ceram. Soc., J. Eur. Ceram. Soc., Opt. Mater., Ceram. Intern., etc.

Dr Peng Liu received his PhD degree in Materials Science from the Shanghai Institute of Ceramics, Chinese Academy of Sciences, Shanghai, China, in 2014. From 2014 to 2016, he worked as a Research Scientist in Temasek Lab at Nanyang Technological University, Singapore. He is currently an Associate Professor in the School of Physics and Electronic Engineering, Jiangsu Normal University. His research interests include high strength $MgAl_2O_4$ transparent ceramics, fluoride laser ceramics and transition metal doped ZnS/ZnSe laser ceramics. He has strong publications in J. Am. Ceram. Soc., Opt. Mater., J. Eur. Ceram. Soc., etc.

Dr Deyuan Shen is a Professor at the School of Physics and Electronic Engineering, Jiangsu Normal University, China. He obtained his PhD degree from Shandong University, China, in 1999. He published about 300 journal papers and invited speakers in various international conferences. His research interests focus on mid-IR high power lasers. He is a senior expert in high power fiber lasers and fiber-solid hybrid lasers.

Dr Mathieu Allix received his PhD degree from University of Caen (F), France, in 2000. His research interests include fabrication and characterization of glass-ceramics and glass materials for various functional applications. He has been coordinators of the CrystOG ANR-JC project, FOCAL ANR project, CEMHTI local coordinator of the GCWEB ANR project. He carried scientific and technical responsibility of a research collaboration contract with Saint-Gobain Recherche. He won Laureate of the 2013 CNRS bronze Medal.

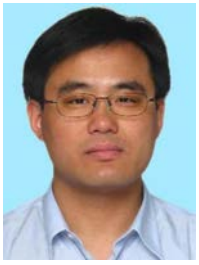

Dr Jian Zhang is a Professor in the Shanghai Institute of Ceramics, Chinese Academy of Science, China. He obtained his BSc in Ceramic Engineering from Jingde Zhen Ceramic Institute, China in 1996 and PhD at Shanghai Institute of Ceramics, Chinese Academy of Sciences in 2005. After that, he worked as a Research Associate in the Institute. In the beginning of 2007, he joined the Institute for Materials, University of Leeds, UK, as a Research Fellow. From Aug. 2008, he was a Research Fellow first and Research Scientist later in the Temasek Lab at Nanyang Technological University. His research interests are transparent ceramics fabrication and their optical spectroscopic properties. He has published more than 200 journal papers, with most of them being on transparent ceramics.

Dr Dingyuan Tang is currently an Associate Professor at the Nanyang Technological University, Singapore. He got his PhD degree from Hannover University, Germany, in 1993. He has over thirty-year research experience on lasers, nonlinear optics and optical materials. Dr Tang has published over 300 international journal papers with ISI citations of > 8000 and an H-index of 46. He has supervised twenty PhD students and was granted funding of more than S$50 million. He is currently an associated editor for the "*Optical Engineering*" and "*Optics Express*" journals. He is a member of Optical Society of America.

SDC EX. 1018 - 66/66